A quantitative Förster resonance energy transfer method reveals functionally relevant structural variations in ErbB transmembrane receptors in cells

Thesis submitted in accordance with the requirements of the University of Liverpool for the degree of Doctor in Philosophy by

Christopher James Tynan

November 2008

Christopher James Tynan

A quantitative Förster resonance energy transfer method reveals functionally relevant structural variations in ErbB transmembrane receptors in cells

Abstract

The ErbB1 receptor is an important receptor tyrosine kinase implicated in many forms of human cancer. The current picture of how the receptor functions is heavily influenced by the few solved crystal structures of ErbB1 fragments that have been published to date.

This thesis describes the development of a method for investigating the three dimensional structure of membrane proteins *in situ* in order to gain insights into the relationship between their structure and function not gained from their high resolution structure determined *in vitro*. Driven by the need to explain discrepancies between the emerging picture of the three-dimensional architecture of signalling ErbB1 complexes in cell membranes and the accepted crystal structures, the developed method evaluates the distance of closest approach of the ErbB1 ligand binding site to the surface of adherent cells using Förster resonance energy transfer (FRET) a spectroscopic ruler widely used to report on distances less than 10 nm. These results are then correlated with the efficiency of FRET between donor and acceptor labelled ligand binding sites under the same experimental conditions, which provides information regarding the lateral topology of interacting receptors. The development of the method was made possible by the implementation of a multidimensional, multicolour confocal microscope which is also described.

Application of the method to ErbB1 receptors in the membranes of cancer cells demonstrated that two functionally distinct classes of the receptor - which transduce different signals in response to ligand binding despite being expressed as a single translation product - adopt different extracellular conformations with respect to the cell surface. This is entirely unanticipated by crystallographic models and not seen in previous FRET studies of receptors in suspended, isolated membranes.

It was shown that the consequences of these different conformations for the function of the receptor can be investigated by repeating the FRET measurements under a range of experimental conditions that disrupt normal ErbB1 function in cells. The orientation and topology of signalling ErbB1 in complexes was found to be variable and these variations may be caused by interactions between ErbB1 receptors and intracellular proteins. Further comparison of the results with complementary biochemical data regarding the phosphorylation state of receptors (which defines the signalling outcome of activated receptors) suggests the possibility that intracellular interaction primed extracellular conformations can produce different signalling outcomes upon ligand binding.

For Mum, Dad and Jem

Acknowledgements

I would like to express my thanks to all of the many people who have helped me in many wonderful ways to complete this thesis. Most of all I would like to thank my supervisor Peter Weightman and my local sponsor at the Science and Technology Facilities Council (STFC) Marisa Martin-Fernandez. Without them I would not have had the opportunity to do this research and I am extremely glad to have had their support.

I have to thank Marisa for placing her confidence in me and providing a never ending supply of enthusiasm and inspiration. I am incredibly grateful to her and her co-workers at Daresbury Laboratory who exposed me to the wide variety of interdisciplinary techniques that made coming into the lab so interesting. The roll call of people who didn't giggle at my many novice mistakes includes Mark Tobin who showed me how to culture animal cells and inadvertently provided me with my first membrane probes, David Clarke who must know the nuances of almost any practical experiment that can be performed and Stephen Webb who is a guru of fluorescence microscopy. It should be noted for posterity that it was Sarah Needham and Selene Roberts who were responsible for showing me how easy it is to manipulate another organism's DNA for my own personal gain. Stephen, Marisa, Sarah and Selene were always willing to lend an extra pair of hands when necessary or just keep me company during long periods of dark room activity which I really appreciated.

Several individuals must be thanked for the major ways that they have contributed to my research. Without the help of Selene Roberts and Daniel Rolfe chapter 6 of this thesis simply would not exist. Selene dropped nearly everything in order to shoulder half of the workload of preparing and imaging the hundreds of cell samples required to attempt the functional tests of ErbB1 structure. Indeed without a second pair of hands and someone to talk to I might still be in a dark room shouting at my samples. I am just as grateful to Dan for running Monte-Carlo simulations and data fitting without which all of that data would still be unanalysed. I am sure we'll be having many more vibrant discussions on the reliability and appropriateness of different data analysis methods in the near future! Steve Crouch, Jean Crouch and Paul Rutland of the 4C's company should also be acknowledged for delivering a working confocal image acquisition system after several adverse years.

My heartfelt thanks go to all of the friends who have helped to keep me sane and not grimaced too much at enthusiastic diatribes regarding the state of my project. Never before has the question 'so how's the work going?' been so dangerous. Jo, Mélodie, Lu, Em, Mark, Rob, Katie, Ally, Ed, Chris, Charlotte, Mark, Cad, Evi, Nick, Jo, Vic, Katie, Ed, Chris and Pete would all get a medal if I was the Queen. I would particularly like to thank my TV wife, Jo, for putting up with me for so long and always being around to make me smile.

Finally, my thanks go to my family for all their love, support and patience. Thank you to Jem and Nan for being a brilliant supply of hugs, and to Mum and Dad for all your love and encouragement.

Contents

List of Figures

List of Tables

Abbreviations

3D	Three dimensional
ACP	Acyl carrier protein
ADAM	A disintegrin and metaloprotease
ADC	Analogue to digital converter
AP	Acceptor peptide
ATP	Adenosine triphosphate
BS	Beam splitter
BSA	Bovine serum albumin
CaM	Calmodulin
Cbl	Cys-B like
CCD	Charged coupled device
CCP4	Collaborative computational project 4
CFD	Constant fraction discriminator
CoA	Co-enzyme A
CQ	Collisional quenching
DAG	1, 2, diaglycerol
DiD	1,1'-dioctadecyl-3,3,3',3'-tetramethylindodicarbocyanine, 4-chlorobenzenesulfo-nate
DiI	1,1'-dioctadecyl-3,3,3'3'-tetramethylindocarbo-cyanine perchlorate
DMD	Digital micromirror device
DNA	Deoxyribose nucleic acid
DSA	Deoxyglucose plus sodium azide
EF	Emission filter
EGF	Epidermal growth factor
eGFP	Enhanced green fluorescent protein
EDTA	ethylenediaminetetra-acetic acid
EGFR	Epidermal growth factor receptor
Em	Emission
Ex	Excitation
eYFP	Enhanced yellow fluorescent protein
FITC	Fluorescein isothiocyanate
FLIM	Fluorescence lifetime imaging microscopy
FRET	Förster resonance energy transfer

FWHM	Full width at half maximum
GFP	Green fluorescent protein
Grb2	Growth factor receptor bound protein 2
GUV	Giant unilamellar vesicle
HA	High affinity
HBSS	Hanks' buffered salt solution
HB-EGF	Heparin binding EGF-like growth factor
HEK	Human embryonic kidney
HER	Human epidermal growth factor receptor
His6	Histidine tag
IC	Internal conversion
IgG	Immunoglobulin G
IP3	Inositol 1, 3, 5 - triphosphate
ISC	Inter-system crossing
JM	Juxtamembrane
JNK	c-Jun N-terminal kinase
LA	Low affinity
mAB 2E9	Monoclonal antibody 2E9
MAPK	Mitogen activated protein kinase
MβCD	Methyl beta cyclodextrin
MBS	Main beam splitter
MCP	Multi-channel plate
MCPI	Multi-channel plate intensifier
mEGF	murine epidermal growth factor
MOPS	3-(N-morpholino) propanesulfonic acid
NA	Numerical aperture
NFκB	nuclear factor kappa-light-chain-enhancer of activated B cells
Ni-NTA	Nickle nitrilotriacetic acid
NMR	Nuclear magnetic r resonance
NRG	Neuregulin
OPO	Optical parametric oscillator
PAM	Programmable array microscope
PBS	Phosphate buffered saline
PC	Personal computer
PFA	Paraformaldehyde
PI3K	Phosphatidyl inositol-3-kinase
PIP_2	PtdIns (4,5)-P2
PKA	Protein kinase A
PKC	Protein kinase C
PLC-γ	Phospholipase C

PMA	Phorbal 12 myristate 13-acetate
PMT	Photomultiplier tube
Pptase	phosphopantetheine transferase
PSF	Point spread function
PT	Protein tomography
PTB	Phosphotyrosine binding
p-Tyr	Phospholated tyrosine
QD	Quantum dot
RISC	Reverse inter-system crossing
RNase A	Ribonuclease A
ROI	Region of interest
rpm	revolutions per minute
RTK	Receptor tyrosine kinase
SA	Spherical aberration
SD	Standard deviation
SH2	Src homology 2
SHG	Second harmonic generation
SoS	Son of sevenless
STAT	Signal Transducer and Activator of Transcription
STFC	Science and Technology Facilities Council
TAC	Time to amplitude converter
TCSPC	Time correlated single photon counting
TE	tris-EDTA
TGF-α	Transforming growth factor alpha
THG	Third harmonic generation
Thr	Threonine
TM	Transmembrane
TMR	Tetramethyl rhodamine
Tris	tris (hydroxymethyl) aminomethane
TTS	Transit time spread
Tyr	Tyrosine
Ub	Ubiquitin
XRD	X-ray diffraction
YFP	Yellow fluorescent protein

1 Introduction

Non-pathogenic diseases such as cancer and neurodegenerative disorders are often caused by the malfunctioning of cellular signalling networks that produce transcriptional changes that control cell growth, differentiation and apoptosis[1]. Structural malfunction of specific proteins (due to mutation in the corresponding gene) in the relevant signal pathways are often associated with these disease states, which are able to ensure that the deregulated signals causing the diseased continue and can somehow bypass therapies targeted at the malfunctioning proteins. The functions of any biological system emerge from the selective interaction of functionally diverse biomolecules[2]. The systems level approach to biology recognises that both the properties of the overall network and the functional properties of individual bio molecules combine to produce coherent behaviours[3]. It is becoming clear that a full understanding of the functioning of signalling networks at a systems level is required to understand non-intuitive features of the networks, the behaviour of diseased states and the mechanisms by which treatments can be evaded by diseased states. While the large numbers of possible interactions between proteins can be catalogued with high throughput proteomic assays[4], elucidating the kinetics and functional properties of interacting proteins is more complicated.

A major step towards understanding how any protein functions is the determination of its three dimensional structure. From this its overall shape, electrostatic properties, juxtaposition of domains, molecular composition of its surface and quaternary structure can be derived[5]. Techniques for determining high resolution protein structures such as x-ray diffraction (XRD) or nuclear magnetic resonance (NMR) provide snapshots of proteins in an unnatural environment (in crystals or at high concentration in solution). Although the static structures of protein-ligand complexes provide some functional insight by specifying the location of the ligand binding sites, what are needed are techniques that bridge the gap between the high resolution structures and the functioning protein *in situ*. A technique for investigating the link between protein

structure and function needs to selectively observe proteins of interest in a non-destructive way and with minimum perturbation to the system being studied. Methods such as protein tomography (PT) are a step in the right direction as they can produce three dimensional images of protein structure in cells[6, 7]. However, PT suffers from several drawbacks; the position of the cell membrane relative to the protein has to be inferred as it is invisible to the technique, proteins need to be tagged with large gold conjugated antibodies and the technique requires the sample to be mechanically sectioned and fixed. PT can therefore provide insight into protein structures in cell membranes but is far from being a perfect method for relating structure to function *in situ*. Fluorescence imaging is currently favoured for observing proteins in live cells, as despite requiring the introduction of extrinsic labels (and potentially disrupting normal protein function), it is a non-destructive optical technique that provides contrast between labelled molecules and the rest of the sample. Multiple types of bio molecules or structures can be observed by labelling with multiple probes that emit fluorescence at different wavelengths. Other properties of the observed fluorescence emission can also be used to report on the environment of the fluorophore (via the fluorescence lifetime) and its rotational mobility (via the fluorescence anisotropy). The effects of Förster resonance energy transfer (FRET) between different fluorophores can also be used to determine their separation. Often referred to as a 'spectroscopic ruler'[8], FRET is widely used to investigate protein interactions below the resolution limit of optical microscopy[9]. With site-specific 1:1 labelling of proteins, the properties of fluorescence emission can be used to infer motions and separations of the labelled sites *in situ* and relate them to known high resolution protein structures.

Two examples of proteins that have recently had their static high resolution structure related to their function by quantitative fluorescence imaging are kinesin and ATP synthase. Kinesin is an ATP fuelled molecular motor that transports cargo along microtubules. The high resolution structure of kinesin is a homodimer with each monomer possessing an identical catalytic head group that bind to microtubules and ATP. In order to move along the microtubule without completely dissociating, the head groups must bind and dissociate in a co-ordinated manner, but the high resolution structure provides no clues as to how

this is achieved. The exact method (hand-over-hand) has been observed with single molecule fluorescence tracking *in vitro*[10] and *in situ*[11]. Likewise the stepwise rotation of γ-subunit of EF0F1-ATP synthase was not predicted from its high resolution structure, but was observed in liposomes by single-molecule FRET[12]. In both of the above examples it is notable that different methods are required to address the biological problem at hand. There is no one technique that is applicable to all proteins in all situations and experimental techniques have to be found or developed to ask the correct questions of the problem under investigation. Also notable is the interdisciplinary nature of the techniques which involve the production of biological samples, chemical or genetic modification of proteins for 1:1 labelling with fluorescent molecules and quantitative fluorescence microscopy.

The biological problem that drives the work in this thesis concerns the ErbB family of receptors which are a paradigm for transmembrane receptor tyrosine kinases[13]. Membrane proteins are important and up to 30% of all proteins encoded in most genomes are membrane proteins[14]. Membrane receptors transduce signals from the cellular environment across the membrane to allow the cell to respond to external stimuli. ErbB1 plays a fundamental role in controlling crucial cellular processes such as proliferation and survival[13, 15, 16]. It is commonly over expressed or mutated in a number of epithelial malignancies and amplification of the ErbB1 gene is often associated with aggressive tumour phenotypes[17]. Targeting of ErbB1 is a major challenge in oncology, and several anti-ErbB1 antibodies and tyrosine kinase inhibitors have been investigated as potential antitumour agents[18]. Despite decades of research the mechanism by which ErbB1 activation by ligand binding produces a variety of signalling outcomes is poorly understood, but is known to involve oligomerisation of receptors[19-25] and allosteric activation of intracellular ErbB1 tyrosine kinase activity[26]. The current model is heavily influenced by the structure of ErbB receptors pieced together from crystallised receptor fragments[19]. Previous FRET studies have sought to investigate the three dimensional architecture of activated receptor oligomers *in situ* by measuring ensemble FRET between fluorescently labelled ligands[25, 27, 28]. This approach provides lateral structural information but

requires prior assumptions regarding the structure of interacting receptors to estimate the separation of ligand binding sites. However, experimental data has consistently been in conflict with the assumption that receptors exclusively form the back-to-back dimers seen in crystallised ErbB1 extracellular domains. Single molecule FRET between labelled ligands requires no structural assumptions to determine inter-ligand separations and confirms distances inconsistent with back-to-back dimers[29]. To gain insight into the discrepancy between the *in situ* FRET results and high-resolution structure an improved method of probing the 3d architecture of activated receptor complexes is required.

In this thesis a method is developed for investigating the spatial relationship between the high resolution structures of membrane receptors and the membrane in which they are embedded. The method provides quantitative distance estimation in an additional dimension that can be correlated with the results of lateral FRET between ligand binding sites under identical experimental conditions. The combination of the two FRET measurements provides a starting point for the determination of a realistic model of the 3D architecture of the protein complex at the plasma membrane. This bi-directional FRET method also allows large scale changes in the receptor orientation to be observed that are not predicted by XRD or NMR snapshots of soluble proteins *in vitro*. These changes may come about from influence of the plasma-membrane or interactions with other plasma-membrane constituents. An important aspect of the method is that the membrane proteins are observed, in cultured adherent cells and are an integral part of a complete biological system when the measurement is made. This is an important progression from previous studies that have observed the location of the ErbB1 ligand binding site in suspended artificial membranes and/or purified cell membranes[30] as ErbB1 receptors outside of the natural cellular environment are known to lack functional aspects of receptors *in vivo* such as high affinity binding[31]. As the method probes membrane protein conformations in adherent cells, the structural measurements can be made under experimental conditions that disrupt normal receptor function or switch on or off parts of the signalling networks that interact with the receptors at the cell surface.

The aspects of fluorescence and FRET theory crucial to relating quantitative FLIM-FRET measurements to distances in biological samples are explained in chapter 2. The current understanding of the biology of ErbB receptors is discussed in chapter 3. Chapter 4 outlines the design and implementation of a multi-dimensional, multi-colour confocal microscope that was crucial to the development of the method. Chapter 5 outlines the additional steps required to quantitatively measure the distance of closest approach between a fluorescently labelled protein and the cell surface. These include Förster radius measurement and consideration of the theory for FRET between multiple donors and acceptors. Chapter 6 details the application of the technique to activated ErbB1 receptors to measure the distance of closest approach of ligand binding sites to the membranes of cancerous cells. The relationship between the three dimensional architecture of ErbB1 receptors and their function is then investigated.

References

1. Bublil, E. M. & Yarden, Y. The EGF receptor family: spearheading a merger of signalling and therapeutics. Current Opinion in Cell Biology 19, 124-134 (2007).
2. Katano, H. Computational systems biology. Nature 420, 206-210 (2002).
3. Katano, H. Systems Biology: A Brief Overview. Science 295, 1662-1664 (2002).
4. Zhu, H. et al. Global Analysis of Protein Activities Using Proteome Chips. Science 293, 2101-2105 (2001).
5. Thornton, J. M., Todd, A. E., Milburn, D., Borkakoti, N. & Orengo, C. A. From structure to function: Approaches and limitations. Nature Structural Biology 7, 991-994 (2000).
6. Lammerts van Bueren, J. J. et al. The antibody zalutumumab inhibits epidermal growth factor receptor signalling by limiting intra- and intermolecular flexibility. PNAS 105, 6109-6114 (2008).

7. Banyay, M. et al. 3D Imaging of *in situ* Specimens with Low-dose Electron Tomography to Analyse Protein Conformation. ASSAY and Drug Development Technologies 2, 561-567 (2004)
8. Stryer, L. & Haugland, R. P. Energy transfer: a spectroscopic ruler. PNAS 58, 719-26 (1967).
9. Vogel, S. S., Thaler, C. & Koushik, S. V. Fanciful FRET. Science's STKE re2 (2006).
10. Yildiz, A., Tomishige, M., Vale, R. D. & Selvin, P. R. Kinesin walks hand-over-hand. Science 303, 677-678 (2004).
11. Cai, D., Verhey, K. J. & Meyhofer, E. Tracking Single Kinesin Molecules in the Cytoplasm of Mammalian Cells. Biophysical Journal 92, 4137-4144 (2007).
12. Börsch, M., Dieza, M., Zimmermanna, B., Reutera, R. & Gräber, P. Stepwise rotation of the γ-subunit of EF0F1-ATP synthase observed by intramolecular single-molecule fluorescence resonance energy transfer. FEBS Letters 527, 147-152 (2002).
13. Schlessinger, J. Cell signalling by receptor tyrosine kinases. Cell 103, 211-225 (2000).
14. Wallin, E. & Heijne, G. V. Genome-wide analysis of integral membrane proteins from eubacterial, archaean, and eukaryotic organisms. Protein Science 7, 1029-1038 (1998).
15. Carpenter, G. Receptors for Epidermal Growth Factor and Other Polypeptide Mitogens. Annual Review of Biochemistry 56, 881-914 (1987).
16. Ullrich, A. et al. Human epidermal growth factor receptor cDNA sequence and aberrant expression of the amplified gene in A431 epidermoid carcinoma cells. Nature 309, 418-425 (1984).
17. Zandi, R., Larsen, A. B., Andersen, P., Stockhausen, M.-T. & Poulsen, H. S. Mechanisms for oncogenic activation of the epidermal growth factor receptor. Cellular Signalling 19, 2013-2023 (2007).
18. Arora, A. & Scholar, E. M. Role of Tyrosine Kinase Inhibitors in Cancer Therapy. Journal of Pharmacology and Experimental Therapeutics 315, 971-979 (2005).

19. Ferguson, K. M. Structure-Based View of Epidermal Growth Factor Receptor Regulation. Annual Review of Biophysics 37, 353-373 (2008).

20. Ferguson, K. M. et al. EGF Activates Its Receptor by Removing Interactions that Autoinhibit Ectodomain Dimerization. Molecular Cell 11, 507-517 (2003).

21. Garrett, T. P. et al. Crystal structure of a truncated epidermal growth factor receptor extracellular domain bound to transforming growth factor alpha. Cell 110, 763-776 (2002).

22. Ogiso, H. et al. Crystal structure of the complex of human epidermal growth factor and receptor extracellular domains. Cell 110, 775-787 (2002).

23. Clayton, A. H. A. et al. Ligand-induced Dimer-Tetramer Transition during the Activation of the Cell Surface Epidermal Growth Factor Receptor-A Multidimensional Microscopy Analysis. The Journal of Biological Chemistry 280, 30392-30399 (2005).

24. Furuuchi, K., Berezov, A., Kumagai, T. & Greene, M. I. Targeted Antireceptor Therapy with Monoclonal Antibodies Leads to the Formation of Inactivated Tetrameric Forms of ErbB Receptors. Journal of Immunology 178, 1021-1029 (2007).

25. Whitson, K. B., Beechem, J. M., Beth, A. H. & Staros, J. V. Preparation and characterization of Alexa Fluor 594-labeled epidermal growth factor for fluorescence resonance energy transfer studies: application to the epidermal growth factor receptor. Analytical Biochemistry 324, 227-236 (2004).

26. Zhang, X., Gureasko, J., Shen, K., Cole, P. A. & Kuriyan, J. An Allosteric Mechanism for Activation of the Kinase Domain of Epidermal Growth Factor Receptor. Cell 125, 1137-1149 (2006).

27. Gadella, T. W., Jr. & Jovin, T. M. Oligomerization of epidermal growth factor receptors on A431 cells studied by time-resolved fluorescence imaging microscopy. A stereochemical model for tyrosine kinase receptor activation. Journal of Cell Biology 129, 1543-58 (1995).

28. Martin-Fernandez, M., Clarke, D. T., Tobin, M. J., Jones, S. V. & Jones, G. R. Preformed Oligomeric Epidermal Growth Factor Receptors

Undergo an Ectodomain Structure Change during Signalling. Biophysical Journal 82, 2415-2427 (2002).

29. Webb, S. E. D. et al. Single molecule imaging and FLIM show different structures for high and low-affinity EGFRs in A431 cells. Biophysical Journal 94, 803-819 (2008).

30. Carraway III, K. L., Koland, J. G. & Cerione, R. A. Location of the Epidermal Growth Factor Binding Site on the EGF Receptor. A Resonance Energy Transfer Study. Biochemistry 29, 8741-8747 (1990).

31. Jones, J. T., Akita, R. W. & Sliwkowski, M. X. Binding specificities and affinities of egf domains for ErbB receptors. FEBS Letters 447, 227-231 (1999).

2 The properties of fluorescence emission and the theoretical basis of quantitative FRET measurement

The phenomenon of fluorescence is used in biological imaging to gain colour contrast between molecular components of interest labelled with a light-emitting molecular tag (fluorophore), and the myriad different molecular components that make up cells and tissues. The properties of fluorescence photons emitted by fluorophores can be further used to gain information regarding their local environment, rotational motion and proximity to other fluorophores. When combined with site specific labelling these observables can be related to the kinetics and dynamics of the interactions between their conjugated biomolecules. This chapter reviews the photophysical origins of fluorescence and the measurable characteristics of the fluorescence emission used throughout this thesis to investigate receptor structural changes at the plasma membrane of intact cells. In addition to fluorescence intensity spectra, these are the fluorescence lifetime and anisotropy. Different approaches to determining the characteristic lifetime of fluorescence intensity decays are outlined. Several different types of fluorescent probe are discussed along with strategies for labelling specific sites of proteins. Finally the theory of Förster resonance energy transfer (FRET) - a popular technique for measuring molecular separations below the resolution limit of fluorescence microscopy to identify molecular interactions - is discussed.

2.1 Luminescence

Luminescence is the name given to light emitted as the result of relaxation of an atom or molecule from electronically excited states to the ground state. Luminescence is formally split into two categories depending upon the electronic states involved in the process. Phosphorescence refers to the process of decay from a triplet excited state to the singlet ground state and the rate of phosphorescence emission is between ~1 and 1000 s^{-1}. Fluorescence refers to

decay from an excited singlet state to the ground state and emission occurs at a much faster rate (~10^8 – 10^9 s^{-1}).

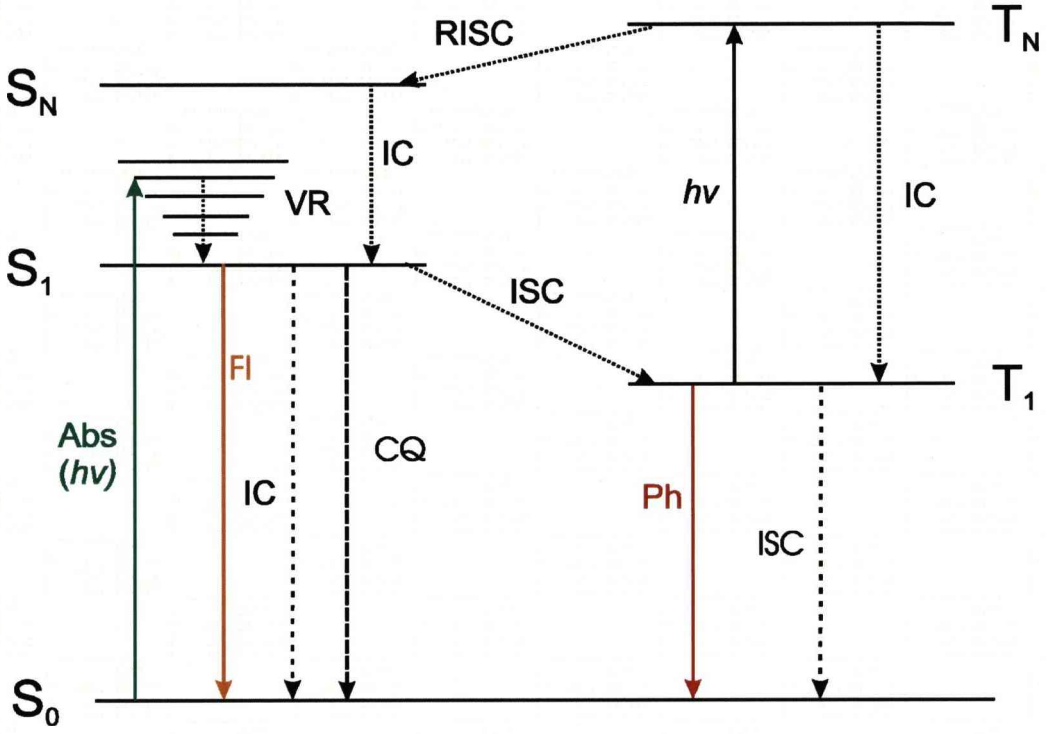

Figure 2.1 A simplified Jablonski diagram detailing the processes available to a single molecule excited from the ground state (S_0) into the first singlet state (S_1) state by absorption of a photon with energy hν. These are fluorescence emission (Fl), Internal Conversion (IC) and collisional quenching (CQ) to return to the ground state. Additionally intersystem crossing (ISC) to the first triplet state (T_1) can be followed by phosphorescence emission (Ph) or ISC to the ground state or absorption of another photon to a higher triplet state (T_N). From the TN state reverse intersystem crossing (RISC) back to a singlet state is possible, IC back to the T_1 state or an excited state reaction with reactive oxygen species resulting in photobleaching. Photochemical reactions that produce non-fluorescent species or resonance energy transfer of excited state energy to another molecule are not shown.

Fluorescence typically occurs in excited aromatic molecules. Figure 2.1 shows a simplified Jablonski diagram that outlines the processes that can occur after excitation of a molecule into an electronically excited state by absorption of a single photon with energy $h\nu$ (alternatively multiple photons of lower energy may be absorbed simultaneously). Shown are the singlet ground state (S_0) and the first (S_1) and a higher (S_N) excited singlet state with the first and higher triplet

states (T_1 and T_N respectively). Excitation transitions between electronic states occur on a timescale that precludes significant displacement of the nuclei in the molecule (~10^{-15} s). This is known as the Franck-Condon principle. At room temperature the molecule will not have sufficient vibrational energy to populate the higher vibrational energy levels of the ground state and absorption occurs from the lowest level of the ground state. Excitation to a vibrational level within one of the excited singlet states is followed by relaxation to the lowest vibrational level in that state by internal conversion (IC). IC occurs on a much faster timescale (~10^{-12} s) than radiative emission, so fluorescence can be considered to occur from the lowest vibrational level of the excited state. Upon returning to the ground state, internal conversion will again ensure that the molecule relaxes to the lowest vibrational energy level. When the S_0 and S_1 states possess similar vibrational energy levels, the fluorescence absorption and emission spectra have a mirror image relationship.

Alternative to fluorescence emission, an excited molecule may undergo intersystem crossing (ISC) to an excited triplet state and decay by phosphorescence. Transitions between triplet states and the singlet ground state are forbidden by the selection rule governing spin multiplicity for electronic transitions. However, coupling of vibrational and electronic motions (vibronic coupling) in the molecule means that the forbidden transitions are actually weakly allowed[1]. Consequently triplet states are long lived and the molecule may absorb another photon and transfer to a higher triplet state (T_N). These high energy states are also long-lived allowing the molecule to undergo photochemical reactions that irreversibly destroy its ability to emit fluorescence. Loss of fluorescence through this mechanism is called photobleaching. Molecules in higher excited triplet states can undergo reverse ISC (RISC) back to an excited singlet state and decay by fluorescence. This photophysical phenomenon is visible in the fluorescence intensity of a continuously excited single fluorescent molecule as 'blinking'.

There are also non-radiative processes available by which the excited molecule can lose energy. These include collisional quenching (CQ), IC to the S_0 state and non-radiative energy transfer to another molecule (see section 2.4).

2.2 Characteristics of Fluorescence Emission

The energy of the photons emitted by fluorescence is generally lower than the energy of the absorbed light. Loss of energy by IC, emission to higher S_0 vibrational levels and solvent relaxation combine to produce this effect which results in the band of emission wavelengths being red-shifted with respect to the absorption band. This is referred to as the Stoke's shift and allows fluorescence emission to be separated from scattered excitation photons. A consequence of the rapid IC from S_1 vibrational levels to the lowest S_1 state is that for a single species of fluorophore, the shape of the emission spectrum is usually independent of the absorption wavelength (for photon wavelengths longer that the excitation wavelength). In addition to the dependence of fluorescence intensity upon excitation and emission wavelengths there are other properties of fluorescence that can be measured in order to obtain information regarding the environment of the fluorescence molecules. These properties are the fluorescence lifetime and anisotropy of the emitted light and are explained in this section.

2.2.1 Fluorescence lifetime

The emission of fluorescence photons is a random process. Under the same environmental conditions each molecule in a population of excited fluorophores will have the same probability of emitting a fluorescence photon in a given time. Fluorescence emission competes with non-radiative decay mechanisms (e.g. quenching, IC, photobleaching etc.) available to the molecules. The quantum yield Q of a fluorescent molecule is defined as the ratio of the number of fluorescence photons emitted to the number of photons absorbed and is related to the rates of radiative (Γ) and non-radiative (k_{NR}) decay by

$$Q = \frac{\Gamma}{\Gamma + k_{NR}} \qquad \text{Eqn. 2-1}$$

Usually the intensity of fluorescence is measured. When a population of non-interacting fluorophores in an isotropic environment is excited by an infinitely short pulse the time dependence of the measured intensity follows

$$\frac{dI(t)}{dt} = -(\Gamma + k_{NR})I(t) \qquad \text{Eqn. 2-2}$$

which can be solved to provide the time dependent intensity decay

$$I(t) = I_0 \exp(-t/\tau) \qquad \text{Eqn. 2-3}$$

where I_0 is the fluorescence intensity at time t = 0 and τ is the fluorescence lifetime of the fluorophores

$$\tau = \frac{1}{\Gamma + k_{NR}} \qquad \text{Eqn. 2-4}$$

The fluorescence lifetime is the time at which the fluorescence intensity of the sample decreases to 1/e of its initial intensity. For true mono-exponential decays it is also the average time that a fluorophore stays in the excited state. From Eqn. 2-4 it can be seen that the fluorescence lifetime is sensitive to environmental factors that alter the overall emission rate of the sample or provide non-radiative pathways for the molecule to return to the ground state. For example the fluorescent dye fluorescein exists in equilibrium between different ionisation states which have different values of Γ [2, 3]. The overall emission rate and hence the lifetime of a sample of fluorescein depends upon the relative proportions of the different ionic species which is dependent upon the pH of their local environment[3]. The presence of nearby energy transfer partners will increase the non-radiative decay rate (and is covered in more detail in section 2.4) as will

dynamic interactions with quenchers of fluorescence. The steady state fluorescence intensity F is the integral of Eqn. 2-3 over all time

$$F = \int_0^\infty I(t)dt = \int_0^\infty I_0 \exp(-t/\tau)dt = I_0\tau \qquad \text{Eqn. 2-5}$$

The initial fluorescence intensity will depend upon the number of fluorescent molecules, the intensity of excitation and the detection efficiency of the experimental set-up. In the case of mono-exponential intensity decays, the steady state fluorescence intensity is proportional to the fluorescence lifetime.

Fluorescence intensity decays in real samples rarely follow mono-exponential decay laws. In biological samples especially, different fluorophores may be in different environments, each combination displaying a different lifetime. Any measured intensity decay will contain contributions from each. Consequently, measured intensity decays are usually fit to a multi-exponential model with i components

$$I(t) = \sum_i \alpha_i \exp(-t/\tau_i) \qquad \text{Eqn. 2-6}$$

where $\sum_i \alpha_i = 1$. Usually it is difficult to relate the obtained values of α_i and τ_i to any properties of the sample and the expectation value of the lifetime $\langle\tau\rangle$ is often reported as it is proportional to the steady state fluorescence

$$\langle\tau\rangle = \sum_i \alpha_i\tau_i \propto \int_0^\infty I(t)dt \qquad \text{Eqn. 2-7}$$

This is particularly important when calculating the efficiency of Förster resonance energy transfer (FRET) from fluorescence lifetime measurements, which is discussed in section 2.4.

2.2.2 Measurement of fluorescence lifetimes

Measurement of fluorescence lifetimes may be achieved using either time-domain or frequency-domain techniques. Figure 2.2 illustrates both concepts.

Time domain techniques involve exciting a sample with a short pulse of light and measuring the subsequent time-resolved intensity decay. The pulse is made to be much shorter than the fluorescence lifetime of the fluorophore species in sample being studied. The fluorescence lifetime is obtained from the intensity decay and is equal to the time taken for the intensity to decrease to 1/e of its initial value. This time can be accurately measured by fitting the slope of log $I(t)$ to the multi-exponential decay model that fits best the data.

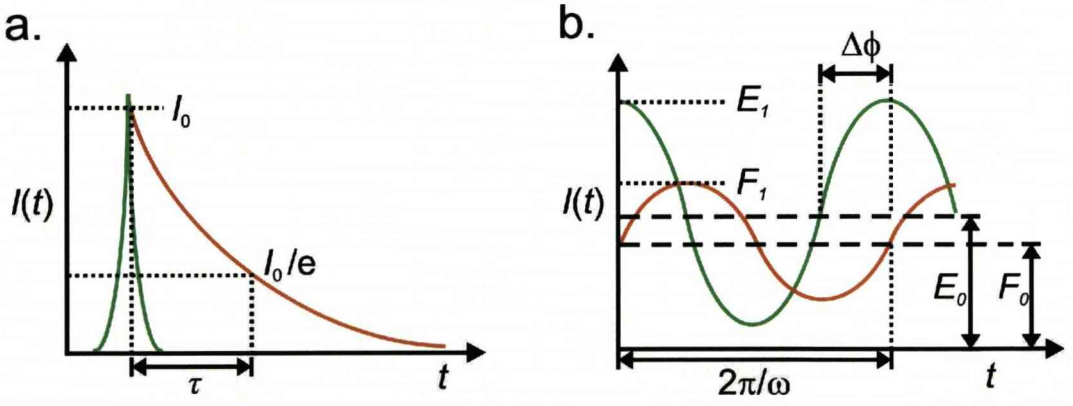

Figure 2.2 a. Time-domain fluorescence lifetime measurement of a sample exhibiting a mono-exponential decay. Excitation with a short pulse of light (green) produces an initial intensity I_0 that decays to I_0 / e in time τ. **b**. Frequency domain lifetime measurement of the same sample. Excitation is amplitude modulated (green, peak intensity E_1) and the fluorescence emission (orange, peak intensity F_1) is modulated with the same angular frequency ω, but with lower modulation amplitude and a phase difference $\Delta\phi$.

Frequency domain measurements make use of intensity modulated illumination, often sinusoidal, at a frequency comparable to the expected decay rate of the sample. The fluorescence intensity is modulated at the same frequency as the excitation, but the emission intensity is convoluted with the impulse decay

(Eqn. 2-3). The consequence of this is a difference in the phase and amplitude modulations between the excitation and fluorescence emission. It is possible to obtain a value for the average lifetime from both measurable differences. The phase lifetime (τ_ϕ) and the modulation lifetime (τ_m) are given by

$$\tau_\phi = \omega^{-1} \tan(\Delta\phi) \qquad \text{Eqn. 2-8}$$

$$\tau_m = \omega^{-1} \sqrt{(m^{-2} - 1)} \qquad \text{Eqn. 2-9}$$

$$m = \frac{F_1 E_0}{E_1 F_0} \qquad \text{Eqn. 2-10}$$

Neither of these lifetimes completely describes the intensity decay of the sample and are unequal for complex decays. In this case both represent a different weighted average of the lifetimes present in the sample.

Frequency domain measurement requires an electro-optical modulator to produce intensity modulation frequencies ~10^9 Hz. Cross-correlation detection makes it possible to obtain the phase shift and modulation of the high frequency fluorescence emission by measuring a low frequency PMT signal. Fast PMTs are desirable as the width of transit time spread (TTS – the spread in the arrival times of electrons at the PMT anode in response to an incident photon) limits the upper modulation frequency that can be resolved.

There are two major methods of acquiring time domain data. The time profile of the fluorescence intensity decay can be obtained by sequentially measuring the number of fluorescence photons emitted at different times after the excitation pulse in sequential short time windows, a technique known as time-gating. Time-gating can be accomplished either by gating the gain of the detector for a short period of the intensity decay following an excitation pulse, or by electronically sampling the response of the detector after an excitation pulse. Time gating has the advantage of being able to reject the earliest response to the excitation pulse which will contain short lifetime components from biological auto-fluorescence and background scattered light. Time gating of charge coupled devices (CCDs)

can be used with widefield fluorescence microscopy to produce FLIM images. The shortest direct time-gate achievable with most commercial CCDs is limited to ~1 ms so these are combined with multi-channel plate intensifiers (MCPI) which can be gated on ns timescales. It is, however, possible to directly time-gate some small commercial CCDs on nanosecond timescales[4, 5] avoiding the need for an MCPI.

Alternatively, time-correlated single photon counting (TCSPC) can be used to acquire a distribution of photon arrival times that is representative of the intensity decay. TCSPC is suitable for use with point scanning microscope techniques[6-8] and provides high temporal accuracy and high detection efficiency by measuring the arrival times of fluorescence photons at the detector relative to the timing of a pulsed light source used to excite the sample. The technique relies upon low excitation levels to avoid biasing the sampled fluorescence photons to those with early arrival times (known as pile-up), which is also beneficial to avoid photodamage to biological samples. To optimise the speed of data collection pulsed sources with high repetition rates (MHz) are used. Figure 2.3 outlines the components that are required to perform TCSPC.

The 'reverse stop-start' method is used so that the TCSPC electronics need only operate at the rate of photon detection rather than the much higher rate of the excitation pulses[9] The time interval that is measured is between the arrival of a fluorescence photon at the detector and the next pulse of the excitation source. Upon detection of a fluorescence photon - recognised by a constant fraction discriminator (CFD) as a voltage signal pulse over a certain threshold and with a steep enough leading edge – a time to amplitude converter (TAC) linearly increases a voltage until stopped by the next reference pulse from the excitation source. This voltage is assigned to a discrete time interval. By repeating the measurement many times and storing the frequency that photons are assigned to these time intervals in a histogram memory, a distribution of photon arrival times can be built up that is representative of the fluorescence intensity decay of the sample. TCSPC can be easily combined with point scanning microscopy techniques by assigning the photons both time values and to the pixels they came from as the focal spot is scanned across the sample[8].

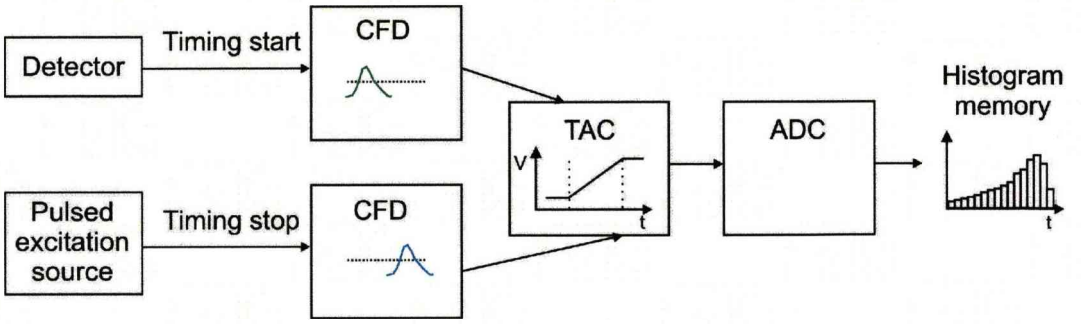

Figure 2.3 The components required for time-correlated single photon counting. A signal input from the fluorescence detector and reference pulses from the excitation source are vetted by constant fraction discriminators (CFDs). In reverse stop-start mode, a time to analogue converter (TAC) converts the interval between detecting a fluorescence photon and receiving the next reference pulse to a voltage which is then assigned to a discrete time interval by the analogue to digital converter (ADC). A histogram memory records the number of photons assigned to each time interval.

2.2.3 Fluorescence anisotropy

Fluorescence anisotropy is widely used to investigate molecular rotations and segmental motions of proteins in solution. When a population of fluorescent molecules is excited with linearly polarised light, the resulting fluorescence emission will also be polarised. In the absence of molecular rotation, the fluorescence emission polarisation of a molecule will be rotated by an angle that depends on the relative orientation of its transition moments for absorption and emission, which lay in specific directions along the structure a fluorescent molecule. The interaction between the exciting photon and a molecule depends on the dot product of the electric vector of the photon and the dipolar excitation moment of the molecule. Molecules that are oriented so that their absorption transition moments are aligned with the electric vector of the incident linearly polarised light will therefore be preferentially excited, an effect known as photoselection. The fluorescence anisotropy r is a measure of the degree of polarisation of the fluorescence emission, which can be reduced from the initial

highly polarised photoselected state by rotational diffusion of the molecules or non-radiative energy transfer to non-photoselected molecules in the ground state.

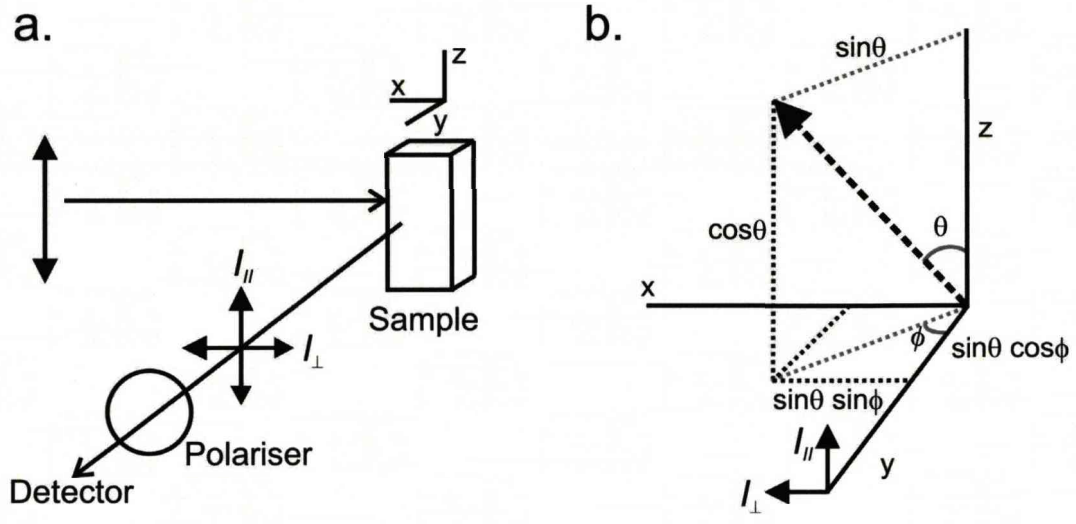

Figure 2.4 a. Experimental measurement of fluorescence anisotropy. Vertically polarised light (with the electric field vector aligned with the z-axis) is incident upon a sample and the fluorescence intensity parallel (I_{II}) or perpendicular ($I_{\perp}$) to the z-axis is selected to proceed to the detector by the polariser. **b**. The projection of a dipole (dotted arrow) in the z- and x-axis. The dipole is oriented at angles θ and ϕ from the z- and y-axes respectively.

Figure 2.4a illustrates the measurement of r and shows a fluorescent sample illuminated with vertically polarized light (the electric vector of the light is oriented parallel to the vertical z-axis in the diagram). The intensity of the emission is measured at a right angle to the direction of excitation to avoid detection of unabsorbed excitation illumination and a polarizer is used to allow light to the detector that is polarised either parallel to the excitation polarisation (I_{II}) or perpendicular to it ($I_{\perp}$). The anisotropy of the emission r is defined as the ratio of the polarized component of the emission to the total fluorescence intensity

$$r = \frac{I_{II} - I_{\perp}}{I_{II} + 2I_{\perp}} \qquad \text{Eqn. 2-11}$$

Figure 2.4b illustrates the anisotropy measurement at the level of a single fluorescent molecule. The molecule is assumed to be stationary and have parallel absorption and emission transition moments which are indicated by the black dashed arrow. It is oriented with respect to the z and x axes by the angles θ and ϕ respectively. Fluorescent molecules behave like radiating dipoles and the intensity of light radiated from a dipole is proportional to the square of its vector projected in the axis of detection. If the emission is polarized along the emission transition moment then the intensities observed when selecting I_{II} or $I_{\perp}$ with a polarizer will be

$$I_{II} = \cos^2\theta \qquad \text{Eqn. 2-12}$$

$$I_{\perp} = \sin^2\theta \sin^2\phi \qquad \text{Eqn. 2-13}$$

Averaged over many molecules in solution, the dependence of $I_{\perp}$ on ϕ is eliminated by noting that the population of fluorescent molecules excited by z polarized light will be symmetrically distributed around the z-axis. The average value of $\sin^2\phi$ is therefore 0.5 and by substituting Eqn.s 2-12 and 2-13 into Eqn. 2-11 and using the identity $\sin^2\theta = 1 - \cos^2\theta$ the following expression for r can be obtained

$$r = \frac{3\langle\cos^2\theta\rangle - 1}{2} \qquad \text{Eqn. 2-14}$$

For the ideal case where the entire population of excited fluorescent molecules have collinear transition moments that are oriented exclusively parallel to the excitation polarisation, then the average value of $\cos^2\theta$ would be 1 resulting in $r = 1$. However, this situation is unrealistic even if rotational diffusion is neglected as fluorescent molecules rarely have collinear transition moments and photoselection on a population of randomly oriented molecules doesn't produce an excited state population perfectly oriented parallel to the excitation polarisation. The probability that a given molecule will absorb vertically

polarized light is also proportional to $\cos^2\theta$, meaning that the transition moment of the fluorophore does not have to be perfectly aligned with the z-axis to be excited. The distribution of fluorescent molecules excited by z polarized light (single photon absorption) as a function of θ, $f(\theta)$ is

$$f(\theta)d\theta = \cos^2\theta \sin\theta \, d\theta \qquad \text{Eqn. 2-15}$$

The maximum value of $\langle \cos^2\theta \rangle$ (for collinear absorption and emission transition moments) is then

$$\langle \cos^2\theta \rangle = \frac{\int_0^{\pi/2} \cos^2\theta \, f(\theta)d\theta}{\int_0^{\pi/2} f(\theta)d\theta} \qquad \text{Eqn. 2-16}$$

Substitution of Eqn. 2-15 into Eqn. 2-16 gives the result $\langle \cos^2\theta \rangle = \frac{3}{5}$. From Eqn. 2-14 the maximum anisotropy is r = 0.4. For two-photon excitation the distribution of excited molecules $f_2(\theta)$ is different and

$$f_2(\theta)d\theta = \cos^4\theta \sin\theta \, d\theta \qquad \text{Eqn. 2-17}$$

The maximum observable anisotropy for two-photon excitation is 0.57.

2.3 Extrinsic fluorescent probes

Extrinsic fluorescent probes are fluorescent molecules that are not naturally found in the sample being studied. They are introduced with the specific purpose of labelling naturally non-fluorescent components of the sample to investigate their localisation and environment. Three major classes of commercially

available extrinsic probe are commonly used for fluorescence imaging; organic dyes, quantum dots and fluorescent fusion proteins.

2.3.1 Organic fluorescent dyes

Organic fluorescent dyes are small carbon based molecules that usually contain multiple aromatic ring systems. The dyes can often be produced with a number of different reactive groups enabling them to be covalently bound to biomolecules such as DNA and proteins. Succinimidyl esters, carboxylic esters and sulfonyl chlorides of dyes can be bound to the amine group, which is the functional group of the amino acid lysine[10]. Dyes with a maleimide group can bind to the thiol group found in the amino-acid cysteine[10]. Although these are the most common labelling targets in proteins, other functional groups such as aldehydes, ketones and alcohols can be used[10]. It is difficult to control the labelling of proteins as they may contain more than one accessible functional group for reaction with the functionalised dye.

Organic dyes are widely used due to their small size and the vast variety of commercially available dyes that allow for many different applications. Not all applications necessitate covalent 1:1 binding of the dye to a target bio-molecule. For example, fluorescein has two ionic forms that exist in a pH dependent equilibrium. These two isomers display distinctly different lifetimes and measurement of the mean lifetime can be used for example to estimate the pH of the local environment of the dye in a cellular organelle. Likewise the calcium indicators Fura-Red[11] and Fluo-4[12] show [Ca^{2+}] dependent absorption and emission spectra and need only be loaded into the cytosolic fluid of a cell to report on cellular [Ca^{2+}].

Fluorescent dye	Peak Absorption / nm	Peak Emission / nm	Quantum Yield	Extinction coefficient (at peak absorption) / $cm^{-1}M^{-1}$	References and Source
FITC	494	521	0.97*	92,000*	13, **a**
Alexa 488	495	518	0.92	71,000	14, **a**
Alexa 532	532	553	0.61	81,000	14, **a**
Alexa 546	556	572	0.79	104,000	14, **a**
Alexa 594	590	617	0.66	73,000	14, **a**
Alexa 647	650	665	0.33	239,000	14, **a**
Atto 488	501	523	0.80	90,000	**b**
Atto 532	532	553	0.90	115,000	**b**
Atto 550	554	576	0.80	120,000	**b**
Atto 594	601	627	0.85	120,000	**b**
Atto 647	645	669	0.20	120,000	**b**
Atto 647N	644	669	0.65	150,000	**b**
Cy3	550	570	0.24	150,000	15
Cy5	640	670	0.20	215,000	15
Vybrant DiI	549	565	-	148,000	**a**
Vybrant DiD	644	665	-	193,000	**a**
DY-485XL	485	560	-	50,000	**c**
DY-480XL	500	630	-	50,000	**c**
TMR	554	573	0.28	103,000	13, **a**
Fluo-4	494	516	0.14**	88,000**	12, **a**
Fura-red	458	597	-	43,000	11, **a**

Table 2.1 Fluorescence properties of commercially available organic dyes (unconjugated). *Measured in basic ethanol. All other quantum yields and extinction coefficients pertain to the unconjugated dye in phosphate buffered saline (PBS). **When bound to Ca^{2+}. Values originate from the references shown, or are provided by the commercial supplier indicated (Key - **a.** Invitrogen **b.** Atto-tec **c.** Dyomics).

Membrane probes are another class of fluorescent dye that do not require covalent modification of target molecules. Instead membrane probes are amphipathic (containing a hydrophobic and a hydrophilic portion) which facilitates their insertion into lipid membranes. The properties of Dialkylcarbocyanine dyes which are extensively used in this thesis are discussed in the next section.

Many commercially available dyes have been developed specifically to suppress environmental sensitivity of their fluorescence and provide bright photostable probes for imaging applications. These include the Alexa Fluor[14] (Invitrogen) and the Atto[16] (Atto-tec) series of dyes. Dyomics have recently developed dyes with extremely large Stokes shifts[17] that minimise the possibility of reabsorption of a fluorescence photon (inner filter effects) and allow multiple probes to be excited by the same laser line.

2.3.2 Dialkylcarbocyanine membrane probes

Dialkylcarbocyanine dyes are fluorescent molecules that are amphipathic (possessing both hydrophobic and hydrophilic regions) and are structurally similar to phospholipids (figure 2.5) in that they have a charged headgroup with two hydrophobic carbon chains. However, they possess two saturated alkyl chains instead of the acyl chains more usual in phospholipids. They are amphipathic because of a positive charge that resonates between the nitrogens of the two indole rings and insert into the outer leaflet of membranes with the fluorophore transition dipoles nearly parallel to the membrane surface[18]. Despite being free to rotate along the axis perpendicular to the membrane surface and diffuse laterally, they are not known to 'flip' between the leaflets of a lipid bilayer[19]. The fluorescence properties of the dyes can be altered by substituting the dimethylated carbon atoms with other groups and altering the separation of the indole groups. Many Dialkylcarbocyanine dyes are commercially available with absorption and emission spectra covering the whole range of visible

wavelengths. Due to the complexity of their full chemical names, they are usually referred to in the form C_nDiX, where C_n gives the number of carbon atoms in the alkyl chains and X is a letter that denotes the particular fluorescent variation. Two of the most commonly used are DiI and DiD which are spectrally similar to the fluorescent dyes Cy3 and Cy5 respectively. Fluorescent filter sets for these popular carbocyanine dyes can therefore also be used to image DiI and DiD. Dialkylcarbocyanine dyes exhibit highly quenched fluorescence in aqueous solution, but are highly fluorescent in lipid environments exhibiting short (~1ns) fluorescence lifetimes characterised by bi-exponential decays[20].

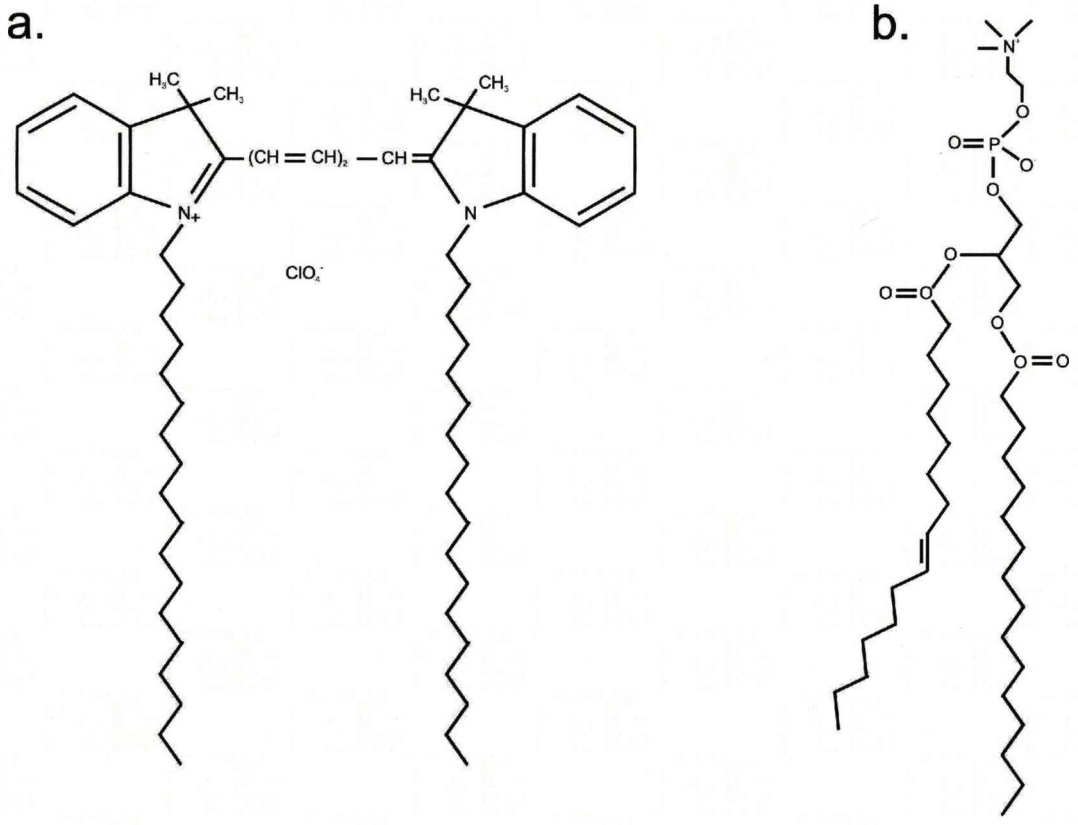

Figure 2.5a. The chemical structure of the lipophilic fluorescent dye, $C_{18}DiD$. **b**. The chemical structure of Phosphatidylcholine.

2.3.3 Quantum dots

Quantum dots (QDs) are semiconductor nanocrystals that posess intense fluorescence emission and are highly resistant to photobleaching [21-23]. This

property makes them useful for tracking singly labelled proteins and their large 2-photon absorption cross-sections are beneficial for imaging at greater depths within a sample[24]. QDs have broad absorption spectra but narrow emission spectra tunable by varying the QD size[21]. However, QDs are disadvantaged by their large size (comparable with the size of GFP) and often need multiple layers of functionalisation and binding intermediates to attach them to the protein of interest[25].

2.3.4 Fluorescent proteins

The importance of the isolation of the green fluorescent protein (GFP) from the jellyfish *Aequorea Victoria*[26], the cloning of the GFP gene for use as a fluorescent probe[27] and the mutation of this protein and others to provide fluorescent proteins over the range of visible wavelengths[28-30] has recently been recognized with the 2008 Nobel prize in Chemistry. Fusion of a gene for a fluorescent protein to the gene encoding a protein of interest results in simultaneous expression of both, covalently linked. This provides a way of monitoring gene expression and the localisation of proteins in living organisms[29]. Expression of fluorescent proteins is generally non-toxic to cells, but fluorescent proteins are large (GFP is ~ 27 kDa) and may interfere with the normal functioning of the protein to which it is fused.

Despite this, fluorescent proteins offer several advantages over extrinsic fluorescent probes: they do not require purifying and production of tagged proteins and their introduction into the cell is performed entirely by cellular machinery resulting in specific 1:1 labelling of the protein of interest. However, they do require the protein of interest to be identified and cloned and the correct functioning of the fusion protein must be verified to ensure that it is not disrupted by the presence of the added protein. Fluorescent proteins are also often able to form dimers and higher order oligomers at high concentrations which can pose a problem for fusion proteins that are localized in cellular compartments. A single point mutation is capable of preventing dimerisation of GFP variants[31] and this

mutation should be present in any GFP variant used for experiments aiming to determine protein interactions or intermolecular distances.

Labelling of cells with fluorescent proteins can also encounter problems due to the inefficiency of gene transfer techniques. DNA encoding a fusion protein is placed in a plasmid (a ring of DNA in this context also known as a vector) and introduced into animal cells either by co-precipitation with calcium phosphate[32] or strontium phosphate[33], electroporation[34] (transient formation of pores in the plasma membrane with an electric field), lipofection[35] (DNA is introduced with cationic liposomes), microinjection[36] of DNA directly to the cytoplasm (or nucleus) or using viral vectors[37]. Only cells that take up the DNA will express the foreign gene and with the exception of microinjection the amount taken up is difficult to control resulting in large variations in expression levels.

Over time most of the foreign DNA taken up by the cells is degraded and the transfection is only transient. Lipofection is commonly used to achieve transient transfection as it has been proven in a variety of cell types and there are a number of commercially available cationic liposome preparations such as Lipofectamine (Invitrogen) and Fugene (Roche). Stable expression only occurs if the foreign gene is incorporated into a chromosome of the host cell; a rare event that occurs is less than 1% of cells. Isolation of these stably transfected cells can be difficult and time consuming.

Variants of GFP commonly used in imaging applications are based on the enhanced version of the protein (eGFP). The peak of natural GFP absorption is at 395nm, which excites considerable auto-fluorescence in biological samples. eGFP contains a single altered amino-acid which shifts this peak to 488nm[38]. Similar mutations have been used to produce fluorescent proteins with shorter (enhanced cyan fluorescent protein, eCFP) or longer (enhanced yellow fluorescent protein, eYFP) excitation and emission spectra[29].

Further mutations of these variants are commonly used to address complications in their photophysical properties such as the environmental sensitivity and poor photostability of eYFP (mutated to produce Citrine). Additionally, other

fluorescent proteins that emit in the orange and red regions have been cloned from the sea anemone *Discosoma striata*[39]. These proteins are known as Ds-orange and Ds-red. A list of commonly used fluorescent protein vectors and the properties of the proteins they encode is provided in table 2.2.

Fluorescent Protein	Peak Excitation / nm	Peak Emission / nm	Quantum Yield	Extinction coefficient / $cm^{-1}M^{-1}$	References
eCFP	433	475	0.40	26,000	29
CyPet	435	477	0.51	35,000	40
Cerulean	433	475	0.62	-	41
eGFP	488	507	0.60	56,000	38, 42
eYFP	514	527	0.61	-	29
YPet	517	530	0.77	104,000	40
Venus	515	528	0.57	92,000	43
Citrine	516	529	0.76	-	44
mOrange	548	562	0.69	71,000	39
tdTomato	554	581	0.69	138,000	39
Ds-Red	556	586	0.10	75,000	39
mStrawberry	574	596	0.29	90,00	39
mCherry	587	610	0.22	72,000	39
mPlum	590	649	0.10	41,000	39

Table 2.2 Commonly used commercially available fluorescent proteins.

2.3.5 DNA transfer based site specific labeling strategies

Recently a new strategy for site specific labelling combining genetic manipulation and labelling with small artificial probes has been developed. Instead of fusing the protein of interest with a protein that is itself fluorescent, a

small peptide sequence is added which will react with a specific functional group under certain conditions. This functional group is placed on a fluorescent probe which can then be bound specifically to the peptide tag that has been added to the protein.

Several different tags have been developed from different natural systems. These include the Histidine (His_6) tag which binds nickle-nitrilotriacetic acid (Ni-NTA)[45, 46], the acyl carrier protein (ACP) or peptide carrier protein (PCP) to which a probe is transfered from coenzyme A (CoA) by the enzyme Pptase[46], and the acceptor peptide (AP) sequence that can be biotinylated by biotin ligase for subsequent binding to a streptavidin functionalised probe[47]. The probe itself is chosen depending upon the location in the cell of protein and the tag. If the tag is outside the plasma membrane on the extracellular portion of a membrane protein then any organic dye or Qdot can be used. If the protein is inside the cell then the probe must be cell permeable.

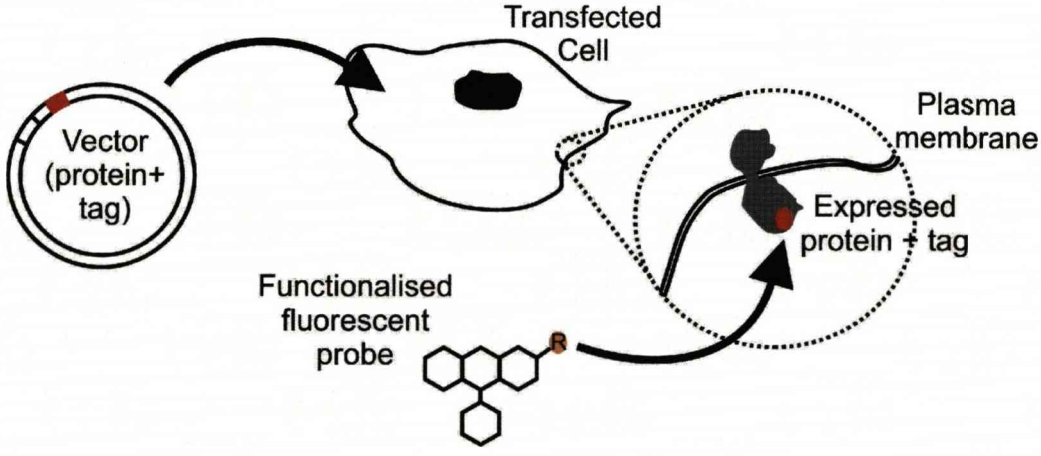

Figure 2.6 The basic principle of introducing small peptide sequences into proteins for site specific labelling. Cells are transfected with a vector that encodes the protein (grey) plus the added peptide sequence (red). These proteins are expressed by the cell and transported to their site of function (in this case the plasma membrane) where they can be covalently bound to a fluorescent probe exhibiting the correct reactive functional group (R).

2.4 Förster resonance energy transfer

In a system of molecules that are well separated (by distances ~10^{-9} – 10^{-8} m), Förster resonance energy transfer (FRET) is the process of non-radiative transfer of excited state energy from a fluorescent molecule that has absorbed a photon to another molecule in its ground state via Van der Waals (dipole-dipole) interactions. FRET occurs without conversion of the excited state energy to thermal vibrational energy or the molecules involved in the transfer process coming into contact through a kinetic collision. FRET was first observed in 1922 as sensitised fluorescence in a mixture of mercury and thallium vapour although transfer of energy by collisions of gaseous atoms could not be ruled out in this case[48, 49]. The non-trivial nature of the non-radiative energy transfer involved was subsequently confirmed, but it was not until 1948 that an accurate theoretical description of FRET was formulated by Theodore Förster[49].

In Förster's theory, the molecule excited by the excitation photon is referred to as the donor, and the molecule to which donor excited state energy is transferred to by FRET is known as the acceptor. If the energy difference for fluorescence emission of the donor corresponds exactly to a transition in a close acceptor molecule, there may be sufficient energetic coupling for the FRET process to be significant in comparison with donor fluorescence emission. The broad emission and absorption spectra of molecules ensures that this condition is met if the emission spectrum of the donor and the absorption spectrum of the acceptor overlap. This condition is exactly the same as the condition required for re-absorption of a donor fluorescence photon by the acceptor, which depends upon Coulombic interactions and has inverse square distance dependence. In contrast the dipole-dipole nature of the non-radiative interaction between the donor and acceptor in FRET results in an inverse sixth power dependence upon the donor-acceptor separation.

2.1.1 FRET between a single donor and acceptor

The rate of transfer κ_T between a donor and acceptor separated by a distance r at thermal equilibrium is given by[50]

$$\kappa_T(r) = \frac{1}{\tau_D}\frac{R_0^6}{r^6} \qquad \text{Eqn. 2-18}$$

where τ_D is the donor fluorescence lifetime in the absence of acceptor and R_0 is the Förster radius which is defined as the donor-acceptor separation at which the rate of donor de-excitation by resonance energy transfer is equal to the rate of de-excitation by fluorescence emission. It is simple to demonstrate that R_0 is the separation at which the efficiency of FRET is 0.5 for a single donor-acceptor pair and hence this quantity is useful for calculating the donor-acceptor separation from a measured FRET efficiency.

R_0 is related to the fluorescence properties of the donor and the acceptor by

$$R_0^6 = Q_D\kappa^2\left[\frac{9000(\ln 10)}{128\pi^5 N n^4}\right]\int_0^\infty f_D(\lambda)\varepsilon_A(\lambda)\lambda^4 d\lambda \qquad \text{Eqn. 2-19}$$

where Q_D is the quantum yield of the donor in the absence of energy transfer, κ^2 is the orientation factor, N is Avogadro's constant, n is the refractive index of the medium containing the donor and acceptor, $\varepsilon_A(\lambda)$ is the extinction coefficient of the acceptor at wavelength λ and $F_D(\lambda)$ is the normalized fluorescence emission spectrum of the donor. FRET is independent of the donor excitation wavelength as long as FRET does not occur before relaxation of the donor to the lowest excited state vibrational energy level.

The efficiency of FRET E_{FRET} is given by

$$E_{FRET} = \frac{\kappa_T}{\kappa_T + \tau_D^{-1}} = \frac{R_0^6}{R_0^6 + r^6} \qquad \text{Eqn. 2-20}$$

Figure 2.7 graphically displays the dependence of E_{FRET} on the donor-acceptor separation. By measuring the efficiency of FRET between donors and acceptors with known R_0 values, this relationship can be used to calculate the separation of donors and acceptors in a sample as long as FRET pairs can be considered to be independent of each other. The dependence of FRET efficiency upon the inverse sixth power of the separation has been experimentally verified at the ensemble and single molecule levels[50, 51].

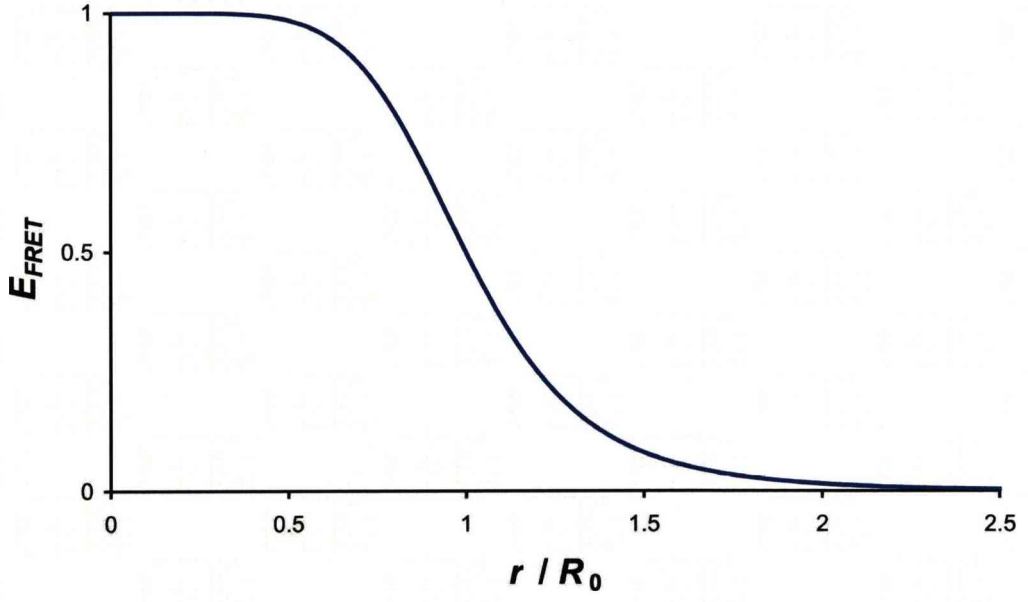

Figure 2.7 The dependence of FRET efficiency (E_{FRET}) upon the donor-acceptor separation r expressed in multiples of the Förster radius R_0.

In the range $0.5 < r / R_0 < 1.5$ there is measurable variation in E_{FRET}. The values of R_0 of FRET pairs comprising fluorescent molecules are usually < 8 nm and donor and acceptor molecules must be separated by < 12 nm for FRET to be unambiguously observable.

The value of R_0 for a given donor-acceptor pair can therefore be calculated by measuring the spectral properties of the donor and acceptor (to calculate the overlap integral), the donor quantum yield and specifying a value for κ^2. The following sections discuss the measurement of the overlap integral and donor quantum yield, plus the errors introduced by assuming an average value for κ^2.

2.4.1 The overlap integral

The overlap integral quantifies the overlap between the donor fluorescence emission and acceptor absorption spectra and is given by[50]

$$J(\lambda) = \int_0^\infty f_D(\lambda)\varepsilon_A(\lambda)\lambda^4 d\lambda = \frac{\int_0^\infty F_D(\lambda)\varepsilon_A(\lambda)\lambda^4 d\lambda}{\int_0^\infty F_D(\lambda)d\lambda} \qquad \text{Eqn. 2-21}$$

$f_D(\lambda)$ is the corrected fluorescence intensity of the donor (with the area under the emission spectrum normalised to unity) and $\varepsilon_A(\lambda)$ is the extinction coefficient of the acceptor at λ. Alternatively, the uncorrected fluorescence intensity of the donor, $F_D(\lambda)$ can be used and the overlap integral normalized by the area under the donor emission spectrum. Therefore $J(\lambda)$ can be calculated by measuring the donor emission spectrum and the acceptor absorption spectrum and numerically integrating Eqn. 2-21.

If the wavelength is in nm and the units of ε_A are $M^{-1}cm^{-1}$ then $J(\lambda)$ is in units of $M^{-1}cm^{-1}nm^4$. The Förster radius can be calculated in angstroms using[47]

$$R_0 = 0.211\left[n^{-4}Q_D\kappa^2 J(\lambda)\right]^{\frac{1}{6}} \quad \text{(in units of Å)} \qquad \text{Eqn. 2-22}$$

2.4.2 Donor quantum yield determination

The fluorescence quantum yield is the ratio of photons absorbed to the number of fluorescence photons emitted by a fluorescent molecule. This property can be measured for an uncharacterised sample by comparing it to standard samples with known quantum yields. If these standard and unknown samples have the same absorbance at a given wavelength, then they will absorb the same number of photons under the same illumination conditions. From this assumption it follows that the ratio of the integrated intensities of an unknown solution and the standard solution obtained under the same experimental conditions gives the ratio of their quantum yields. The quantum yield of the unknown sample could then be calculated from the known quantum yield of the standard.

However, quantum yield determination with real samples must avoid inner filter effects (re-absorption of fluorescence emission that can lead to an apparent decrease in the quantum yield or distortion of fluorescence spectra) and it is not always possible to maintain the exact same experimental conditions as those used for the standard sample. Different solvents may have to be used for different samples and as a consequence the observed fluorescence intensity will vary due to their different refractive indices. Consequently a more reliable way of comparing an unknown sample with a standard is to obtain the integrated fluorescence intensities I_f over a range of sample concentrations with an absorbance < 0.1 [53]. In the absence of concentration effects the integrated intensity will be a linear function of the absorbance with a gradient proportional to the quantum yield of the sample. The fluorescence intensity observed from a medium of refractive index n_1 by a detector in a medium of refractive index n_0 is scaled by a factor of $(n_1/n_0)^2$. The unknown quantum yield can then be calculated using the equation

$$Q_x = Q_R \left(\frac{Grad_x}{Grad_R} \right) \left(\frac{n_x}{n_R} \right)^2 \qquad \text{Eqn. 2-23}$$

where Q_x is the unknown quantum yield to be determined, Q_R is the quantum yield of the reference sample, $Grad_{x,\ R}$ are the gradients of the integrated fluorescence intensity vs. absorbance plots for the unknown and reference samples and $n_{x,\ R}$ are the refractive indices of the solvents in the two samples.

This approach can also be extended to the comparison of samples that are not excited at the same wavelength by correcting the integrated fluorescence intensity for wavelength dependent changes in excitation intensity.

2.4.3 The Orientation factor

The orientation factor κ^2 is defined as[40]

$$\kappa^2 = (\cos\theta_T - 3\cos\theta_D \cos\theta_A)^2 = (\sin\theta_D \sin\theta_A \cos\phi - 2\cos\theta_D \cos\theta_A)^2$$

Eqn. 2-24

where θ_T is the angle between the donor emission dipole and the acceptor absorption dipole, θ_D and θ_A are the angles between the same dipoles and the vector joining the donor and acceptor positions. ϕ is the angle between the planes of the two dipoles. Figure 2.8 is a diagram showing these angles.

The possible range of κ^2 values is between 0 (perpendicular dipoles) and 4 (collinear dipoles). $\kappa^2 = 1$ for parallel dipoles. An ensemble of FRET pairs tagged to elements of a biological sample will contain a distribution of κ^2 values and it is usual practice to assume an average value for the orientation factor when calculating R_0[54].

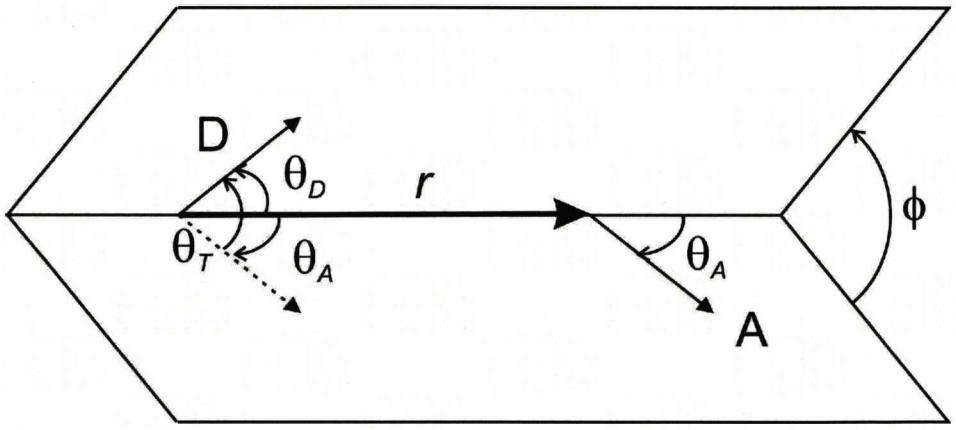

Figure 2.8 A donor emission dipole (D) and an acceptor absorption dipole (A) separated by a distance r. The angles relevant to the determination of the orientation factor κ^2 are also shown.

Fluorophores attached to proteins usually retain a limited freedom of motion about the point of conjugation which can randomise their orientation. Donors and acceptors can be considered as having some ability to reorient with respect to the proteins they are bound to, with the macromolecular structures of the proteins defining their separation. $\kappa^2 = 2/3$ is the value expected for donor and acceptor transition dipoles that are free to sample all possible orientations through rotational diffusion during the time the donor spends in the excited state, hence randomising the value of κ^2 for each FRET pair. This is referred to as the dynamic averaging limit. The range and speed of the allowed motion will vary between different conjugations of proteins and dyes, but will make the value of κ^2 close to the dynamic averaging limit. Determination of intramolecular distances in the protein F-actin by FRET (with $\kappa^2 = 2/3$ assumed) and by x-ray diffraction of crystallized protein has been shown to give the same results[55], providing confidence that it is valid to use the dynamic averaging limit when dealing with FRET pairs tagged to proteins. The average value expected for a range of static donor-acceptor orientations (the static averaging limit) is $\kappa^2 = 0.476$, but the use of this static averaging limit was shown to be inappropriate for fluorophores conjugated to biomolecules[56].

Fluorescence anisotropy measurements can be used to characterise the mobility of a conjugated dye. A population of fluorophores excited with vertically polarised light will be photoselected for molecules with absorption dipoles aligned in the same direction. Any ability of the dye molecule to reorient during the excited state lifetime results in a reduction of the measured anisotropy from the maximum possible value, (r_{max} = 0.4 for single photon excitation). From the measurable depolarisation of the donor and acceptor it is possible to set lower and upper bounds on the value of κ^2 [54, 56]. An alternative approach to estimating the error introduced by using $\kappa^2 = 2/3$ considers the consequences of a population of randomly oriented but static fluorophores that have overlapping electronic transitions. Many fluorescent dyes exhibit mixed transitions that reduce their fundamental anisotropy below r_{max} and further reduce any error introduced by using the dynamic averaging limit. From this approach, the error in any distance determined via an R_0 value calculated with $\kappa^2 = 2/3$ is < 10% when the measured donor and acceptor anisotropies are less than 0.22 [57].

2.4.4 Methods of observing FRET

There are three main approaches to the observation of FRET through its influence on different properties of donor and acceptor fluorescence emission[58]. These are by measurement of

1 changes in the donor and acceptor fluorescence intensities (either separately or together)
2 the apparent reduction in donor fluorescence lifetime resulting from competition with FRET
3 the reduction in anisotropy of the total fluorescence emission that accompanies FRET.

These three methods are illustrated in figure 2.9.

Monitoring intensity changes in the donor and acceptor fluorescence emission is perhaps the easiest method to implement as no specialised equipment is required beyond a standard widefield fluorescence microscope equipped with suitable filter sets. The FRET efficiency is related to the donor fluorescence intensity in the presence (F_{DA}) and absence of acceptor (F_D) by[50]

$$E_{FRET} = 1 - \frac{F_{DA}}{F_D} \qquad \text{Eqn. 2-25}$$

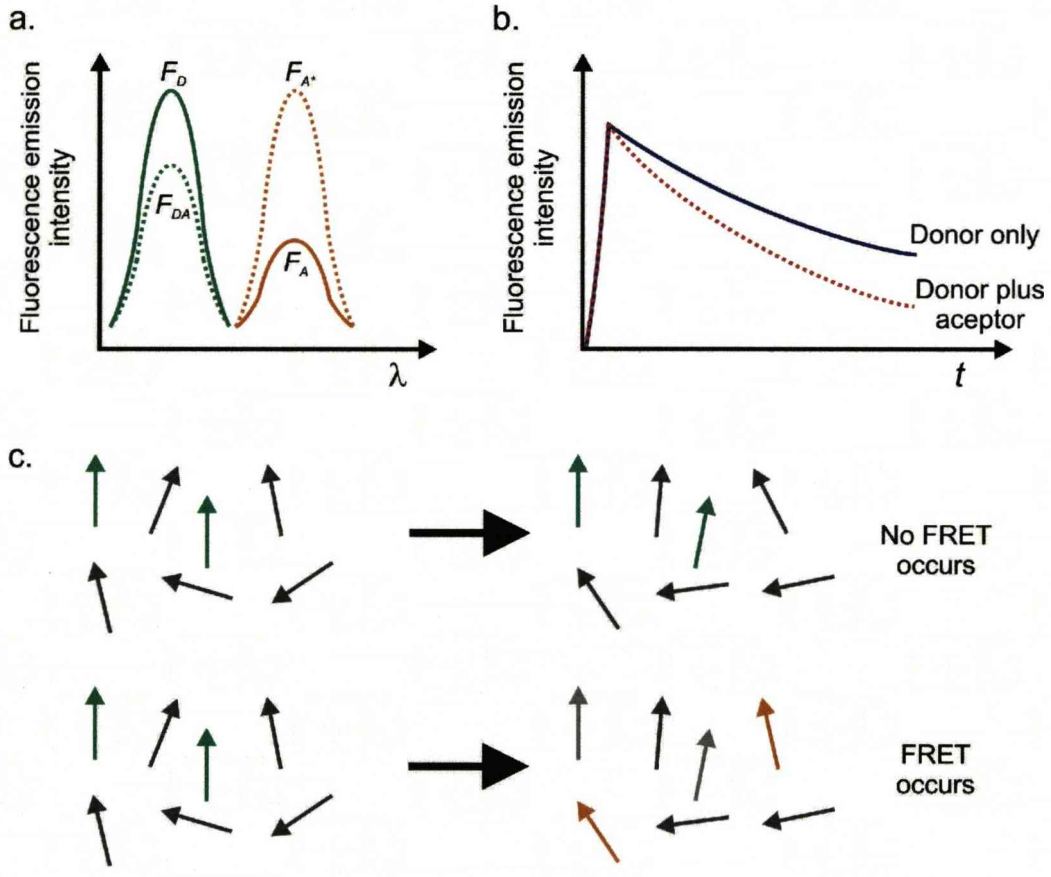

Figure 2.9 The effect of FRET upon measurable fluorescent properties. **a.** The donor fluorescence intensity (F_D) is quenched in the presence of a FRET (F_{DA}). FRET also leads to sensitised acceptor fluorescence emission (F_{A*}). (F_A) is the acceptor fluorescence emission due to direct excitation. **b.** The fluorescence lifetime of the donor (blue intensity decay) is reduced in the presence of the acceptor (red dashed intensity decay). **c.** Arrows represent the orientation of excited donor molecules (green), unexcited donors and acceptors (grey) and excited acceptors (orange). Transfer of excited state energy to non-photoselected acceptors will reduce the fluorescence anisotropy of a sample.

Alternatively it can be shown that it is also related to the intensity of the sensitised acceptor emission, F_{A*} by

$$E_{FRET} = \left(1 + \frac{F_{DA}}{F_{A*}}\right)^{-1} \qquad \text{Eqn. 2-26}$$

However, intensity based methods are complicated by cross-talk between donor and acceptor channels, and residual direct excitation of the acceptor at the wavelength used to excite the donor. Many different variations of intensity measurements exist that attempt to address these issues[59-61]. Commonly used is the 'three cube' technique[61, 62] that measures the fluorescence intensity of donors and acceptors when directly excited before using these to correct the measured sensitised acceptor intensity. This method has the advantage of fast acquisition, but the corrected FRET measurement is still a function of the concentration of donors and acceptors, the excitation intensity, excitation wavelength and the detection efficiency of the instrument used. Consequently it is difficult to compare FRET efficiencies measured this way between different experiments or instruments[58].

In contrast FRET efficiency determination from the reduction in donor lifetime caused by FRET is independent of the donor and acceptor concentrations and unaffected by donor photobleaching. As the lifetime of the intensity decay is proportional to the area underneath it (the integrated fluorescence intensity) the lifetime in the presence (τ_{DA}) and absence of acceptor (τ_D) is related to the FRET efficiency in a manner analogous to Eqn. 2-25

$$E_{FRET} = 1 - \frac{\tau_{DA}}{\tau_D} \qquad \text{Eqn. 2-27}$$

This expression assumes that there is a single donor-acceptor separation and that both fluorescence decays are described by single exponential functions so that their lifetimes are proportional to the area under the intensity decay. It is also

valid for multi-exponential decays as long as the τ_{DA} and τ_D used are the weighted means of the multi-exponential lifetime components[60]. τ_D can be obtained either from a separate sample lacking acceptor or from the same sample after complete photobleaching of the acceptor. Acceptor bleaching can also be used as an independent test to verify that any measured reduction in donor lifetime is indeed due to FRET. Intensity decay measurements have the disadvantages of taking relatively long times to acquire large numbers of photons. This also increases the possibility of causing photodamage or bleaching of the sample.

Finally, fluorescence anisotropy measurements can be used[63-65]. The excited state population of donors is photoselected by the polarisation of the illuminating light (described in section 2.2.3). The fluorescence emission of these donors is similarly polarised unless depolarised by rotational diffusion of the donors. FRET provides another mechanism for depolarisation as excited state energy can be transfered to any acceptor within the range of FRET, providing the relative orientations of donor emission and acceptor absorption dipoles are not perpendicular. The correlation between the highly oriented population of excited donors does not extend to the total fluorescence emission from both the donors and acceptors. As well as being able to quantify FRET between different fluorescent species[63] (hetero-FRET) it has the advantage of being the only method capable of measuring FRET when the donor and acceptor are the same fluorescent species (homo-FRET)[58, 64, 65].

References

1. Wayne, R. P. Principles and Applications of Photochemistry (Oxford University Press, 1988).

2. Klonis, N. & Sawyer, W. H. Spectral Properties of the Prototropic Forms of Fluorescein in Aqueous Solution. Journal of Fluorescence 6, 147-157 (1996).

3. Sjöback, R., Nygren, J. & Kubista, M. Absorption and fluorescence properties of fluorescein. Spectrochimica Acta Part A 51, L7-L21 (1995).

4. Mitchell, A. C., Wall, J. E., Murray, J. G. & Morgan, C. G. Measurement of nanosecond time-resolved fluorescence with a directly gated interline CCD camera. Journal of Microscopy 206, 233-238 (2002).

5. Mitchell, A. C., Dad, S. & Morgan, C. G. Selective detection of luminescence from semiconductor quantum dots by nanosecond time-gated imaging with a colour-masked CCD detector. Journal of Microscopy 230, 172-176 (2008).

6. Duncan, R. R., Bergmann, A., Cousin, M. A., Apps, D. K. & Shipston, M. J. Multi-dimensional time-correlated single photon counting (TCSPC) fluorescence lifetime imaging microscopy (FLIM) to detect FRET in cells. Journal of Microscopy 215, 1-12 (2004).

7. Becker, W. et al. Fluorescence Lifetime Imaging by Time-correlated Single-Photon Counting. Microscopy Research and Technique 63, 58-66 (2005).

8. Becker, W. et al. High-Speed FLIM Data Acquisition by Time-Correlated Single Photon Counting. Proc. SPIE 5323 (2004).

9. O'Connor, D. V. & Phillips, D. Time correlated single photon counting (Academic Press, London, 1984).

10. Holmes, K. L. & Lantz, L. M. in Cytometry (ed. Darzynkiewicz, Z.) 185-202 (Academic Press, 2000).

11. Kurebayashi, N., Harkins, A. B. & Baylor, S. M. Use of fura red as an intracellular calcium indicator in frog skeletal muscle fibers. Biophysical Journal 64, 1934–1960 (1993).

12. Gee, K. R., Brown, K. A., Chen, W-N. U., Bishop-Stewart, J., Gray, D. & Johnson, I. Chemical and physiological characterization of fluo-4 Ca^{2+}-indicator dyes. Cell Calcium 27, 97-106 (2000).

13. Haugland, R. P. in Excited States of Biopolymers (ed. Steiner, R. F.) 29-53 (Plenum Press, New York, 1983).

14. Nataliya, P., et al. Alexa Dyes, a series of New Fluorescent Dyes that Yield Exceptionally Bright, Photostable Conjugates. The Journal of Histochemistry and Cytochemistry 47, 1179-1188 (1999).
15. Malicka, J. et al. Photostability of Cy3 and Cy5-Labeled DNA in the Presence of Metallic Silver Particles. Journal of Fluorescence 12, 439-447 (2002).
16. Buschmann, V., Weston, K. D. & Sauer, M. Spectroscopic Study and Evaluation of Red-Absorbing Fluorescent Dyes. Bioconjugate Chemistry 14, 195-204 (2003).
17. Resch-Genger, U., Grabolle1, M., Cavaliere-Jaricot, S. Nitschke, R. & Nann, T. Quantum dots versus organic dyes as fluorescent labels. Nature Methods 5, 763-775 (2008).
18. Axelrod, D. Carbocyanine dye orientation in red cell membrane studied by microscopic fluorescence polarization. Biophysical Journal 26, 557-73 (1979).
19. Wolf, B. E. Determination of the sidedness of carbocyanine dye labeling of membranes. Biochemistry 24, 582-586 (1985).
20. Packard, B. S. & Wolf, B. E. Fluorescence lifetimes of carbocyanine lipid analogues in phospholipid bilayers. Biochemistry 24, 5176-5181 (1985).
21. Jr., M. B., Moronne, M., Gin, P., Weiss, S. & Alivisatos, A. P. Semiconductor Nanocrystals as Fluorescent Biological Labels. Science 281, 2013-2015 (1998).
22. Chan, W. C. W. & Nie, S. Quantum Dot Bioconjugates for Ultrasensitive Nonisotopic Detection. Science 281, 2016-2018 (1998).
23. Warnement, M. R. & Rosenthal, S. J. in Fluorescence Spectroscopy in Biology (eds. Hof, M., Hutterer, R. & Fidler, V.) 263-274 (Springer, 2005).
24. Larson, D. R. et al. Water-Soluble Quantum Dots for Multiphoton Fluorescence Imaging in Vivo. Science 300, 1434-1436 (2003).
25. Michalet, X. et al. Quantum Dots for Live Cells, in Vivo Imaging, and Diagnostics. Science 307, 538-544 (2005).
26. Shimomura, O., Johnson, F. H. & Saiga, Y. Extraction, purification and properties of aequorin, a bioluminescent protein from the luminous

hydromedusan, Aequorea. Journal of Cellular and Comparative Physiology 59, 223-239 (1961).

27. Chalfie, M., Tu, Y., Euskirchen, G., Ward, W. W. & Prasher, D. C. Green fluorescent protein as a marker for gene expression. Science 263, 802-805 (1994).

28. Shaner, N. C., Steinbach, P. A. & Tsien, R. Y. A guide to choosing fluorescent proteins. Nature Methods 2, 905-909 (2005).

29. Tsien, R. Y. The Green Fluorescent Protein. Annual Review of Biochemistry 67, 507-544 (1998).

30. Shaner, N. C. et al. Improving the photostability of bright monomeric orange and red fluorescent proteins. Nature Methods 5, 545-551 (2008).

31. Zacharias, D. A., Violin, J. D., Newton, A. C. & Tsien, R. Y. Partitioning of Lipid-Modified Monomeric GFPs into Membrane Microdomains of Live Cells. Science 296, 913-916 (2002).

32. Chen, C. & Okayama, H. High-Efficiency Transformation of Mammalian Cells by Plasmid DNA. Molecular and Cellular Biology 7, 2745-2752 (1987).

33. Brash, D. E., Reddel, R. R., Quanrud, M., Yang, K., Farell, M. P., Harris, C. C. Strontium phosphate transfection of human cells in primary culture: stable expression of the simian virus 40 large-T-antigen gene in primary human bronchial epithelial cells. Molecular and Cellular Biology 2, 2031-2034 (1987).

34. Wong,.T.-K. & Neumann, E. Electric field mediated gene transfer. Biochemical and Biophysical Research Communications 107, 584-587 (1982).

35. Felgner, P. L. et al. Lipofection: A highly efficient, lipid-mediated DNA-transfection procedure. PNAS 84, 7413-7417 (1987).

36. Mueller, C., Graessmann, A. & Graessmann, M. Mapping of Early SV40-Specific Functions by Microinjection of Different Early Viral DNA Fragments. Cell 15, 579-585 (1978).

37. Cepko, C. L., Roberts, B. E. & Mulligan, R. C. Construction and Applications of a highly transmissible murine retrovirus shuttle vector. Cell 37, 1053-1062 (1984).

38. Heim, R., Cubitt, A. & Tsien, R. Improved Green Fluorescence. Nature 373, 663-664 (1995).

39. Shaner, N. C. et al. Improved monomeric red, orange and yellow fluorescent proteins derived from *Discosoma* sp. red fluorescent protein. Nature Biotechnology 22, 1567-1572 (2004).

40. Nguyen, A. W. & Daugherty, P. S. Evolutionary optimization of fluorescent proteins for intracellular FRET. Nature Biotechnology 23, 355-360 (2005).

41. Rizzo, M. A., Springer, G. H., Granada, B. & Piston, D. W. An improved cyan fluorescent protein variant useful for FRET. Nature Biotechnology 22, 445-449 (2004).

42. Patterson, G. H., Knobel, S. M., Sharif, W. D., Kain, S. R. & Piston, D. W. Use of the Green Fluorescent Protein and Its Mutants in Quantitative Fluorescence Microscopy. Biophysical Journal 73, 2782-2790 (1997).

43. Nagai, T. et al. A variant of yellow fluorescent protein with fast and efficient maturation for cell biological applications. Nature Biotechnology 20, 87-90 (2002).

44. Griesbeck, O. et al. Reducing the Environmental Sensitivity of Yellow Fluorescent Protein. The Journal of Biological Chemistry 276, 29188-29194 (2001).

45. Guignet, E. G., Hovius, R. & Vogel, H. Reversible site-selective labeling of membrane proteins in live cells. Nature Biotechnology 22, 440-444 (2004).

46. Chen, I. & Ting, A. Y. Site-specific labeling of proteins with small molecules in live cells. Current Opinion in Biotechnology 16, 35-40 (2005).

47. Howarth, M., Takao, K., Hayashi, Y. & Ting, A. Y. Targeting quantum dots to surface proteins in living cells with biotin ligase. PNAS 102, 7583-7588 (2005).

48. Cario, G. & Franck, J. Über Sensibilisierte Fluoreszenz von Gasen. Z Physik 17, 202-212 (1923).

49. Förster, T. Transfer Mechanisms of Electronic Excitation. Tenth Spiers Memorial Lecture (1959).

50. Lakowicz, J. R. Principles of Fluorescence Spectroscopy (Kluwer Academic / Plenum Publishers, New York, 1999).

51. Schuler, B., Lipman, E. A., Steinbach, P. J., Kumke, M. & Eaton, W. A. Polyproline and the "spectroscopic ruler" revisited with single molecule fluorescence. PNAS 102, 2754-2759 (2005).

52. Stryer, L. & Haughland, R. P. Energy transfer: a spectroscopic ruler. PNAS 58, 719-726 (1967).

53. Williams, A. T. R., Winfield, S. A. & Miller, J. N. Relative fluorescence quantum yields using a computer controlled luminescence spectrometer. The Analyst 108, 1067 (1983).

54. Meer, B. W. v. d. Kappa-squared: from nuisance to new sense. Reviews in Molecular Biotechnology 82, 181-196 (2002).

55. Remedios, C. G. D. & Moens, P. D. J. Fluorescence Resonance Energy Transfer Is a Reliable "Ruler" for Measuring Structural Changes in Proteins. Journal of Structural Biology 115, 175-185 (1995).

56. Dale, R. E., Eisinger, J. & Blumberg, W. E. Orientational Freedom of Molecular Probes - Orientation Factor in Intra-Molecular Energy-Transfer. Biophysical Journal 26, 161-193 (1979).

57. Haas, E., Katchalski-Katzir, E. & Steinberg, I. Effect of the orientation of donor and acceptor on the probability of energy transfer involving electronic transitions of mixed polarization. Biochemistry 17, 5064-70 (1978).

58. Vogel, S. S., Thaler, C. & Koushik, S. V. Fanciful FRET. Science's STKE re2 (2006).

59. Gordon, G. W., Berry, G., Liang, X. H., Levine, B. & Herman, B. Quantitative Fluorescence Resonance Energy Transfer Measurements Using Fluorescence Microscopy. Biophysical Journal 74, 2702-2713 (1998).

60. Jares-Erijman, E. A. & Jovin, T. M. FRET Imaging. Nature Biotechnology 21, 1387-1395 (2003).

61. Chen, H., Puhl, H. L., Koushik, S. V., Vogel, S. S. & Ikeda, S. R. Measurement of FRET Efficiency and Ratio of Donor to Acceptor Concentration in Living Cells. Biophysical Journal: Biophysical Letters 91, L39-L41 (2006).

62. Zal, T. & Gascoigne, N. R. Photobleaching-Corrected FRET Efficiency Imaging of Live Cells. Biophysical Journal 86, 3923-3939 (2004).

63. Rizzo, M. A., Piston, D. W. High-contrast imaging of fluorescent protein FRET by fluorescence polarization microscopy. Biophysical Journal 88, L14-L16 (2005)

64. Gautier, I. et al. Homo-FRET Microscopy in Living Cells to Measure Monomer-Dimer Transition of GFP-Tagged Proteins. Biophysical Journal 80, 3000-3008 (2001).

65. Clayton, A. H., Hanley, Q. S., Arndt-Jovin, D. J., Subramaniam, V., Jovin, T. Dynamic fluorescence anisotropy imaging microscopy in the frequency domain (rFLIM). Biophysical Journal 83, 1631-1649 (2002).

3 ErbB transmembrane receptors: A paradigm in membrane protein signalling

3.1 The Epidermal Growth Factor

Growth factors are small, soluble proteins that are produced by cells and released into the extracellular environment to act as chemical messengers. The function of signalling molecules is to allow communication between cells that are not in physical contact, or necessarily in the same tissue. To achieve this they must produce a response from the cells that they come into contact with. As the name suggests, growth factors are important in controlling the growth and proliferation of cells within multicellular organisms. They are especially important in the development of embryos where well timed signals are required to instruct cells to continue dividing, to become specialised (differentiate) or undergo programmed cell death (apoptosis) depending upon their location in the embryo at a particular stage of development[1].

The first growth factor to be identified was the Epidermal Growth Factor (EGF) which was isolated from the submaxillary gland of mice in 1962 by Stanley Cohen[2]. It was identified due to its ability to promote tooth growth and eyelid opening in newborn mice. EGF is produced as a precursor transmembrane protein that is biologically active at the cell surface, before cleavage of the extracellular portion of this protein releases the soluble growth factor into the extracellular environment[3]. The family of membrane bound metalloproteases known as ADAMs (a disintegrin and metalloprotease) appears to be responsible for this cleavage[3, 4], but the exact mechanisms controlling such a major step in the regulation of growth factor signals is not yet known.

3.2 The ErbB family of growth factor receptors

In order for extracellular chemical messengers to induce a cellular growth response they must either: (i) cross the cell plasma membrane to interact directly with precursors, activators or regulators of DNA replication or transcription; or (ii) their presence in the extracellular environment must be detected at the cell boundary (the plasma membrane) and be translated across this barrier leading to activation of other signalling molecules inside the cell. EGF is far too large to pass across the plasma membrane, but instead binds to a receptor protein at the cell surface. The EGF receptor (EGFR, also known as ErbB1 and HER1 in humans) is a transmembrane protein with a glycosylated extracellular region that binds to growth factor ligands, a single pass α-helix transmembrane domain and a large cytoplasmic region. The cytoplasmic region includes a flexible domain juxtaposed to the inner leaflet of the plasma membrane (known as the juxtamembrane domain), a tyrosine kinase domain and a c-terminal domain containing multiple tyrosine residues[5]. A map of the secondary structure of ErbB1 highlighting the different regions can is shown in figure 3.1. Transmembrane proteins such as ErbB1 are known as receptor tyrosine kinases (RTKs).

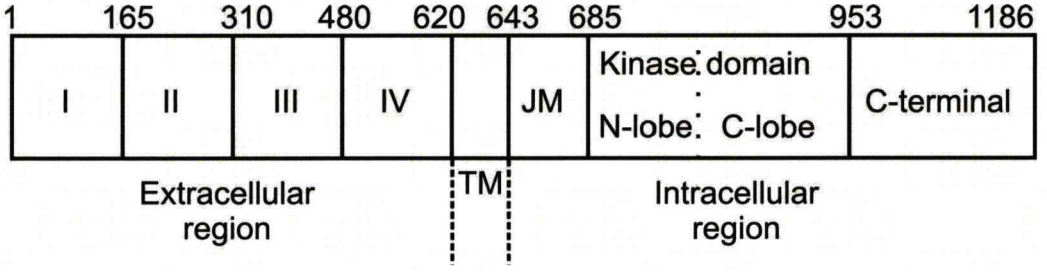

Figure 3.1 The domain structure of ErbB1. Amino-acid residues are numbered from the N-terminus at the start of domain I. The boundary of the transmembrane region (TM) is indicated by dashed lines. JM is the juxtamembrane domain. The kinase domain is divided into two lobes named for their proximity in the secondary structure to the N- and C-termini of the receptor.

A tyrosine kinase is an enzyme that catalyses a reversible covalent modification that adds a phosphate group to the hydroxyl group of the amino acid tyrosine. The phosphate group can be removed by other enzymes known as phosphatases. Phosphorylation is a simple method of altering the tertiary structure of a protein in order to activate or deactivate an enzyme or adjust its ability to bind to other proteins. The early realisation that growth factor-induced ErbB1 activation is associated with dimerisation and/or oligomerisation suggested that trans-phosphorylation of ErbB1 tyrosine residues by neighbouring ErbB1 kinase domains was involved in receptor activation[6]. This suggests an intuitive mechanism for how growth factor signals might be transduced across the plasma membrane by a single pass transmembrane receptor like ErbB1, where the tyrosine kinase is inactive in the absence of extracellular ligand binding but is able to trans-phosphorylate its own tyrosine residues or those of other intracellular proteins when growth factor binding causes clustering of two or more receptors. The tyrosine residues in the C-terminal domain serve as docking sites for signalling molecules with SH2 and PTB homologies[7]. The pattern of phosphorylation influences which molecules are able to bind and hence which signals are transduced upon activation.

Subsequent to the discovery of ErbB1, three more homologous receptors were identified that are now known as ErbB2-4. The ErbB family (also known as the HER family in humans) bind to ligands that all contain a conserved EGF-like binding domain. Table 3.1 lists all the known ErbB ligands, any commonly used acronyms and the ErbB members to which they bind[8-24]. ErbB ligands are generally divided into two groups – those that bind to ErbB1 and the neuregulins which bind to ErbB3 and ErbB4 only[7]. Three ErbB1 binding ligands can also bind to ErbB4 and are known as the bispecific ligands. Notably, ErbB2 has no known ligand and ErbB3 possesses a non-functioning kinase domain, suggesting that their activity is dependent upon heterodimerisation with other ErbB family members[25]. ErbB4 is the most recently identified family member and the least well characterised[26]. ErbB4 is known to exist in a number of isoforms that possess differences in their justamembrane and c-terminal domains that alter the receptors ability to bind to intracellular effectors[7, 26].

	Receptors				
Ligand	**ErbB1**	**ErbB2**	**ErbB3**	**ErbB4**	**Reference**
Epidermal growth factor (EGF)	**X**				2
Transforming growth factor alpha (TGF-α)	**X**				9
Heparin binding EGF like growth factor (HB-EGF)	**X**			**X**	10
Amphiregulin	**X**				11
Betacellulin	**X**			**X**	12
Epigen	**X**				13
Epiregulin	**X**			**X**	14
Neuregulin-1 (NRG-1)			**X**	**X**	15-18
Neuregulin-2 (NRG-2)			**X**	**X**	19-22
Neuregulin-3 (NRG-3)				**X**	23
Neuregulin-4 (NRG-4)				**X**	24

Table 3.1 The known growth factor ligands that bind to the four members of the ErbB family of receptor tyrosine kinases. Isoforms of the Neuregulins are not listed.

3.3 ErbB structure and signal transduction

The currently accepted model of ErbB signal transduction is heavily influenced by recently solved crystal structures of extracellular domain fragments of ErbB receptors and of the intracellular tyrosine kinase domain of ErbB1[27-34]. X-ray crystallography provides high resolution structural information about proteins and macromolecular complexes providing that they can be grown as a crystal. Unexpectedly, the crystallographic extracellular dimer fragment that dominates the current model was found to be mediated entirely by receptor-receptor contacts (on domain II) in a conformation that placed the bound ligands far from the dimerisation interface[27-34]. In the absence of ligand all ErbB members with the exception of ErbB2 crystallised in the form of an autoinhibited 'tethered'

monomer[30]. In this conformation, domains II and IV are held together burying the regions of domain II involved in dimerisation[29]. In order for a ligand to bind to both binding sites on domains I and II a large rearrangement of domains is required from the tethered conformation. Mutations designed to disrupt the tether don't, however, lead to an increased affinity for ligand or constitutively activated receptors[31, 32]. It is thought that the ErbB extracellular domain exists in a dynamic equilibrium of different conformations and that ligand binding stabilises the extended conformation of the receptor and allowing the formation of receptor dimers[29, 33]. Stable dimers then allow transactivation of tyrosine kinases and transphosphorylation of tyrosine residues[35]. ErbB2 was found to adopt an extended conformation stabilised by a direct interaction between domains I and III[36]. As ErbB2 appears to have no available ligand binding site it has been proposed that no ErbB2 ligands will ever be found[29]. That ErbB2 exists in a conformation constitutively primed to interact with other ErbB receptors is consistent with the observation that ErbB2 over expression (but not ErbB1) results in the transformation of cells[9, 37]. ErbB2 doesn't appear to homodimerise due to small but important deviations between the extended ErbB2 structure and that of ErbB1 which might be optimal for heterodimerisation[38].

Early crystal structures of the ErbB1 intracellular kinase domain suggested a protein with the characteristics of an activated kinase[39], consistent with the observation that phosphorylation of the single tyrosine residue present in the ErbB1 kinase domain is not required for receptor activation[40, 41]. Inactive ErbB1 kinase domains were subsequently crystallised but only when bound to lapatinib, a tyrosine kinase inhibitor[42]. More recent structural data has shown that the ErbB1 kinase domain can be activated by increasing its local concentration or by mutating a leucine residue (L843R) in the kinase activation loop[34], providing evidence that kinase domains are autoinhibited until intermolecular interactions promote its activation. The data also showed that kinase domains can form an asymmetric dimer in a manner similar to Cyclin A activation of cyclin-dependent kinases (CDKs)[34]. The observed asymmetry provides a mechanism for receptor activation by homo- or hetero-dimerisation that allows ErbB3 to be part of an active dimer without possessing any enzymic activity. The currently accepted picture of ErbB1 activation by EGF is shown in figure 3.2.

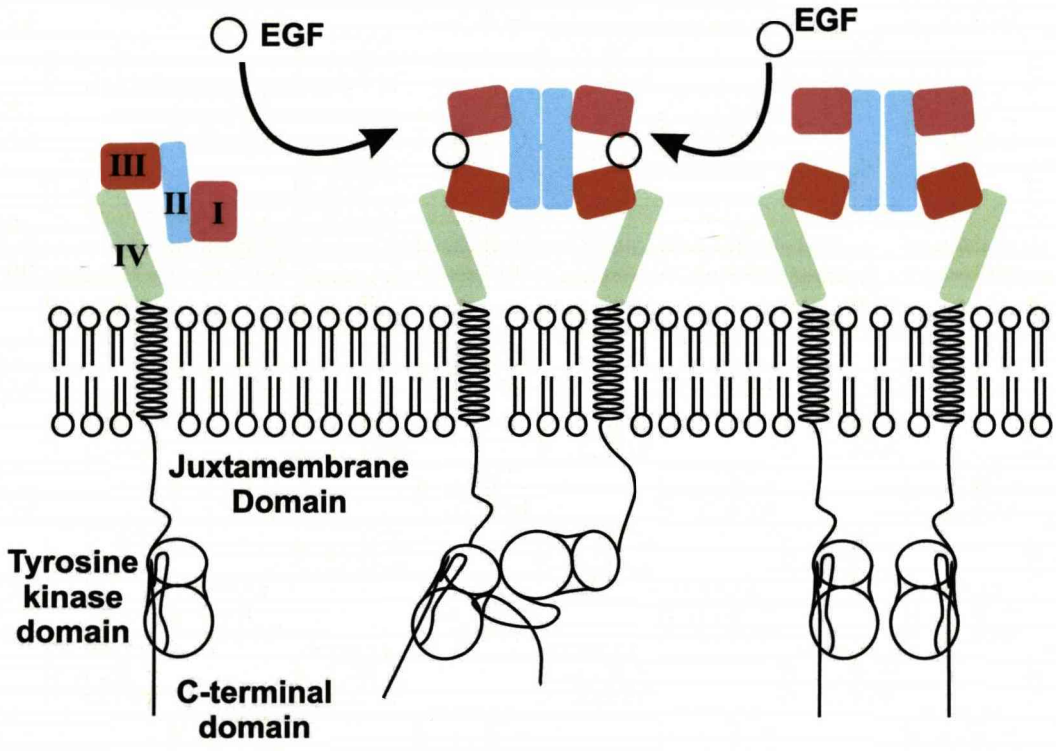

Figure 3.2 The crystal structure derived model of ligand induced ErbB receptor activation. Binding of EGF ligand to domains I and III of the extracellular region results in a conformational change from a tethered monomer to an extended conformation capable of homo- or hetero-dimerisation with other ErbB receptors. Ligand binding may also stabilise pre-formed dimers. Dimerisation of receptors allows the formation of asymmetric intracellular tyrosine kinase dimers and transphosphorylation of c-terminal tyrosine residues on one receptor.

It must be noted that the solved crystal structures represent at best snapshots of the dynamic protein structure, a crucial caveat for the understanding of relationships between structure and function[43]. Furthermore, as proteins often contain flexible domains that cannot be crystallised, pictures of large protein structures are often a best guess composite of the different crystallisable domains. This is certainly the case with the picture of ErbB receptors which lacks structural information regarding three important sections of the receptor - the transmembrane domain, juxtamembrane domain and c-terminal domain[8, 30]. It is known that isolated transmembrane domains, which are presumed to be helical, can associate with other transmembrane domains in cell membranes and may help stabilise dimers[44]. The juxtamembrane region contains non-tyrosine

phosphorylation sites, several protein binding domains and is suspected of playing a part in the regulation of ErbB activity[45]. The conformation of the C-terminal domain has so far only been related to the position of the tyrosine kinase domain via FRET studies that have shown that the two become separated after receptor activation[46]. Additionally, ErbB receptors are known to be glycosylated at several sites[47] and any oligosaccharides bound to the receptor at these sites are not fully visualised by the x-ray crystallography techniques[30].

3.4 Beyond the crystallographic dimer model

Despite the insights provided by the structural studies of ErbB receptors, there is still no clear description of how the dimerisation and activation mechanisms allow the receptors to function in the plasma membranes of live cells. The binding of EGF to ErbB1 is the most extensively characterised ErbB family signalling event, yet there are still a number of outstanding challenges in the understanding of ErbB1 signalling that are not addressed by the structural studies.

Binding studies of EGF to ErbB1 in many different cell types display two distinct classes of receptor that bind to EGF with different affinities[48, 49]. The affinity of the receptor for its ligand depends on both the rate at which ligand binds (the 'on' rate, k_f) and dissociates from the receptor (the 'off' rate, k_r)[50]. Binding affinity is expressed in terms of the equilibrium dissociation constant, K_D

$$K_D = \frac{k_r}{k_f} \qquad \text{Eqn. 3-1}$$

A small population of ErbB1 receptors bind ligand with high affinity ($K_D \sim 10$ - 100 pM) while the majority of ErbB1 bind to ligand with low affinity ($K_D \sim 1 - 10$ nM). There is evidence that an increased rate of ligand association is responsible for high affinity binding and that both affinity classes possess

similar dissociation rates[51]. These affinity classes can be made selectively available to ligand by binding appropriate monoclonal antibodies to the receptors in the vicinity of the ligand binding site[48, 51]. High affinity ErbB1 have been shown to be predominantly responsible for the transduction of most growth factor signals across the membrane[48]. Low affinity receptors are responsible for regulating the influx of Ca^{2+} into the cell immediately following ligand binding[52]. Interestingly, high affinity ligand binding to ErbB1 is not seen outside of a cellular environment[53]. It was initially expected that the affinity classes of receptor would correspond to the tethered and extended conformations of the ErbB1 extracellular region, but binding kinetics data and modelling has shown that it is not possible to account for experimentally measured EGF binding data with these two receptor states alone[32]. The mechanism that confers different binding affinities to identical translation products is still elusive although it has be shown that variations in ErbB glycosylation can alter receptor affinity for ligand but without reproducing the K_D values seen in live cells[47]. It is also possible to reproduce the ligand binding results seen in cells using a model that invokes negative cooperativity between receptors (where K_D increases as a function of the occupancy of ligand binding sites) in an aggregating system[54].

Also, imaging studies of ErbB receptors in cells have also consistently produced results that suggest that in a cellular context the structure of ErbB complexes is more complicated than the dimer model predicted by x-ray crystallography. Oligomers larger than dimers have been observed[55, 56] and there is evidence from single molecule FRET studies that they contain interfaces other than the back-to-back dimer[57]. There is also evidence that ErbB receptors form inactive dimers in live cells[58, 59].

3.5 ErbB1 Signalling Networks

ErbB1 is the most extensively studied member of the ErbB family and a diverse array of different intracellular molecular adapters and effector proteins and molecules has been found in complex with or to be phosphorylated by activated

ErbB1[40]. These adapters and effectors act either to promote or inhibit the signal transduced in response to extracellular ligand binding. Most of the proteins that bind directly to the ErbB1 intracellular domain bind to the sites of phosphorylated tyrosine residues (p-Tyr). The intracellular domain also contains binding sites with serine and threonine residues that can be phosphorylated. Adapter proteins are able to recruit other intracellular proteins (both enzymes and substrates) to form extended complexes with the activated ErbB1 receptors in order to subsequently activate and propagate signalling pathways that eventually result in the promotion or inhibition of different gene transcription programs.

Simultaneous activation of multiple linear pathways is common after EGF stimulation[1, 7, 35] and Figure 3.3 is a simplified diagram of some of the identified signalling pathways that are activated by ErbB1. The mitogen activated protein kinase (MAPK) pathway is activated in response to ErbB1 binding to the adapter protein Grb2 either directly or indirectly through Src homology and collagen binding protein (Shc)[41, 60, 61]. Relocation of Grb2 and son of sevenless (SoS) complexes to the membrane facilitates activation of the serine/threonine kinase Ras by SoS. The MAPK pathway is an example of a kinase cascade in which activated kinases phosphorylate and activate multiple kinases in the next step of the cascade, producing an amplification of the signal. Activated MAPK is also able to dissociate GrbB2/SoS complexes through SoS phosphorylation providing a negative feedback mechanism to control the cascade.

Grb2 also mediates interaction of the protein Cbl with ErbB1. Cbl adds ubiquitin molecules to ErbB1 targeting these receptors for degradation upon endocytosis instead of recycling back to the membrane[62]. Consequently this interaction is considered one of the most important negative regulators of ErbB1 activity[63].

Activated ErbB1 also directly and indirectly activates kinases and phosphatases involved in pathways that alter phospholipid metabolism such as phosphatidylinositol-3-kinase (PI3K) and phospholipase C-γ (PLC-γ). Both of these enzymes can produce activation of protein kinase C (PKC) which requires Ca^{2+} and the cofactor 1,2-diacylglycerol (DAG)[40]. PLC-γ catalyses the hydrolysis

of PtdIns(4,5)-P_2 (PIP_2) into inositol 1,3,5,-triphosphate (IP_3) and DAG. IP_3 mediates the release of Ca^{2+} from intracellular stores facilitating PKC activation. PKC itself can bind to the juxtamembrane region of ErbB1 and phosphorylate a threonine residue (Thr-654)[64] causing an inhibitory effect on ErbB1 activity and the loss of high affinity for EGF[65]. ErbB1 stimulation of PI3K also activates a cell survival pathway mediated by the enzyme Akt[41].

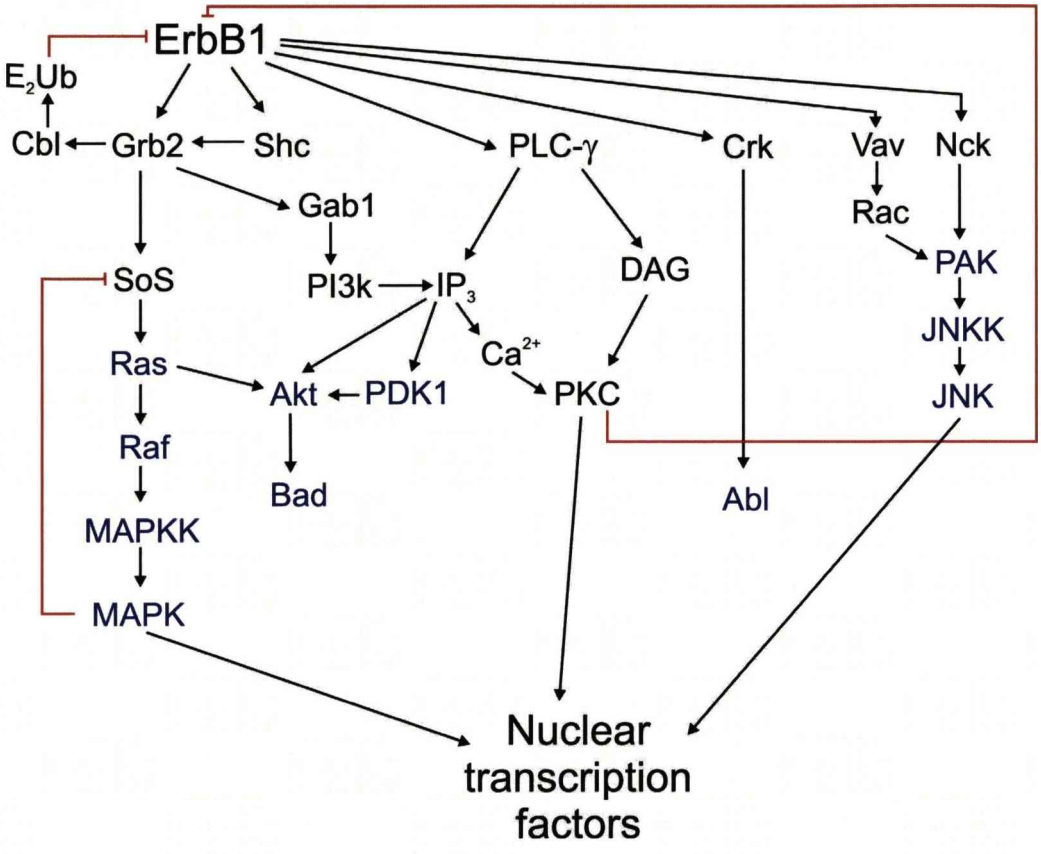

Figure 3.3 Some of the signalling networks that are stimulated by activation of ErbB1 receptors. Black lettering denotes adapter proteins and blue lettering denotes enzymes involved in signalling cascades. Black arrows represent associations that produce positive effects such as protein phosphorylation or production of secondary messengers. Red arrows represent inhibitory effects.

The vast majority of additional complexity due to cross-talk between signalling pathways, protein translocation throughout the cell, the formation of different signalling complexes and positive and negative feedback loops is ignored in figure 3.3. For example calcium release allows ErbB1 activation to indirectly activate calcium dependent pathways such as NFκB[66] and PKC is able to activate

components of the MAPK and JNK pathways[41]. ErbB1 is also known to interact with the actin[67] and EGF stimulation causes rearrangement of the actin cytoskeleton mediated by substrates of the kinase c-Src[68]. ErbB1 and Src share many substrates (such as PI3K) making it difficult to ascertain whether they are stimulated directly or indirectly by ErbB1[41]. Enzymes normally associated with cytokine receptor activation such as STAT and JAK kinases are also known to associate with ErbB1[41].

3.6 The influence of plasma membrane properties upon ErbB signalling

The plasma membrane is an inhomogeneous two-dimensional bi-layer system comprising of distinct localised microenvironments dictated by the distribution of different proteins and several types of lipids that make up the membrane[69]. The plasma membrane is an environment that is very distinct to that experienced by proteins in three-dimensional crystals, highlighting the important role played by cell based methodologies such as fluorescence imaging and FRET to provide complementary structural information in the plasma membrane. ErbB1 has been observed in both caveolae and so called 'lipid rafts' - microdomains with decreased fluidity due to increased cholesterol and sphingolipid content[70, 71]. However, ErbB1 is not exclusively associated with either of these microdomains and is randomly distributed at the plasma membrane[72]. Depletion of cholesterol from cell membranes results in an increase in surface EGF binding and an increase in ErbB1 phosphorylation[73, 74]. This observation was made under conditions that inhibit phosphotyrosine phosphatases and under which receptor trafficking cannot occur indicating that the apparent increases in tyrosine kinase activity and available cell surface ErbB1 are not due to a change in the rate of ErbB1 dephosphorylation or translocation of extra ErbB1 to the membrane from an intracellular source[73]. This suggests that depletion of cholesterol releases ErbB1 receptors from the lipid raft environment which normally has an

inhibitory effect on ErbB1 binding and tyrosine kinase activity[73, 75] but this doesn't appear to change the affinity of ErbB1 for ligand[72, 73].

Three types of electric potential are associated with cell plasma membranes [76]. Proteins contain many areas of charge density that allow them to interact with these electric potentials. In a resting state, the concentration of metal ions (for example Ca^{2+}, K^+, Na^+ etc.) within a cell is strictly controlled so that there is a potential difference across the plasma membrane which varies with cell type and is commonly referred to as the membrane potential[77]. The associated chemical gradients are also exploited by the cells to regulate crucial cellular functions. For example, activation of PLC-γ by ErbB1 results in the production of IP_3 and a release of Ca^{2+} from intracellular stores. Additionally, there is an influx of Ca^{2+} from outside the cell through voltage-independent calcium channels in response to EGF binding to low affinity ErbB1[48, 52]. The result of this wave of calcium ions is to cause a transient increase in $[K^+]$ through activation of K^+ channels. This causes a transient hyperpolarisation of the cell membrane[78, 79]. The increase in $[K^+]$ is only transient as PKC concurrently activated by Ca^{2+} downregulates K^+ channel activity[52].

There is also evidence that negatively charged regions at the surface of the ErbB1 kinase domain and juxtamembrane regions bind electrostatically to acidic lipids in the inner leaflet of the plasma membrane[80]. This would provide a mechanism for the autoinhibition of the kinase domain. It has been proposed that this inhibition is removed by the binding of Ca^{2+}/calmodulin (Ca^{2+}/CaM) complex to the juxtamembrane region[81, 82], causing a reversal of the net charge of the juxtamembrane domain that repels the intracellular region from the negatively charged inner leaflet[80]. Evidence that this mechanism may contribute to inhibition of ErbB1 activity comes from a reduction in the initial rate of ErbB1 phosphorylation upon ligand binding[81] and an increase in ErbB1 activity in the absence of ligand in response to membrane permeable bases (sphingosine) and increased salt concentrations[83].

It is also interesting to note that this electrostatic interaction with the membrane can sequester PIP_2[84], the precursor of PKC activating DAG and IP_3[80]. PKC phosphorylation of Thr654 inhibits calmodulin binding to the ErbB1 juxtamembrane region[85] and calmodulin has been observed to interfere with MAPK signalling and transactivation of ErbB1 by PKC[86]. How the interplay between PKC and CaM might regulate ErbB1 signal transduction has yet to be investigated.

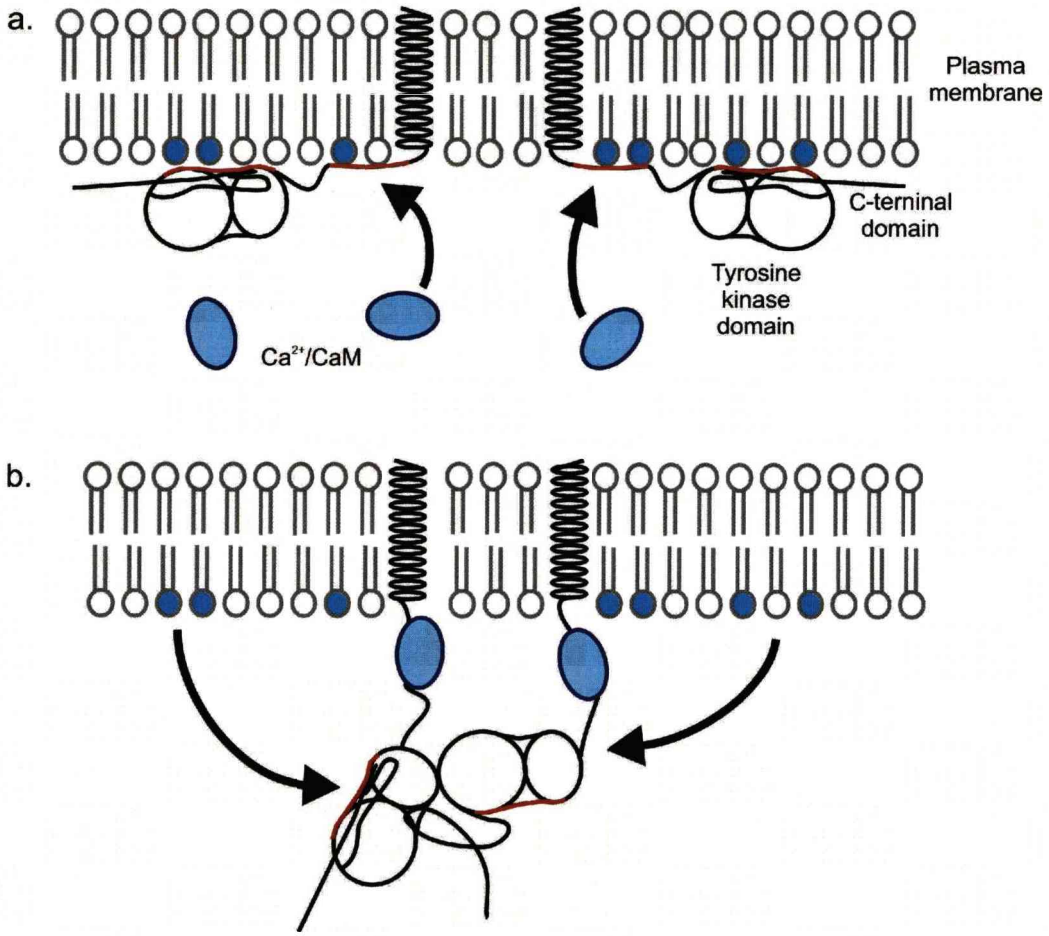

Figure 3.4 The electrostatic engine model for ErbB autoinhibition. **a.** Positively charged regions of the intracellular domain (red) interact electrostatically with negatively charged components of the plasma membrane inhibiting interactions between intracellular domains. **b.** Binding of Ca^{2+}/CaM to the juxtamembrane region of the receptor causes the intracellular domains of the receptors to be repelled from the membrane, allowing them to interact.

3.7 ErbB receptor trafficking

Although ErbB family members are predominantly localised at the cell surface, they are constantly trafficked to endosomes before being recycled back to the membrane[87]. The redistribution of membrane proteins within the cell is regulated by the presence or absence of motifs in their intracellular domain. ErbB1 undergoes rapid endocytosis upon ligand binding[88] and notably it is the only member of the ErbB family that does so[89]. Multi-ubiquitination of ErbB1 by the protein Cbl is known to target ErbB1 for destruction in lysosomes[90] but only after disassociation of Cbl from the complex[91].

There are two routes of receptor mediated endocytosis that act in parallel on different constituents of the membrane – through clathrin coated vesicles and through lipid raft based caveolae[92]. Upon stimulation with a low dose of EGF ErbB1 is efficiently endocytosed through the clathrin mediated pathway[92-95] and ErbB1 recruitment to lipid rafts has been observed in response to ligand[96]. In response to a high dose of EGF, ErbB1 internalisation proceeds mainly via the non-clathrin mediated route[93]. In the absence of ligand protein kinase A (PKA) activity appears to play a part in ErbB1 avoidance of internalisation[97] with PKA activity being reduced by activated ErbB1. In contrast, protein kinase C (PKC) phosphorylation of ErbB1 Thr654 enhances ligand induced internalisation, but prevents transport of receptors to lysosomes instead targeting them for recycling back to the plasma membrane[98].

EGF dissociates from ErbB1 at endosomal pH (~pH 5) and initially it was thought that the sole purpose of ligand induced internalisation was to desensitise the receptor to ligand (downregulation)[87, 99], but there is also evidence that receptors continue to signal in endosomes[60, 100-102]. ErbB1 internalisation also serves to alter the availability of signalling substrates over time and different signalling outcomes result from receptors at the membrane and in endosomes[100, 101, 103]. The defective downregulation of RTKs has been repeatedly implicated in the oncogenic transformation of cells[63]. ErbB1 with a disruptive mutation to its only site of direct cbl binding produces stronger mitogenic signals than wildtype

ErbB1[99, 104]. In order to observe activated ErbB1 receptors at the plasma membrane ligand-induced internalisation must be prevented. Ligand-induced internalisation occurs within minutes at 37°C, but can be slowed by reducing the temperature. At 4°C ligand induced internalisation of ErbB1 is almost completely inhibited[58] without preventing receptor activation upon ligand binding[57, 105].

References

1. Alroy, I. & Yarden, Y. The ErbB signaling network in embryogenesis and oncogenesis: signal diversification through combinatorial ligand-receptor interactions. FEBS Letters 410, 83-86 (1997).
2. Cohen, S. Isolation of a mouse submaxillary gland protein accelerating incisor eruption and eyelid opening in the new-born animal. The Journal of Biological Chemistry 237, 1555-1562 (1962).
3. Dempsey, P. J., Meise, K. S., Yoshitake, Y., Nishikawa, K. & Coffey, R. J. Apical Enrichment of Human EGF Precursor in Madin-Darby Canine Kidney Cells Involves Preferential Basolateral Ectodomain Cleavage Sensitive to a Metalloprotease Inhibitor. The Journal of Cell Biology 138, 747-758 (1997).
4. Blobel, C. P. ADAMS: key components in EGFR signaling and development. Nature Reviews Molecular Cell Biology 6, 32-43 (2005).
5. Schlessinger, J. Cell signaling by receptor tyrosine kinases. Cell 103, 211-225 (2000).
6. Yarden, Y. & Schlessinger, J. Self-Phosphorylation of Epidermal Growth Factor Receptor: Evidence for a Model of Intermolecular Allosteric Activation. Biochemistry 26, 1434-1442 (1987).
7. Yarden, Y. & Sliwkowski, M. X. Untangling the ErbB signalling network. Nature Reviews Molecular Cell Biology 2, 127-137 (2001).

8. Linggi, B. & Carpenter, G. ErbB receptors: new insights on mechanisms and biology. TRENDS in Cell Biology 16, 649-656 (2006).

9. Massagué, J. Transforming growth factor-α. The Journal of Biological Chemistry 265, 21393-21396 (1990).

10. Higashiyama, S. et al. Structure of Heparin-binding EGF-like Growth Factor. The Journal of Biological Chemistry 267, 6205-6212 (1992).

11. Shoyab, M., McDonald, V. L., Bradley, J. G. & Todaro, G. J. Amphiregulin: A bifunctional growth-modulating glycoprotein produced by the phorbol 12-myristate 13-acetate-treated human breast adenocarcinoma cell line MCF-7. PNAS 85, 6528-6532 (1988).

12. Shing, Y., Christofori, G., Hanahan, D., Ono, Y., Sasada, R., Igarashi, K. & Folkman, J. Betacellulin: a mitogen from pancreatic beta cell tumors. Science 259, 1604-1607 (1993).

13. Strachan, L. et al. Cloning and Biological Activity of Epigen, a Novel Member of the Epidermal Growth Factor Superfamily. The Journal of Biological Chemistry 276, 18265-18271 (2001).

14. Toyoda, H. et al. Epiregulin. The Journal of Biological Chemistry 270, 7495-7500 (1995).

15. Wen, D. et al. Neu differentiation factor: a transmembrane glycoprotein containing an EGF domain and an immunoglobulin homology unit. Cell 69, 559-572 (1992).

16. Peles, E. et al. Isolation of the Neu/HER-2 stimulatory ligand: A 44 kd glycoprotein that induces differentiation of mammary tumor cells. Cell 69, 205-216 (1992).

17. Holmes, W. E. et al. Identification of heregulin, a specific activator of p185erbB2. Science 256, 1205-1210 (1992).

18. Goodearl, A. D. J. et al. Purification of multiple forms of glial growth factor. The Journal of Biological Chemistry 18095-18102 (1992).

19. Carraway, K. L. et al. Neuregulin-2, a new ligand of ErbB3/ErbB4-receptor tyrosine kinases. Nature 387, 512-516 (1997).

20. Chang, H., Riese, D. J., Gilbert, W., Stern, D. F. & McMahan, U. J. Ligands for erbB-family receptors encoded by a neuregulin-like gene. Nature 387, 509-512 (1997).

21. Higashiyama, S. et al. A novel brain-derived member of the epidermal growth factor family that interacts with ErbB3 and ErbB4. The Journal of Biochemistry 122, 675-680 (1997).

22. Busfield, S. J. et al. Charaterization of a neuregulin-related gene, don-1, that is highly expressed in restricted regions of the cerebellum and hippocampus. Molecular and Cellular Biology 17, 4007-4014 (1997).

23. Zhang, D. et al. Neuregulin-3 (NRG3): a novel neural tissue-enriched protein that binds and activates ErbB4. PNAS 94, 9562-9567 (1997).

24. Harari, D. et al. Neuregulin-4: a novel growth factor that acts through the ErbB-4 receptor tyrosine kinase. Oncogene 18, 2681-2689 (1999).

25. Citri, A., Skaria, K. B. & Yarden, Y. The deaf and the dumb: the biology of ErbB-2 and ErbB-3. Experimental Cell Research 284, 54-65 (2003).

26. Carpenter, G. ErbB-4: mechanism of action and biology. Experimental Cell Research 284, 66-77 (2003).

27. Garrett, T. P. et al. Crystal structure of a truncated epidermal growth factor receptor extracellular domain bound to transforming growth factor alpha. Cell 110, 763-776 (2002).

28. Ogiso, H. et al. Crystal structure of the complex of human epidermal growth factor and receptor extracellular domains. Cell 110, 775-787 (2002).

29. Burgess, A. W. et al. An Open-and-Shut Case? Recent Insights into the Activation of EGF/ErbB Receptors. Molecular Cell 12, 541-552 (2003).

30. Ferguson, K. M. Structure-Based View of Epidermal Growth Factor Receptor Regulation. Annual Review of Biophysics 37, 353-373 (2008).

31. Dawson, J. P. et al. Epidermal growth factor receptor dimerisation and activation require ligand-induced conformational chnages in the dimer interface. Molecular Cell Biology 25, 7734-7742 (2005).

32. Mattoon, D., Klein, P., Lemmon, M. A., Lax, I. & Schlessinger, J. The tethered configuration of the EGF receptor extracellular domain exerts only a limited control of receptor function. PNAS 101, 923-928 (2004).

33. Ferguson, K. M. et al. EGF Activates Its Receptor by Removing Interactions that Autoinhibit Ectodomain Dimerization. Molecular Cell 11, 507-517 (2003).

34. Zhang, X., Gureasko, J., Shen, K., Cole, P. A. & Kuriyan, J. An Allosteric Mechanism for Activation of the Kinase Domain of Epidermal Growth Factor Receptor. Cell 125, 1137-1149 (2006).

35. Schlessinger, J. Common and distinct elements in cellular signaling via EGF and FGF receptors. Science 306, 1506-1507 (2004).

36. Garrett, T. P., McKern, N. M., Lou, M., Elleman, T. C. & Adams, T. E. The crystal structure of a truncated ErbB2 ectodomain reveals an active conformation, poised to interact with other ErbB receptors. Molecular Cell 11, 495-505 (2003).

37. Di Fiore, P. P. et al. erbB-2 is a potent oncogene when overexpressed in NIH/3T3 cells. Science 237, 178-182 (1987).

38. Franklin, M. C. et al. Insights into ErbB signalling from the structure of the ErbB2-peruzumab complex. Cancer Cell 5, 317-328 (2004).

39. Stamos, J., Sliwkowski, M. X. & Eigenbrot, C. Structure of the epidermal growth factor receptor kinase domain alone and in complex with a 4-anilinoquinazoline inhibitor. The Journal of Biological Chemistry 277 (2002).

40. Gotoh, N., Tojo, A., Hino, M., Yazaki, Y. & Shibuya, M. A highly conserved tyrosine residue at codon 845 within the kinase domain is not required for the transforming activity of human epidermal growth factor receptor. Biochemical and Biophysical Research Communications 186, 768-774 (1992).

41. Jorissen, R. N. et al. Epidermal growth factor receptor: mechanisms of activation and signalling. Experimental Cell Research 284, 31-53 (2003).

42. Wood, E. R., Truesdale, A. T., McDonald, O. B., Yuan, D. & Hassall, A. A unique structure for epidermal growth factor receptor bound to GW572016 (Lapatinib): relationships among protein conformation, inhibitor off-rate and receptor activity in tumour celss. Cancer Research 64, 6652-6659 (2004).

43. Thornton, J. M., Todd, A. E., Milburn, D., Borkakoti, N. & Orengo, C. A. From structure to function: Approaches and limitations. Nature Structural Biology (2000).

44. Mendrola, J. M., Berger, M. B., King, C. R. & Lemmon, M. A. The single transmembrane domains of ErbB receptors self-associate in cell membranes. The Journal of Biological Chemistry 277, 4704-4712 (2002).

45. Hubbard, S. R. & Till, J. H. Protein tyrosine kinase structure and function. Annual Review of Biochemistry 69, 373-398 (2000).

46. Lee, N. Y. & Koland, J. G. Conformational changes accompany phosphorylation of the epidermal growth factor receptor C-terminal domain. Protein Science 14, 2793-2803 (2005).

47. Whitson, K. B. et al. Functional Effects of Glycosylation at Asn-579 of the Epidermal Growth Factor Receptor. Biochemistry 44, 14920-14931 (2005).

48. Defize, L. H. K. et al. Signal Transduction by Epidermal Growth Factor Occurs Through the Subclass of High Affinity Receptors. The Journal of Cell Biology 109, 2495-2507 (1989).

49. Özcan, F., Klein, P., Lemmon, M. A., Lax, I. & Schlessinger, J. On the nature of low- and high-affinity EGF receptors on living cells. PNAS 103, 5735-5740 (2006).

50. Lauffenburger, D. A. & Linderman, J. J. Receptors: Models for Binding, Trafficking and Signalling (Oxford University Press, 1993).

51. Bellot, F. et al. High-Affinity Epidermal Growth Factor Binding Is Specifically Reduced by a Monoclonal Antibody and Appears Necessary for Early Responses. The Journal of Cell Biology 110 (1990).

52. Peppelenbosch, M. P., Tertoolen, L. G. & de Laat, S. W. Epidermal growth factor-activated calcium and potassium channels. The Journal of Biological Chemistry 266, 19938-19944 (1991).

53. Jones, J. T., Akita, R. W. & Sliwkowski, M. X. Binding specificities and affinities of egf domains for ErbB receptors. FEBS Letters 447, 227-231 (1999).

54. Macdonald, J. L. & Pike, L. J. Heterogeneity in EGF-binding affinities arises from negative cooperativity in an aggregating system. PNAS 105, 112-117 (2008).

55. Clayton, A. H. A. et al. Ligand-induced Dimer-Tetramer Transition during the Activation of the Cell Surface Epidermal Growth Factor

Receptor-A Multidimensional Microscopy Analysis. The Journal of Biological Chemistry 280, 30392-30399 (2005).

56. Furuuchi, K., Berezov, A., Kumagai, T. & Greene, M. I. Targeted Antireceptor Therapy with Monoclonal Antibodies Leads to the Formation of Inactivated Tetrameric Forms of ErbB Receptor. Journal of Immunology 178, 1021-1029 (2007).

57. Webb, S. E. D. et al. Single molecule imaging and FLIM show different structures for high and low-affinity EGFRs in A431 cells. Biophysical Journal 94, 803-819 (2008).

58. Martin-Fernandez, M., Clarke, D. T., Tobin, M. J., Jones, S. V. & Jones, G. R. Preformed Oligomeric Epidermal Growth Factor Receptors Undergo an Ectodomain Structure Change during Signalling. Biophysical Journal 82, 2415-2427 (2002).

59. Tao, R.-H. & Maruyama, I. N. All EGF (ErbB) receptors have preformed homo- and heterodimeric structures in living cells. Journal of Cell Science 121, 3207-3217 (2008).

60. Sorkin, A., McClure, M., Huang, F. & Carter, R. Interaction of EGF receptor and Grb2 in living cells visualized by fluorescence resonance energy transfer (FRET microscopy. Current Biology 10, 1395-1398 (2000).

61. Carpenter, G. The EGF receptor: a nexus for trafficking and signaling. BioEssays 22, 697-707 (2000).

62. Melker, A. A. d., Horst, G. v. d. & Borst, J. c-Cbl directs EGF receptors into an endocytic pathway that involves the ubiquitin-interacting motif of Eps15. Journal of Cell Science 117, 5001-5012 (2004).

63. Bache, K. G., Slagsvold, T. & Stenmark, H. Defective downregulation of receptor tyrosine kinases in cancer. EMBO Journal 23, 2707-2712 (2004).

64. Hunter, T., Ling, N. & Cooper, J. A. Protein kinase C phosphorylation of the EGF receptor at a threonine residue close to the cytoplasmic face of the plasma membrane. Nature 311, 480-483 (1984).

65. Davis, R. J. Independent Mechanisms Account for the Regulation by Protein Kinase C of the Epidermal Growth Factor Receptor Affinity and Tyrosine-Protein Kinase Activity. The Journal of Biological Chemistry 263, 9462-9469 (1988).

66. Sun, L. & Carpenter, G. Epidermal growth factor activation of NFkappaB is mediated through IkappaBalpha degradation and intracellular free calcium. Oncogene 16, 2095-2102 (1998).

67. Hartigh, J. C. d., Henegouwen, P. M. P. v. B. e., Verkleij, A. J. & Boonstra, J. The EGF Receptor is an Actin-binding Protein. The Journal of Cell Biology 119, 349-355 (1992).

68. Chang, J., Gill, S., Settleman, J. & Parsons, S. c-Src regulates the simultaneous rearrangement of actin cytoskeleton, p190RhoGAP, and p120RasGAP following epidermal growth factor stimulation. The Journal of Cell Biology 130, 355-368 (1995).

69. Simons, K. & Toomre, D. Lipid rafts and signal transduction. Molecular Cell Biology 1, 31-41 (2000).

70. Waugh, M. G., Lawson, D. & Hsuan, J. J. EGF receptor activation is localized within low-buoyant density, non-caveolar membrane domains. Biochemical Journal 337, 591-597 (1999).

71. Mineo, C., Gill, G. N. & Anderson, R. G. Regulated migration of EGF receptor from caveolae. The Journal of Biological Chemistry 274, 30636-30643 (1999).

72. Ringerike, T., Blystad, F. D., Levy, F. O., Madshus, I. H. & Stang, E. Cholesterol is important in control of EGF receptor kinase activity but EGF receptors are not concentrated in caveolae. Journal of Cell Science 115, 1331-1340 (2002).

73. Pike, L. J. & Casey, L. Cholesterol Levels Modulate EGF Receptor-Mediated Signaling by Altering Receptor Function and Trafficking. Biochemistry 41, 10315-10322 (2002).

74. Ge, G., Wu, J. & Lin, Q. Effect of membrane fluidity on Tyrosine Kinase Activity of Reconstituted Epidermal Growth Factor Receptor. Biochemical and Biophysical Research Communications 282, 511-514 (2001).

75. Westover, E. J., Covey, D. F., Brockman, H. L., Brown, R. E. & Pike, L. J. Cholesterol Depletion Results in Site-specific Increases in Epidermal Growth Factor Receptor Phosphorylation due to Membrane Level Effects. Studies with cholesterol enatiomers. The Journal of Biological Chemistry 278, 51125-51133 (2003).

76. Olivotto, M., Arcangeli, A. & Carla, M. Electric fields at the plasma membrane level: a neglected element in the mechanisms of cell signalling. BioEssays 18, 495-504 (1996).

77. O'Shea, P. Intermolecular interactions with / within cell membranes and the trinity of membrane potentials: kinetics and imaging. Biochemical Society Transactions 31, 990-996 (2003).

78. Enomoto, K., Cossu, M. F., Maeno, T., Edwards, C. & Oka, T. Involvement of the Ca^{2+} dependent K^{+} channel activity in the hyperpolarizing response induced by epidermal growth factor in mammary epithelial cells. FEBS Letters 203, 181-184 (1986).

79. Pandiella, A., Magni, M., Lovisolo, D. & Meldolesi, J. The Effects of Epidermal Growth Factor on Membrane Potential. The Journal of Biological Chemistry 264, 12914-12921 (1989).

80. McLaughlin, S., Smith, S. O., Hayman, M. J. & Murray, D. An Electrostatic Engine Model for Autoinhibition and Activation of the Epidermal Growth Factor Receptor (EGFR/ErbB) Family. Journal of General Physiology 126, 41-53 (2005).

81. Li, H., Ruano, M. J. & Villalobo, A. Endogenous calmodulin interacts with the epidermal growth factor receptor in living cells. FEBS Letters 559, 175-180 (2004).

82. Aifa, S. et al. Interactions between the juxtamembrane domain of the EGFR and calmodulin measured by surface plasmon resonance. Cellular Signalling 14, 1005-1013 (2002).

83. Davis, R. J. & Faucher, M. Two alternative mechanisms control the interconversion of functional states of the epidermal growth factor. The Journal of Biological Chemistry 262, 5373-5379 (1988).

84. Sato, T., Pallavi, P., Golebiewska, U., McLaughlin, S. & Smith, S. O. Structure of the Membrane Reconstituted Transmembrane-Juxtamembrane Peptide EGFR(622-660) and Its Interaction with Ca^{2+}/Calmodulin. Biochemistry 45, 12704-12714 (2006).

85. Aifa, S. et al. Phosphorylation of Thr654 but not Thr669 within the juxtamembrane domain of the EGF receptor inhibits calmodulin binding. Biochemical and Biophysical Research Communications 347, 381-387 (2006).

86. Tebar, F., Llado, A. & Enrich, C. Role of calmodulin in the modulation of the MAPK signalling pathway and the transactivation of epidermal growth factor receptor mediated by PKC. FEBS Letters 517, 206-210 (2002).

87. Wiley, H. S. Trafficking of the ErbB receptors and its influence on signaling. Experimental Cell Research 284, 78-88 (2003).

88. Carpenter, G. & Cohen, S. 125I-labeled human epidermal growth factor. Binding, internalization, and degradation in human fibroblasts. The Journal of Cell Biology 71, 159-171 (1976).

89. Baulida, J., Kraus, M. H., Alimandi, M., Fiore, P. P. D. & G. Carpenter. All ErbB receptors other than the epidermal growth factor receptor are endocytosis impaired. The Journal of Biological Chemistry 271, 5251–5257 (1996).

90. Grovdal, L. M., Stang, E., Sorkin, A. & Madshus, I. H. Direct interaction of Cbl with pTyr 1045 of the EGF receptor (EGFR) is required to sort the EGFR to lysosomes for degredation. Experimental Cell Research 300, 388-395 (2004).

91. Pennock, S. & Wang, Z. A tale of two Cbls: Interplay of c-Cbl and Cbl-b in Epidermal Growth Factor Regulation. Molecular Cell Biology 28, 3020-3037 (2008).

92. Waterman, H. & Yarden, Y. Molecular mechanisms underlying endocytosis and sorting of ErbB receptor tyrosine kinases. FEBS Letters 490, 142-152 (2001).

93. Sigismund, S. et al. Clathrin-independent endocytosis of ubiquitinated cargos. PNAS 102, 2760-2765 (2004).

94. Jiang, X., Huang, F., Marusyk, A. & Sorkin, A. Grb2 Regulates Internalization of EGF Receptors through Clathrin-coated Pits. Molecular Biology of the Cell 14, 858-870 (2003).

95. Ehrlich, M. et al. Endocytosis by Random Initiation and Stabilization of Clathrin-Coated Pits. Cell 118, 591-605 (2004).

96. Puri, C. et al. Relationships between EGFR Signaling–competent and Endocytosis-competent Membrane Microdomains. Molecular Biology of the Cell 16, 2704–2718 (2005).

97. Salazar, G. & González, A. Novel Mechanism for Regulation of Epidermal Growth Factor Receptor Endocytosis Revealed by Protein Kinase A Inhibition. Molecular Biology of the Cell 13, 1677-1693 (2002).

98. Bao, J. et al. Threonine Phosphorylation Diverts Internalized Epidermal Growth Factor Receptors from a Degradative Pathway to the Recycling Endosome. The Journal of Biological Chemistry 275, 26178-26186 (2000).

99. Wells, A. et al. Ligand-induced transformation by a noninternalizing epidermal growth factor receptor Science 247, 962-964 (1990).

100. Vieira, A. V., Lamaze, C. & Schmid, S. L. Control of EGF Receptor Signaling by Clathrin-Mediated Endocytosis. Science 274, 2086-2089 (1996).

101. Haugh, J. M., Huang, A. C., Wiley, H. S., Wellsi, A. & Lauffenburger, D. A. Internalized Epidermal Growth Factor Receptors Participate in the Activation of $p21^{ras}$ in Fibroblasts. The Journal of Biological Chemistry 274, 34350–34360 (1999).

102. Sorkin, A. Internalization of the epidermal growth factor receptor: role in signalling. Biochemical Society Transactions 29, 480-484 (2001).

103. Miaczynska, M., Pelkmans, L. & Zerial, M. Not just a sink: endosomes in control of signal transduction. Current Opinion in Cell Biology 16, 400-406 (2004).

104. Waterman, H. et al. A mutant EGF-receptor defective in ubiquitylation and endocytosis unveils a role for Grb2 in negative signaling. EMBO Journal 21, 303-313 (2002).

105. McCune, B. K. & Earp, H. S. The epidermal growth factor receptor tyrosine kinase in liver epithelial cells. The effct of ligand-dependent changes in cellular location. The Journal of Biological Chemistry 264, 15501-15507 (1989).

4 Design and commissioning of a multicolour confocal microscope for *in situ* determination of membrane protein structure

This chapter describes the building, implementation and commissioning of a fluorescence microscope for making quantitative FRET measurements in cells. The microscope was built for the particular purpose of investigating the three-dimensional structure of membrane protein complexes and was used to develop the method described in chapters 5 and 6. Optical sectioning is important to reject background fluorescence and ensure that the fluorescence signal used to determine FRET comes from the cell membrane. The method for protein structure determination involves measuring FRET between proteins specifically labelled with FRET donors and either (i) acceptor labelled proteins or (ii) acceptor labelled membrane. In (ii) the FRET efficiency is a function of acceptor density as well as donor-acceptor separation (discussed in Chapter 5.3) so FRET measurement by monitoring the reduction in donor fluorescence lifetime with fluorescence lifetime imaging microscopy (FLIM) is preferred to intensity based FRET imaging. As video rate imaging is not required, FLIM was implemented with TCSPC and laser scanning confocal microscopy. Multi-colour capability is required to identify cells co-labelled with multiple fluorescent dyes and to quantify FRET between donors and multiple acceptors.

The theory of optical sectioning with a confocal microscope is discussed along with the factors influencing the choice of individual components of the microscope. The optical layout and characteristics of the multi-dimensional, multi-colour microscope are outlined. The multi-colour sectioning capability of the microscope is demonstrated by simultaneously imaging members of the ErbB family of membrane receptors in cells that are labelled with different fluorescent probes. Finally the FLIM-FRET capability of the microscope is tested in cells expressing a diagnostic fluorescent protein consisting of a donor and acceptor linked by a short amino-acid sequence.

4.1 Optical sectioning and confocal microscopy

4.1.1 Optical Sectioning Techniques

A standard widefield optical microscope possesses poor axial resolution and consequently has weak sectioning ability. The resulting background fluorescence is disadvantageous for methods such as lifetime imaging that seek to quantify fluorescence properties and localise them to a specific volume of the sample. A number of techniques are commonly employed to obtain optical sectioning of fluorescent samples including confocal microscopy, multiphoton microscopy and structured illumination microscopy.

The image produced by a microscope is a convolution between the object and the microscope point spread function (PSF)[1].

$$image(x,y,z) = Object(x,y,z) \otimes PSF(x,y,z) \qquad \text{Eqn. 4-1}$$

Where the lateral axes x, y define the plane perpendicular to the optical axis of the microscope (z). The PSF is the image produced by the microscope of a point object and indicates how the optical system blurs the object during the imaging process. The PSF of a microscope is the product of the PSFs for illumination and detection of a point object.

Confocal microscopy achieves optical sectioning by restricting the excitation and detection PSFs to a small diffraction limited volume that is raster scanned over the focal plane to acquire a digital image one pixel at a time. Multiphoton microscopy works in a similar manner except the excitation and detection PSFs are restricted to the focal plane (maximum excitation power) by non-linear excitation of fluorophores with multiple photons of energy lower than the excitation transition[2]. Widefield structured illumination takes a different approach. By imaging a repeating pattern of equally spaced lines onto the sample, the lateral spatial frequencies transmitted by the microscope are

modulated with the frequency of the structured illumination[3]. The image of the sample from the focal plane can be retrieved from three separate images with the structured illumination placed at three different positions[4].

All three approaches have their advantages and disadvantages for different fluorescence imaging applications. Confocal fluorescence microscopy is a dependable technology that utilises visible wavelengths of light to excite fluorophores and can be used with many commercial lasers or relatively inexpensive diodes. Multiphoton excitation requires expensive, pulsed infra-red lasers to produce the high energy densities required but requires no confocal pinhole to reject out of focus light providing the advantage of increased detection efficiency. Reduced scattering of lower energy photons improves the depth to which a sample can be sectioned, but the reduction in photodamage often attributed to multiphoton imaging is still under debate[5-8]. Both confocal and multiphoton microscopies suffer from long acquisition times due to the point scanning nature of the techniques although video frame rates can be achieved with expensive kHz scanning mirrors, multi-aperture scanning methods such as Nipkow discs[9] or scanned line illumination. It must be noted that all three techniques also provide an improvement in lateral resolution over widefield microscopy, although in the case of the structured illumination method considered above this is only in the direction perpendicular to the direction of the illumination line structure[10]. Programmable array microscopes (PAMs) use a spatial light modulator (either a digital micromirror array or liquid crystal layer) to produce an arbitrary illumination (and/or detection) pattern and image the response on a CCD[11-13]. PAMs can utilise the most appropriate sectioning technique for a given experiment with fast image acquisition rates without the need for macroscopic moving parts[14].

It must be noted that all of these techniques also provide an improvement in lateral resolution over widefield microscopy, although in the case of the structured illumination method this is only in the direction perpendicular to the direction of the lines imaged onto the sample[10].

4.1.2 Single Point Confocal Microscopy

The basic principle of confocal microscopy is displayed in figure 4.1. The illumination on the sample is confined to a diffraction limited spot and a pinhole confocal to this spot suppresses light from out of focus regions of the sample.

A digital image of a section through the sample can be formed one pixel at a time by either scanning the sample through the focal point or scanning the focal point over the sample. This requires computer control of the scanning method in order to ensure that the detector output is attributed to the correct pixels. The use of infinity optics makes it possible to obtain stacks of optical sections by altering the axial position of the objective with respect to the sample. These can be used to produce three-dimensional reconstructions of samples.

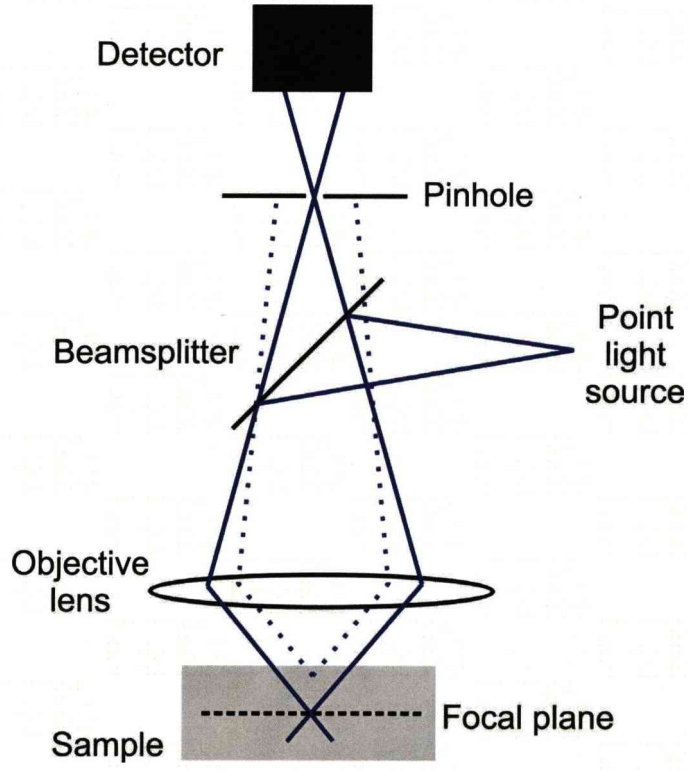

Figure 4.1 The principle of confocal microscopy. A point light source and a pinhole are confocal with the focal point of the objective. Light from outside the focal plane will form an extended disc in the plane of the pinhole, preventing the majority of out of focus light from reaching the detector (dotted lines).

4.1.3 Resolution of confocal fluorescence images

The image formed of an incoherent point source by an imaging system will be an Airy disc, which is the Fraunhofer diffraction pattern of a circular aperture and proportional to the square of the J_1 Bessel function[15]. The Rayleigh criterion is a commonly used measure of the resolving power of an imaging system and states that two incoherent point sources of equal intensity will be just resolved when the centre of one Airy disc coincides with the first minimum of the second Airy disc[15]. The distance from the centre of an Airy disc to the first minimum L_0 then defines the lateral resolution of the imaging system. For an objective lens with a given numerical aperture (NA) collecting light of wavelength λ, the distance L_0 is given by

$$L_0 = \frac{0.61\lambda}{NA} \qquad \text{Eqn. 4-2}$$

In confocal microscopy, the illumination PSF is the size of the focal spot produced by the objective and both this and the detection PSF are determined by the NA of the objective. The overall PSF for identical excitation and detection wavelengths is

$$PSF_{conf} = \left|PSF_{ex}\right|^2 \qquad \text{Eqn. 4-3}$$

The position of the first minimum will remain the same despite the fact that the full width at half maximum (FWHM) of the confocal PSF is smaller than that of the excitation PSF, making direct application of the Rayleigh criterion inappropriate. However, a reasonable approximation can be made to relate it to the FWHM of the PSF of an imaging system[1]

$$FWHM \approx L_0 \qquad \text{Eqn. 4-4}$$

Using the approximation in Eqn. 4-4 and further approximating the central peak of the PSF to a Gaussian distribution, it can be shown that the FWHM of the lateral confocal PSF, $FWHM_{conf}^{L}$ is related to that of the lateral excitation PSF by

$$FWHM_{conf}^{L} \approx \frac{1}{\sqrt{2}} FWHM_{ex}^{L} \approx \frac{0.61\lambda_{ex}}{NA\sqrt{2}} \qquad \text{Eqn. 4-5}$$

However, when dealing with fluorescent samples, the detected light is of a longer wavelength than the illuminating light due to the Stokes shift and the illumination and detection PSFs are different. Then $FWHM_{conf}^{L}$ becomes

$$FWHM_{conf}^{L} \approx \frac{1}{\sqrt{1+\beta^2}} FWHM_{ex}^{L} \approx \frac{1}{\sqrt{1+\beta^2}} \left(\frac{0.61\lambda_{ex}}{NA} \right) \qquad \text{Eqn. 4-6}$$

where β is the ratio of the excitation and detection wavelengths, $\beta = \lambda_{ex} / \lambda_{det}$. Similar expressions can be obtained for the axial resolution

$$Z_0 = \frac{2n\lambda}{(NA)^2} \qquad \text{Eqn. 4-7}$$

$$FWHM_{conf}^{Z} \approx \frac{1}{\sqrt{1+\beta^2}} FWHM_{ex}^{Z} \approx \frac{1}{\sqrt{1+\beta^2}} \left(\frac{2n\lambda_{ex}}{(NA)^2} \right) \qquad \text{Eqn. 4-8}$$

where n is the refractive index of the object medium. It should be emphasised that these are only approximations for the lateral and axial resolutions of a confocal microscope. However, they are useful to estimate the digital image resolution required to avoid undersampling and the introduction of artefacts into the image. Nyquist's sampling theorem which pertains to the discrete sampling

of continuous signals states that the sampling frequency should be at least twice the maximum frequency in the signal in order to accurately reconstruct the signal[1, 16]. In practice the maximum lateral spatial frequency in the scanned confocal fluorescence signal is set by the lateral resolution of the microscope[17] given by Eqn. 4-6. Hence to fulfil the Nyquist criterion the size of each pixel *Px* should be set such that

$$Px = \frac{FWHM_{conf}^{L}}{2} \qquad \text{Eqn. 4-9}$$

For a given wavelength of excitation and emission only one pixel size and hence only one digital 'zoom' magnification will fulfil this criterion. It also follows that for simultaneous multi-colour excitation and detection the pixel size can only be set to fulfil this criterion for one fluorophore and images of the others will either be slightly under- or oversampled. By fulfilling Eqn. 4.9 for the fluorophore with the shortest wavelength excitation and emission images of all other fluorophores will be oversampled which will ensure faithful image reproduction at the expense of increasing photobleaching and reducing the size of the scan area.

4.1.4 Aberrations in image forming systems

Geometric optics treats light as rays that propagate through an optical system obeying the laws of reflection and refraction. This is also known as first order or Gaussian theory and assumes that the angle light rays make with the optical axis are infinitely small, allowing the following simplifying identity to be used

$$\sin\theta \approx \theta \qquad \text{Eqn. 4-10}$$

This is known as the paraxial approximation and allows the derivation of the Gaussian formula for thin lenses

$$\frac{1}{f} = (n_1 - 1)\left(\frac{1}{R_1} - \frac{1}{R_2}\right) = (n_1 - 1)\rho \qquad \text{Eqn. 4-11}$$

where f is the focal length of the lens, n_1 is the refractive index of the lens material, and R_1 and R_2 are radii of curvature of the two lens surfaces.

Aberrations are deviations of the image formed by an optical system from the image expected from Gaussian ray-tracing. They can be split into two categories: monochromatic and chromatic. Monochromatic aberrations are a consequence of the breakdown of the paraxial approximation for rays entering the entrance pupil of the optical system at larger angles and occur independently of the wavelength of the propagating light. Chromatic aberrations arise because the refractive indices of lens materials are wavelength dependent. Both kinds of aberrations are discussed in the following two sections as well as ways in which they can be minimised.

4.1.4.1 Monchromatic Aberrations

There are five primary monochromatic aberrations; spherical (SA), coma, astigmatism, field curvature and distortion. These are displayed in figure 4.2.

Spherical aberration arises because a wide beam of rays incident on a lens parallel to the optical axis is not brought into focus at a unique point. This is shown in figure 4.2a. Incident rays hitting the lens further from the optical axis are focused to a point closer to lens than the paraxial focal point. Longitudinal spherical aberration is the separation of the focal point of a ray and the paraxial focus along the optical axis. The traverse SA is the height at which a ray crosses paraxial focal plane. The circle of least confusion exists in the plane where the traverse spherical aberration is minimised. The effect of SA on the image of a point object is to transfer intensity from the central peak of the airy disc into the surrounding rings. The SA of a single plano-convex lens can be minimised by

reversing its orientation. It must be noted that SA only pertains to objects on the optical axis.

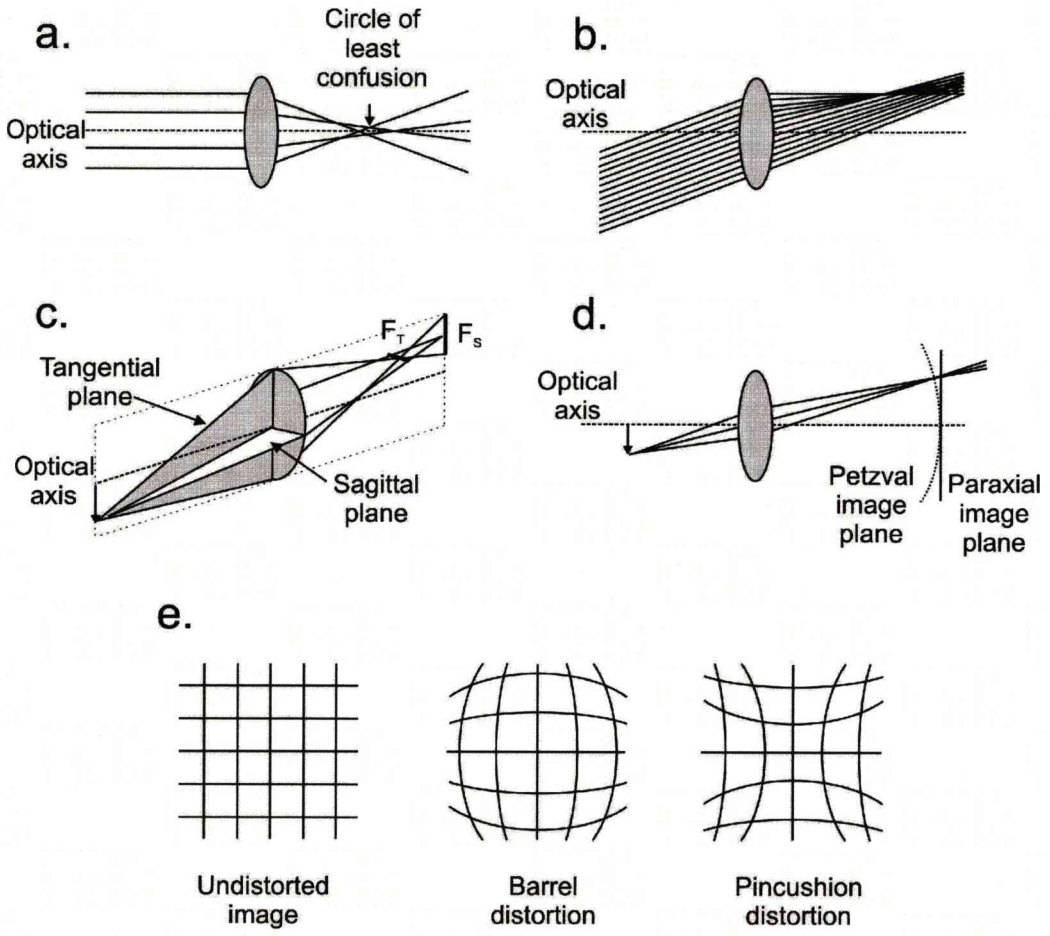

Figure 4.2 The five primary aberrations (monochromatic). **a**. Spherical. **b**. Coma. **c**. Astigmatism, F_T and F_S are the focal points of tangential and sagittal rays respectively. **d**. Field curvature. **e**. Distortion.

Coma is named after the comet like appearance of the image of a point object located just off the optical axis. As can be seen in figure 4.2b, oblique rays from an off-axis point are not imaged at a single point. Coma is dependent upon lens shape and can be made exactly zero for a single lens at a given object distance. The shape of this lens is nearly convex-plano, the lens configuration that also minimises SA.

Astigmatism affects the imaging of objects that are away from the optical axis and arises from rays striking a spherical lens asymmetrically. Unlike the other panels in figure 4.2, figure 4.2c is drawn in perspective in order to display two orthogonal planes. The tangential plane contains the optical axis and the object. The sagittal plane is perpendicular to the tangential and also contains the optical axis. All rays outside of the tangential plane are referred to as skew rays (including those in the sagittal plane). Rays from the tangential and sagittal planes are brought to focus at different points. The distance between the two focal planes is referred to as the astigmatic difference. Objects on the optical axis have an astigmatic difference of zero due to the symmetry of tangential and sagittal rays incident upon the spherical lens.

In the absence of the above monochromatic aberrations, an optical system will form images of point objects that are on and off the optical axis. However, non-paraxial rays are imaged upon a curved Petzval surface. Consequently if the image is formed onto a flat plane then the centre of the image will be in sharp focus but the edges will be blurred. A combination of positive and negative lens can correct for field curvature.

The final monochromatic aberration is distortion. Distortion arises when the magnification of the optical system is a function of the off-axis image distance. This arises from different areas of a lens having different focal lengths and hence different magnifications. The effect of distortion is a misshapen image despite all points being in focus.

4.1.4.2 Chromatic Aberration

The refractive index of a material is a function of the wavelength of light propagating through it, an effect known as dispersion. Consequently the focal length of a lens is also wavelength dependent and rays of different wavelengths

will propagate through an optical system along different paths. This is shown in figure 4.3a.

Positive and negative lenses with different dispersions can be combined to produce a system that minimises chromatic aberration at two or more wavelengths. Such compound lenses are called achromats.

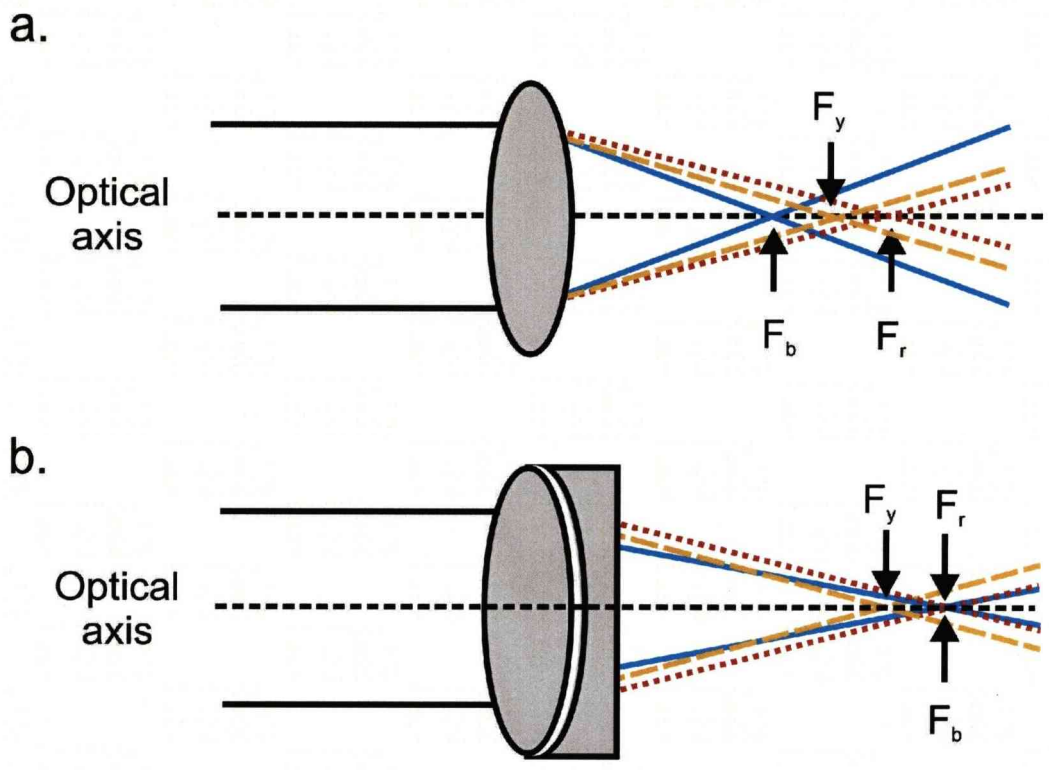

Figure 4.3 a. Chromatic aberration in a single lens. The focal points of blue (solid lines), yellow (dashed lines) and red (dotted lines) light (F_b, F_y and F_r respectively) are marked. **b**. The focal points of the same wavelengths propagating through an achromatic doublet.

Two lenses separated by a distance d have a combined focal length f_C that is related to the individual focal lengths f_1 and f_2 by

$$\frac{1}{f_C} = \frac{1}{f_1} + \frac{1}{f_2} - \frac{d}{f_1 f_2} \qquad \text{Eqn. 4-12}$$

As f_1 and f_2 are functions of $n(\lambda)$ (equation 4.11) f_C is also a function of wavelength of light propagating through it. If the two lenses in combination are to bring two specified wavelengths λ_a and λ_b to a common focus

$$\frac{1}{f_{C\lambda_a}} = \frac{1}{f_{C\lambda_b}} \qquad \text{Eqn. 4-13}$$

by combining Eqns. 4.11 and 4.12 to obtain expressing for the combined focal lengths and substituting them into Eqn. 4.12 for the condition $d = 0$

$$\frac{\rho_1}{\rho_2} = \frac{n_{2\lambda_a} - n_{2\lambda_b}}{n_{1\lambda_a} - n_{1\lambda_b}} \qquad \text{Eqn. 4-14}$$

A third wavelength λ_c can be used to specify reference values for the focal lengths of the two lenses

$$\frac{1}{f_{1\lambda_c}} + \frac{1}{f_{2\lambda_c}} = \left(n_{1\lambda_c} - 1\right)\rho_1 + \left(n_{2\lambda_c} - 1\right)\rho_2 \qquad \text{Eqn. 4-15}$$

which can be rearranged to give

$$\frac{\rho_1}{\rho_2} = \frac{\left(n_{2\lambda_c} - 1\right)}{\left(n_{1\lambda_c} - 1\right)} \frac{f_{2\lambda_c}}{f_{1\lambda_c}} \qquad \text{Eqn. 4-16}$$

Equating equations 4.14 and 4.16

$$\frac{f_{2\lambda_c}}{f_{1\lambda_c}} = -\frac{\left(n_{2\lambda_a} - n_{2\lambda_b}\right)/\left(n_{2\lambda_c} - 1\right)}{\left(n_{1\lambda_a} - n_{1\lambda_b}\right)/\left(n_{1\lambda_c} - 1\right)} \qquad \text{Eqn. 4-17}$$

The dispersive powers of the two lenses are given by

$$\frac{n_{1\lambda_a} - n_{1\lambda_b}}{n_{1\lambda_c} - 1} \text{ and } \frac{n_{2\lambda_a} - n_{2\lambda_b}}{n_{2\lambda_c} - 1}$$

Eqn. 4-18 and Eqn. 4-19

and their reciprocals V_2 and V_1 are known as the dispersive indices of lenses. As V_2 and V_1 are always positive, one of the lenses must have a negative focal length to satisfy

$$f_{1\lambda_c} V_{1\lambda_c} + f_{2\lambda_c} V_{2\lambda_c} = 0 \qquad \text{Eqn. 4-20}$$

Fraunhofer lines are commonly used to provide precise reference values across the spectral range. For visible wavelength achromats, the C, F and D_3 Fraunhofer lines are used which correspond to wavelengths of 656.2816 nm, 486.1327 nm and 587.5618 nm respectively. A dispersive index calculated for these wavelengths is commonly designated V_d. For two lenses made with materials with dispersive indices V_{1d} and V_{2d}, equations 4.20 and 4.12 can be solved simultaneously to determine the individual focal lengths required to produce the desired compound focal length. Other factors to be considered include the avoidance of small individual focal lengths that would require highly curved lenses and the minimisation of monochromatic aberrations.

In such an achromatic doublet only the wavelengths of the C and F lines share the same focal point and the D_3 wavelength serves as a reference only. This and all other intervening wavelengths do not have a common focus and the residual chromatic aberration is known as the secondary spectrum of the achromat. It is possible to produce triplets that bring three or four wavelengths to a common focus and exhibit reduced secondary spectra, but these require the use of calcium fluorite which is currently more expensive than other lens materials.

4.1.5 The components of a Confocal Microscope

This section provides an overview of the important components of a confocal microscope and the considerations that informed the choice of individual components of the microscope described in section 4.2.

4.1.5.1 Scanning the focal spot

The concept of a point scanning microscope was outlined by Young and Roberts in 1951[18], and a confocal microscope had been developed by Minsky in 1955[19]. However, confocal microscopy was neglected as a research tool for almost thirty years until fluorescent labelling emerged as a key technique in biological imaging[20]. The first confocal microscopes developed for biological imaging were based on a sample scanning system where the focal point of the objective is static and the entire sample stage is raster scanned[21, 22]. Although sample scanning has the advantage of a static optical arrangement that is free from off-axis optical aberrations, scanning speeds are slow due to the large mass that must be scanned and the forces involved in moving the sample can cause living samples suspended in solution to distort[23]. Laser scanning methods where the sample is stationary and the focal spot is scanned are now used in most modern confocal microscopes[20].

Close coupled scanning mirrors are employed only for scanning the focal spot over the imaged area, while large scale movement between different sample areas is accomplished with a translating microscope stage. Figure 4.4 shows the optical arrangement required to produce nearly distortion free scanning using close coupled scanning mirrors[20]. A simple telescope arrangement was implemented to ensure that the raster scanning of the mirrors was translated into a rotation of a collimated excitation beam about the back aperture of an infinity corrected objective. Infinity corrected objectives allow optical components to be placed in the light path of the microscope without introducing additional aberrations. This produces raster scanning of the focal spot in the focal plane.

The degree to which the beam is scanned off-axis is exaggerated in Figure 4.4 for clarity, but efforts must still be made to reduce off axis aberrations in the scan optics. The beam will still undergo a small amount of translation across the objective back aperture as the mirrors scan, but by ensuring that the beam overfills the back aperture inhomogeneous excitation of the imaged area can be avoided. Commercial microscopes often solve this problem without discarding excitation illumination by using a hemispherical mirror system that accomplishes perfect translation of mirror scanning to beam rotation about the objective back aperture[20]. Fluorescence (or reflected light) is collected by the same objective and is de-scanned by the scanning mirrors allowing a stationary confocal pinhole to be used.

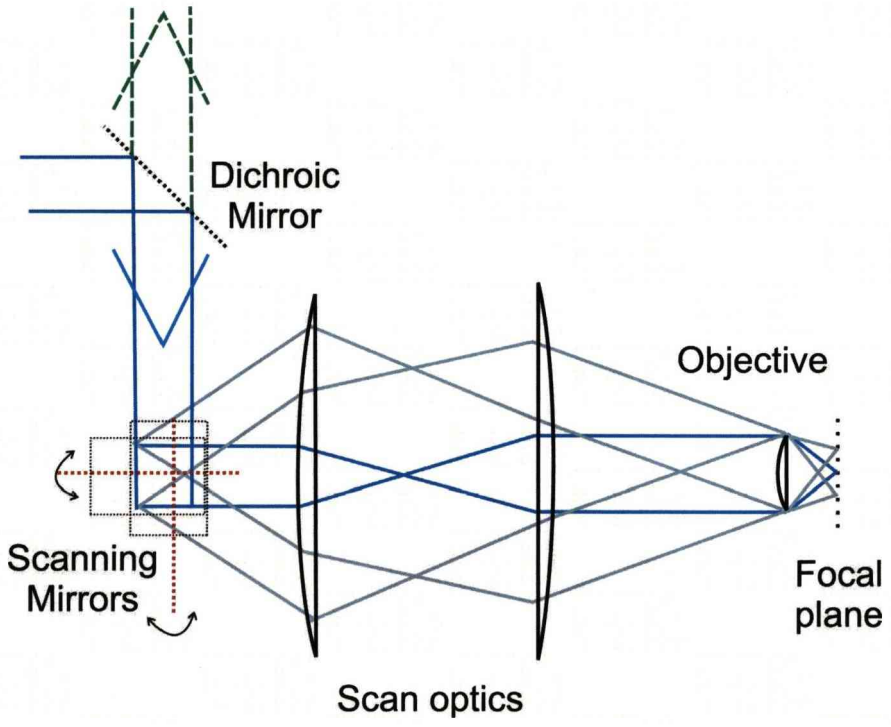

Figure 4.4 The scanning of laser focal point using close-coupled scanning mirrors and an infinity corrected objective. The excitation beam (blue) is reflected to the first scanning mirror by a dichroic beam splitter. The beam is then reflected in the direction out of the page to the second scanning mirror that redirects the beam to the scan optics and the objective. Rotation of the scanning mirrors about the dotted red axes produces raster scanning of the focused laser spot in the focal plane. Fluorescence emission (green) is collected by the same objective and de-scanned by the scanning mirrors before passing through the beam splitter and along the detection optical path.

Scanning mirrors are not the only way to implement laser scanning confocal microscopy. Multiple focal spots can be used to acquire pixel intensities in parallel using a Nipkow disc[24]. The disc contains a spiral pattern of pinholes such that every point in the imaged area receives an identical amount of illumination as the disc is spun. A second rotating disc is placed between the objective and the dicroic beam splitter to provide the necessary confocal pinhole for each excitation pinhole on the first disc. The original Nipkow disc design has been improved by the use of microlenses that increase the light efficiency through the discs by focusing light through the second disc pinholes[9]. The benefit of multi-point confocal systems is that they are capable of faster real-time image acquisition but may suffer from cross-talk between pinholes. Line scanning can also be employed to increase the speed of image acquisition and is used in the commercially available Zeiss LSM 5 *LIVE*. However, the benefits of line scanning can only be realised with the use of a line CCD as a detector. Figure 4.5 compares these two different methods of parallel pixel acquisition.

Programmable array microscopes (PAMs) are a class of microscopes characterised by the use of digital micromirror devices (DMD) or liquid crystal layers to produce arbitrarily modulated illumination and/or detection patterns. This provides PAMs with the flexibility to perform optical sectioning in many ways; scanning multi-aperture patterns in a manner similar to Nipkow disc confocal microscopy[11], line scanning[12], line patterns[25] and pseudo-random patterns[11].

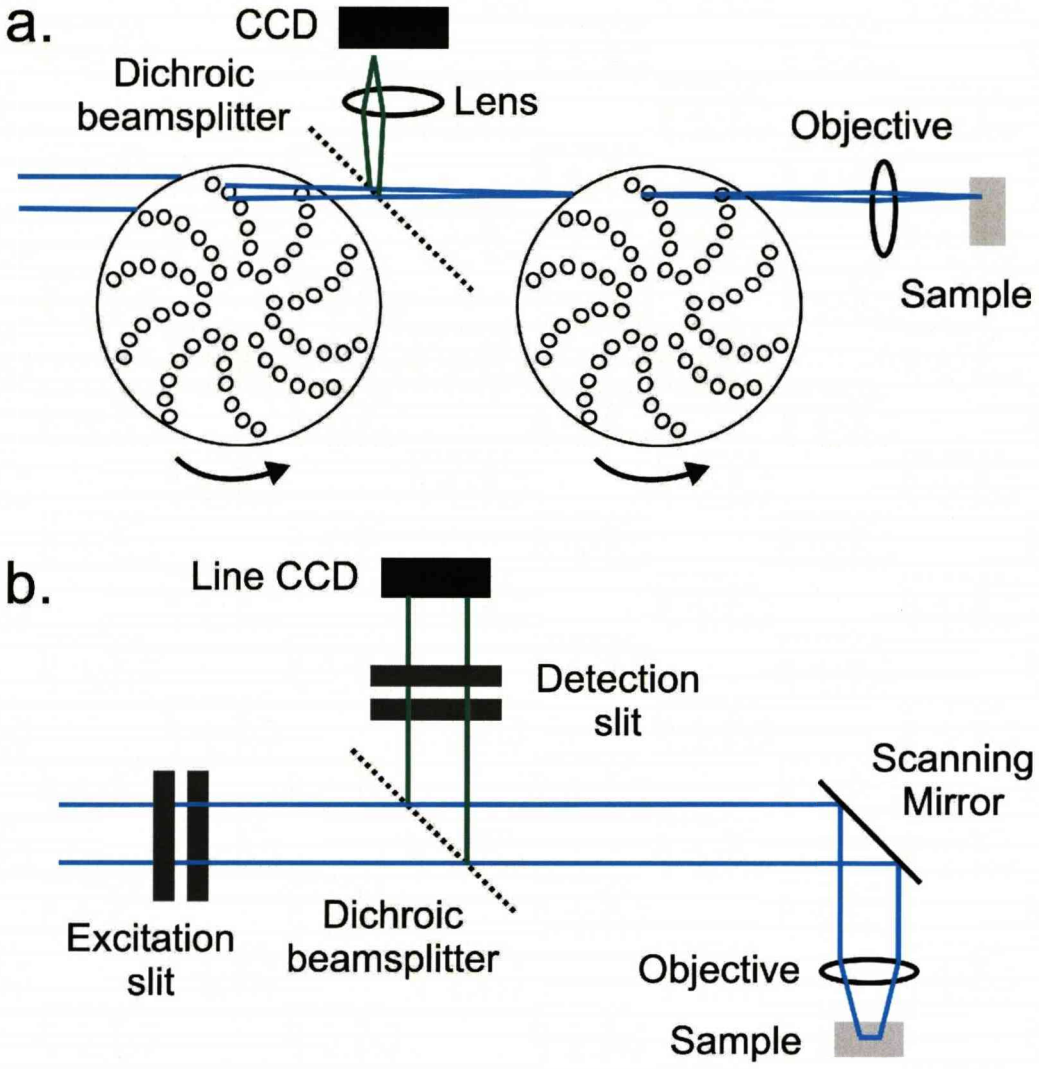

Figure 4.5 Two methods of parallel pixel acquisition in confocal microscopy **a**. Nipkow disc confocal microscopy. Only one beam is shown passing through the discs for clarity. **b**. Line scanning confocal microscopy.

4.1.5.2 Objectives for confocal microscopy

The objective is among the most important components in a confocal microscope as it both focuses the excitation light onto the sample and collects the light that is detected. Confocal microscopy forms a digital image and an increase in magnification is achieved by sampling a smaller area with the same number of pixels. This 'digital zoom' is limited by the microscope resolution which depends upon the NA of the objective and is discussed in greater detail in section 4.1.3. In order to maximise the confocal resolution high NA oil or water immersion

objectives (NA > 1.3) are used. These objectives are designed to minimise aberrations introduced by refractive index mismatch when they are used with sample coverslips of the correct material and thickness. When using coverslips it is also important to ensure that the coverslip thickness does not exceed the working distance of the objective (the separation of the objective and the focal plane).

4.1.5.3 The confocal pinhole

The confocal pinhole is responsible for reducing the sensitivity of the microscope to detecting out of focus light. The size of the pinhole compared to the image of the Airy disc formed before the detector determines the sectioning strength and the improvement of lateral resolution over widefield microscopy of the confocal microscope. Smaller pinholes will improve the lateral resolution at the expense of the detected signal level. The maximum pinhole size that does not cause a reduction of the axial resolution is 65% of the diameter of the Airy disc[1]. The pinhole size that produces the greatest possible increase in lateral resolution results in a signal level 5% of the maximum possible[26]. Most implementations of confocal microscopy use pinhole sizes that offer minimal improvement in lateral resolution, but guarantee optical sectioning with good signal to noise ratio.

4.1.6 Optical sectioning with fluorescence lifetime imaging microscopy (FLIM)

Fluorescence lifetime imaging microscopy involves the measurement of the characteristic lifetime of the fluorescent light that contributes to each pixel in a fluorescence image. As discussed in chapter 2.2.2, the fluorescence lifetime of an ensemble of fluorescent molecules can be obtained via time-domain or frequency-domain measurements.

Confocal and multiphoton microscopies can be combined with either time- or frequency-domain lifetime imaging[27, 28]. As each image pixel is acquired separately they are particularly suitable for combination with TCSPC[29-31]. TCSPC requires fast PMTs that give rise to narrow instrumental responses and a pulsed excitation source, but the rest of the TCSPC electronics may be treated as a separate module that replaces the scanned image acquisition system. There are currently two major commercial suppliers of TCSPC modules for scanning microscopes: Becker-Hickl GmbH and Picoquant. The requirement of low excitation powers for TCSPC to avoid biasing photon density distributions to shorter arrival times (through pile-up) can result in long acquisition times[30]. The total acquisition time required to record sufficient photons in each pixel for fitting the data to multi-exponential models is dependent upon the number of pixels and the count-rate of photon arrivals at the detector. As a general rule at least 1000 photons should make up the photon density distribution for accurate fitting to a multi-exponential decay model[29, 30] and acquisition of a lifetime image fulfilling this criterion can take minutes even at count-rates as high as 10^6 s^{-1}. However, it is often preferred to other methods because of its accuracy and because low-intensity of illumination conditions are beneficial for minimising the photobleaching of samples. TCSPC benefits from nearly ideal counting efficiency conferring an advantage when imaging weakly fluorescent samples[27, 32].

Widefield sectioning allows much faster acquisition of sectioned images than point scanning methods. In order to maintain this advantage, widefield FLIM systems have previously utilised time-gating to obtain lifetime images and widefield optical sectioning by structured illumination has been integrated with time-gated detection on a standard widefield microscope[4]. A recently developed wide-field photon-counting detector now makes it possible for microscopes capable of multi-aperture illumination and detection to take advantage of TCSPC[33]. A DMD based PAM has been combined with a modulated image intensifier based FLIM system[14] and Nipkow disc confocal microscopes have been adapted for frequency domain[34] and time-gated FLIM[35].

4.2 Implementation of a multi-dimensional, multi-colour laser scanning confocal microscope

Figure 4.6 displays the components of a multi-dimensional, multi-colour confocal microscope that achieves laser beam scanning with close-coupled scanning mirrors.

The design was implemented using a Zeiss Axiovert 135 inverted microscope as sample stage. Three different laser beams are input into the optical path via optical fibres and combined before being sent to the objective. The use of optical fibres allows laser sources to be located on a separate optical table to avoid introducing mechanical vibration to the microscope. The laser sources can also be shared with other microscopes. The returning fluorescence emission is split by wavelength and the output of the detectors can be sent to a either the confocal image acquisition system (4C's Enterprises, Somerset UK) or a TCSPC lifetime imaging system (Becker-Hickl GmbH).

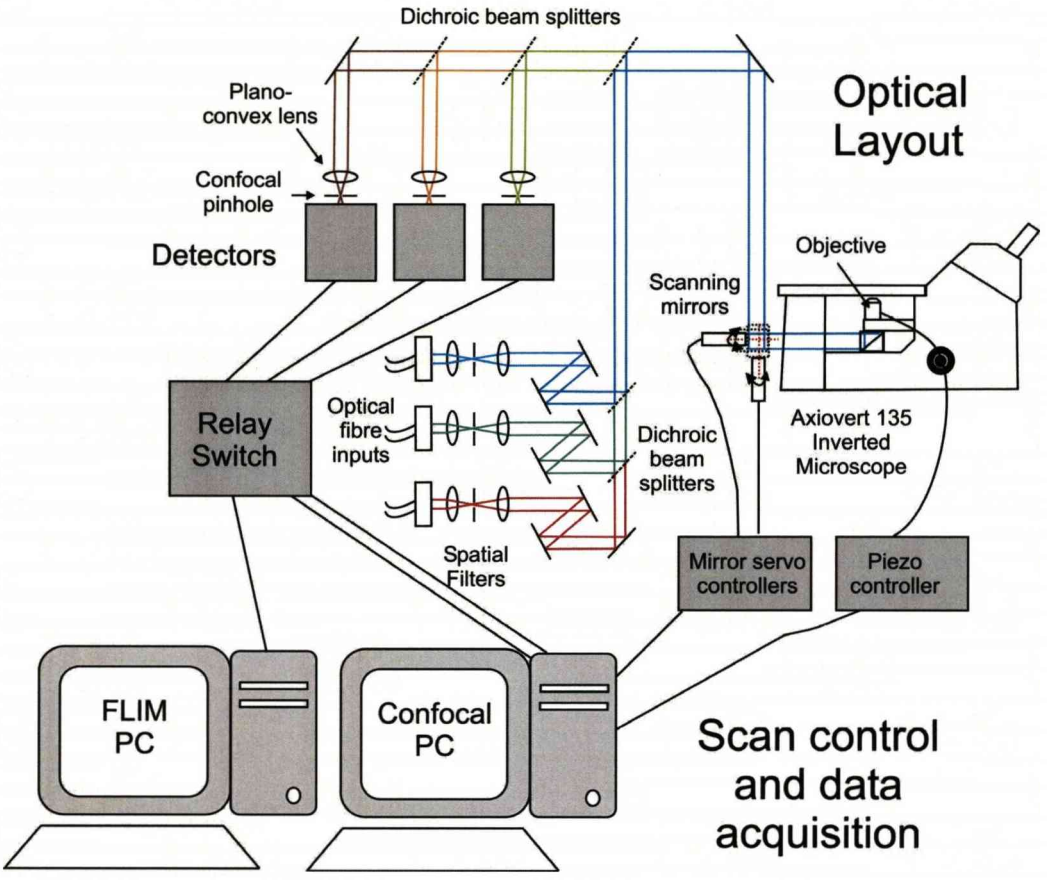

Figure 4.6 A multi-dimensional, multi-colour laser scanning confocal microscope. The upper part of the diagram consists of components that are in the optical layout placed on an optics bench. All other components are involved in scanning mirror control and data acquisition. Neither the scan optics or the objective and sample temperature control components are shown.

Table 4.1 lists the laser sources available for input into the microscope.

The design of the microscope allows for all three detector outputs to be routed to the Becker-Hickl TCSPC lifetime imaging system so that three lifetime images can be simultaneously acquired[31]. However, the Ti:Sapphire laser system that was used for the FLIM/FRET measurements of in situ ErbB1 structure can only excite a sample with pulsed excitation one wavelength at a time. An upgrade is currently underway to utilise a recently purchased supercontinuum laser source (Fianium) that will make full use of the colour versatility of this confocal microscope. The PMC-100 detectors are preferred for lifetime imaging as they yield an instrument response function with a much shorter width (< 200ps) than standard PMTs.

Laser Source	Wavelength / nm	Maximum available output power / mW	Time
Coherent Mira OPO	520 – 640	408 (Maximum achieved at 545 nm)	200 fs pulses, 76 MHz repetition rate
INRAD 5-050 Ultrafast SHG/THG	400 – 500	107 (Maximum achieved at 440 nm)	100 fs pulses, 76 MHz repetition rate
PTI IQ4C 445	445	25	Continuous Wave (CW)
Melles Griot 35-LAL-415 Ar^+	488	145	CW
NLC 800GL	514	100	CW
LCS-DTL-317	532	50	CW
PTI IQ4C 639	639	17.5	CW

Table 4.1 Available laser sources for single photon excitation of visible wavelength fluorescence dyes

Sections 4.2.1 – 4.2.3 describe; the optical layout, confocal scanning control and image acquisition system and the lifetime image acquisition system in greater detail.

4.2.1 Optical Layout

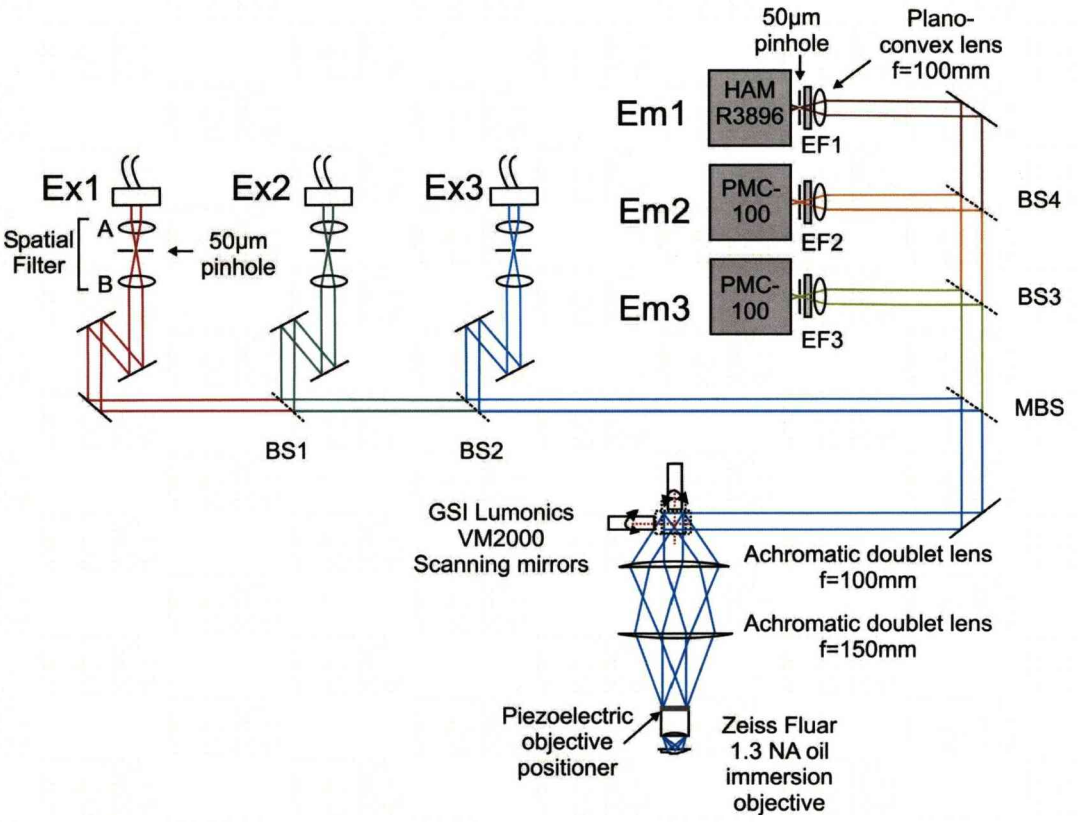

Figure 4.7 Optical layout of a confocal microscope with three excitation inputs (Ex1 – 3) and three emission pathways (Em1 – 3). Optical fibres input each excitation beam into a spatial filter and the beam width is controlled with two plano-convex lenses (A and B). The layout contains five dichroic beam splitters that can be swapped to accommodate different combinations of fluorescence excitation and emission wavelengths. Four of these beam splitters (BS1 – 4) serve to combine excitation wavelengths or split emission wavelengths. The fifth is the main dichroic beam splitter (MBS) that separates the excitation and emission paths. Between the MBS and the objective multiple excitation and emission wavelengths are present in the optical path. Achromatic doublet lenses are used in positions along this section to minimise chromatic aberrations. EF1 – 3 are emission filters placed before the detector pinholes. All detection pinholes are 50µm in diameter and placed before a 100mm tube lens.

The three optical fibre inputs (Ex1 – 3) are a single-mode, multi-mode and single-mode fibre respectively. The divergent light exiting each fibre is collimated before being passed through a spatial filter to guarantee a beam with a Gaussian profile. Two steering mirrors are used to align each beam into the same excitation path and beam combination is achieved using suitable long pass beam

splitters in positions BS1 and BS2. Flippable plane mirrors can also be used when a suitable dichroic mirror is unavailable and/or when simultaneous excitation with different wavelengths is not required to increase the efficiency of fluorescence detection. The width of the three beams is approximately matched by selecting combinations of spatial filter lenses A and B that expand the beams by the required amount. The beam widths can only be matched approximately due to restrictions imposed by the available standard focal lengths of plano-convex lenses. Matching of beam widths ensures that the achromatic scan optics expand all three beams to fill the back aperture of the objective. Achromatic doublets with focal lengths of 100 mm and 150 mm (Thorlabs, AC264-100-A1 and AC264-150-A1 respectively) form the scan optics. The residual chromatic focal shift of these two lenses calculated by ray-tracing software (Zeemax) is shown in figure 4.8. The scan optics acts as a 1:1.5 beam expander (although the residual chromatic focal shift of the achromats will result in minor differences between wavelengths) and the back aperture of the objective is 10mm in diameter. The beam width of the three beams entering the scan optics must be greater than 6.7 mm to fill the objective back aperture. The objective itself is a Zeiss Fluar 1.3 NA oil immersion objective. This objective was chosen for its high numerical aperture and high transmission of visible wavelengths which makes it particularly suited to photon counting applications with weakly fluorescent samples. Table 4.2 lists the details of the spatial filters.

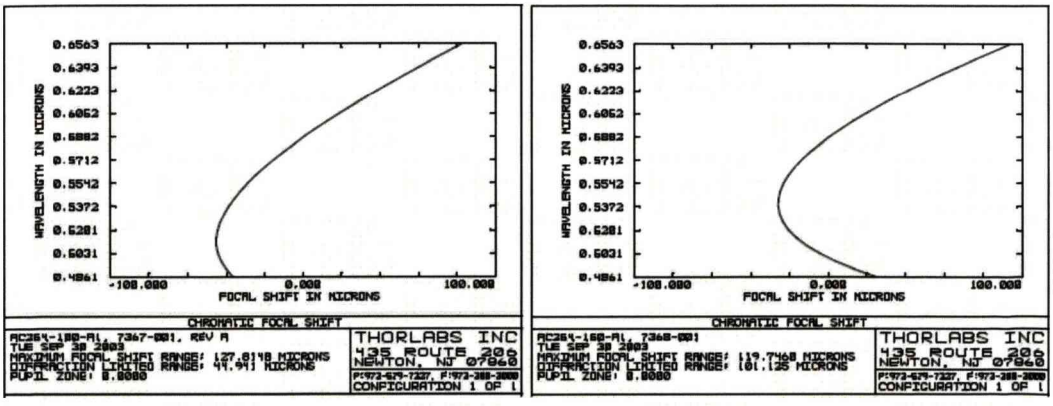

Figure 4.8 Chromatic focal shift of the achromatic doublets used in the scan optics. Left – AC264-100-A1. Right – AC264-150-A1.

Excitation Input	Optical fibre type	Focal length / mm		Expansion factor	Final beam width / mm
		A	B		
Ex1	Single mode	25.4	50.0	1.97	7
Ex2	Multimode	35.0	50.0	1.43	8
Ex3	Single mode	30.0	75.0	2.50	7

Table 4.2 Details of excitation inputs. Spatial filter lens A and B produce an expansion of the collimated beam exiting the fibre coupler. The focal lengths of A and B are chosen to produce three beams of approximately equal width.

Scanning of the beams is accomplished with GSI lumonics VM2000 scanning mirrors. To minimise aberrations, the resting positions of the mirrors when powered on are set so as to align the beams through the centre of the scan optics achromatic doublets. The system that controls the scanning mirrors and image acquisition is described in section 4.2.3.

The setup of the microscope is completely flexible in terms of the excitation and emission wavelengths that can be selected, requiring only an alteration of the relevant dichroic beam splitters and adjustment of spatial filters to compensate for any chromatic aberration in the plan-convex lenses. Combinations of fluorescent dyes that can be excited and imaged simultaneously in the microscope are, however, limited by the commercially available multi wavelength dichroic mirrors that are available to separate the excitation and emission paths at the MBS position. Two multi-wavelength dichroic beam splitters were found that can be used with the most commonly used combinations of fluorescent probes. These are designed for use with the dye combinations; CFP, YFP and Cy5 (61009bs, Chroma), and FITC, Cy3 and Cy5 (61005bs, Chroma) but are suitable for use with any probes with similar spectral characteristics. The transmission of these beam splitters as a function of the wavelength of incident light is shown in figure 4.9.

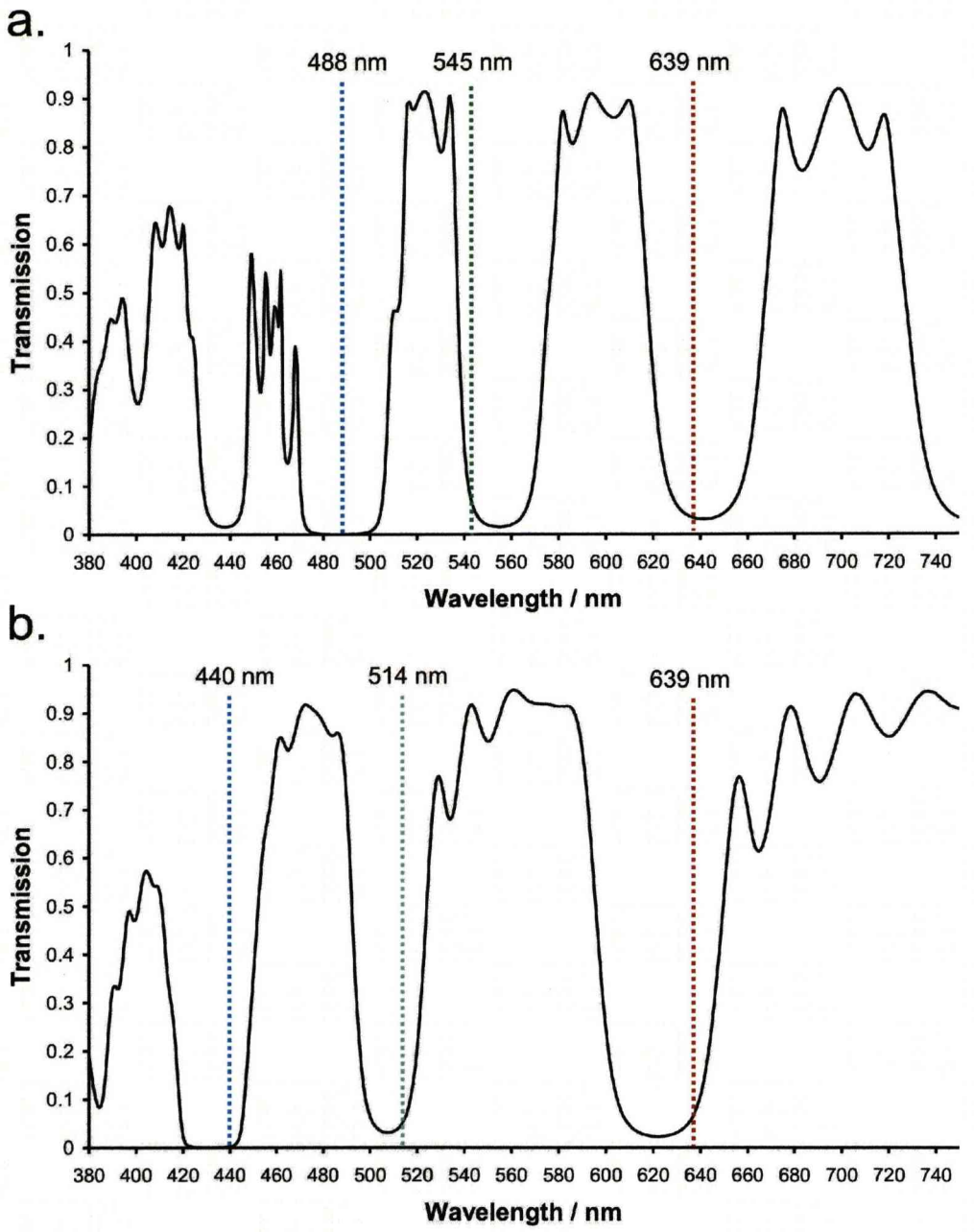

Figure 4.9 Transmission profiles of **a.** the Chroma FITC – Cy3 – Cy5 beam splitter **b**. the Chroma CFP – YFP – Cy5 beam splitter. Laser lines that coincide with regions of near zero transmission of each beam splitter are shown.

Table 4.3 lists the excitation and emission beam splitters (BS1 – 4) used with each MBS.

Component	Main Beam splitter (MBS)	
	CFP – YFP – Cy5	**FITC – Cy3 – Cy5**
BS1	Nikon DM580LP	Nikon DM580LP
BS2	Nikon DM455 LP	Nikon DM510LP
BS3	Nikon DM510LP	CHROMA Q555LP
BS4	CHROMA Q625LP	CHROMA Q625LP
EF1	HQ 700/75	HQ 700/75
EF2	HQ 535/30	HQ 610/75
EF3	HQ 470/30	HQ 525/50

Table 4.3 Beam splitter and emission filter combinations for different combinations of fluorescent probes.

4.2.2 Sample Temperature Control

The microscope uses a Delta T4 dish system (Bioptechs) to control the temperature of cell samples. Cells are cultured in Delta T glass bottomed culture dishes which can be heated by applying an electric current to a thin film coating the underside of the glass. A thermocouple in contact with the underside of the glass surface completes a feedback loop which maintains the desired temperature. To obtain temperatures lower than the ambient room temperature, a cooling ring (Bioptechs) connected to a refrigerated water bath can be lowered into the Delta T dish.

In order to maintain the microscope objective at the same temperature of the sample an objective heating collar and an objective cooling collar (both Bioptechs) were attached to the objective. Nitrogen gas is flowed past the back aperture of the objective to prevent the formation of condensation.

4.2.3 The 'Confocalscope' Image Acquisition system

The 'Daresbury Confocalscope' system that controls the GSI Lumonics scanning mirrors and converts detector output into intensity images was designed and built by 4C's Enterprises (Somerset, UK). The system is based upon 4C's Enterprises C-vision image analysis software running on a network of four Windows 2000 PCs. Two PCs each contain an individual intensity data acquisition card and a third contains a lifetime imaging data acquisition card (discussed in the next section). A master PC controls the GSI Lumonics scanning mirrors and remotely handles the acquisition of intensity confocal images through the network. As such the system is currently capable displaying the confocal data from two detectors simultaneously as it is acquired in real-time. 128 x 128, 256 x 256 and 512 x 512 pixel resolutions are supported. At the lowest pixel resolution an image can be scanned of a 65 x 65 μm area in 1.02 s facilitating the optimisation of confocal pinhole and lens positions, and the position of the objective in real-time. A line profile through the centre of the image that updates in real-time can also be used to optimise the focus of the microscope. Additionally, the C-vision software allows intensity images to be displayed with a colour coded logarithmic scale for finding regions of interest in weakly fluorescent samples.

Intensities are generated by counting the number of photons that arrive at each detector while the excitation spot is scanning across a given pixel. The intensity imaging system operates separately to the lifetime imaging system discussed in the next section but the C-vision interface is capable of remotely operating the lifetime imaging software. A manual electronic switch (designed and constructed by Steve Davis at the STFC Daresbury Laboratory) is used to send detector signals to either the Confocalscope or lifetime imaging data acquisition cards. No external pixel clock is used to operate the scanning mirrors.

4.2.4 Time-domain Confocal Fluorescence Lifetime Imaging Microscopy

The lifetime imaging capability of the microscope is provided by a Becker-Hickl SPC-730 TCSPC module. The module contains all the TCSPC electronics (CFD, TAC, ADC and histogram memory) on a single computer card. The SPC-730 contains enough onboard memory to acquire FLIM data with a pixel resolution of 256 x 256 pixels and a temporal resolution of 64 time bins. The number of time bins can be increased by reducing the pixel resolution.

Three sets of input signals are required by the SPC-730; the signal from a fast PMT detector, a synchronisation signal from the pulsed excitation source and timing signals from the scan mirror controllers. A pixel clock signal is also required in order for the module to assign detected photons to the correct image pixels. In the absence of an external pixel clock in the confocal image acquisition system, the internal pixel clock of the SPC-730 was used and manually set to the pixel time of the confocal scan settings. A relay switch designed and built by Steve Davis at STFC Daresbury Laboratory is used to divert signals from the PMC-100 detectors to either the confocal image acquisition system or the SPC-730 module. The synchronisation signal is produced by a photodiode in the Ti:Sapphire laser system that is connected to the SPC-730. To ensure correct recording of photon density distributions the length of the synchronisation signal cable can be adjusted to maintain the correct delay between the synchronisation and detector signals.

4.2.4.1 Analysis of fluorescence lifetime images

This section mainly describes the features of the SPCImage 2.9 (Becker-Hickl GmbH) lifetime image analysis software used extensively throughout this thesis to analyse the lifetime images produced by the multi-dimensional, multi-colour confocal microscope described in this chapter.

The time-resolved information in fluorescence lifetime images needs to be extracted by post-processing of the data. Each pixel contains a photon density distribution which is derived from the emission of many fluorophores, all of which can be in different photophysical states due to their existence is different microenvironments. In order to characterise the form of the density distribution a suitable model for the density distribution must be specified and for each pixel the model parameters are found that best fit the model to the data. Colour coded images are then used to display the model parameter of interest. SPCImage fits time domain lifetime data to a multi-exponential decay model with a maximum of three exponential components

$$F(t) = a_0 + \sum_j a_j e^{-t/\tau_j} \quad \text{Eqn. 4-21}$$

where a_I and τ_j are the exponential decay coefficients and lifetimes respectively. $J = 1, 2, 3$. a_0 is an offset that can take into account ambient light and detector dark noise.

The graphical interface of SPCImage version 2.9 is displayed in figure 4.10. The interface is split into five panels labelled a-e in the figure. They contain an intensity image obtained from summing all of the photons counted in each pixel (a.), a colour coded image displaying a user selected model parameter (b.), a histogram of the pixel frequency of the same model parameter (c.) and the recorded photon density and model fit for the pixel selected by the blue cross visible in a. and b. The final panel (e.) allows the user to select the number of exponential decay components used in the model and allows the model parameters to be manually fixed.

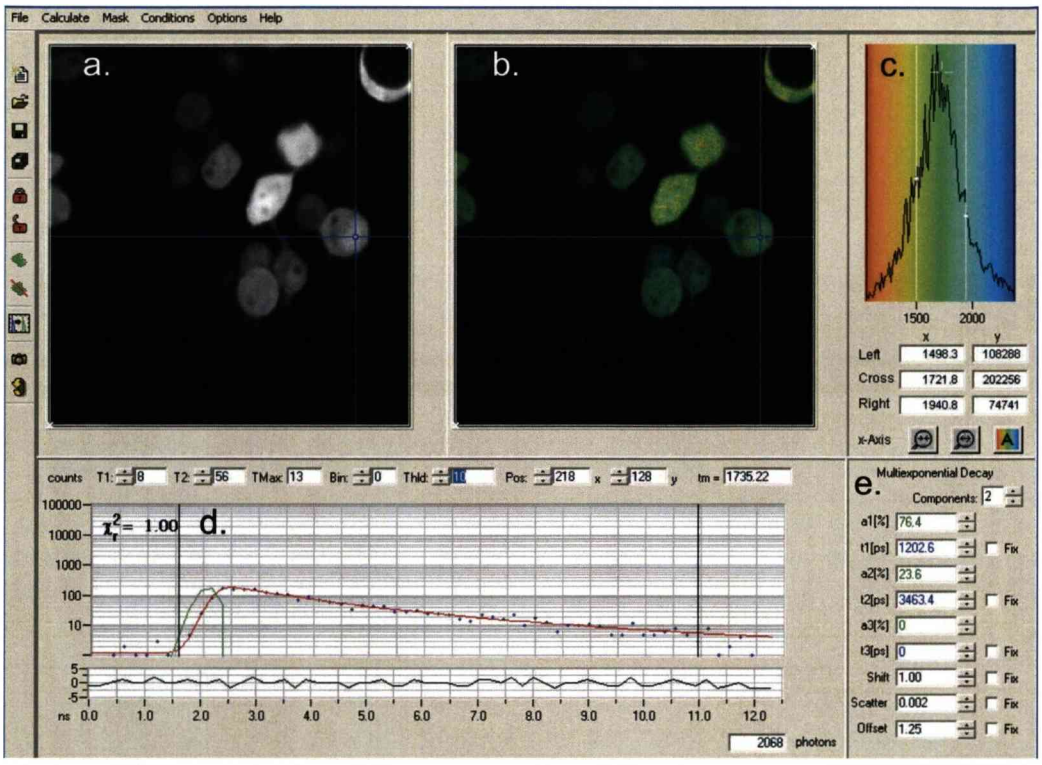

Figure 4.10 Screen capture of the SPCImage 2.9 time domain lifetime image analysis program. The file under analysis is a lifetime image of HEK293 cells transiently transfected with CFP and YFP linked by 16 amino-acids (see section 3.3 for further details). The lifetime data has been fit to a bi-exponential decay model. The software interface displays **a**. an intensity image. **b**. a colour coded image of a selected model parameter (here the weighted mean lifetime of the two exponential decay components). **c.** the intensity weighted pixel frequency histogram of the mean lifetimes present in the colour coded image. **d.** the photon density distribution and multi-exponential fit of the pixel selected with the blue cursor. The total number of photons in the distribution is shown in the bottom right of the panel. **e**. Multiexponential decay model parameters.

Once the number of components in the exponential decay model has been selected, additional parameters that account for shift, scatter and offset of the photon density distribution in the time window can be fixed and specified. The shift parameter defines where the instrumental response function is in relation to the rising edge of the photon density distribution. The scattering parameter accounts for photons that arise from scattering of excitation light that breaks through the emission barrier filters instead of fluorescence emission. The offset parameter accounts for a non-zero baseline in the data due to detector noise or the detection of ambient light and is estimated from the average number of photons in histogram bins preceding the rising edge of the photon distribution.

The software requires ~ 6 bins preceding the rising edge of the photon density distribution to calculate the offset. The position of the leading edge in the histogram can be adjusted by altering the length of the electrical cables carrying the detector and synchronisation signals to introduce a delay between the two.

Before the model is fitted to the data, two more parameters must be set: the threshold and binning. The threshold parameter defines the number of photons in the peak bin of the photon density distribution required for the pixel to be fitted to the model. The threshold can be set so that pixels that only contain scattered light are ignored completely, reducing computation time and suppressing outliers in the parameter histogram. The number of photons recorded in each pixel can be increased by binning pixels and sacrificing spatial resolution. This might be required to increase the signal-to-noise ratio of the image.

A region of interest (ROI) can be selected using a rectangle tool or a polygon tool with user defined points. The specified model is fit to the time resolved data contained within the pixels in the ROI using least-squares fitting that seeks to minimise the chi-squared value between the data and the model function. Once the model fitting is complete, the user can choose which model parameters are to be displayed in the colour coded image and pixel frequency histogram. In order to gauge whether fitting has been successful the chi-squared value is one of the parameters that can be displayed. The other parameters include the individual model parameters a_j and τ_j, the weighted mean lifetime τ_m,

$$\tau_m = \frac{\sum a_j \tau_j}{\sum a_j} \qquad \text{Eqn. 4-22}$$

the relative quantum yield (the fractional contribution of each component to the steady state fluorescence intensity) q_j,

$$q_j = \frac{a_j \tau_j}{\sum a_j \tau_j} \qquad \text{Eqn. 4-23}$$

the intensity weighted mean lifetime, τ_i.

$$\tau_i = \frac{\sum a_j \tau_j^2}{\sum a_j \tau_j} \qquad \text{Eqn. 4-24}$$

The intensity weighted mean lifetime with pile-up correction can also be calculated if the total measurement time, laser repetition rate and detector dead time are precisely known.

4.3 Demonstration of multicolour optical sectioning and lifetime imaging

The first imaging test of the multi-dimensional, multi-colour confocal microscope was to image optical sections of fluorescently labelled ErbB family members in live A431 cells. The A431 cell line is derived from a human epithelial carcinoma which express at their plasma membranes ~ 1-2 x 10^6 ErbB1 receptors per cell[36]. These cells also express low levels of ErbB2 and ErbB3, but lack endogenous ErbB4[37]. Labelling of endogenous ErbB1 was achieved by binding EGF-Cy3 or EGF-Alexa 647 to membrane localised receptors. ErbB2 and ErbB3 fused to variants of GFP were transiently transfected into A431 cells. Two colour images and single colour z-stacks of the fluorescently tagged ErbB receptors were acquired to demonstrate the imaging ability of the microscope.

HEK293 cells, a cell line generated by transformation of human embryonic kidney cells[38] were used to ascertain the correct functioning of the Becker-Hickl fluorescence lifetime imaging module. These cells were used as they are straightforward to transfect with genes for non-native proteins. They were first transiently transfected with the gene for CFP and observed with the lifetime imaging mode of the microscope. CFP lifetimes measured by time-domain techniques previously reported in the literature range between 2.49 - 2.72 ns[39-42]. As a positive control, the ability of a multi-colour microscope to demonstrate

FRET was tested using HEK293 cells that were transfected with CFP linked to YFP by a short (16 amino acid) linker. In these samples quenching of the CFP fluorescence by FRET is expected and can be unambiguously demonstrated by observing the recovery of the reduced CFP lifetime after photobleaching the acceptor.

4.3.1 Materials and Methods

4.3.1.1 Maintenance of Cell Cultures

A431 and HEK293 cells were were obtained from the European Collection of Animal Cell Cultures. Both were cultured adhered to 75 cm^2 flat bottom flasks in Dulbecco's modified Eagle's medium supplemented with 10% fetal bovine serum, 2 mM glutamine and 1% penicillin/streptomycin (all Invitrogen), but without phenol red which leads to increased cellular background fluorescence. Cells were incubated at 37°C in the presence of 5% CO_2 in air.

Both cell types reached 70-80% confluency after 2-3 days of incubation at which point they were passaged using the following procedure. First the media was removed from the culture flasks and the cells washed in Hanks' balanced salt solution (HBSS, Invitrogen). After removal of the HBSS 1 ml of Trypsin (0.5% in EDTA w/v, Invitrogen), diluted in HBSS to a total volume of 10 ml was added to each flask and the cells were incubated at 37°C in the presence of 5% CO2 in air for either 15 minutes (A431 cells) or 10 minutes (HEK293) cells. This was sufficient to detach the majority of the cells from the surface of the flask as observed by light microscopy. 3 ml of culture media was added to the flasks at this point to reduce further trypsination of cell surface proteins. Centrifugation for 5 minutes at 500 g was then used to separate cells from the trypsin soultion. After removing the supernatant with a pippette, pellets of cells were resuspended in 10 ml of culture media. 2 ml of resuspended cells (constituting ~20% of the harvested cells) was placed into a new 75 ml flask each containing 10 ml of culture media. The density of cells in the remaining suspension was determined

using a haemocytometer and used to plate glass bottomed dishes as required. All liquid waste including unwanted cells adherent culture or in suspension were placed in Virkon, a broad spectrum disinfectant, for 24 hours before disposal. Flasks, pipette tips and falcon tubes used for cell culture were also placed in Virkon for 24 hours before being autoclaved and removed for incineration.

4.3.1.2 Binding of EGF fluorescent probe conjugates to A431 cell surface ErbB1 receptors

$1.5x10^5$ A431 cells were plated onto DeltaT glass bottomed dishes (Bioptech) in complete medium and incubated overnight at 37°C in the presence of 5% CO_2 in air to achieve ~80% confluency. Murine EGF (mEGF) was obtained from Peprotech, both Cy3 and Alexa 647 dyes were obtained from Invitrogen and conjugations of dyes to the N-terminus of mEGF were performed by Cambridge Research Biochemicals. Pre-chilled cells were incubated at 4°C with either an excess (>200 nM) or physiological concentration (15 nM) of mEGF-Cy3, or 100 nM mEGF-Alexa 647 for 30 minutes in the presence of 5% CO_2 in air. The cells samples were subsequently washed three times with ice cold PBS to remove unbound fluorescently labelled mEGF before imaging.

4.3.1.3 Preparation of DNA plasmids

DNA Plasmids encoding cyan fluorescent protein (CFP), yellow fluorescent protein (YFP) and CFP linked to YFP by 16 amino-acids (CFP-16aa-YFP) were a gift from Dr Nick Gay of the University of Cambridge. Plasmids encoding ErbB3 fused with enhanced green fluorescent protein (ErbB3-eGFP) were a gift from Dr Maddy Parsons of King's College London. Plasmids encoding ErbB2-eYFP were a gift from Dr Mads Lerdrup of The University of Copenhagen. The A206K mutation was introduced to these two ErbB fusion protein constructs with site directed mutagenesis by Dr Selene Roberts at the STFC Daresbury Laboratory. The two mutants were designated

ErbB3-eGFPA206K and ErbB2-eYFPA206K. The A206K mutant of GFP variants is advantageous as it does not homo-dimerise[43]. Stock solutions of plasmids in tris-EDTA (TE) were stored at 4°C.

Large quantities of plasmids for the transient transfection of mammalian cells were obtained from the original stock plasmid solutions using the Maxiprep procedure (Qiagen, Germany). The desired plasmid is replicated by bacteria grown in culture before being removed using alkaline lysis and purified. An outline of the procedure follows and a list of the buffers referred to in the procedure and their compositions can be found in table 4.4.

DH5α *E. Coli* were transformed with the DNA plasmids and cultured on Luria-Bertani (LB) agar plates. 1 L of LB media contains 10g of Bacto-tryptone, 5 g of Bacto-yeast extract and 10 g of NaCl in distilled water, pH 7.0. The selective antibiotic for all constructs was kanamycin which was included in all LB media at a concentration of $25\mu gml^{-1}$. For each construct a single colony was picked and used to innoculate 3 ml of LB media. These cultures were grown up overnight at 37°C with 225 rpm agitation. 0.5 ml of each suspended culture was then removed and added to 500 ml of LB media and further incubated at 37°C overnight. Cultures were removed from the conical flasks and centrifuged at 6000 rpm for 10 minutes at 4°C. The supernatant was removed and the pellets of bacteria were resuspended in 10 ml of resuspension buffer. To lyse the bacteria, 10 ml of a lysis buffer containing sodium dodecyl sulfate (SDS) was added to the resuspended cells and mixed vigorously (without vortexing as this may shear genomic DNA) until a homogenously coloured suspension was obtained. The lysis reaction was allowed to proceed for no more than 5 minutes at room temperature before 10 ml of neutralization buffer containing potassium acetate was added, again with vigorous mixing. At this point a white precipitate containing genomic DNA, protein and cell debris was visible. This was cleared from the lysate by filtration using a QIAfilter cartridge. The filtered lysate was collected in a Qiagen HiSpeed Maxi tip that had been previously prepared by allowing 10 ml of equilibration buffer to flow through it. The HiSpeed tip contains a resin that binds plasmid DNA but allows the lysate to pass through the

tip by gravity flow. 60 ml of wash buffer was allowed to flow through the HiSpeed tip before eluting the DNA with 15 ml of elution buffer.

Buffer	Composition	Storage Temperature
Resuspension buffer	50 mM Tris-Cl, pH 8.0 10 mM EDTA 100 $\mu g ml^{-1}$ RNase A	2-8°C after addition of RNase A
Lysis buffer	200 mM NaOH 1 % SDS (w/v)	15-25°C
Neutralisation buffer	3.0 M potassium acetate, pH 5.5	15-25°C
QIAfilter wash buffer	1 M potassium acetate, pH 5.0	15-25°C
Equilibration buffer	750 mM NaCl 50 mM MOPS, pH 7.0 15% isopropanol (v/v) 0.15% Triton X-100 (v/v)	15-25°C
Wash buffer	1.0 M NaCl 50 mM MOPS, pH 7.0 15% isopropanol (v/v)	15-25°C
Elution buffer	1.25 M NaCl 50 mM Tris-Cl, pH 8.5 (15% isopropanol (v/v))	15-25°C
TE	10 mM Tris-Cl, pH 8.0 1mM EDTA	15-25°C
STE	TE with 100 mM NaCl	15-25°C

Table 4.4 List of buffers used in the Qiagen Maxiprep procedure with their compositions and storage conditions.

The eluate was collected in a Vulcan tube and the DNA precipitated by adding 10.5 ml of isopropanol and incubating at room temperature for 5 minutes. The tube and its contents were then centrifuged for 30 minutes at 110000 rpm. The isopropanol was poured off and 5 ml of 70% ethanol in deionised water added to the pellet before being centrifuged for a further 5 minutes. The ethanol was then removed and the pellet of DNA left to dry in air for 5 minutes before being

resuspended in 500 ul of TE and transferred to an eppendorf tube. DNA purity and concentration were assessed from the absorbance of the resuspended sample at 260 nm and 280 nm, which are the peaks of DNA and protein absorption spectra respectively.

4.3.1.4 Transient transfection of A431 cells

$1.5x10^5$ A431 cells were plated onto DeltaT glass bottomed dishes (Bioptech) in antibiotic free medium and incubated overnight at 37°C in the presence of 5% CO_2 in air to achieve ~80% confluency.

The media in each dish was then replaced with a transfection mixture comprising 2 μg of DNA plamids encoding either ErbB3-eGFPA206K or ErbB2-eYFPA206K, 6 μl the transfection reagent fugene and 2 ml of serum free media. Cells were incubated in the transfection mixtures at 37°C in the presence of 5% CO_2 in air before being replaced with fresh complete medium. The samples were then incubated for 18 – 24 hours before imaging the expressed fluorescent proteins.

4.3.1.5 Transient transfection of HEK293 cells

$1.5x10^5$ HEK293 cells were plated onto DeltaT glass bottomed dishes (Bioptech) in antibiotic free medium and incubated overnight at 37°C in the presence of 5% CO_2 in air to achieve ~80% confluency.

The media in each dish was then replaced with a transfection mixture comprising 1μg of DNA plasmids, 2.5 μl of lipofectamine (a different transfection reagent best suited for these cells) and 2 ml of serum free media. Transfection mixtures contained either the CFP construct alone, CFP and YFP constructs (present in a in a 1:1 molar ratio) or the CFP-16aa-YFP construct. Cells were incubated in the transfection mixtures for 4 hours at 37°C in the presence of 5% CO_2 in air before

being replaced with fresh complete medium. The samples were then incubated for 18 – 24 hours before imaging the expressed fluorescent proteins.

4.3.2 Distribution of endogenous and transiently transfected ErbB family members in A431 cells

Figure 4.11 shows two confocal images obtained by this microscope during its initial commissioning phase. The images show optical sections through a sample of live A431 cells that have been exposed to an excess of mEGF-Cy3. The sample was excited with 545 nm pulsed excitation light (76 MHz repetition rate) and Cy3 fluorescence was detected between 572.5 and 647.5 nm. The images are of a 65 x 65 μm field of view at a resolution of 512 x 512 pixels. A431 cells are distinguished by their irregular shapes and sizes as they grow in an uncontrolled fashion. The cells were imaged at room temperature.

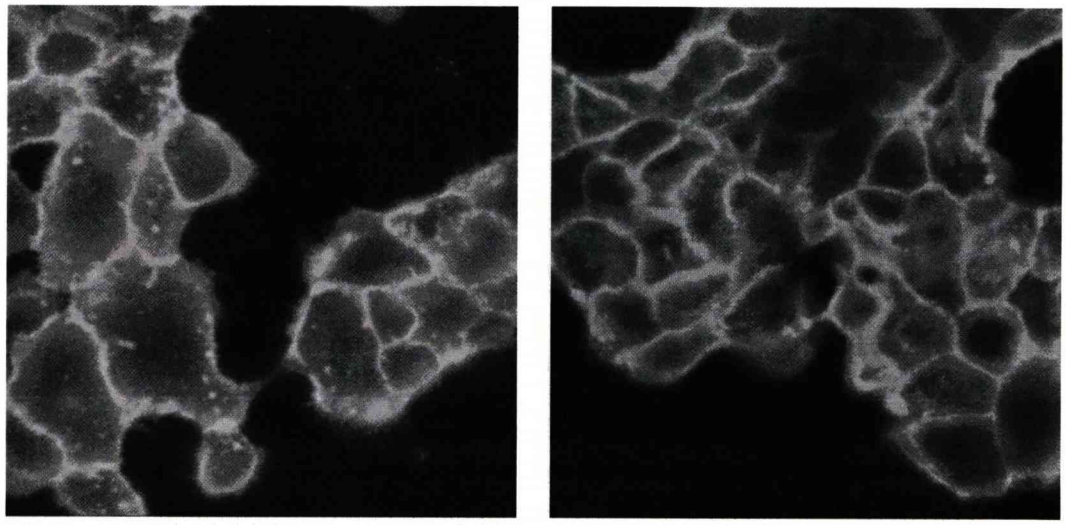

Figure 4.11 A431 carcinoma cells probed with an excess of EGF-Cy3 at room temperature. Both images are of a 65 x 65 μm field of view.

The largest source of fluorescence is located the membrane of the cells (where ErbB1 resides), but a consequence of the temperature being above 4°C, some of the mEGF-Cy3 ligands have been internalised via receptor mediated endocytosis and are visible as large vesicles and an increase in background fluorescence

within the confines of the cell membranes. In the left hand image, some philopodia are also visible.

To demonstrate multi-colour sectioning and correct imaging of cell samples A431 cells were transfected with either ErbB2-eYFPA206K, or ErbB3-eGFPA206K before incubation with mEGF-Alexa 647. Of the two fluorescence protein constructs, the expressed ErbB2-YFPA206K was known not to be transported to the cell membrane and should not co-localise with mEGF-Alexa 647 (from a personal communication with Dr Mads Lerdrup, The University of Copenhagen). In contrast, the expressed ErbB3-eGFPA206K was known to be transported to the cell membrane therefore should co-localise with mEGF-Alexa 647. Samples were excited with 488 nm and 639 nm light. GFP / YFP fluorescence was detected between 500 and 550 nm. Alexa 647 fluorescence was detected between 662.5 and 737.5 nm. Figure 4.12a and b shows 65 x 65 μm fields of A431 cells where several cells are expressing ErbB2-eYFPA206K. Cells transiently expressing fluorescent protein fusion products usually display cytosolic fluorescence from proteins being produced inside the cell and transported throughout the cell. No fluorescence in the transfected cells appears to co-localise with the mEGF-Alexa 647 visible at the cell membrane. This is in contrast to figure 4.12c which shows A431 cells transiently transfected with ErbB3-eGFPA206K which appears to be localised in the cytosol and the cell membrane.

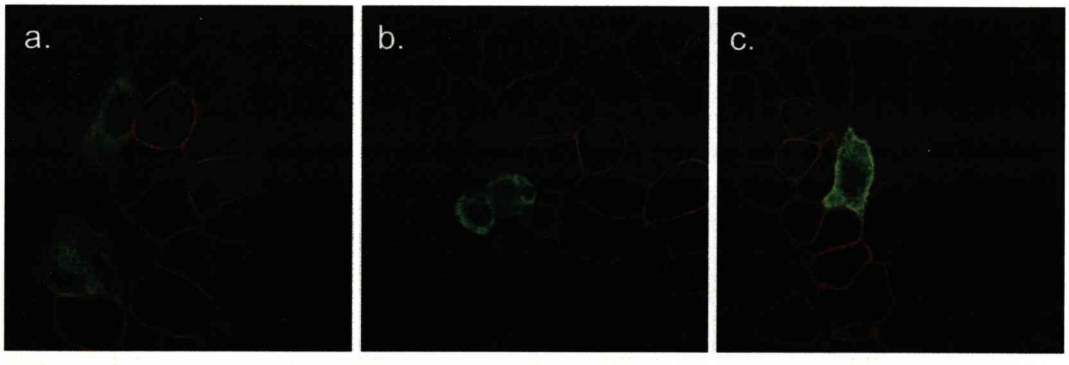

Figure 4.12 Two colour images of mEGF-Alexa 647 bound to ErbB1 (displayed as red) and ErbB2-eYFPA206K (**a, b.**) or ErbB3-eGFPA206K (**c.**). In all three images fusion proteins are displayed green. Samples were imaged at 4°C. The field of view of the images is 65 x 65 μm.

The sectioning ability of the microscope was further tested by imaging z-stacks through A431 cell samples labelled with mEGF-Cy3 bound to endogenous ErbB1 or A431 cells transiently transfected with ErbB3-eGFP. The z-stacks through a volume of each sample are shown in Figures 4.13 and 4.14. Both image series begin just above the basalateral membrane of the cell (the membrane in contact with the glass coverslip) and the focal plane of the microscope was moved through the sample using the piezo-electric objective positioner. The apical surface of the layer of A431 cells appears to occur between 18 - 20 μm from the axial position of the first image. Both image stacks show different distributions of fluorescence throughout the samples that highlight differences between the ways the receptors have been tagged with fluorophores in each figure.

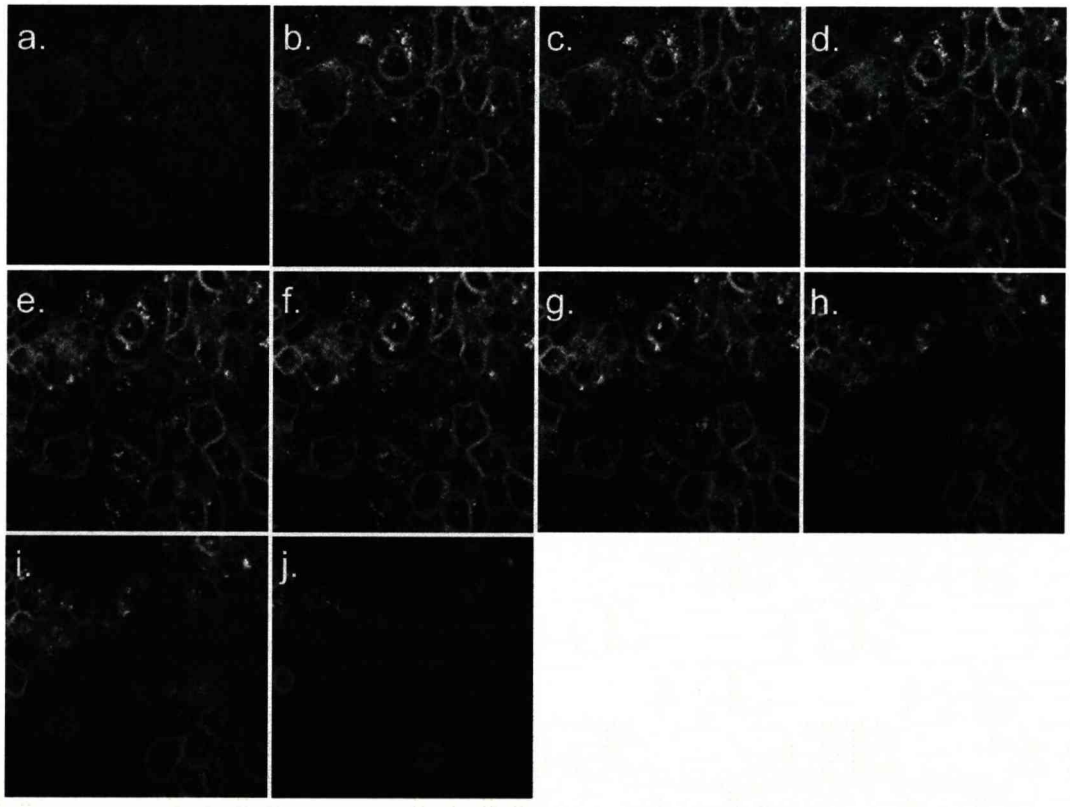

Figure 4.13 Endogenous ErbB1 in A431 cells after exposure to 15nM mEGF-Cy3 at room temperature for 10 minutes. a. A section close to the basalateral membrane of the cell sample. b – j are sections imaged at 2 μm intervals through the z-axis. The field of view of the images is 65 x 65 μm.

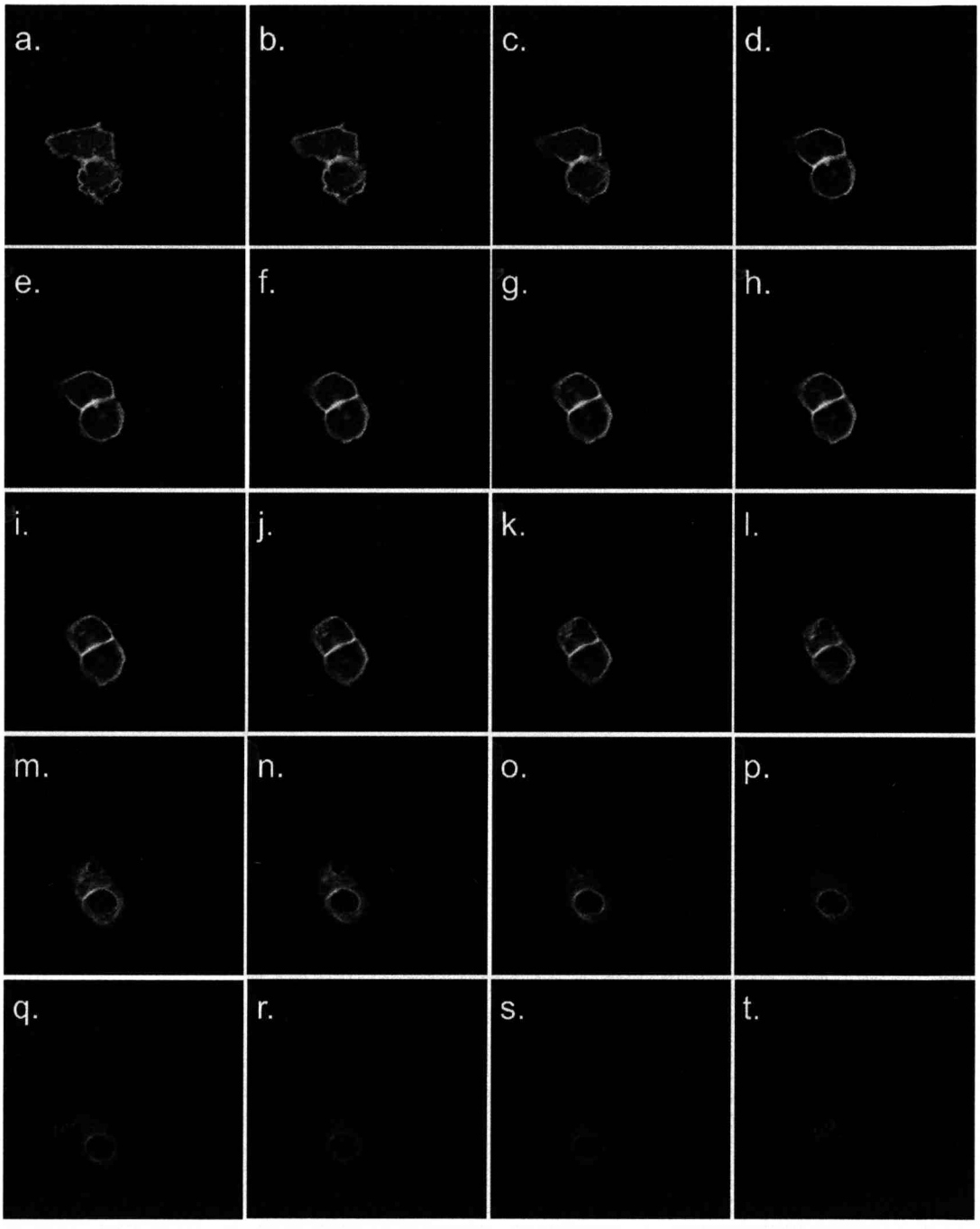

Figure 4.14 ErbB3-eGFPA206K transiently expressed in A431 cells. Images a - t are sections taken at 1 μm intervals from the imageable section closest to the basal membrane. The field of view of the images is 65 x 65 μm.

The images in Figure 4.13 show the distribution of ErbB1 receptors that can bind mEGF-Cy3 at the plasma membrane, or that have bound to mEGF-Cy3 before being internalised. All the cells in the field of view are labelled. The reduced

fluorescence intensity of 4.13a compared to 4.13b-j could be due either to reduced amounts ErbB1 receptor in the region of the basalateral membrane or a consequence of restricted mEGF-Cy3 diffusion to the bottom of the cell layer.

The images in figure 4.14 show the distribution of all ErbB3-eGFP fusion proteins expressed by the two cells in the field of view that have been successfully transfected. As each ErbB3 receptor is transcribed labelled 1:1 with eGFP, all ErbB3-eGFP complexes are seen immediately after eGFP maturation after which the eGFP labels become fluorescent. Receptors observed include membrane localised ErbB3 is seen as well as protein that is being produced and transported around the inside of the cell. A gradual loss of membrane bound fluorescence between images 4.14i-m can be observed and as cytosolic ErbB3-eGFP can still be seen this indicates that the ErbB3 distribution in A431 cells is polarised. Membrane bound ErbB3-eGFP is found only in the bottom half of the cell, whereas the top half appears to contain mainly cytosol localised receptor only.

4.3.3 FLIM of fluorescent proteins in live cells

Figure 4.15a is a fluorescence lifetime image of a group of HEK293 cells expressing CFP which can be seen throughout the cytosol. CFP was excited with 440 nm pulsed excitation (76 MHz repetition rate) and the CFP fluorescence was detected between 455 and 485 nm. The samples were kept at room temperature. CFP fluorescence emission is characterised by a temperature dependent bi-exponential intensity decay[39]. The data was fitted to a bi-exponential decay model and the image displays the weighted mean of the two lifetime components, τ_m. τ_m values between 1 and 4 ns are represented by a continuous range of colours from red to blue respectively. The mean of the τ_m distributions from the pixels in each cell were obtained for a total of 31 transfected cells. The average value of τ_m over all the cells was 2.82 ns with a standard deviation of 0.06 ns. This is similar to the mean CFP fluorescence lifetimes previously

measured using TCSPC FLIM (2.72 ns [40] and 2.50 ± 0.02 ns [41]) and a novel time and space correlated single-photon counting detector (2.49 ± 0.18 ns)[42].

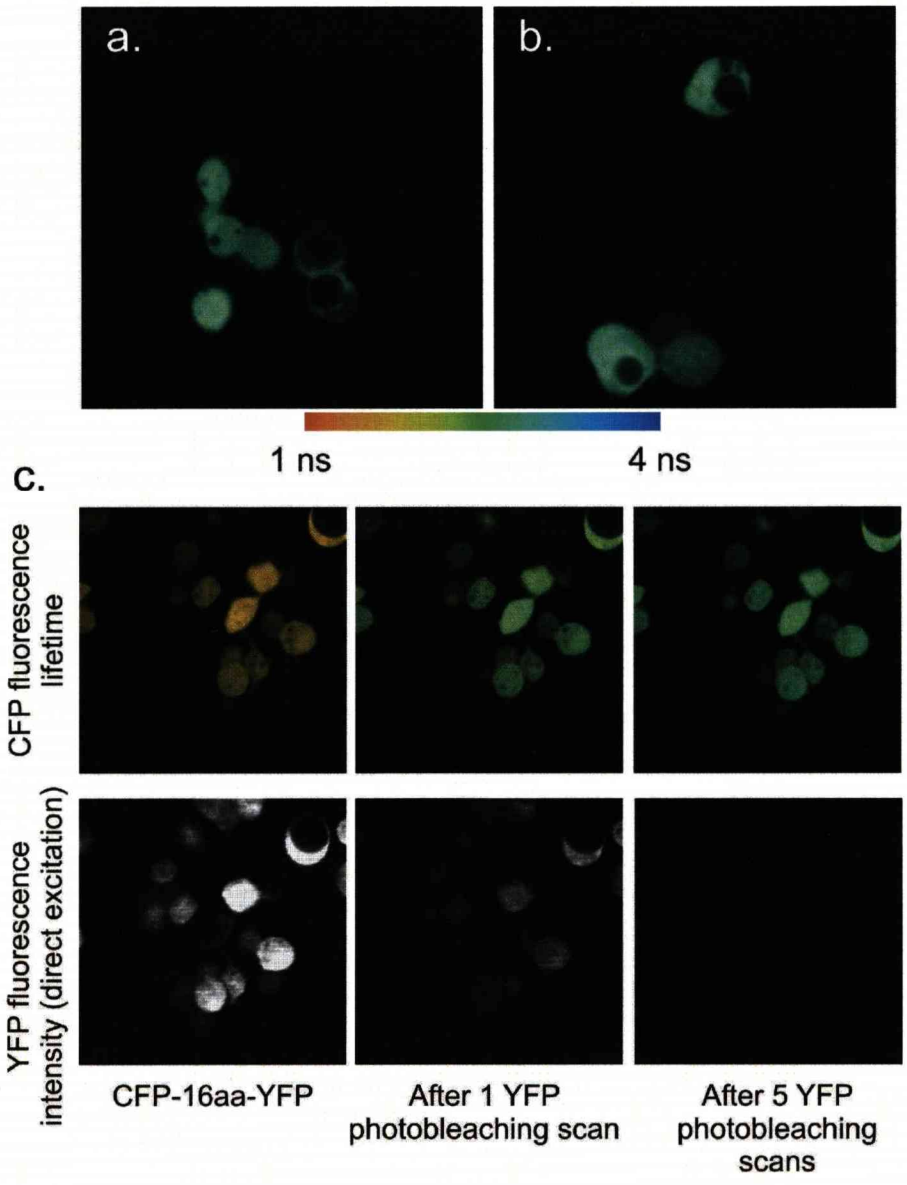

Figure 4.15 Confocal lifetime images of CFP τ_m in HEK 293 cells transfected with **a.** CFP only **b.** CFP and YFP (unlinked) **c.** Top - Lifetime images of CFP τ_m when linked to YFP by a 16 amino-acid linker before and after photobleaching of YFP. The corresponding YFP intensity taken after the lifetime images is shown underneath each lifetime image. All images are of a 63 x 63 μm field of view.

Expression product	Average CFP τ_m / ns	Standard deviation / ns	Number of cells sampled
CFP	2.82	0.06	31
CFP + YFP (unlinked)	2.75	0.02	37
CFP-16aa-YFP	1.78	0.09	34

Table 4.5 The value of CFP τ_m in HEK 293 cells measured by confocal FLIM and averaged over all cells.

Figure 4.15b is a fluorescence lifetime image of CFP in HEK293 cells transiently transfected with both CFP and YFP (unlinked, negative control of FRET). It can be seen qualitatively that the CFP lifetimes in these cells are similar to those in figure 4.15a. The average value of τ_m was 2.75 ns with a standard deviation of 0.02 ns. This demonstrates that there is negligible quenching of the CFP lifetime due to random association with YFP within the cells. This is in stark contrast to the results from samples transfected with the CFP-16aa-YFP construct where each CFP donor is positioned close enough to its linked YFP acceptor partner to be able to transfer excited state energy via FRET (figure 4.15c and table 4.5). The average value of τ_m was 1.78 ns with a standard deviation of 0.09 ns. Figure 4.16 compares the intensity weighted pixel frequency of the τ_m values contained in images 4.15a (dark green dotted line) 4.15b (light green dashed line) and the first FLIM image of 4.15c. This plot clearly shows the differences in fitted CFP lifetimes between the three sample types.

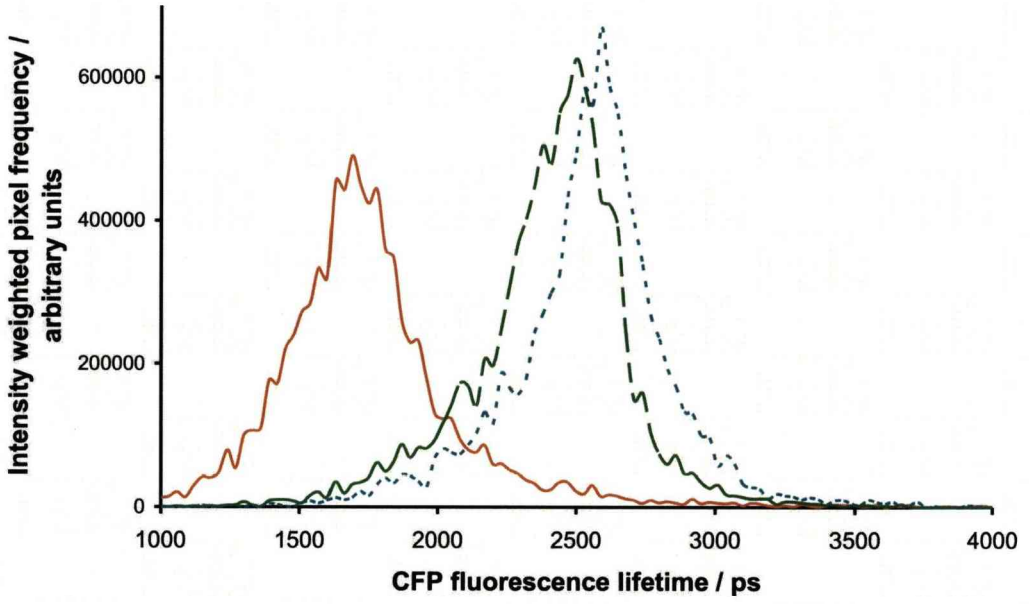

Figure 4.16 The intensity weighted distribution of CFP fluorescent lifetimes (τ_m) from the pixels contained within the lifetime images in figure 4c. Shown is CFP-16aa-YFP before YFP bleaching (continuous orange), after a single YFP photobleaching scan (dashed green) and after 5 YFP photobleaching scans (dotted blue-green).

Using

$$E_{FRET} = 1 - \frac{\tau_{m(CFP-16aa-YFP)}}{\tau_{m(CFP)}} \qquad \text{Eqn. 4-25}$$

the average efficiency of FRET between CFP and YFP in the CFP-16aa-YFP fusion protein was calculated to be 0.37 ± 0.03. Neglecting the possibility of FRET between CFP and YFPs from other constructs the average separation r of CFP and YFP in the construct was estimated by using the equation

$$E_{FRET} = \frac{R_0^6}{R_0^6 + r^6} \qquad \text{Eqn. 4-26}$$

Taking $R_0 = 4.92 \pm 0.10$ nm for the CFP/YFP FRET pair[44], $r = 5.38 \pm 0.13$ nm.

The value of r determined is reasonable close to that expected from a straight chain of 16 amino-acids (6.4 nm). The difference may be due to flexibility of the 16 amino-acid linker and the fact that the errors quoted do not take into account uncertainties that arise from assuming an average value of the orientation factor and are likely to be larger.

To confirm the presence of FRET, the YFP in the CFP-16aa-YFP construct was photobleached by direct excitation with 514 nm CW laser light scanned slowly across the image region (63.45s per scan). After each photobleaching scan, the resulting YFP intensity image was saved before the acquisition of a new CFP lifetime image. Figure 4.15c shows these images for an area of cells after 1 and 5 photobleaching scans. Figure 4.17 plots the mean value of CFP τ_m for each successive photobleaching scan and compares them to the values for CFP in the absence of YFP and when connected to YFP by 16 amino acids.

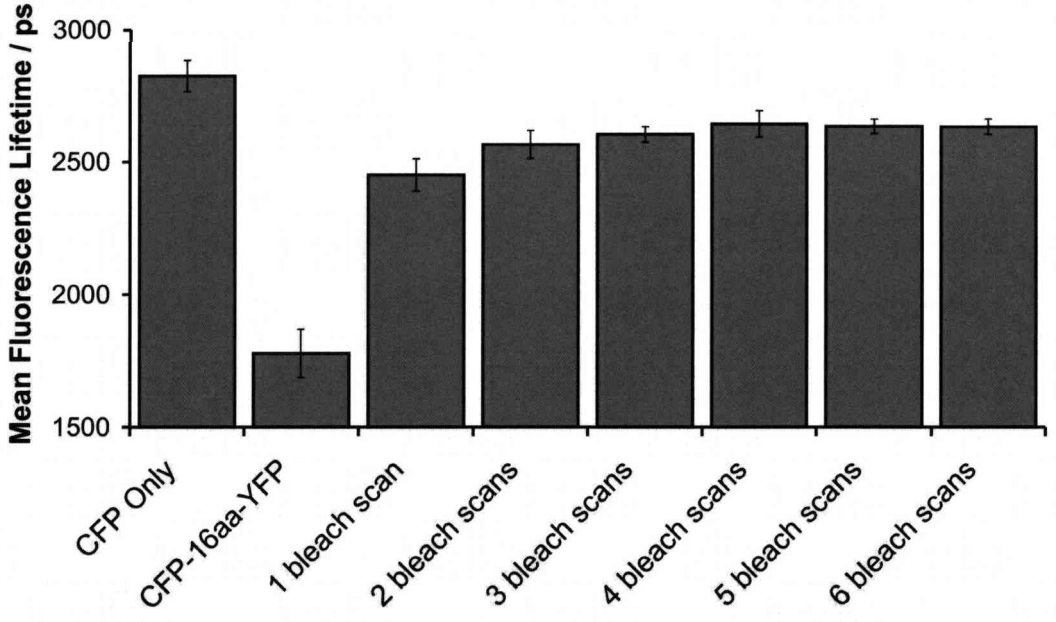

Figure 4.17 Bar chart of mean CFP fluorescent lifetimes comparing the results from HEK 293 cells transfected with CFP only, CFP-16aa-YFP and CFP-16aa-YFP after YFP photobleaching. All results from CFP-16aa-YFP expressing cells are derived from the same field of view. Error bars represent the standard deviation of the average CFP fluorescent lifetime from a sample of 31 cells (expressing CFP only) or 18 cells (expressing CFP-16aa-YFP).

It is clear after the first bleaching scan that the photobleaching of YFP causes some recovery of the CFP lifetime, confirming that the quenching of the CFP lifetime is indeed due to FRET between CFP and YFP. However, even after repeating the photobleaching scan 6 times and reducing the YFP fluorescence intensity to <10% of its initial value, complete recovery of the CFP only lifetime does not occur. It is possible that the CFP lifetime is quenched as a result of fusion to the linker and YFP even when the YFP chromophore has been photobleached. Other studies that have failed to recover the donor only reference value of the CFP lifetime upon the complete photobleaching of linked YFP have been attributed to the creation of photoproducts during YFP irradiation that contaminate the CFP fluorescence detection channel[41].

4.4 Summary

A multi-dimensional, multi-colour confocal microscope for the quantitative measurement of FRET between donor and acceptor labelled proteins *in situ* has been designed and implemented. Multi-colour optical sectioning of biological samples was demonstrated by imaging fluorescently labelled ErbB receptors in live cells. Two different approaches to the 1:1 labelling of ErbB receptors with a fluorophore were tested; the binding of fluorescently labelled ligand to the extracellular domain and expression of the receptor fused at the c-terminus with a fluorescent protein. The capability of the system to quantitatively measure FRET efficiencies using FLIM was tested in live cells expressing a fluorescent protein consisting of a FRET donor and acceptor linked by a short peptide sequence. The use of the microscope described in this chapter for developing a FRET-based method for investigating the three dimensional structure of membrane proteins *in situ* is described in the chapters that follow.

References

1. Mueller, M. Introduction to Confocal Fluorescence Microscopy (SPIE Press, 2006).
2. Denk, W., Strickler, J. H. & Webb, W. W. Two-photon laser scanning fluorescence microscopy Science 248, 73-76 (1990).
3. Neil, M. A. A., Juskaitis, R. & Wilson, T. Method of obtaining optical sectioning by using structured light in a conventional microscope. Optics Letters 22, 1905-1907 (1997).
4. Siegel, J. et al. Whole-field five-dimensional fluorescence microscopy combining lifetime and spectral resolution with optical sectioning. Optics Letters 26, 1338-1340 (2001).
5. König, K., So, P. T. C., Mantulin, W. W. & Gratton, E. Cellular response to near-infrared femtosecond laser pulses in two-photon microscopy. Optics Letters 22, 135-137 (1997).
6. König, K., So, P. T. C., Mantulin, W. W., Tromberg, B. J. & Gratton, E. Two-photon excited lifetime imaging of autofluorescence in cells during UVA and NIR photostress. Journal of Microscopy 183, 197-204 (1996).
7. Svoboda, K., Denk, W., Kleinfeld, D. & Tank, D. W. In vivo dendritic calcium dynamics in neocortical pyramidal neurons. Nature 385, 161-165 (1997).
8. König, K. & Tirlapur, U. K. in Confocal and Two-Photon Microscopy: Foundations, Applications and Advances (ed. Diaspro, A.) 191-205 (Wiley-Liss, Inc., New York, 2002).
9. Ichimura, A. et al. High-speed confocal fluorescence microscopy using a nipkow scanner with microlenses for 3-D imaging of single fluorescent molecule in real time. Bioimages 4, 57-62 (1996).
10. Schermelleh, L. et al. Subdiffraction Multicolor Imaging of the Nuclear Periphery with 3D Structured Illumination Microscopy. Science 320, 1332-1336 (2008).
11. Verveer, P. J., Hanley, Q. S., Verbeek, P. W., Vliet, L. J. & Jovin, T. M. Theory of confocal fluorescence imaging in the programmable array microscope (PAM). Journal of Microscopy 189, 192-198 (1997).

12. Hanley, Q. S., Verveer, P. J., Gemkow, M. J., Arndt-Jovin, D. & Jovin, T. M. An optical sectioning programmable array microscope implemented with a digital micromirror device. Journal of Microscopy 196, 317-331 (1999).
13. Smith, P. J., Taylor, C. M., Shaw, A. J. & McCabe, E. M. Programmable array microscopy with a ferroelectric liquid-crystal spatial light modulator. Applied Optics 39, 2664-2669 (2000).
14. Hanley, Q. S., Lidke, K. A., Rainer Heintzmann, Arndt-Jovin, D. J. & Jovin, T. M. Fluorescence Lifetime Imaging in an Optically Sectioning Programmable Array Microscope (PAM). Cytometry Part A 67A, 112-118 (2005).
15. Hecht, E. Optics (Addison Wesley, 2002).
16. Pawley, J. in Handbook of Biological Confocal Microscopy (ed. Pawley, J.) 19-37 (Plenum Press, New York, 1995).
17. Webb, R. H. & Dorey, C. K. in Handbook of Biological Confocal Microscopy (ed. Pawley, J.) 55-67 (Plenum Press, New York, 1995).
18. Young, J. Z. & Roberts, F. A flying spot microscope. Nature 167, 231 (1951).
19. Minsky, M. Memoir on inventing the confocal scanning microscope. Scanning 10, 128-138 (1988).
20. Amos, W. B. & White, J. G. How the Confocal Laser Scanning Microscope entered Biological Research. Biology of the Cell 95, 335-342 (2003).
21. Cox, I. J. Scanning optical fluorescence microscopy. Journal of Microscopy 133, 149-154 (1984).
22. Brakenhoff, G. J., Blom, P. & Barends, P. Confocal scanning light microscopy with high aperture immersion lenses. Journal of Microscopy 165, 139-146 (1979).
23. Stelzer, E. H. K. in Handbook of Biological Confocal Microscopy (ed. Pawley, J.) 139-154 (Plenum Press, New York, 1995).
24. Petran, M., Hadravsky, M., Egger, M. D. & Galambos, R. Tandem-scanning reflected-light microscope. Journal of the Optical Society of America 58, 661-664 (1968).

25. Fukano, T. & Miyawaki, A. Whole-field fluorescence microscope with digital micromirror device: imaging of biological samples. Applied Optics 42, 4119-4124 (2003).

26. Centonze, V. & Pawley, J. in Handbook of Biological Confocal Microscopy (ed. Pawley, J.) 549-568 (Plenum Press, New York, 1995).

27. Gratton, E., Breusegem, S., Sutin, J., Ruan, Q. & Barry, N. Fluorescence lifetime imaging for the two-photon microscope: time-domain and frequency-domain methods. Journal of Biomedical Optics 8, 381-390 (2003).

28. Gerritsen, H. C., Asselbergs, M. A., Agronskaia, A. V. & Sark, W. G. V. Fluorescence lifetime imaging in scanning microscopes: acquisition speed, photon economy and lifetime resolution. Journal of Microscopy 206, 218-224 (2002).

29. Becker, W. et al. Fluorescence Lifetime Imaging by Time-correlated Single-Photon Counting. Microscopy Research and Technique 63, 58-66 (2005).

30. Becker, W. et al. High-Speed FLIM Data Acquisition by Time-Correlated Single Photon Counting. Proc. SPIE 5323 (2004).

31. Duncan, R. R., Bergmann, A., Cousin, M. A., Apps, D. K. & Shipston, M. J. Multi-dimensional time-correlated single photon counting (TCSPC) fluorescence lifetime imaging microscopy (FLIM) to detect FRET in cells. Journal of Microscopy 215, 1-12 (2004).

32. O'Connor, D. V. & Phillips, D. Time correlated single photon counting (Academic Press, London, 1984).

33. Michalet, X. et al. in Advanced Photon Counting Techniques (ed. Becker, W.) (Proceedings of SPIE, 2006).

34. Munster, E. B., Goedhart, J., Kremers, G. J., Manders, E. M. M. & Gadella Jr, T. W. J. Combination of a spinning disc confocal unit with frequency-domain fluorescence lifetime imaging microscopy. Cytometry Part A 71A, 207-214 (2007).

35. Grant, D. M. et al. High speed optically sectioned fluorescence lifetime imaging permits study of live cell signaling events. Optics Express 15, 15656-15673 (2007).

36. Fabricant, R. N., De Larco, J. E. & Todaro, G. J. Nerve growth factor receptors on human melanoma cells. PNAS 74, 565-569 (1977).

37. Olayioye, M. A., Beuvink, I., Horsch, K., Daly, J. M. & Hynes, N. E. ErbB Receptor-induced Activation of Stat Transcription Factors Is Mediated by Src Tyrosine Kinases. The Journal of Biological Chemistry 274, 17209-17218 (1999).

38. Graham, F. L., Smiley, J., Russell, W. C. & Nairn, R. Characteristics of a Human Cell Line Transformed by DNA from Human Adenovirus Type 5. Journal of General Virology 36, 59-72 (1977).

39. Pepperkok, R., Squire, A., Geley, S. & Bastiaens, P. I. H. Simultaneous detection of multiple green fluorescent proteins in live cells by fluorescence lifetime imaging microscopy. Current Biology 9, 269-272 (1999).

40. Spriet, C. et al. Correlated Fluorescence Lifetime and Spectral Measurements in Living Cells. Microscopy Research and Technique 70, 85-94 (2007).

41. Grailhe, R. et al. Monitoring Protein Interactions in the Living Cell Through the Fluorescence Decays of the Cyan Fluorescent Protein. ChemPhysChem 7, 1442-1454 (2006).

42. Tramier, M. et al. Picosecond-Hetero-FRET Microscopy to Probe Protein-Protein Interactions in Live Cells. Biophysical Journal 83, 3570-3577 (2002).

43. Zacharias, D. A., Violin, J. D., Newton, A. C. & Tsien, R. Y. Partitioning of Lipid-Modified Monomeric GFPs into Membrane Microdomains of Live Cells. Science 296, 913-916 (2002).

44. Patterson, G. H., Piston, D. W. & Barisas, B. G. Förster Distances between Green Fluorescent Protein Pairs. Analytical Biochemistry 284, 438-440 (2000).

5 Towards FRET measurement of the distance of closest approach between a protein and the plasma membrane

This chapter describes the steps taken in preparation for using a bi-directional FRET method developed to investigate the 3D structure of transmembrane proteins with respect to the plasma membrane of cells in adherent culture. The method requires the use of two different FRET pairs: (i) to probe the lateral distance between EGF ligands bound to cell surface ErbB1 where each ligand is covalently bound in a 1:1 ratio with a FRET donor or acceptor (ii) to determine the distance between bound EGF and the plasma membrane and acquire a 3D view of the ErbB1 receptors comprising the EGF-ErbB1 complexes. In (ii) the acceptor is not covalently bound to any protein but is instead a fluorescent lipophilic probe that inserts itself into lipid environments (such as cell plasma membranes). The donor fluorophore is covalently bound to the ligand EGF molecules as in (i).

Quantitative FRET measurement requires a number of calibration steps. The first is the determination of the Förster radius of the FRET pair to be employed which is required to derive distances from the associated FRET measurement. The series of measurements performed to calculate the Förster radii are described in section 5.1. Choosing the right FRET pair for a particular distance measurement is crucial as different pairs have different ranges of donor-acceptor separations over which variations in FRET efficiency can be unambiguously detected. As this range is centred around the Förster radius it can be used to gauge the applicability of the pair to study proteins of a given size (which will determine the likely range of distances involved in dynamic interactions) when planning a FRET experiment. The suitability of the FRET pairs chosen to investigate the 3D structure of the ErbB1 receptor (a > 10 nm long, 170KDa protein) was ascertained from the Förster radius measurements and the measurement of the

steady state anisotropy of the dyes involved. Anisotropy measurements determine the accuracy of the distances that can be derived via FRET for a given donor/acceptor pair.

The FRET pair chosen to investigate the separation of EGF binding sites in EGF-ErbB1 complexes was Alexa 546 and Atto 647N and the one chosen to measure the distance of closest approach of these sites to the cell surface was Alexa 546 and Vybrant C_{18}DiD. Considering the known ErbB1 crystallographic structures and results of previous FRET studies of EGF binding site separations the calculated Förster radii are large enough for measurements on ErbB1 receptors. The suitability of the Alexa 546 / Vybrant C_{18}DiD FRET pair for use in adherent cells is confirmed in section 5.2 by a preliminary experiment that tests whether there are ErbB1 conformations in cultured cell membranes that produce unexpected EGF-membrane separations.

The chapter ends with a description of an extended FRET theory required to move from this preliminary experiment to a quantitative distance determination in the experimental situation where the ratio of donors and acceptors is dynamic and non- stoichiometric, which is the case when donors are bound to a membrane protein and acceptors are free to diffuse in the membrane.

5.1 Measurement of the Förster radius of FRET pairs

The calculation of the Förster radius of a FRET pair requires the donor quantum yield, donor emission spectrum and acceptor absorption spectrum to be known. Additionally, an average value for the orientation factor must be specified. Measurement of the steady-state anisotropy of the donor and acceptor conjugates is required to determine the likely error introduced by using this average value. This section describes the measurement of these physical properties and the calculation of the Förster radius for the FRET pairs mEGF-Alexa 546 and mEGF-Atto 647N, and mEGF-Alexa 546 and Vybrant C_{18}DID.

5.1.1 Materials and Methods

5.1.1.1 Preparation of Donor and acceptor samples in solution

Stock solutions of mEGF (Peprotech, USA) conjugated to Alexa 546 (Invitrogen, USA, conjugation to mEGF performed by Cambridge Research Biochemicals, UK) and Atto 647N (Atto-Tec GmbH, Germany, EGF conjugation by Cambridge Research Biochemicals, UK) were diluted in PBS to a concentration such that the absorbance of the fluorescent dye at its emission maximum was less than 0.1, in order to avoid inner filter effects (caused by reabsorption of fluorescence photons by fluorescent dye molecules). A suspension of small phosphatidylcholine vesicles in PBS (highly diluted to minimise light scattering by the vesicles) was labelled with Vybrant C_{18}DiD (Invitrogen, USA), again such that the absorbance of the fluorescent dye at its emission maximum was less than 0.1. Small phosphatidylcholine vesicles were prepared by sonication from multilamellar vesicles prepared by vortex mixing of 50 mM sodium phosphate buffer and 0.1 M NaCl (pH 6.0) over a film of phosphatidylcholine deposited in a glass tube. Table 5.1 lists the properties of the fluorescent dyes used.

Probe	Excitation max / nm	Emission max / nm	ε_A / $M^{-1}cm^{-1}$
Alexa 546	556	572	$0.99x10^5$
Atto 647N	644	669	$1.50x10^5$
Vybrant C_{18}DiD	644	665	$1.93x10^5$
Tetramethyl Rhodamine	540	567	$1.03x10^5$

Table 5.1 Spectral properties of the fluorophores used in this chapter. Excitation max and Emission max are the wavelengths of peak excitation and fluorescence emission respectively. ε_A is the absorption coefficient at the wavelength of peak absorption.

5.1.1.2 Donor and acceptor samples in glycerol

Samples of EGF-conjugates were prepared as in 5.1.1.1 except that the PBS buffer was substituted for glycerol. Dye conjugates were mixed slowly with the viscous glycerol gel to avoid introducing air bubbles to the sample. EGF-dye conjugates in glycerol will have almost completely restricted mobility.

5.1.1.3 Measurement of absorption and emission spectra

Samples were placed in a quartz cuvette and the absorption spectra of mEGF-Alexa 546 and Vybrant C_{18}DiD in the 500-750 nm range were measured using a PerkinElmer Lambda 35 spectrophotometer. The emission spectrum of mEGF-Alexa 546 was measured over the same wavelength range using a Jobin Yvon Fluorolog fluorimeter with a Xenon arc-lamp light source. These spectra were corrected with the absorbance or emission spectra of the appropriate buffer over the same wavelength range.

5.1.1.4 Measurement of the EGF-Alexa546 donor quantum yield

Samples of mEGF conjugated to Alexa 546, prepared as in section 5.2.1, were further diluted in PBS to obtain samples that ranged in maximum absorbance between 0.01 and 0.1. The absorption spectra of these mEGF-Alexa 546 samples were measured over a wavelength range of 500-650 nm with a PerkinElmer Lambda 35 spectrophotometer. The fluorescence emission spectra of the samples over the same wavelength range were also measured when excited at a wavelength of 545 nm using a Jobin-Yvon Fluorolog fluorimeter with a Xenon lamp illumination source.

Reference samples of unconjugated Alexa 546 and tetramethylrhodamine (TMR) were prepared in same manner as the mEGF-Alexa 546 conjugate. Alexa 546 in PBS has a quantum yield Q = 0.79 (Invitrogen) and TMR in PBS has a Q between 0.174 [1] and 0.28 [2]. These dyes were chosen to be references as they can be excited at the same wavelength as mEGF-Alexa 546 and emit fluorescence in the same wavelength range, simplifying comparison of their quantum yields. Accordingly, the absorption and emission spectra (545nm excitation) of these samples were also recorded between 500-650nm, along with the spectra of a blank sample consisting only of PBS.

The appropriate blank spectrum was subtracted from all emission spectra to obtain the corrected emission spectra $F(\lambda)$. The integrated fluorescence intensity

$$I_f = \int_{\lambda=500nm}^{\lambda=750nm} F(\lambda)d\lambda \qquad \text{Eqn. 5-1}$$

was evaluated for each emission spectrum using the integration function of the Origin 7.5 data analysis software. This function uses the trapezoid method of numerical integration.

5.1.2 Förster radius calculations

5.1.2.1 Evaluation of overlap integrals

Figure 5.1 shows the peak-normalised emission spectrum of mEGF-Alexa 546 when excited with 545 nm light. The absorption spectrum of Vybrant C_{18}DiD in lipid vesicles and mEGF-Atto 647N in PBS are also plotted.

The overlap integral for the FRET pairs mEGF-Alexa 546 / Vybrant C_{18}DiD and mEGF-Alexa 546 / mEGF-Atto 647N was calculated from Eqn. 5-2 both by numerically integrating the numerator and denominator using Origin and by using a simple summation[3] between λ_1 and λ_2

$$J(\lambda) = \frac{\int_0^{\infty} F_D(\lambda)\varepsilon_A(\lambda)\lambda^4 d\lambda}{\int_0^{\infty} F_D(\lambda) d\lambda} = \frac{\sum_{\lambda_1}^{\lambda_2} F_D(\lambda)\varepsilon_A(\lambda)\lambda^4}{\sum_{\lambda_1}^{\lambda_2} F_D(\lambda)} \qquad \text{Eqn. 5-2}$$

The results are summarised in table 5.2.

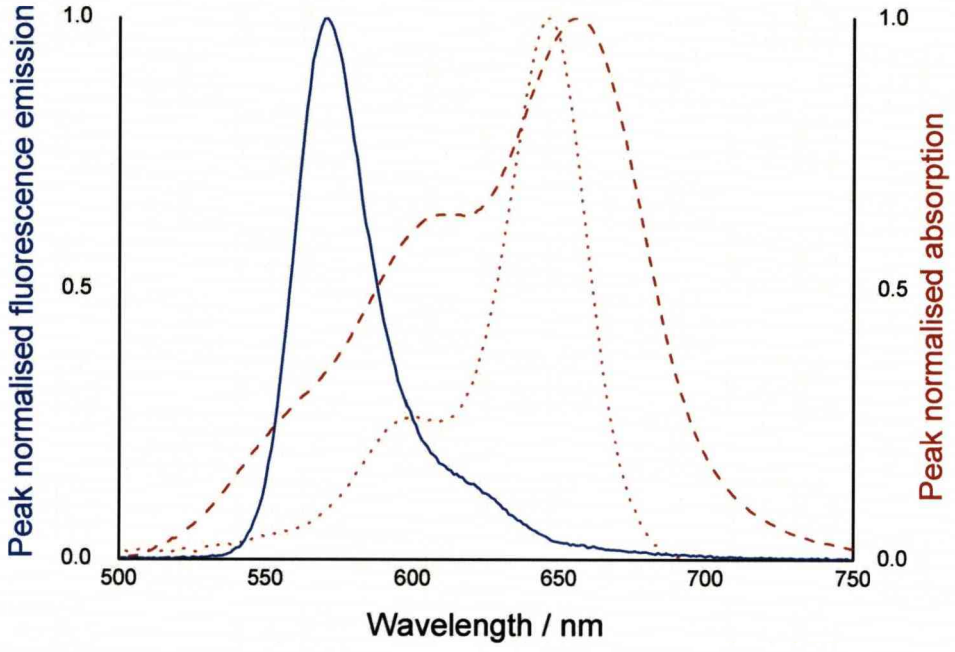

Figure 5.1 The peak normalized fluorescence emission spectrum of mEGF-Alexa546 (solid blue line) plotted with the peak normalized absorption spectra of Vybrant C_{18}DiD (dashed red line) and mEGF-Atto 647N (dotted red line).

FRET pair	$J(\lambda)$ (Origin) / $M^{-1}cm^{-1}nm^4$	$J(\lambda)$ (Simple summation) / $M^{-1}cm^{-1}nm^4$
mEGF-Alexa 546 / Vybrant C_{18}DiD	1.10306×10^{16}	1.10304×10^{16}
mEGF-Alexa 546 / mEGF-Atto 647N	2.44572×10^{15}	2.44569×10^{15}

Table 5.2 Values of the overlap integral evaluated by numerical integration in Origin or the simple summation method.

As can be seen in table 5.2, the results are identical for both methods of evaluating the overlap integral up to five significant figures. It is notable that despite the similarity of the absorption spectra of Vybrant C_{18}DiD and Atto 647N, the values of their overlap integrals differ by an order of magnitude due to the slightly larger shoulder of Vybrant C_{18}DiD absorption between 550 and 650 nm and the smaller absorption coefficient of Atto 647N. The consequence of this will be a smaller Förster radius for the mEGF-Alexa 546 / mEGF-Atto 647N FRET pair.

5.1.2.2 Calculation of the EGF-Alexa546 quantum yield

For each sample the fluorescence emission spectra was measured and the integrated fluorescence intensity calculated. This was repeated three times to account for fluctuations in the excitation intensity and the mean integrated fluorescence intensity was plotted as a function of the absorbance at 545nm for each sample which is shown in figure 5.2. The data from each sample was fit to the form of a straight line passing through the origin using the linear regression function in Origin. The standard deviations of the mean integrated intensities were used to weight each data point when minimising a sum of the squares of the residuals to find the most likely parameters. The best fit parameters are summarised in table 5.3.

The gradients of these fits were used first to check that the values of the reference quantum yields were consistent with each other before calculation of the quantum yield of mEGF-Alexa 546. Taking Alexa 546 as the reference first ($Q = 0.79$, Invitrogen) yields $Q = 0.23$ for TMR. This is the average of the published values quoted in section 5.1.1.4 and consequently the two reference samples were deemed consistent with each other. The value obtained for the quantum yield of mEGF-Alexa 546 using either the Alexa 546 quantum yield or the average TMR quantum yield was 0.71.

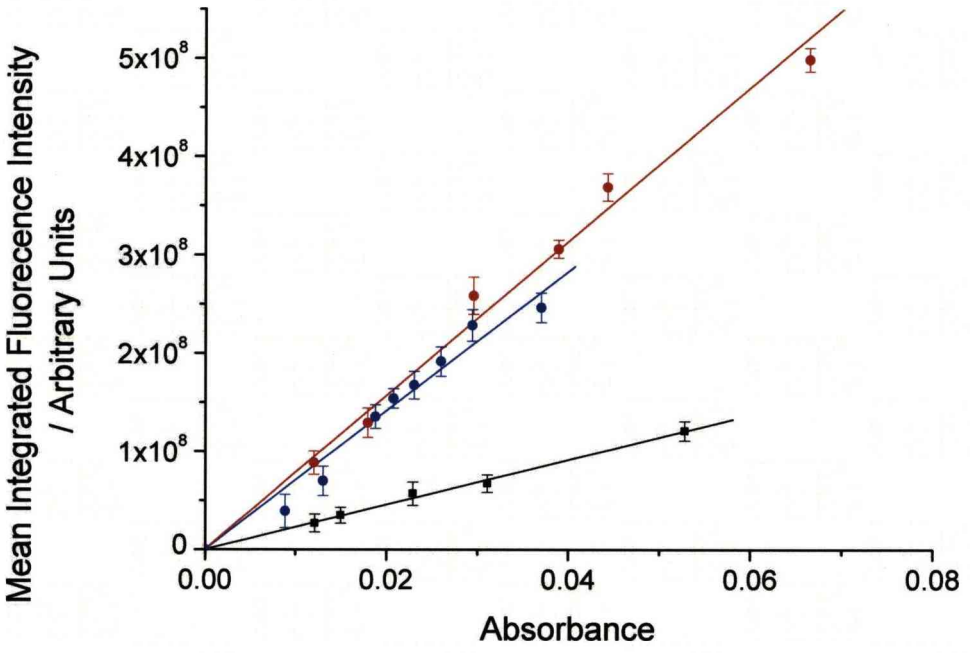

Figure 5.2 Mean integrated fluorescence intensity plotted as a function of Absorbance for TMR in PBS (black squares), mEGF-Alexa546 in PBS (blue circles) and Alexa546 in PBS (red circles). Error bars represent the standard deviation of three measurements of the integrated fluorescence intensity made on each sample.

Sample	B	Error	N	R^2
Alexa 546 in PBS	7.834×10^9	1.824×10^8	7	0.990
mEGF-Alexa 546 in PBS	7.069×10^9	2.266×10^8	9	0.972
TMR in PBS	2.285×10^9	3.964×10^7	6	0.996

Table 5.3 Best fit parameters for the data in figure 5.2. fitted to a straight line of the form Y=BX, where B is the gradient of the line. N is the number of data points fitted. R^2 is the square of the correlation coefficient of the fit and represents the proportion of variation in Y that is accounted for by the determined line of best fit.

5.1.3 Orientation factor: Measurement of steady state fluorescence anisotropies

In order to gauge the accuracy of calculating R_0 values for the FRET pairs using the dynamic averaging limit of the orientation factor, the steady state fluorescence anisotropies of mEGF-Alex 546, mEGF-Atto 647N, EGF-fluorescein (Invitrogen) and Vybrant C_{18}DiD (in lipid vesicles) samples were determined using an L-format Jobin-Yvon Fluorolog fluorimeter with a Xenon lamp as an light source. mEGF-fluorescein is used in section 5.2 and its steady state anisotropy is also measured in this section in order to check the validity of using the Förster radius of the fluorescein / C_{18}DiI FRET pair calculated in the literature[4] to interpret FRET experiments using an EGF-fluorescein conjugate. Each sample was illuminated with vertically polarised light and the integrated fluorescence intensities (integrated over 1s) from vertical and horizontal emission polarisations were measured. EGF-Alexa 546 was excited at 545nm and fluorescence detected at the peak of fluorescence emission, 572 nm. Vybrant C_{18}DiD and Alexa 647N were excited at 639nm and their fluorescence detected at 667 nm. The geometry of the L-format method is shown in figure 5.2.

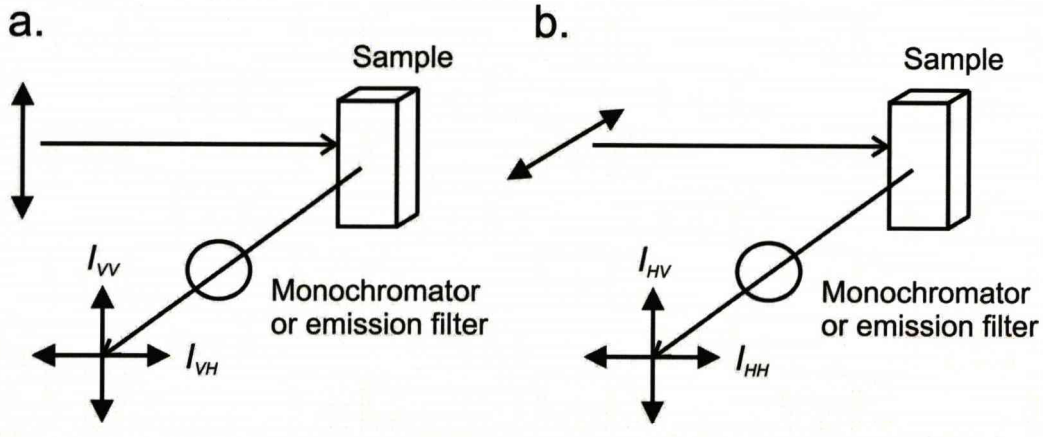

Figure 5.3 Geometry of the L-format fluorescence anisotropy measurement with a. vertically polarized excitation and b. horizontally polarized excitation.

The anisotropy can be calculated using the formula[5]

$$r = \frac{I_{VV}}{I_{VH}} \frac{1}{G} \qquad \text{Eqn. 5-3}$$

where I_{xy} is the measured intensity with excitation polarization X and emission polarization Y. V and H represent vertical and horizontal polarizations respectively. The G-factor (the ratio of the responses of the fluorimeter for vertically and horizontally polarised light) for each combination of excitation and emission wavelengths was determined by measuring the response of the fluorimeter to a weak scattering solution (Ludox in deionised H_20) when illuminated with horizontally polarised light. In the L-format method, horizontally polarised excitation is perpendicular to both detected polarisation orientations. Therefore variations the intensities I_{HV} and I_{HH} are due to the response of the fluorimeter only and the G- factor was calculated using

$$G = \frac{I_{HV}}{I_{HH}} \qquad \text{Eqn. 5-4}$$

Once the G-factors had been determined, Eqn. 5-3 was used to calculate the fluorescence anisotropies of the samples. Measurements of dye conjugates in glycerol were also performed in order to determine their limiting anisotropies.

The steady state anisotropies of mEGF-Alexa 546, mEGF-Atto 647N, mEGF-fluorescein and Vybrant C_{18}DiD in lipid vesicles are shown in table 5.4 for samples prepared in PBS and glycerol. From these results their depolarisation factors, D, are calculated using the identity

$$r = r_0 D \qquad \text{Eqn. 5-5}$$

These depolarisation factors can be used to lookup the likely minimum and maximum values of κ^2 even though the depolarisation factor due to energy

transfer is not known[6, 7]. Additionally for FRET pairs where both fluorophores exhibit anisotropies < 0.22, the error introduced into donor-acceptor separations determined using a Förster radius calculated using a value of $\kappa^2 = 2/3$ is <10%[8].

The minimum and maximum values of κ^2 for both FRET pairs were found by comparing the depolarization factors in table 5.4 to those expected from numerical simulations reported in the literature[7] of ensembles of FRET pairs with different relative orientations and values of κ^2. The minimum and maximum values of κ^2 for mEGF-Alexa 546 / Vybrant C_{18}DiD FRET pair are 0.35 and 1.8 respectively. The minimum and maximum values for the mEGF-Alexa 546 / mEGF-Atto 647N FRET pair are 0.3 and 2. As the steady-state anisotropy of mmEGF-fluorescein was found to be very small (and hence the fluorescein molecule retains a large amount of rotational mobility), using the Förster radius of unconjugated fluorescein and C_{18}DiI found in the literature to interpret FRET experiments between the EGF-fluorescein conjugate and DiI should not introduce considerable extra errors.

Probe	**Buffer**	**Steady State Anisotropy**	**Depolarisation Factor**
mEGF-Alexa 546	PBS	0.194	0.537
	Glycerol	0.361	
mEGF-Atto 647N	PBS	0.203	0.567
	Glycerol	0.358	
mEGF-fluorescein	PBS	0.077	0.246
	Glycerol	0.313	
Vybrant C_{18}DiD	lipid vesicles (PBS)	0.154	0.428

Table 5.4 Steady state anisotropies of EGF-dye conjugates and Vybrant C_{18}DiD in a lipid environment.

5.1.4 Calculated Förster radii of the different FRET pairs

The Förster radius for FRET between mEGF-Alexa 546 and Vybrant C_{18}DiD was calculated using a value of 1.1×10^{16} $M^{-1}cm^{-1}nm^4$ for the overlap integral $J(\lambda)$, $Q_D = 0.71$ and assuming the dynamic averaging value of the orientation factor $\kappa^2 = 2/3$. The Förster radius for mEGF-Alexa 546 and mEGF-Atto 647 was calculated to be 5.5 nm using $J(\lambda) = 2.4 \times 10^{15}$ $M^{-1}cm^{-1}nm^4$.

The values of R_0 were also calculated using the values for minimum and maximum values of κ^2 given in the previous section. The resulting minimum and maximum values of R_0 were 6.4nm and 8.4nm for the mEGF-Alexa 546 / Vybrant C_{18}DiD FRET pair and 4.9nm and 6.7nm for the mEGF-Alexa 546 / mEGF-Atto 647N FRET pair. From these values, the error resulting from using $\kappa^2 = 2/3$ is between 10 - 20%.

5.1.5 Estimation of the range of distances that can be measured with the FRET pairs

The variation of the FRET efficiency (within a single FRET pair) with donor-acceptor separation for the R_0 values calculated in section 5.1.4 plus the fluorescein / C_{18}DiI FRET pair are displayed in figure 5.4.

Due to the dependence of FRET efficiency on the inverse sixth power of the donor-acceptor separation, changes in separation produce large changes in FRET efficiency in a limited range around the Förster radius. This range for mEGF-Alexa 546 and Vybrant C_{18}DiD is approximately between 4.5 and 10.0 nm. For mEGF-Alexa 546 and mEGF-Atto 647N this range is approximately between 3.5 and 8.0 nm. For fluorescein and C_{18}DiI this range is approximately between 2.0 and 5.5 nm.

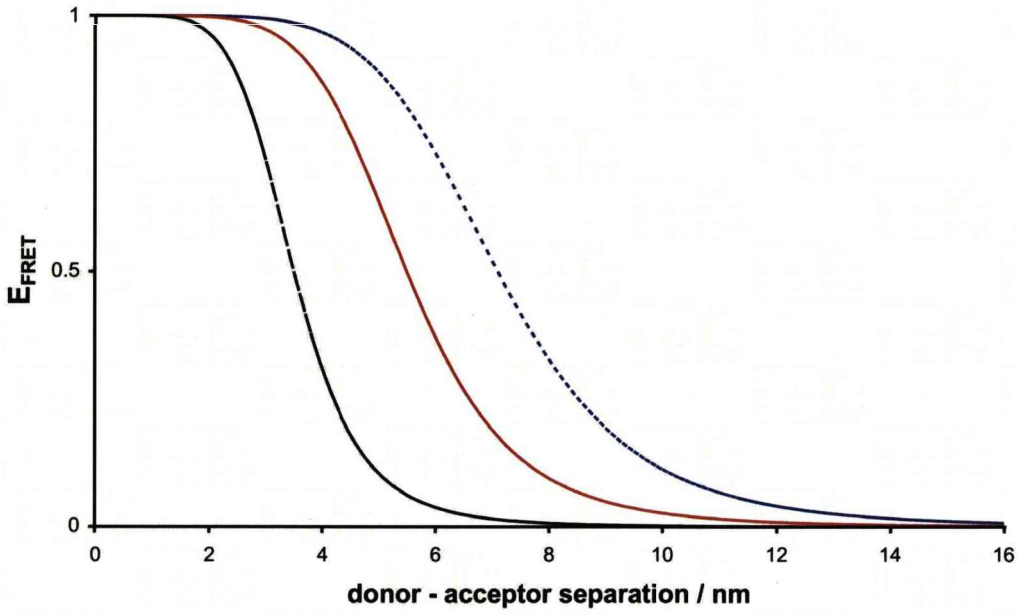

Figure 5.4 FRET efficiency (E_{FRET}) as a function of donor-acceptor separation for FRET pairs with experimentally determined Forster radii of 5.5 nm (red solid line) and 7.0 nm (blue dotted line). The FRET efficiency as a function of separation of a fluorescein and C_{18}DiI pair (black dashed line, R_0 =3.5 nm)[4] is also shown.

The current picture of the three dimensional organization of ErbB1 receptor extracellular domains on the surface of cells is heavily influenced by x-ray diffraction studies of crystallised ErbB1 fragments[9-12]. These studies suggest that the receptor exists as a tethered monomer, extended monomer or a dimer of extended monomers mediated by receptor-receptor contacts but stabilized by the binding of a ligand such as EGF. EGF is able to bind to all three conformations which are assumed to adopt an upright orientation with respect to the membrane.

Although the separation of ligands bound to ErbB1 in a back-to-back dimer can be unambiguously determined from the crystal structures, the separation of ligands and the cell surface cannot. The positions of the ligand binding sites with respect to the membrane in a tethered ErbB1 monomer, an extended ErbB1 monomer and a back-to-back ErbB1 dimer have been estimated using atomistic molecular dynamics simulations of ErbB1 extracellular domains with their transmembrane α-helices in a phospholipid bilayer by Johannes Kästner and

Martyn Winn of Collaborative Computational Project 4 (CCP4, currently unpublished). As the full ErbB1 extracellular region together with the transmembrane region has not yet been crystallised, the 1IVO crystal structure[11] of an ErbB1 back-to-back dimer was used as a starting point and the missing domain IV regions included based upon the co-ordinates from the 1NQL tethered monomer crystal structure[10]. Transmembrane helices previously modelled for an ErbB2 homodimer[13] but mutated to the ErbB1 sequence were added to the two domain IV C-termini to anchor the extracellular regions to an atomistically modelled phosphatidylcholine bilayer. The structure was simulated for 70 ns and from this the separation between the EGF N-termini and the surface of the outer leaflet of the bilayer was estimated to be 8 nm. The strcuture of the extended ErbB1 monomer was assumed to be the same as a single ErbB1 from this dimeric structure. Similar simulations of the 1NQL tethered monomer crystal structure with the transmembrane helix estimated the EGF N-terminus to be 7 nm from the surface of the phospholipid bilayer. Figure 5.5 is a cartoon representation of the three structures in the membrane and displays the estimated distances of the EGF binding sites to the membrane and the separation of EGF binding sites.

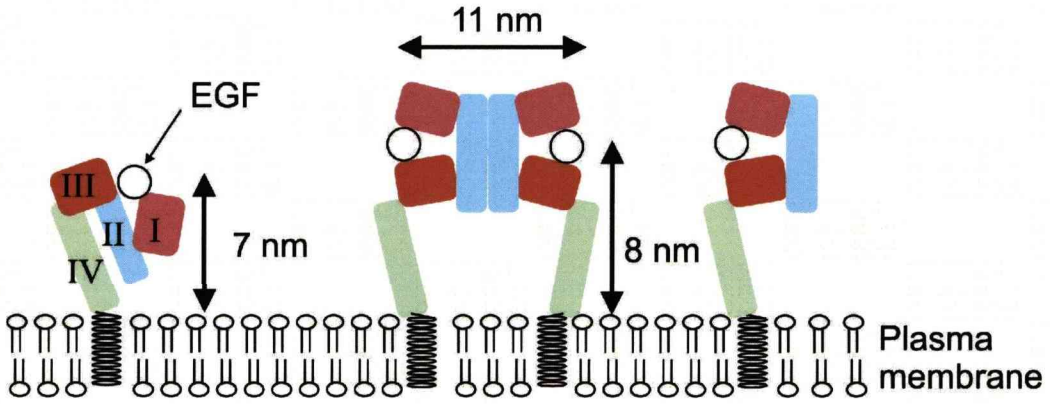

Figure 5.5 Conformations of the ErbB1 extracellular region in the membrane derived from published crystal structures and molecular dynamics simulations (by Kästner and Wynn, CCP4, unpublished). The extracellular region consists of four distinct domains. EGF binds to both domains I and III to stabilize the receptor in an extended conformation that can form a dimer through interactions of domain II of the receptor.

Measurements made with suspended, isolated A431 cell membranes suggest that the mean separation between ErbB1 EGF binding sites and the surface of isolated A431 cell membranes is between 5.2 and 8.2 nm [14]. This falls within the range of distances for which the mEGF-Alexa 546 / Vybrant C_{18}DiD FRET pair are suitable, suggesting that this would be a suitable FRET pair to investigate the distance between ErbB1 ligand binding sites and the surface of cells.

However, it is already known that this model doesn't represent all the possible conformations the receptor can adopt at the plasma membrane. The separation predicted by the crystal structures between EGF binding sites in an ErbB1 dimer are ~ 11 nm. However, numerous ensemble[15-18] and single molecule FRET measurements[19] with other EGF conjugated FRET pairs have shown significant FRET efficiencies between donor and acceptor labelled EGF. These results are inconsistent with the crystallographic dimer being the only ErbB1 interaction present in cells. mEGF-Alexa 546 and mEGF-Atto 647N has a Förster radius equal or larger than those previously employed and is therefore suitable for investigating of EGF-EGF distances. It is possible that in intact adherent cells other receptor conformations might exist for which the mEGF-Alexa 546 and Vybrant C_{18}DiD FRET pair is unsuitable. The next section describes a preliminary experiment performed to ascertain if this is indeed the case.

5.2 Probing for unexpected ErbB1 ectodomain conformations using FLIM-FRET of EGF-fluorescein in C_{18}DiI labeled cells

This section describes a FRET experiment performed to investigate if there are activated ErbB1 ectodomain conformations present in adherent cells that produce separations between the EGF-binding site and the cell surface different to those predicted by the current model of ErbB1 signalling (shown in figure 5.5 in the previous section). This was done using the EGF-fluorescein / C_{18}DiI FRET pair which has a short Förster radius (3.5 nm)[4] to investigate the EGF-membrane

distance in the high-affinity and low-affinity classes of ErbB1 receptors in adherent cells. The labelling strategy is shown in figure 5.6. To attempt to observe receptors in inactive as well as active conformation, light fixation was employed before or after binding of the EGF-fluorescein conjugate.

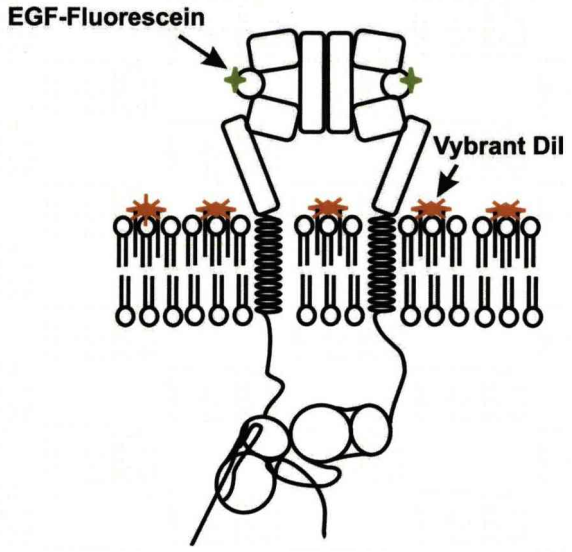

Figure 5.6 Labelling strategy for control FLIM-FRET based observations of EGF-membrane FRET. The mEGF-fluorescein FRET donor is bound specifically to the extracellular region of ErbB1. The acceptor, Vybrant C_{18}DiI is free to diffuse in the outer leaflet of the cell membrane.

5.2.1 Materials and Methods

5.2.1.1 Cell culture

A431 cells were obtained from the European collection of Animal Cell Cultures and cultured in Dulbecco's modified Eagles medium without phenol red and supplemented with 10% fetal bovine serum, 2mM glutamine and 1% penicillin/streptomycin. Cells were incubated at 37°C in the presence of 5% CO_2 in air. $1x10^5$ A431 cells were added to glass bottomed dishes and incubated until they reached 80% confluency. Cell cultures were maintained as described in section 4.3.1.1.

5.2.1.2 Blocking of low-affinity EGF binding to cell surface ErbB1 receptors

Before labelling with fluorescent probes, half of the samples of A431 cells were treated with 200 nM anti-ErbB1 clone 2E9 (mAb 2E9) and incubated with gentle rocking at 4°C for 4 hours. This antibody binds to low-affinity (LA) ErbB1s and prevents EGF binding to this class of ErbB1 receptor[20].

5.2.1.3 Fluorescent labelling of cell membranes with lipophilic dye

The culture medium was removed from glass bottomed dishes containing A431 cells to be labelled with membrane probe and replaced with 100 µl of 5 µM Vybrant C_{18}DiI in serum free media. Cells were incubated at 37°C in the presence of 5% CO_2 in air for 10 minutes before washing off excess Vybrant C_{18}DiI with PBS. The C_{18}DiI was observed to be uniformly distributed across cell plasma membranes.

5.2.1.4 Binding of EGF-Fluorescein to cell surface ErbB1 receptors and cell fixation

Cells were lightly fixed with exposure to 1% paraformaldehyde (Electron Microscopy Sciences) for 10 minutes at room temperature either before or after binding of fluorescein tagged EGF. This causes sufficient cross-linking within a complex containing ErbB1 to inhibit further conformational changes of the receptor and lateral diffusion in the plasma-membrane[19, 21]. Murine epidermal growth factor (mEGF) singly labelled at the N-terminus with fluorescein (Invitrogen) was added at a saturating concentration (100 nM in phosphate buffered saline) to A431 cells at 4°C to inhibit ligand-induced internalisation of

ErbB1 receptors. After 30 minutes, the cells were washed three times with chilled PBS to remove unbound mEGF-fluorescein.

5.2.1.5 FLIM measurement of FRET between EGF-Fluorescein and C_{18}DiI

Fluorescence lifetime images of EGF-fluorescein (the FRET donor) bound to ErbB1 in cell membranes of A431 cells with or without Vybrant C_{18}DiI (the FRET acceptor) were acquired using the multicolour, multidimensional confocal microscope described in chapter 4. mEGF-fluorescein was excited with 460 nm pulsed laser light using a frequency doubled Titanium:Sapphire laser (Coherent, 76 MHz repetition rate) and fluorescein fluorescence was detected between 480 and 520 nm. Time-resolved images were collected with SPC-730 time correlated photon counting (TCSPC) electronics and analysed using SPCImage FLIM analysis software (both Becker-Hickl GmbH).

5.2.2 Results and Discussion

Time-resolved images of A431 cells were fitted to mono-exponential (for cells labelled with mEGF-fluorescein only) or bi-exponential (cells labelled with both EGF-fluorescein and Vybrant C_{18}DiI) decay models. To the right of Figure 5.7a and 5.7b are representative examples of analysed lifetime images of donor and acceptor labelled cells. Figure 5.7a shows cells in which the LA receptors have been blocked with mAb 2E9 and figure 5.7b shows cells in which all cell surface ErbB1s are able to bind to mEGF-fluorescein. The colour coded parameter displayed in the images is the intensity weighted mean lifetime τ_m.

The distributions of τ_m shown to the left of figure 5.7a are from images of cells where mEGF-fluorescein binding to LA ErbB1s was blocked with mAb 2E9 and labelled with Vybrant C_{18}DiI acceptor (solid lines) or without acceptor (dotted

lines). Each distribution represents a different imaged field of view. Samples labelled with donor and acceptor produce distributions that peak at much shorter lifetimes than those labelled with just the donor. As expected, this change in τ_m cannot be due to acidification effects in the local environment of the cell membrane (figure 5.8) and was found for cells fixed before (red) and after (blue) binding mEGF-fluorescein. The corresponding distributions from images of cells not exposed to mAb 2E9 contains contributions from both LA and HA (< 10 %) receptors but unlike the previous data do not show a large and consistent reduction in peak τ_m (figure 5.7b). This suggests that there is FRET between mEGF-fluorescein and Vybrant C_{18}DiI when the mEGF-fluorescein is bound to HA ErbB1 but not LA ErbB1. The mean FRET efficiency calculated from the observed reductions in EGF-fluorescein τ_m when bound to HA ErbB1 was 0.5. The FRET efficiency calculated when EGF-donor is bound to the whole receptor population was negligible. The absence of FRET in the LA case is unlikely to be due to preferential partitioning of Vybrant C_{18}DiI in the membrane as ErbB1 has been observed in all domains of the membrane including lipid rafts[22].

It therefore appears possible that the positions of EGF binding sites with respect to the cell surface are very different for the two different affinity classes of receptor. If all ErbB1 receptors adopt the same extended crystallographic configuration upon binding EGF, this implies that HA and LA ErbB1 receptor ectodomains would need to adopt different orientations with respect to the cell surface. As there is no change in FRET efficiency between cells fixed before and after binding mEGF-fluorescein, these different orientations would appear to be constitutively adopted by the receptors. However, there are some important caveats to the interpretation of these FLIM-FRET results. First, the absence of FRET observed within the combined LA and HA receptor population may be hiding differences between active and inactive conformations that are out of the range of the FRET pair used. Although it appears that the distances involved in this case are too long for FRET within the mEGF-fluorescein / C_{18}DiI pair, the mEGF-Alexa546 / Vybrant C_{18}DiD FRET pair has a longer R_0 value that should be suitable for measuring these longer distances.

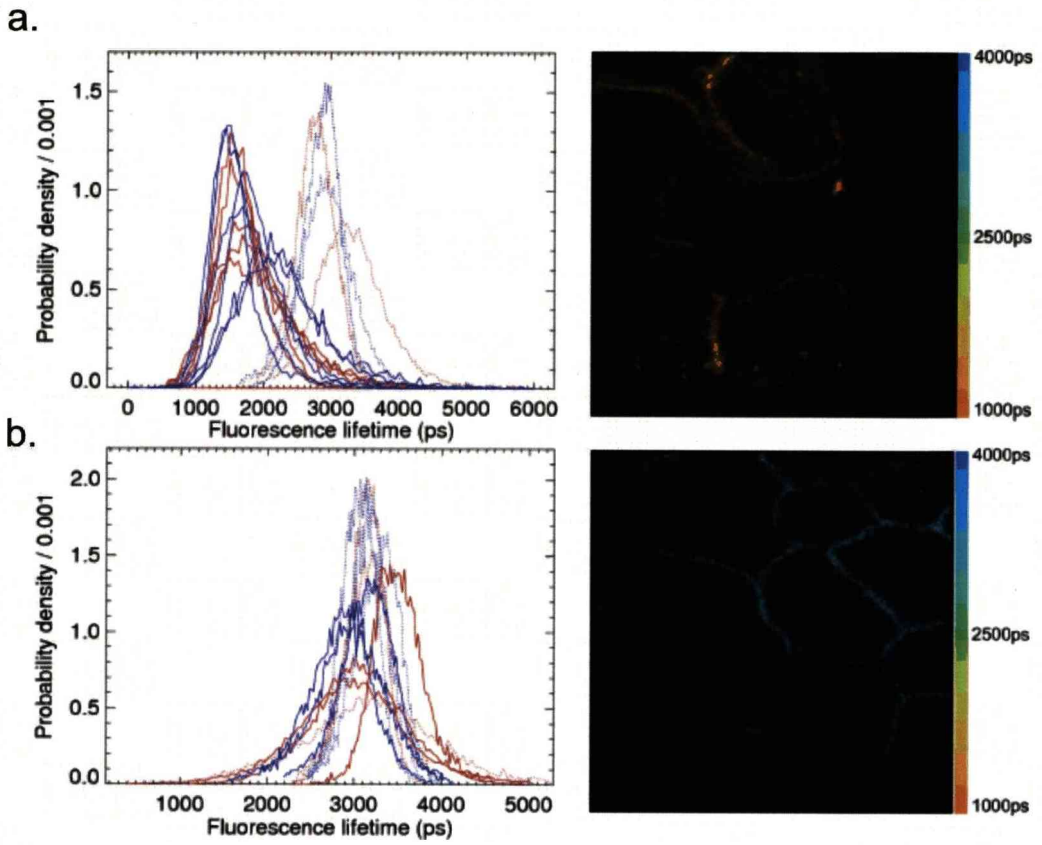

Figure 5.7 a. Distributions of τ_m for mEGF-fluorescein bound to ErbB1s in A431 cells where LA binding is blocked by mAb 2E9 and whose plasma-membranes were labelled with Vybrant C_{18}DiI and fixed before (solid red lines) or after (solid blue lines) binding mEGF-fluorescein. Control FLIM data from mEGF-fluorescein bound to HA ErbB1s in the absence of Vybrant C_{18}DiI are shown as dotted lines. Each curve represents a different field of view, an example of which is shown to the right. Curves are normalized as photon-weighted fluorescence lifetime distributions. **b.** The equivalent distributions and example image obtained when mEGF-fluorescein is allowed to bind to all cell surface ErbB1s.

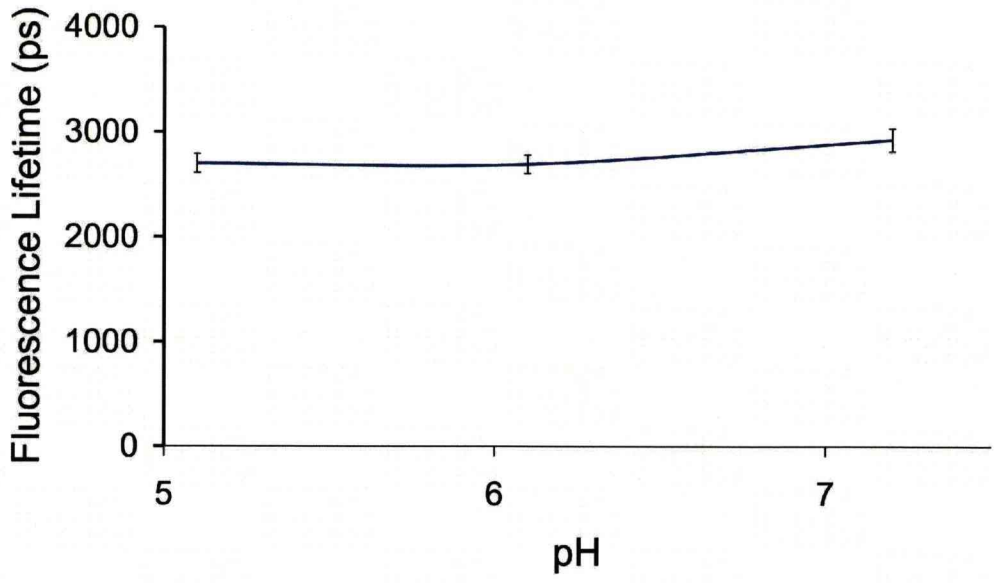

Figure 5.8 pH dependence of mEGF-fluorescein fluorescent lifetime between pH 5 and pH 7.5.

Second, the exact stoichiometry of this FRET experiment is unknown. Although the EGF binding sites of the ErbB1 receptors are specifically labelled in a 1:1 ratio with EGF-fluorescein, the Vybrant C_{18}DiI acceptor is free to diffuse in the cell membrane and individual donors may have multiple FRET partners or none at all. The FLIM-FRET results in this chapter cannot distinguish between a change in separation and a change in acceptor availability for FRET. In order to fully quantify the distance between the EGF-binding sites and the acceptor labelled membrane would require repetition of the experiment over a range of acceptor surface densities[14, 23]. The theory behind this is discussed in the next section of this chapter.

5.3 Extended FRET theory for measurements between multiple donors and acceptors

Förster's theory for resonant energy transfer within a single donor-acceptor pair was discussed in chapter 2.4. The rate of energy transfer from the donor to the

acceptor in this simple case depends upon the spectral properties of the donor and acceptor, their spatial separation and the relative orientations of the relevant transition dipole moments. Situations where there are multiple donors and acceptors must also take into account their stoichiometry. In the case of a donor situated a fixed distance 1 R_0 from two identical acceptors (all free to rotate in their fixed positions such that the dynamic averaging limit can be applied to κ^2, Figure 5.9a) the rate at which energy is transferred to each acceptor and the rate at which excited state energy is lost by fluorescence are equal.

The efficiency of FRET that would be measured in this case would be 0.67, larger than the value of 0.5 expected from a single donor and acceptor with the same separation (Figure 5.9b). Without considering the stoichiometry of the systems, the FRET efficiencies would lead to the erroneous conclusion that the donor-acceptor separations in each case are different. Likewise, if donors are in competition to transfer energy to the same acceptor the efficiency of FRET measured will be lower than that expected for a single FRET pair (Figure 5.9c).

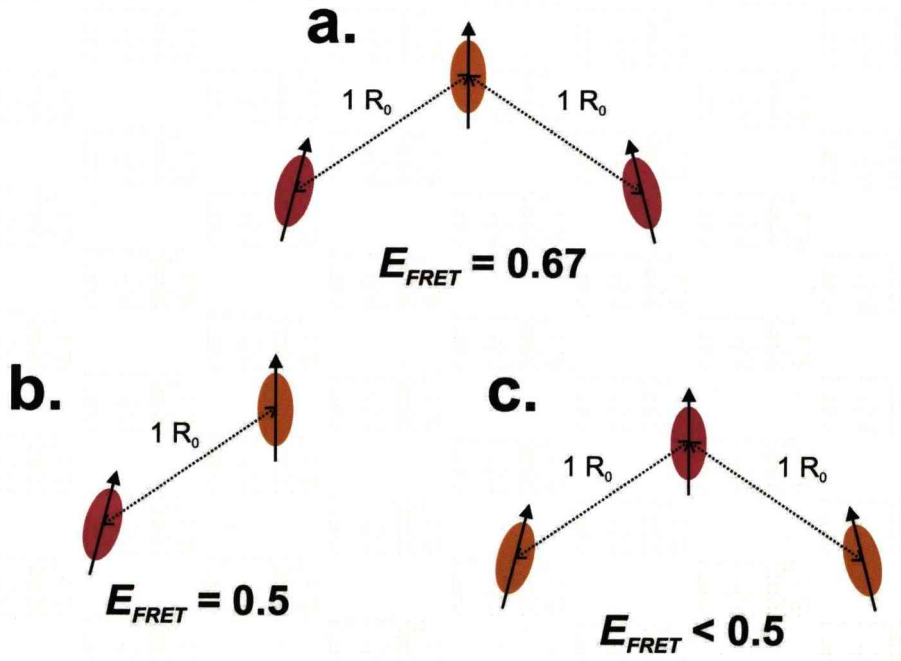

Figure 5.9 The FRET efficiency (E_{FRET}) measured between multiple donors (orange) and acceptors (red) is dependent upon fluorophore stoichiometry.

5.3.1 FRET between donor labeled membrane proteins and membrane localised acceptor

There has been considerable interest over the last 40 years in finding solutions to the problem of FRET between many donors and acceptors distributed in a plane, or distributed within two spatially separated planes[23-27]. This is because of the potential of measuring FRET between donors and acceptors in membrane systems where donors and acceptors are unlinked and their stoichiometry and separation can be dynamic. FRET experiments have been used to probe the domain structure of model and cell membranes, aggregation of proteins in cell membranes and find the distance of closest approach of membrane protein domains to the cell membrane[14, 24, 27, 28]. Figure 5.10 illustrates the added complexity in experiments of this kind with an example of a possible FRET experiment aiming to provide spatial information regarding the position of a protein domain with respect to the cell membrane. The donor is specifically tagged to a position on the protein and the acceptor is localised to the outer leaflet of the membrane where it is free to diffuse laterally. As the donor-acceptor separations and stoichiometry are dynamic, the measured FRET efficiency is dependent upon both the separation of the donor and the surface of the cell membrane and the density of acceptors around the donor labelled protein. In order to determine the distance of closest approach of donors to the membrane in this experiment, the FRET efficiency must be measured over a range of acceptor densities and compared to the results expected for a range of donor-membrane separations. Due to the complexity of the problem, it is necessary to calculate the expected FRET efficiency for a given distance of closest approach and acceptor density from numerical approximations or computer intensive simulations.

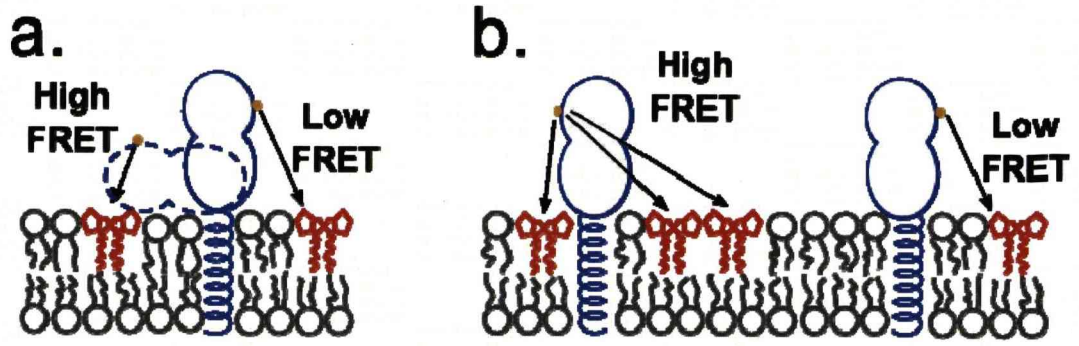

Figure 5.10 Cartoon representation of a FRET acceptor (red) labelled membrane containing a membrane protein specifically labeled at a single domain with a donor fluorophore (orange). A high FRET efficiency can be caused either by **a.** changes in protein conformations that places the donor closer to the acceptor labeled membrane or **b.** increased density of acceptors around the donor labeled protein.

5.3.2 Analytical solutions for FRET between multiple donors and acceptors in 2-dimensions

Before it was possible to produce computer intensive simulations or complicated numerical solutions using desktop computers, analytical solutions were sought for the problem of Forster energy transfer in two dimensions. These calculations are complex and involve assumptions that restrict their validity to specific Forster radii, ranges of acceptor density or donor-acceptor plane separations.

One of the most popular analytical solutions has proved to be that derived by Wolber and Hudson for the case when the orientation factor is independent of donor-acceptor separation[23]. Its appeal to experimental scientists, particularly biologists derives from two points. First, the solutions for given distances of closest approach of donors and acceptors can be accurately approximated by a bi-exponential equation allowing quick and easy graphical comparison with experimental data

$$E_{FRET} = 1 - \left(A_1 e^{-k_1 D} + A_2 e^{-k_2 D} \right) \qquad \text{Eqn. 5-6}$$

where D is the two-dimensional density of acceptors and the values of the fitted parameters A_1, A_2, k_1 and k_2 can be found for a given distance of closest approach (expressed as a fraction of the Förster radius) in a look-up table[23]. Figure 5.11 shows some of these approximations graphically.

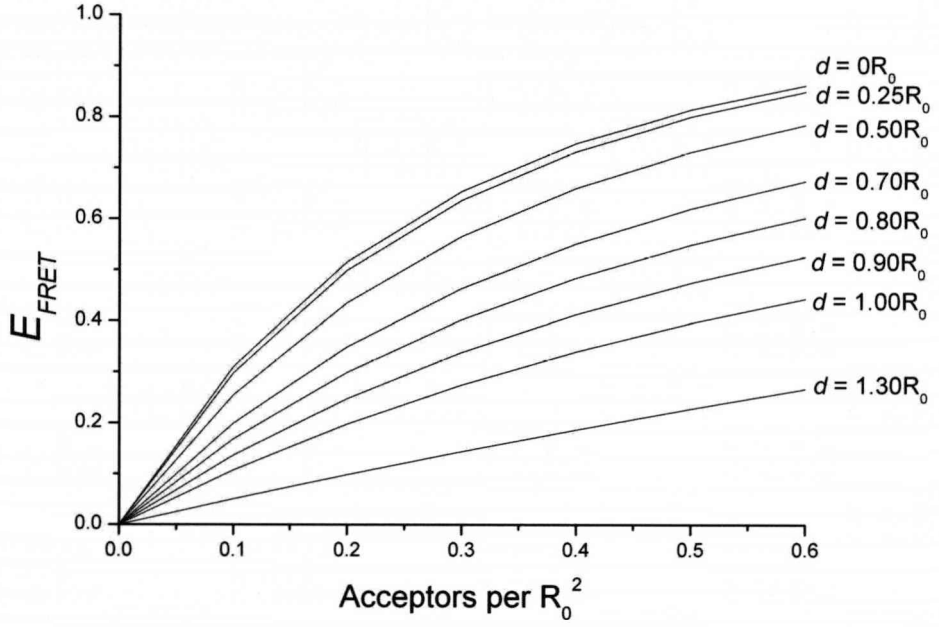

Figure 5.11 FRET efficiency (E_{FRET})as a function of acceptor density for a plane of randomly distributed donors and a plane of randomly distributed acceptors separated by a distance d. FRET efficiencies for plane separations ranging from $1.3R_0$ to the case when the plane separations are negligible compared to R_0 were plotted using the table of look-up values for the Wolber et al. analytical solution to this problem

Secondly, the value of R_0 doesn't appear in the expression for FRET efficiency, but is part of a scaling factor for the acceptor surface density. The same solutions can therefore be applied to any donor-acceptor pair if acceptor density is in units of acceptors per R_0^2.

However, the approximation given by Eqn. 5-6 is only accurate for acceptor densities between 0 - 0.5 acceptors per R_0^2, for donor-acceptor distances of closest approach less than $1.3R_0$ and apply only to randomly distributed donors and acceptors in the same, or two separate planes. To obtain solutions for complicated situations, such as when distribution of fluorophores is non-random

due to conjugation to proteins, exclusion regions resulting from membrane proteins or partitioning in lipid domains as is commonly encountered experimentally in cell membranes it is now more common to turn to computational simulations.

5.3.3 Computer intensive simulation of FRET between multiple donors and acceptors

Monte-Carlo simulations are being used increasingly often to calculate FRET between donors and acceptors in many different situations including random 2D and 3D distributions of donors and acceptors[29], a single donor bound to a protein in a plane of acceptors[30] and FRET between fluorophores on actin filaments[31]. A variety of methods for obtaining FRET efficiency from the simulations have been implemented such as calculating the quantum yield decrease of the donor or by using the mean of randomly generated decay rates. More recently, algorithms for calculating FRET efficiency from explicitly simulated fluorescence and FRET events have been used[24, 27].

This simpler approach models the incoming excitation radiation as discrete 'excitons' as well as a distribution of fluorophores, allowing effects such as photobleaching, competition between donors for acceptors and experimental conditions such as the light source to be easily incorporated into the model. Figure 5.12 is flowchart for this kind of Monte-Carlo algorithm as implemented by Berney and Denuser[27], and Corry[24].

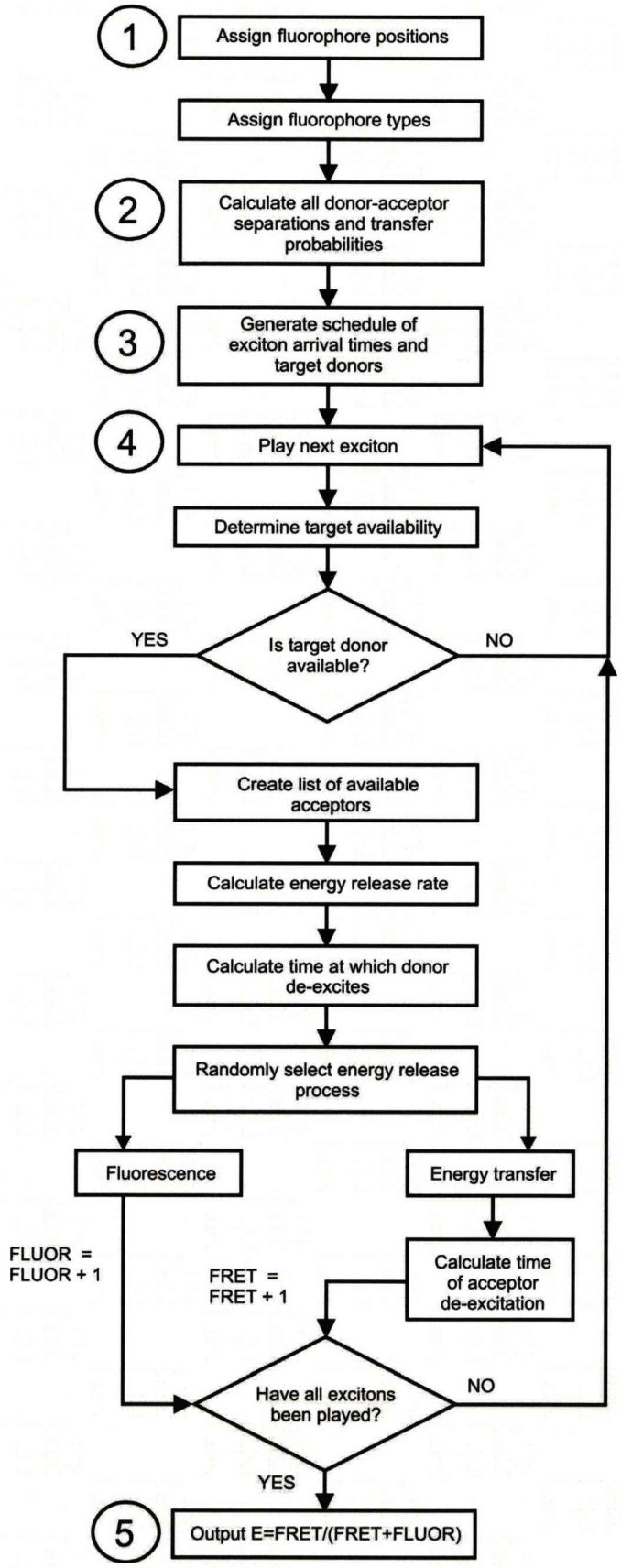

Figure 5.12 Flowchart for a basic Monte-Carlo algorithm that simulates FRET between a distribution of donors and acceptors.

The basic steps of the simulation process are

1) Generate fluorophore positions for donors and acceptors
2) Calculate probabilities of energy transfer
3) Generate a schedule of excitons
4) Play excitons and record the number of time a donor fluoresces or transfers energy to an acceptor
5) Calculate FRET efficiency

Repeat steps 1-5 for many configurations

In step one fluorophore positions are pseudo-randomly generated depending upon the situation being modelled. For example donors might be generated in pairs to simulate tagged protein dimers and surrounded by randomly distributed acceptors. Alternatively fluorophore positions might be generated and randomly assigned to be donors or acceptors to simulate competitive binding of fluorescent probes to the same site of a protein. Each randomly generated fluorophore position must be checked to ensure that it does not overlap with another and any overlaps are adjusted by annealing the position of one of the overlapping fluorophores. A buffer region around the simulated area must be included to ensure that donor positions around the edge of the simulation have as many neighbouring fluorophore positions as those well inside the area and prevent underestimation of the overall FRET efficiency.

Once the fluorophore positions are assigned, the separations of each possible donor-acceptor pair R_{ij} are calculated. The probability of transferring energy from each donor i to every acceptor j, P_{ij}, can be calculated from these distances

$$P_{ij} = \left(\frac{R_0}{R_{ij}} \right)^6 \qquad \text{Eqn. 5-7}$$

Specifying the value of R_0 here simplifies the model as the fluorophore transition dipole orientations need not be considered and the orientation factor, κ^2, need not

then be calculated for every possible FRET pair. Instead it can be dealt with during the determination of the Förster radius.

In step three an exciton schedule is generated based on the properties of the illuminating laser and the size of the irradiated area. The flux of excitons and the time interval for irradiation gives the total number of excitons. Each exciton is then given a random arrival time within the time interval, and randomly assigned a target donor.

The excitons are then played in chronological order to see whether they are absorbed by their target donors and if they are whether that donor fluoresces or transfers energy to an available acceptor. If the target donor is unavailable because it is already excited, then that exciton is discarded. The time taken for an excited donor to release its energy is decided using the formula

$$T_D = \tau_T \ln \gamma_D \qquad \text{Eqn. 5-8}$$

where y_D is a uniformly distributed random number between 0-1 and τ_T is the de-excitation rate of the donor due to radiative and non-radiative transfer

$$\tau_T^{-1} = \tau_D^{-1}\left(1 + \sum_{j=1}^{A_{free}} P_{ij}\right) \qquad \text{Eqn. 5-9}$$

where τ_D is the experimentally measured donor lifetime in the absence of acceptors and A_{free} is the total number of acceptors available for energy transfer. Once a release time has been decided the simulation must decide the method of de-excitation. The probabilities of de-excitation by fluorescence emission or resonant energy transfer to an acceptor are given by

$$\frac{\tau_T}{\tau_D}, \; and \; \frac{\tau_T}{\tau_D} P_{ij} \qquad \text{Eqn. 5-10}$$

respectively. A cumulative histogram of each possible de-excitation event is produced and a uniform randomly generated number between 0 and 1 used to pick which release class will be used and which acceptor will be involved in energy transfer if necessary. A score is then simply kept that counts how many excited donors fluoresce (retained in a variable, *FLUOR*) and how many transfer energy to an acceptor (retained in a variable, *FRET*). Acceptor unavailability from previous excitation can be included in the exact same way as donor availability for subsequent excitons. The time the acceptor remains in the excited state is decided using

$$T_A = \tau_A \ln y_A \qquad \text{Eqn. 5-11}$$

where τ_A is the experimentally measured acceptor fluorescence lifetime and y_A is a uniform random number between 0 and 1.

Once all excitons have been played, the FRET efficiency (E_{FRET}) is simply calculated from the variables *FLUOR* and *FRET* from

$$E_{FRET} = \frac{FRET}{FRET + FLUOR} \qquad \text{Eqn. 5-12}$$

The simulation is then repeated many times for new fluorophore distributions and exciton schedules in order to obtain a mean FRET efficiency over many configurations. The results of this averaging can be improved by increasing the size of the modelled area or by increasing the number of repeats. It has been shown that this kind of simulation can accurately describe FRET between randomly distributed fluorophores in three and two dimensions[24, 27].

5.4 Summary

Determination of distances from quantitative FRET measurements requires as a minimum the Förster radius of the FRET pair involved to be known. The Förster radius has been calculated for two FRET pairs that can be used to investigate the three dimensional structure of signalling ErbB1 receptor complexes at the cell surface. These two FRET pairs EGF-Alexa 546 / C_{18}DiD and EGF-Alexa 546 / EGF-Atto 647N have Förster radii of 7.0 nm and 5.6 nm respectively. The former pair is used in the next chapter to investigate the separation of the EGF binding site to the cell surface while the latter pair is suitable for measurements investigating the lateral separation of EGF binding sites in receptor complexes. The distances expected from the high resolution structure of ErbB1 dimers and monomers, plus previous studies of FRET between donor and acceptor labelled ErbB1 ligands suggest that these FRET pairs will be suitable. A control experiment using a previously characterised FRET pair[4] with a low Förster radius confirmed a previously unknown structural difference between the functionally distinct high- and low-affinity classes of ErbB1 receptors that should be detectable by the EGF-Alexa 546 / C_{18}DiD FRET pair.

Accurate determination of distances from ensemble FRET efficiencies must also avoid biasing of the FRET efficiencies through incorrect assumptions regarding the stoichiometry of donors and acceptors. In the case of the EGF-Alexa 546 / C_{18}DiD FRET pair where the donor is bound to a membrane protein and the acceptor is free to diffuse in the outer leaflet of the cell membrane the stoichiometry is dynamic during measurement of the donor lifetime. Quantification of the distance of closest approach of donors to the acceptor labelled cell surface requires computational simulation of the experiment in order to predict how the measured average FRET efficiency will vary with the density of acceptors in the membrane, for a given distance of closest approach.

References

1. Selvin, P. R. & Hearst, J. E. Luminescence energy transfer using a terbium chelate: Improvements on fluorescence energy transfer. PNAS 91, 10024-10028 (1994).
2. Haugland, R. P. in Excited States of Biopolymers (ed. Steiner, R. F.) 29-53 (Plenum Press, New York, 1983)
3. Wu, P. & Brand, L. Resonance Energy Transfer: methods and Applications. Analytical Biochemistry 218, 1-13 (1994).
4. Shahrokh, Z., Verkman, A. & Shohet, S. Distance between skeletal protein 4.1 and the erythrocyte membrane bilayer measured by resonance energy transfer. The Journal of Biological Chemistry 266, 12082-12089 (1991).
5. Lakowicz, J. R. Principles of Fluorescence Spectroscopy (Kluwer Academic / Plenum Publishers, New York, 1999).
6. Meer, B. W. v. d. Kappa-squared: from nuisance to new sense. Reviews in Molecular Biotechnology 82, 181-196 (2002).
7. Dale, R. E., Eisinger, J. & Blumberg, W. E. Orientational Freedom of Molecular Probes - Orientation Factor in Intra-Molecular Energy-Transfer. Biophysical Journal 26, 161-193 (1979).
8. Haas, E., Katchalski-Katzir, E. & Steinberg, I. Effect of the orientation of donor and acceptor on the probability of energy transfer involving electronic transitions of mixed polarization. Biochemistry 17, 5064-70 (1978).
9. Garrett, T. P. et al. Crystal structure of a truncated epidermal growth factor receptor extracellular domain bound to transforming growth factor alpha. Cell 110, 763-776 (2002).
10. Ferguson, K. M. et al. EGF Activates Its Receptor by Removing Interactions that Autoinhibit Ectodomain Dimerization. Molecular Cell 11, 507-517 (2003).
11. Ogiso, H. et al. Crystal structure of the complex of human epidermal growth factor and receptor extracellular domains. Cell 110, 775-787 (2002).

12. Dawson, J. P. et al. Epidermal growth factor receptor dimerisation and activation require ligand-induced conformational chnages in the dimer interface. Molecular Cell Biology 25, 7734-7742 (2005).

13. Bagossi, P. et al. Molecular modelling of nearly full-length ErbB2 receptor. Biophysical Journal 88, 1354-1363 (2005).

14. Carraway, K. L., Koland, J. G. & Cerione, R. A. Location of the epidermal growth factor binding site on the EGF receptor. A resonance energy transfer study. Biochemistry 29, 8741-8747 (1990).

15. Martin-Fernandez, M. L., Clarke, D. T., Tobin, M. J., Jones, S. V. & Jones, G. R. Preformed oligomeric epidermal growth factor receptors undergo an ectodomain structure change during signalling. Biophysical Journal 82, 2415-2427 (2002).

16. Gadella, T. W. & Jovin, T. M. Oligomerization of epidermal growth factor receptors on A431 cells studied by time-resolved fluorescence imaging microscopy. A stereochemical model for tyrosine kinase receptor activation. Journal of Cell Biology 129, 1543-1558 (1995).

17. Clayton, A. H. A. et al. Ligand-induced Dimer-Tetramer Transition during the Activation of the Cell Surface Epidermal Growth Factor Receptor-A Multidimensional Microscopy Analysis. The Journal of Biological Chemistry 280, 30392-30399 (2005).

18. Whitson, K. B., Beechem, J. M., Beth, A. H. & Staros, J. V. Preparation and characterization of Alexa Fluor 594-labeled epidermal growth factor for fluorescence resonance energy transfer studies: application to the epidermal growth factor receptor. Analytical Biochemistry 324, 227-236 (2004).

19. Webb, S. E. D. et al. Single molecule imaging and FLIM show different structures for high and low-affinity EGFRs in A431 cells. Biophysical Journal 94, 803-819 (2008).

20. Defize, L. H. K. et al. Signal Transduction by Epidermal Growth Factor Occurs Through the Subclass of High Affinity Receptors. The Journal of Cell Biology 109, 2495-2507 (1989).

21. Barisas, B. G., Wade, W. F., Jovin, T. M., Arndt-Jovin, D. & Roess, D. A. Dynamics of molecules involved in antigen presentation: effects of fixation. Molecular Immunology 36, 701-708 (1999).

22. Ringerike, T., Blystad, F. D., Levy, F. O., Madshus, I. H. & Stang, E. Cholesterol is important in control of EGF receptor kinase activity but EGF receptors are not concentrated in caveolae. Journal of Cell Science 115, 1331-1340 (2002).

23. Wolber, P. K. & Hudson, B. S. An analytic solution to the Forster energy transfer problem in two dimensions. Biophysical Journal 28, 197-210 (1979).

24. Corry, B., Jayatilaka, D. & Rigby, P. A Flexible Approach to the Calculation of Resonance Energy Transfer Efficiency between Multiple Donors and Acceptors in Complex Geometries. Biophysical Journal 89, 3822-3836 (2005).

25. Yguerabide, J. Theory for Establishing Proximity Relations in Biological Membranes by Excitation Energy Transfer Measurements. Biophysical Journal 66, 683-693 (1994).

26. Capeta, R. C., Poveda, J. A. & Loura, L. M. S. Non-Uniform Membrane Probe Distribution in Resonance Energy Transfer: Application to Protein-Lipid Selectivity. Journal of Fluorescence 16, 161-172 (2006).

27. Berney, C. & Danuser, G. FRET or No FRET: A Quantitative Comparison. Biophysical Journal 84, 3992-4010 (2003).

28. Chigaev, A., Buranda, T., Dwyer, D. C., Prossnitz, E. R. & Sklar, L. A. FRET Detection of Cellular α4-Integrin Conformational Activation. Biophysical Journal 85, 3951-3962 (2003).

29. Snyder, B. & Freire, E. Fluorescence energy transfer in two dimensions. A numeric solution for random and nonrandom distributions. Biophysical Journal 40, 137-148 (1982).

30. Zimet, D. B., Thevenin, B. J., Verkman, A. S., Shohet, S. B. & Abney, J. R. Calculation of resonance energy transfer in crowded biological membranes. Biophysical Journal 68, 1592-1603 (1995).

31. Frederix, P., Beer, E. L. d., Hamelink, W. & Gerritson, H. C. Dynamic Monte Carlo simulations to model FRET and photobleaching in systems with multiple donor-acceptor interactions. Journal of Physical Chemistry B 106, 6793-6801 (2002).

6 Investigating three-dimensional structural variations in activated ErbB1 receptors

The motivation for developing the bi-directional FRET technique and its adaptation to adherent cells was to investigate the three dimensional conformation of ErbB1 with respect to the plasma membrane. In this chapter the method is described and used to confirm structural differences between the low- and high-affinity classes of the ErbB1 receptor in adherent cells. It is then demonstrated how the results of the FRET measurements can be related to the early signalling functions of the receptor by repeating the FRET measurement under experimental conditions that disrupt normal receptor function and correlating them with complimentary information regarding receptor oligomerisation and phosphorylation states.

6.1.1 The 3D architecture of signaling ErbB1 complexes

In chapter 2 the currently accepted model of the 3D architecture of the ErbB family of receptor tyrosine kinases and the currently proposed mechanism of signal transduction by ErbB1 was discussed. This model is a composite of biochemical evidence[1, 2] and structural insights derived from crystallography[3-8]. However, a wealth of evidence from the literature has suggested that the 3D architecture of signalling ErbB1 complexes on the surface of cells is more complex than that put together from crystallographic data of ErbB1 fragments[9-14]. As discussed in the previous chapter, ensemble and single molecule FRET experiments designed to measure the distance between ligand binding sites in cellular ErbB1 complexes have consistently returned mean donor-acceptor separations much shorter and therefore inconsistent with the ~ 11 nm distance found between ligand binding sites in the crystallographic back-to-back dimer. The results shown in section 5.2 suggest that in a ligand-bound extended state[3, 4]

ErbB1 adopts at least two different conformations with respect to the cell membrane that place the ligand binding site at different distances from the cell surface and are associated with the two binding affinity classes of ErbB1 found in cells. That this has not been observed before is perhaps unsurprising as previous FRET studies aiming to measure ErbB1 ligand-membrane separation have investigated receptor in non-cellular contexts where ErbB1 receptors do not display high binding affinity for ligand[15]. The mean distance of closest approach of the ErbB1 ligand binding site to the surface of isolated membranes is 6.7 nm[16]. It has been proposed that high affinity ErbB1 might adopt a 'flat' conformation parallel to the cell surface whereas low affinity receptors could be perpendicular to it standing 'proud'[13]. This would enable high affinity receptors to form interactions other than the back-to-back dimer inaccessible to the low affinity population. It is also notable that this is unanticipated from the crystal structures alone, although very recently, protein tomography studies of ErbB1 in fixed cells performed at the same time as this work detected receptor ectodomains that were oriented parallel to the membrane[17].

Because ErbB1 is expressed as a single translation product[18] and given that HA and LA ErbB1 ectodomains appear to adopt their orientation relative to the membrane prior to and unaffected by growth factor binding[13], it would follow that ErbB1 ectodomains need to be somehow be 'primed' after translocation to adopt the very different ectodomain orientations associated with high or low affinity EGF-binding status. A similar observation has been previously reported for the Integrin receptor[19]. Whether priming of EGFR actually occurs and/or which interactions may be involved is not yet known.

6.2 Materials and methods

6.2.1 Cell Culture

A431 and HeLa cells were purchased from the European Collection of Animal Cell Cultures. A431 cells were cultured in Dulbecco's modified Eagles medium

without phenol red and supplemented with 10% fetal bovine serum, 2 mM glutamine, and 1% penicillin/streptomycin. HeLa cells were cultured in minimum essential medium with Earle's salts without phenol red, supplemented with 10% fetal bovine serum and 2 mM glutamine (all Invitrogen). Cells were incubated at 37°C in the presence of 5% CO_2 in air. Maintanence of cells in culture was performed as described in section 4.3.1.1.

6.2.2 Fluorescent labelling

In this chapter two fluorescent probes are used to specifically label the EGF binding site of ErbB1 with a FRET donor or acceptor to investigate the oligomerisation of receptors. A third membrane localised acceptor is used in separate experiments with the same donor to investigate the distance of closest approach of the EGF binding site to the membrane surface.

Murine Epidermal Growth Factor (mEGF, Peprotech) singly labelled at the N-terminus with Alexa 546 (Invitrogen) or Atto 647N (AttoTec) binds specifically in a 1:1 ratio with ErbB1 (conjugation of mEGF and dyes performed by Cambridge Research Biochemicals). These dyes have emission and excitation spectra suitably separated for two colour imaging but can act as a FRET pair. Vybrant C_{18}DiD (Invitrogen) is a lipophilic phospholipid analogue that is able to insert into and freely diffuse in the outer leaflet of the cell membrane, and exhibits similar fluorescence spectra to Atto 647N. The Förster radii for these two FRET pairs calculated in chapter 5 are 7.0 nm for mEGF-Alexa 546 / Vybrant C_{18}DiD and 5.6nm for mEGF-Alexa 546 / mEGF-Atto 647N.

Samples with acceptor labelled membranes were prepared by adding 100 µL of 5 µM or 1 µM Vybrant C_{18}DiD in serum free media to A431 or HeLa cells that had been deprived of serum for 16 hours upon reaching 80% confluency. This was done to remove the effect of EGF and other growth factors present in serum. After incubation at 37°C for 8-15 minutes excess Vybrant C_{18}DiD was washed off with serum free media. 40-80% of cells were found to have incorporated

Vybrant C_{18}DiD into their membranes after this treatment. Example confocal images of A431 cells labelled in this way with Vybrant C_{18}DiD and excited with a 639 nm CW laser are shown in figure 6.1. It was found that although individual cells had uniformly labelled membranes, variation was observed in the amount of membrane probe incorporated by different cells and Vybrant C_{18}DiD was not completely restricted to the plasma membrane.

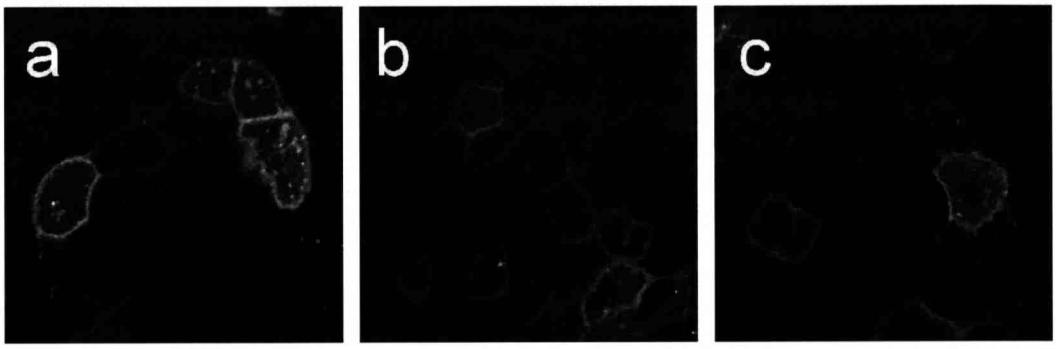

Figure 6.1 a-c. Confocal images of A431 cells labelled with Vybrant C_{18}DiD. The image resolution is 256 x 256 pixels and the field of view is 63 x 63 μm.

Binding of dye-conjugated ligand to ErbB1 in A431 cells was achieved either by adding a saturating concentration of EGF-Alexa546 (200nM) or 1:1 mEGF-Alexa 546 : mEGF-Atto 647N (total EGF concentration 400nM) in PBS to cells at 4°C for 30 minutes. At this temperature ligand-induced endocytosis is inhibited. Cells were lightly fixed by exposure to 1% paraformaldehyde (electron microscopy sciences) for 10 minutes at room temperature either before or after ligand binding, which causes sufficient cross-linking within a complex containing ErbB1 to inhibit further conformational changes of the receptor and lateral diffusion in the plasma-membrane[20]. It has been shown previously that cross-linking with 1% paraformaldehyde does not cause additional aggregation of ErbB1[13].

6.2.3 Blocking of low-affinity EGF binding to cell surface ErbB1 receptors

A431 or HeLa cells were treated with 200 nM anti-ErbB1 clone 2E9 and incubated with gentle rocking at 4°C for 4 hours. This antibody binds to low-affinity ErbB1s on the surface of cells and prevents EGF from binding to this class of receptor[21]. This was done before depolarization of the plasma membrane or activation of PKC, after depletion of membrane cholesterol and during inhibition of ATP production in the sample treatments described in the following section.

6.2.4 Disruption of normal ErbB1 function in cells

In order to demonstrate how the results of FLIM-FRET experiments designed to investigate ErbB1 conformation and lateral organisation can be related to receptor function, cell samples were exposed to four treatments that disrupt the normal function of the receptor. These aimed to

1. Activate protein kinase C (PKC), an intracellular protein that binds to the juxtamembrane region of ErbB1 inhibiting ErbB1 kinase activity and abolishing high-affinity ligand binding (whilst ensuring that ErbB1 is targeted for recycling[22-24])
2. Disrupt lipid rafts by depletion of membrane cholesterol. ErbB1 localised in rafts is thought to be inhibited by the raft environment and cholesterol depletion results in an increase in receptor activity[25, 26]
3. Inhibit cellular ATP production, which prevents receptor intracellular domain phosphorylation and hence phosphorylation dependent binding of intracellular effectors
4. Depolarise the tightly controlled plasma membrane potential which prevents EGF-induced hyperpolarisation of the membrane potential[27]

Although these treatments do not specifically affect the ErbB1 receptor only, any variation in ErbB1 structure seen under the different experimental conditions would validate the bi-dimensional FRET methods ability to relate structure and function.

6.2.4.1 Incubation with PMA (PKC activation)

A431 cells were incubated in 100 nM phorbol 12-myristate 13-acetate (PMA), diluted in PBS and containing 0.01% DMSO, for 30 minutes at 37°C to activate PKC.

6.2.4.2 Depletion of plasma membrane cholesterol

A431 cells were treated with 10 mM methyl-β-cyclodextrin (MβCD) diluted in serum free media for 30 minutes at 37°C to deplete their membranes of cholesterol. Cells were then triply washed with PBS before treatment with mAb-2E9 if necessary and fluorescent labelling.

6.2.4.3 Inhibition of cellular ATP production

For experiments requiring the inhibition of ATP-dependent cellular processes, A431 cells were treated with 10 mM 2-Deoxyglucose + 10 mM Sodium Azide + 0.1 %BSA (DSA) for 20 minutes at 37°C. This treatment inhibits the production of ATP by glycolysis and oxidative phosphorylation respectively.

6.2.4.4 Depolarisation of plasma membranes

The membranes of pre-chilled A431 cells were partially depolarised by incubation with 100 μM Ouabain diluted in PBS for 10 minutes at 4°C. Samples with acceptor-doped membranes were labelled with Vybrant C_{18}DiD prior to depolarization. The partial depolarisation was maintained whilst the cells were incubated in dye conjugated mEGF solutions by diluting the mEGF-dye conjugates in PBS supplemented with 100 μM Ouabain. The total incubation time in Ouabain was 40 minutes at 4°C.

6.2.5 Measurement of intracellular calcium concentration during EGF signaling in wildtype and partially depolarised A431 cells

A431 cells were simultaneously loaded with Fluo-4 and FuraRed Ca^{2+} indicators by incubation with a 5 μM Fluo-4 and 10μM FuraRed in PBS with 0.02% (weight per volume) Pluronic F-127 for 1 hour at 37°C. Pluronic F-127 is a non-ionic detergent that assists in dispersing the non-polar Fluo-4 and FuraRed in aqueous media. The calcium indicator solution was then washed off with PBS. Some of these samples were then incubated with 100 μM Ouabain for 40 minutes before being imaged immediately.

The concentration of intracellular calcium as reported by the ratio of Fluo-4/FuraRed fluorescence intensity was measured in live A431 cells after the addition of mEGF at 21°C. Both dyes were excited by 488nm CW laser light from an Ar^{+} laser. Fluo-4 and FuraRed fluorescence was split by at 580 nm long pass dichroic mirror (Nikon DM 580) with Fluo-4 fluorescence detected between 500 nm and 550 nm and FuraRed fluorescence detected between 572.5 nm and 647.5 nm. 512 x 512 pixel images of both channels were scanned simultaneously every 30 seconds (frame time = 10 seconds) for 16 minutes. Cells were imaged in glass bottomed culture dishes that initially contained 0.5ml of PBS which was enough to cover the cells. At 120 seconds 0.5ml of 400nm mEGF was added

drop-wise to give a final concentration of 200nM. This was done rather than perform a complete change of media to ensure that the focal plane was not lost whilst minimizing the time taken for the added mEGF to diffuse into the existing media.

6.2.6 FLIM-FRET measurements

Fluorescence lifetime images of mEGF-Alexa 546 (donor) bound to ErbB1 in cell membranes prepared with or without Vybrant C_{18}DiD acceptor were acquired using the multicolour, multi-dimensional laser scanning confocal microscope described in Chapter 4. mEGF-Alexa 546 was excited with 545 nm pulsed laser light (Coherent, MIRA-OPO. 76 MHz repetition rate) and the Alexa546 fluorescence was detected between 575 and 625 nm. The resulting time-resolved images were analysed using SPCImage (Becker-Hickl GmbH) FLIM analysis software.

Fluorescence intensity decays were fitted to a single exponential decay model when only donor was present and a bi-exponential model when both donor and acceptor were present to extract weighted mean lifetimes. The reduced χ^2 parameter was used to judge the goodness of fit, which was deemed acceptable when $0.8<\chi^2<1.2$. The measured efficiency of FRET, E_{FRET}, is related to the lifetime of the donor in the presence (τ_{DA}) and absence (τ_D) of acceptor by

$$E_{FRET} = 1 - \frac{\tau_{DA}}{\tau_D} \qquad \text{Eqn. 6-1}$$

For each imaged cell, a value for τ_D or τ_{DA} was obtained by taking the mean of the distribution of lifetimes of pixels in the cell membrane. For bi-exponential fits these distributions were of the weighted means of the two fitted lifetime components for each pixel, τ_m.

In the case of FLIM acquisitions of cells labelled with both donor and acceptor, a corresponding confocal image of Vybrant C_{18}DiD was taken afterwards. A 639nm CW laser (PTI) was used to directly excite the membrane localised DiD and the emitted fluorescence was collected at wavelengths >670 nm from the same field of view as the FLIM data. Vybrant C_{18}DiD images were acquired at a 256x256 pixel resolution so as to be directly comparable to the FLIM images. ImagePro (Media Cybernetics) was used to manually obtain the mean Vybrant C_{18}DiD fluorescence intensity in the plasma-membranes of cells. By taking advantage of the variation in Vybrant C_{18}DiD labelling between cells exposed to the same Vybrant C_{18}DiD loading solution, τ_{DA} could be measured for a large distribution of acceptor densities with far fewer samples. Values of FRET efficiency and acceptor intensity were obtained from areas of individual cell membranes containing approximately the same intensity of membrane probe. Acceptor intensity was normalised to the 639 nm laser power at the time of measurement. Datasets were typically constructed from analysis of >100 cells. 545 nm laser power incident on the sample was kept <125 μW, 639 nm laser power was <100 μW.

6.2.7 Calibration of acceptor density in cell membranes

Phosphatidylcholine giant unilamellar vesicles (GUVs) in distilled water were prepared using a rapid GUV process[51]. Vybrant C_{18}DiD (acceptor) and Vybrant C_{18}DiI (donor) were added to the GUV suspension to a total concentration of 5μM and 0.5μM respectively and incubated for 20 minutes at 37°C. 0.5ml of the suspension was then added to a glass-bottomed microscope dish and labelled lipids spontaneously formed monolayers on the glass surface. FLIM images and corresponding C_{18}DiD intensity images were acquired as in section 6.2.6 and acceptor photobleaching with 639 nm CW laser light was used to reduce the density of acceptors whilst keeping the donor density the same. The data was fitted to the analytical expression for zero distance of closest approach between donors and acceptors derived by Wolber et al[28], as has been previously validated[16].

$$1 - E_{FRET} = 0.6463e^{-4.7497D} + 0.3537e^{-2.0618D}, \text{ where } D = KI \qquad \text{Eqn. 6-2}$$

Where D is the density of acceptor, I is the measured Vybrant C_{18}DiD fluorescence intensity and K is a constant factor (with dimensions of inverse fluorescence intensity) that converts this into acceptor density. The units of acceptor density are acceptors per R_0^2. The value for K was found to be 0.089±0.003.

6.2.8 Monte-Carlo simulation of FRET between ErbB1-EGF-Alexa546 and membrane localised Vybrant C_{18}DiD

Pseudo-random fluorophore distributions produced by simulated annealing were obtained using a custom implementation in C++ produced by Dr Daniel Rolfe of STFC Daresbury Laboratory which was based upon the Monte-Carlo FRET algorithm developed by Ben Corry[29]. Dr Rolfe's software simulated FRET between ErbB1-mEGF-Alexa546 and membrane localised Vybrant C_{18}DiD and then fit the results of the simulations to the experimental data. The basic function of the algorithm is outlined in Chapter 5.3. Modifications to this algorithm to take into account the details of the experimental FLIM-FRET measurements being simulated plus the details of the fluorophore distributions used make up the rest of this section.

6.2.8.1 Simulated distributions of donors and acceptors

EGF-Alexa 546 (donors) bound to ErbB1 in a membrane containing a random distribution of Vybrant C_{18}DiD (acceptors) were modelled as two flat, independent planes of donors and acceptors separated by a distance, d (Figure 6.2a).

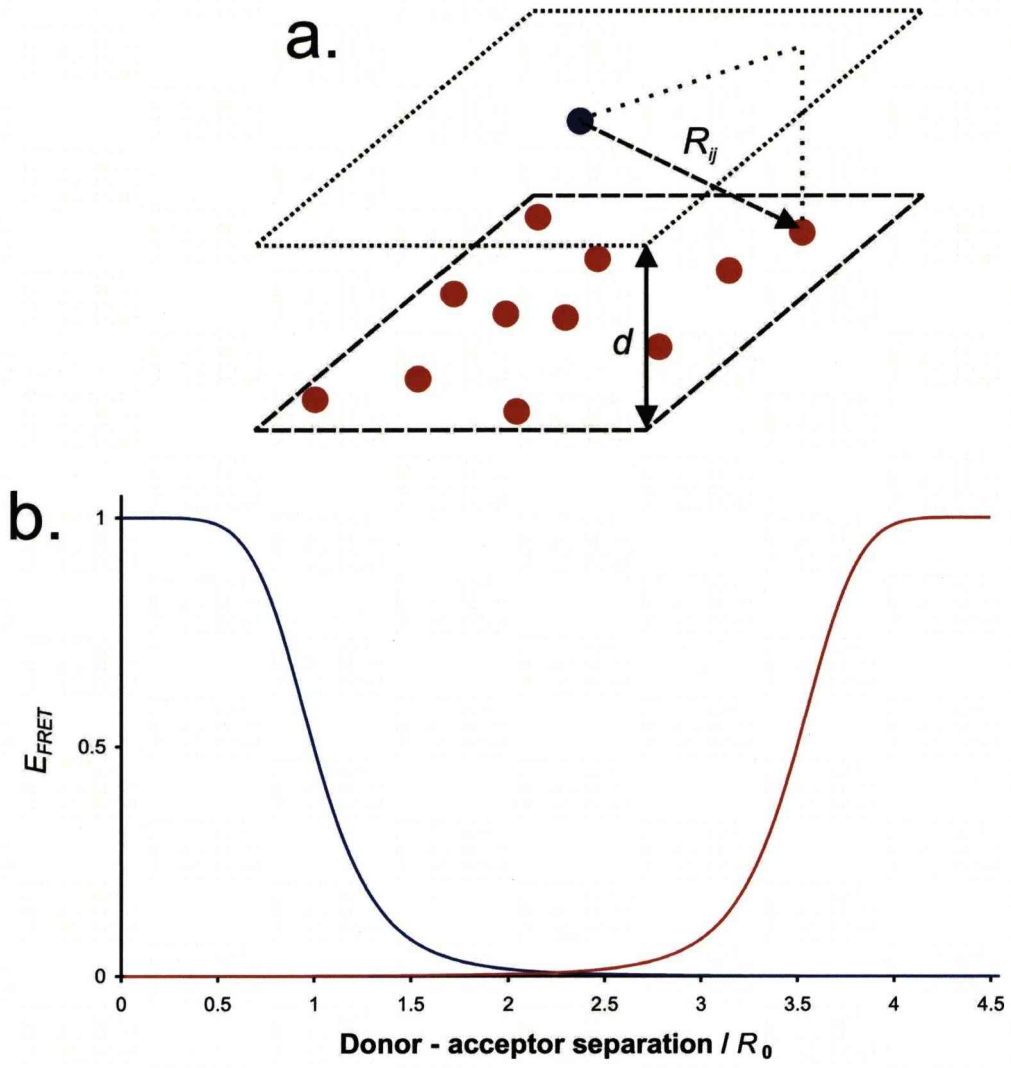

Figure 6.2 a. Donors are modeled as occupying a flat two-dimensional plane positioned a distance d above a similar plane of acceptors. The separation R_{ij} between each donor i and acceptor j can be determined simply from d and their lateral separation. **b**. FRET efficiency as a function of donor – acceptor separation shown for two identical donors separated by 4.5 times the donor – acceptor Förster radius.

Donors and acceptors were considered to be circles of radius 1nm for the purpose of producing distributions of non-overlapping fluorophores. The surface density of membrane bound ErbB1 is in the range 50-1000 receptors per μm^2 in A431 cells[30, 31]. The Forster radius, R_0, of the EGF-Alexa 546 / Vybrant C_{18}DiD FRET pair is 7nm to the nearest nm. Simulations of receptor positions randomly distributed with a surface density of 1000 receptors per μm^2 showed that the mean separation of receptors was greater than 4.5 times this R_0. Because of this donors bound to individual receptors, or receptor oligomers are considered not be

competing with donors on other receptor complexes to transfer energy to acceptors (Figure 6.2b).

Donors were modelled above the middle of an area of randomly distributed acceptors. A small exclusion zone underneath each donor is included to mimic the area excluded by the receptor transmembrane domain. As more than one dimeric ErbB1 interface may be possible and the structure of ErbB1 tetramers is uncertain[9, 10, 13], these were simulated by placing donors at intervals of π or $\pi/2$ radians around the circumference of a circle of radius R_{mult} such that the oligomer orientation was random. This is a valid approximation that accounts for donors bound to receptors in a complex competing for acceptors because the FRET efficiency returned by the simulation (and indeed the experimental data) is an average over many acceptor distributions. Two different methods of generating the random distributions were used, depending upon the range of acceptor densities required. To produce simulated FRET results in the range 0-5 acceptors per R_0^2, a simulated annealing procedure was used whereby random positions in the simulated area were allocated to acceptors and the position of any overlapping acceptors was randomly altered until no overlaps remained. However, this process failed to find non-overlapping acceptor positions for acceptor densities > 5 per R_0^2, so a second procedure was used for simulations that required high acceptor densities. This second algorithm began with the simulated area completely saturated with hexagonally packed acceptor before randomly removing acceptors to achieve the required surface density. The position of each acceptor was then randomised one by one (with ten passes of randomisation in total). This procedure is capable of producing random distributions up to the hexagonal close packing limit and succeeds where the original simulated annealing procedure fails because it begins from a non-random but already non-overlapping distribution.

6.2.8.2 The exciton Schedule

The exciton schedules used were generated using the properties of the illuminating laser used to obtain the FLIM-FRET data to be compared to the simulations. The excitation source was a MIRA-OPO pumped by a Ti:Sa laser that produced pulses of 545nm laser light, 200fs in duration at a repetition rate of 76 MHz. Due to the confocal geometry of the FLIM-FRET experiment, 84% of the laser power falls within a radius R_{84}, the distance from the centre of the illuminated area to the first minima of an airy disc. All excited receptors fall within this region as experimentally, fluorescence from outside this region will be rejected by the confocal pinhole. To simplify the model, the laser profile was assumed to be uniform within the simulated region with power per unit area F_{laser} given by

$$F_{laser} = \frac{0.84 P_{laser}}{\pi R_{84}^2} \qquad \text{Eqn. 6-3}$$

where P_{laser} is the laser power measured exiting the microscope objective. From this the number of photons produced per pulse that reach the simulated area A_{sim} can be easily determined by

$$N_{phot} = \frac{\lambda F_{laser} A_{sim}}{hcf_{pulse}} \qquad \text{Eqn. 6-4}$$

where f_{pulse} is the repetition rate of the pulsed excitation. h is Planck's constant and c is the speed of light in vacuum. For each donor, the mean number of photons that excite it (hence the mean number of excitons per donor per pulse) can be calculated from the concentration of donor molecules Σ_{donor} and their absorption cross-section at λ, X_{donor}

$$N_{excitons} = X_{donor} \Sigma_{donor} N_{phot} \qquad \text{Eqn. 6-5}$$

A schedule for these photons was created one pulse at a time for a total of N_{pulses}, set by the user. For each pulse the number of photons is sampled from a poisson distribution with mean $N_{exciton}$. The arrival time of each photon is selected from a random uniform distribution and randomly assigned to a donor.

6.2.8.3 Simulation results

Each simulation was repeated for 2000-6000 configurations for a given set of parameters, with new donor-acceptor distributions and exciton schedules generated for each configuration. From these repeats, the mean and standard deviation of the FRET efficiency were calculated. Table 6.1 contains a list of the parameter values used and an explanation of their origin. FRET efficiency as a function of acceptor density was determined using the Monte-Carlo algorithm for donor plane to acceptor plane separations, d, from 0.5 to 20nm in steps of 0.5nm for donors as monomers, dimers and tetramers.

These results are shown for the acceptor density range 0-2 acceptors per R_0^2in Figure 6.3. Note that the curves converge at large distances and also for increasing acceptor density at short distances. The effect of simulating multiple donors in close proximity is a reduction in the FRET efficiency for a given acceptor density and is most pronounced at short plane separations.

Σ_{don}	500 μm^{-2}	Mean value of heterogeneous ErbB1 density in cells[30, 31]
receptor type	monomer, dimer, tetramer	
R_{don}	1 nm	Length of Alexa546 fluorophore long axis
R_{excl}	1 - 2 nm	Radius of area excluded to acceptors due to the ErbB1 transmembrane domain
R_{mult}	2 nm	Based on probe dimensions (R_{don})
donor lifetime, τ_D	3.2 ns	EGF-Alexa546 fluorescence lifetime
X_{donor}	$3.3x10^{-16}$ cm^2	Calculated from the measured EGF-Alexa546 Absorption coefficient at 545nm
R_{acc}	1 nm	Length of Vybrant C_{18}DiD fluorophore long axis
acceptor lifetime, τ_A	1.2 ns	Fluorescence lifetime of Vybrant C_{18}DiD
donor-acceptor Förster radius, R_0	7.018 nm	(details of calculation can be found in section 5.7)
t_{pulse}	0.0002 ns	Pulse duration of Coherent MIRA
f_{pulse}	$7.6x10^7$	Pulses per second generated by Ti:Sa pumped Coherent MIRA OPO
N_{pulse}	500	
λ	545 nm	Donor excitation wavelength (used to calculate number of photons per pulse from P_{laser})
P_{laser}	125 µW	Laser power incident on sample (measured after microscope objective)
R_{84}	0.256 µm	Distance from centre of the diffraction limited confocal spot to the 1st minimum of an Airy disc for λ = 545 nm
N_{config}	2000-6000	

Table 6.1 Parameter list for Monte-Carlo simulation of FRET between EGF-Alexa 546 bound to ErbB1 in a flat membrane labeled with Vybrant C_{18}DiD.

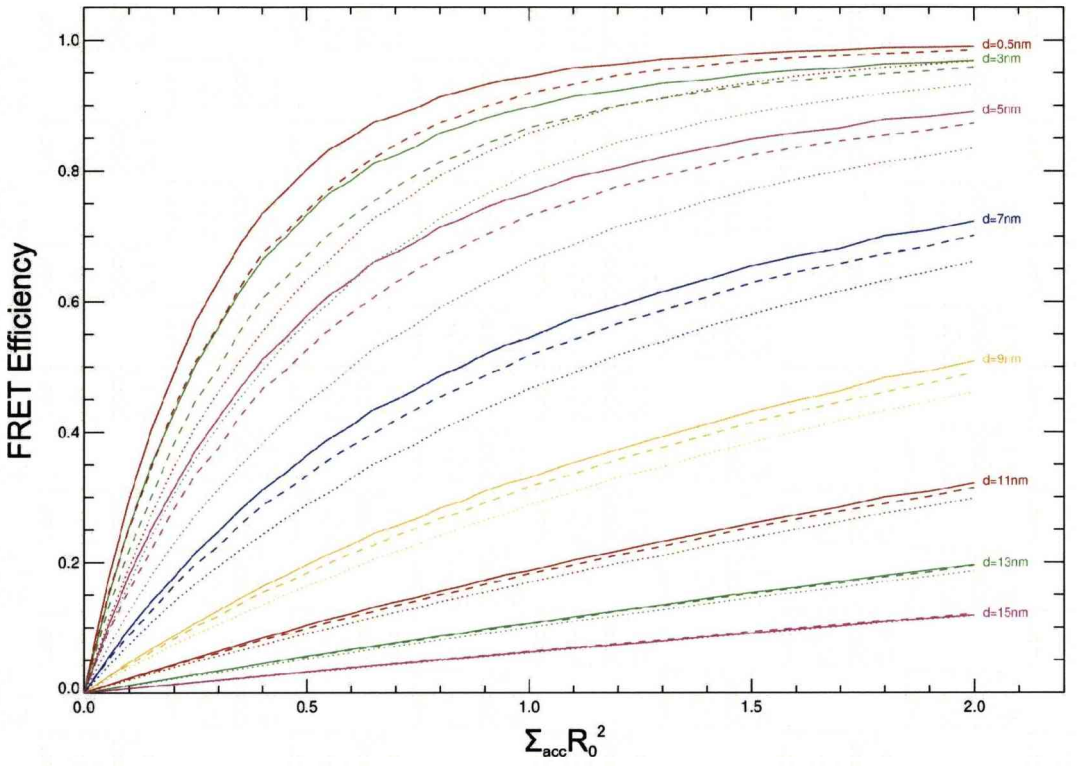

Figure 6.3 Results of Monte-Carlo simulations of FRET between donors and randomly distributed acceptors occupying two spatially separated planes produced by Dr Daniel Rolfe. Simulated FRET efficiency as a function of acceptor density is shown for donor-acceptor plane separations, *d*, between 0.5-15 nm for monomeric (lines), dimeric (dashed lines) or tetrameric (dotted lines) donors. The Förster radius used in the simulation is 7nm.

6.3 Results and discussion

6.3.1 FRET between EGF-Alex 546 and Vybrant DiD in wildtype A431 cells

Figure 6.4 shows an example of A431 cells labelled with Vybrant DiD and lightly fixed after binding EGF-Alexa 546.

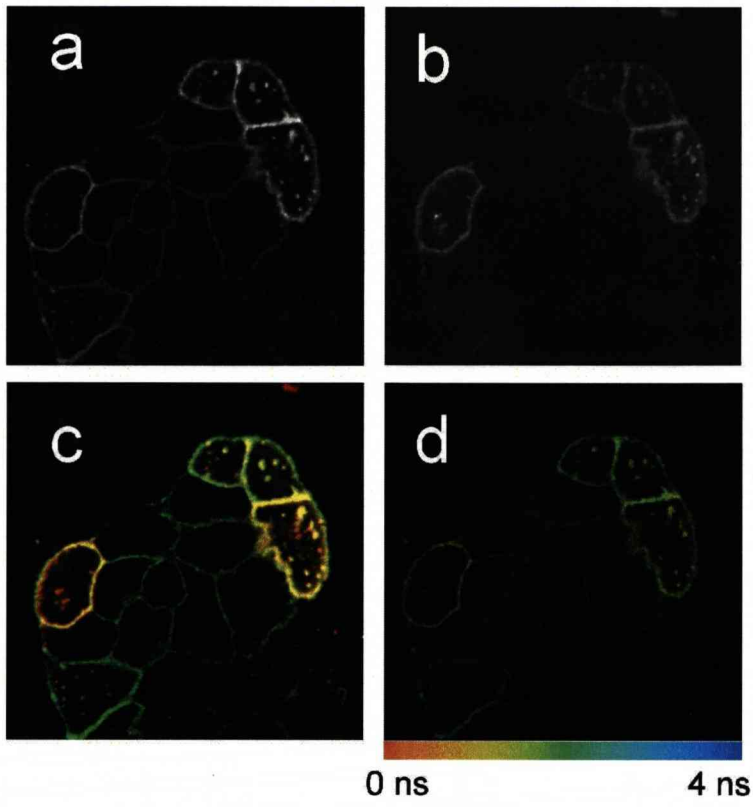

Figure 6.4 Images of wildtype A431 cells labelled with Vybrant C_{18}DiD and fixed after binding mEGF-Alexa 546. **a.** mEGF-Alexa 546 fluorescence intensity **b.** Vybrant C_{18}DiD fluorescence intensity **c.** Composite fluorescence intensity image of mEGF-Alexa546 (green) and Vybrant C_{18}DiD (red) **d**. mEGF-Alexa546 fluorescence lifetime. Images are of a 63 x 63 μm field of view.

Figure 6.4a is an intensity image of mEGF-Alexa 546 bound to ErbB1 in the membranes of a cluster of A431 cells. Figure 6.4b shows the intensity of Vybrant C_{18}DiD and displays clear variation in Vybrant C_{18}DiD surface density between cells. This could be because the poor solubility and consequent inhomgeneity of the diluted Vybrant C_{18}DiD results in variations in the amount of probe that comes into contact with each cell during labelling. The density of acceptor in the membrane of each cell is much more homogeneous, presumably due to diffusion of Vybrant C_{18}DiD through the cell membrane. Figure 6.3c is a false colour image of combined EGF-Alexa 546 (green) and Vybrant C_{18}DiD (red) intensity. The corresponding fluorescence lifetime image of EGF-Alexa 546 is shown in figure 6.4d. Increasing levels of Vybrant C_{18}DiD labelling correlate with a reduction in EGF-Alexa 546 lifetime due to FRET between the two fluorophores. Despite the fact that samples were prepared at 4°C to prevent ligand induced

internalisation before fixation, EGF-Alexa 546 and Vybrant C_{18}DiD is seen in a small number of vesicles as well as in the plasma membrane.

Figure 6.5 shows FRET efficiency as a function of Vybrant C_{18}DiD density measured in wildtype A431 cells lightly fixed after binding EGF-Alexa 546. The data acquired from cells where low-affinity EGF-Alexa 546 binding was blocked with mAb-2E9 (red crosses) is visibly different to the data acquired from cells unexposed to the antibody (blue crosses). Each data point represents the average value from the pixels in the membrane of an individual cell.

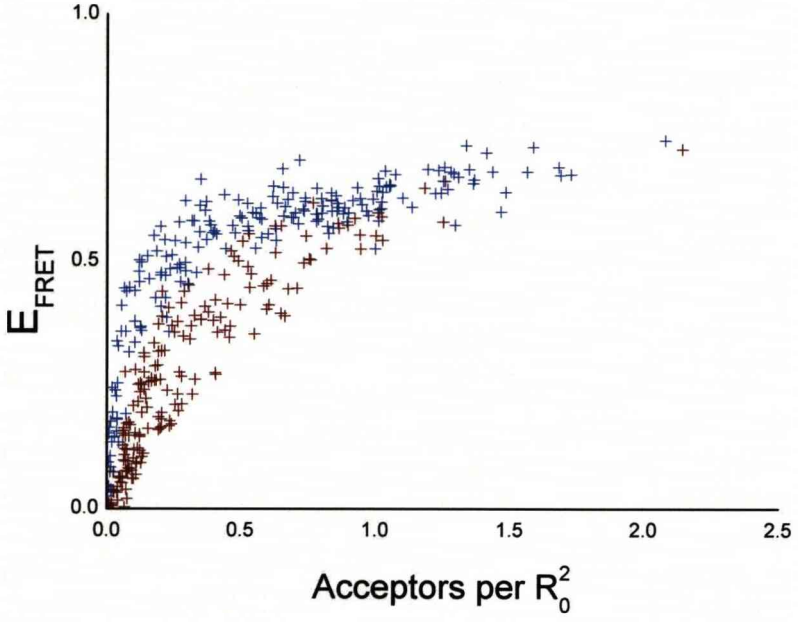

Figure 6.5 FRET efficiency as a function of acceptor density measured between EGF-Alexa 546 bound to ErbB1 and Vybrant C_{18}DiD in the cell membrane of wildtype A431 cells. Blue crosses represent data from the whole cell surface population of ErbB1 receptors and red crosses represent data where EGF-Alexa 546 binding to low-affinity receptors has been blocked.

Least squares fits of the model E vs Σ_{acc} curves shown in figure 6.3 to the data were performed by the modelling software to obtain the best-fit plane separation d. The software used linear interpolation in d to obtain model curves for d values between those simulated. The program estimated errors in the fitted values of d using the bootstrap procedure[32], where 500 resampled datasets were generated

from each dataset, and fitted using the same procedure as the real data. The distribution of fitted parameters from the resampled datasets gives an estimate of the parameter probability distribution arising from random errors in the data. Each resampled dataset has the same number of points as the real dataset, but the points were randomly selected (with replacement) from the real dataset. For each bootstrap fit the model curve was also randomised by adding a random Gaussian error to the FRET efficiency using the (small) standard error in the mean determined from the multiple Monte-Carlo configurations. This was done to propagate the random errors in the Monte-Carlo simulations into the bootstrap parameter distribution estimates.

Figure 6.6 shows the output of the fitting routine for the data acquired from ErbB1 receptors wildtype A431 cells. The data obtained in the absence of mAb 2E9 (Figure 6.6a) returns a best fit for the distance of closest approach of EGF binding sites to the cell surface of 6.34 nm. However, in the data from A431 wildtype cells where LA binding is blocked with mAb 2E9 (Figure 6.6b), there is a clear plateau in the FRET efficiency and E tends to a value ~0.6 as the acceptor density increases. This does not fit the models, where E tends to a value of 1 as acceptor density increases and plane separation decreases. In addition, the same data shows an initial rise in E as a function of Σ_{acc} which is much steeper than in the models.

The discrepancies between the data and the model in this case suggest that some of the model assumptions do not hold for the mAb 2E9 challenged ErbB1 dataset. Removing the assumption that the local acceptor concentration around the labelled receptors was the same as measured average acceptor concentration would account for the unexpectedly steep initial rise in FRET efficiency with acceptor density. To account for this in the model it was proposed that the experimentally measured mean acceptor density could be lower than the acceptor density in the submicroscopic region around the donors by some factor, Σ_{fac}. Applying a $\Sigma_{fac} > 1$ effectively compresses the model curves by a factor Σ_{fac}. Unsurprisingly, when refitting the high-affinity data to the model curves with Σ_{fac} allowed to vary the effect of Σ_{fac} on the curves is correlated with that of the plane separation d, requiring constraints to be set on the permissible values of Σ_{fac}.

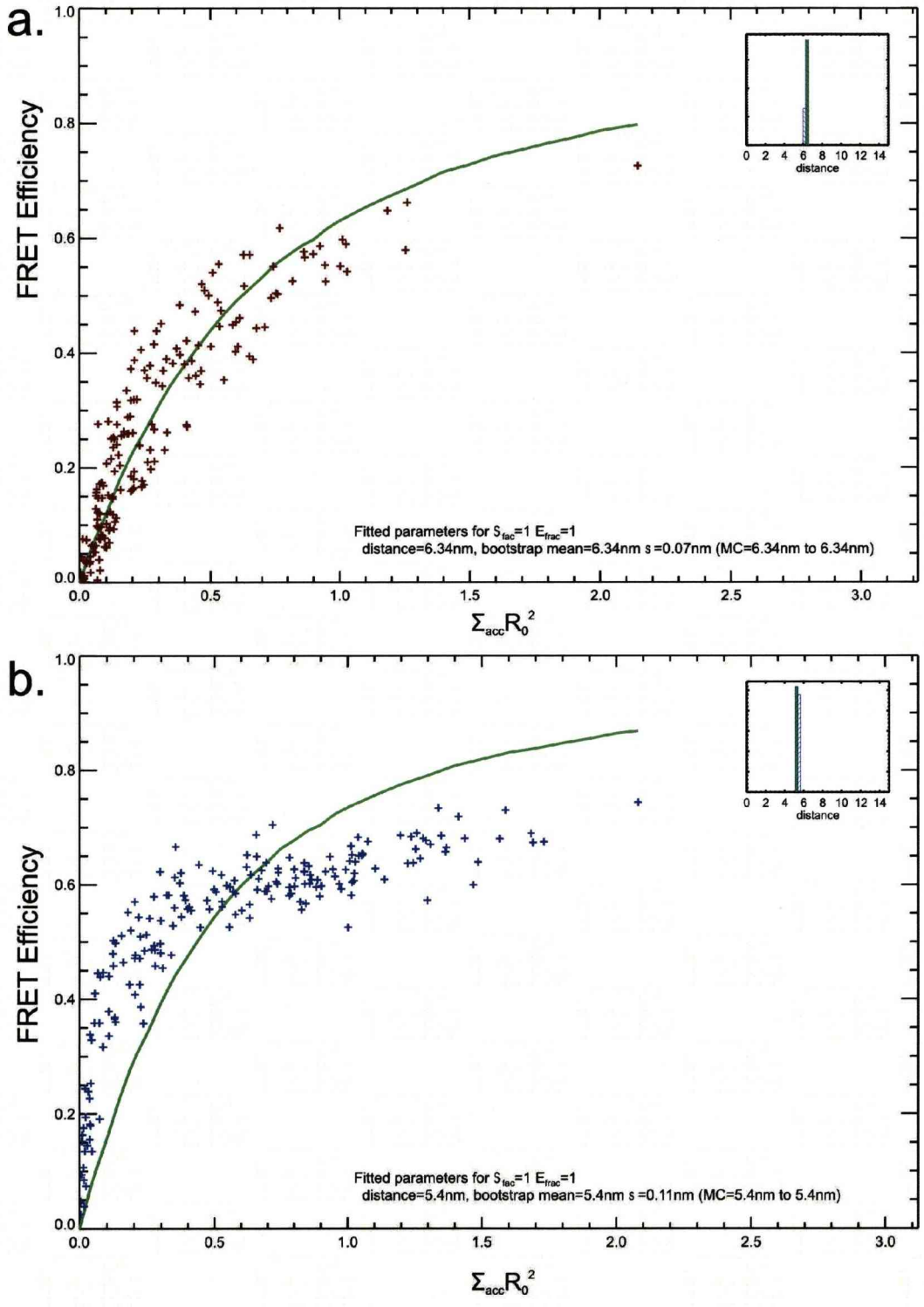

Figure 6.6 Results of fitting model E vs $\Sigma_{acc}R_0^2$ curves to the FRET efficiency as function of acceptor density obtained from **a.** the entire cell surface ErbB1 population and **b.** high-affinity ErbB1s only. Green curves represent the best fit curve and the corresponding donor-acceptor plane separation, *d*, is displayed in the bottom right of the panels along with the mean value of d obtained using the bootstrapping procedure.

Dialkylcarbocyanine dyes preferentially dwell in phospholipid phases depending upon lipid chain length and have been observed to avoid sphingomyelin and raft-marker rich liquid ordered domains[33, 34]. The Vybrant C_{18}DiD acceptor in the system being modelled has a chain length of 18 and therefore preferentially partitions with gel phase phospholipids of similar chain lengths. This partitioning is the most likely source of any discrepancy between the measured mean acceptor density and the actual local acceptor density around a donor. As the experimentally measured Vybrant C_{18}DiD surface densities are low, it was assumed that this partitioning is independent of the total amount of probe incorporated with the membrane and that Σ_{fac} is not a function of Σ_{acc}. An upper limit of $\Sigma_{fac} = 3$ can be set from the experimentally measured partitioning coefficient (the ratio of dye concentrations in the gel phase and the fluid phase) of C18 chain length dialkylcarbocyanine dyes in model membranes consisting of two pure phases at room temperature[35]. This will be the maximum factor by which the acceptor concentration can be enhanced given that cell plasma-membranes are of considerably lower purity than model membranes.

A similar option was considered to explain the unexpected plateau in the data. By removing the assumption that all donors can transfer their excited state energy to the acceptors through FRET by postulating there is a population of donors in the sample which are somehow unable to do this, the results of the Monte-Carlo simulations can be adjusted to take this into account. Possible reasons for supposing such a population exists, include: (i) some donors being attached to receptors in a conformation that places the donor >>~15 nm from the acceptor labelled cell surface; (ii) donors being attached to receptors localised to fractions of the membrane to which the DiD acceptor is somehow excluded (either through membrane level effects or aggregation of large protein complexes). Given the ErbB1 ectodomain crystal structures reported in the literature so far, (i) was considered unlikely.

If an exciton is incident on one of these donors which cannot be involved in FRET, it is either absorbed leading to fluorescence emission from that donor, or not absorbed if that donor is already excited. If a fraction E_{frac} of donors is

potentially able to transfer energy to acceptors, while the fraction unable to FRET is 1-E_{frac}, then the effective FRET efficiency of the combined population is

$$E_{all} = \frac{E_{frac} E_2}{E_{frac}(E_2 + A_2) + A_1(1 - E_{frac})} \qquad \text{Eqn. 6-6}$$

where A_1 is the proportion of donors which are not able to FRET but do absorb incident excitons and thus directly fluoresce. A_2 is the fraction of those donors which are able to FRET but which absorb an exciton then directly fluoresce, while E_2 is the fraction of donors able to FRET which do transfer their energy to an acceptor. A_1, E_2 and A_2 can all be obtained from the simulation results, so for a given E_{frac} it is straightforward to calculate E_{all} vs Σ_{acc} curves.

Although it is not an ideal situation, combining E_{frac} with d and Σ_{fac} gives an extended model with three parameters which can be used to fit the available data to the available model E_{all} vs Σ_{acc} curves.

6.3.2 Results of extended model fitting

It cannot be assumed that the extended model is not applicable to the datasets that do not appear by eye to require the extra variable parameters E_{frac} and Σ_{fac} to fit the original simulations. Attempts were therefore made to determine realistic constraints on the extra parameters so that they could be applied to all datasets.

Fits of all three parameters to the two high-affinity ErbB1 datasets that clearly require them (wild-type receptors and depolarised membranes), with E_{frac} constrained to the range 0-1 and Σ_{fac} to 0.1-3, returns best fit values of $\Sigma_{fac} = 3$ and $E_{frac} \approx 0.55$ to 0.65 (Figure 6.7) depending on which Monte-Carlo models are used (monomer, dimer etc.).

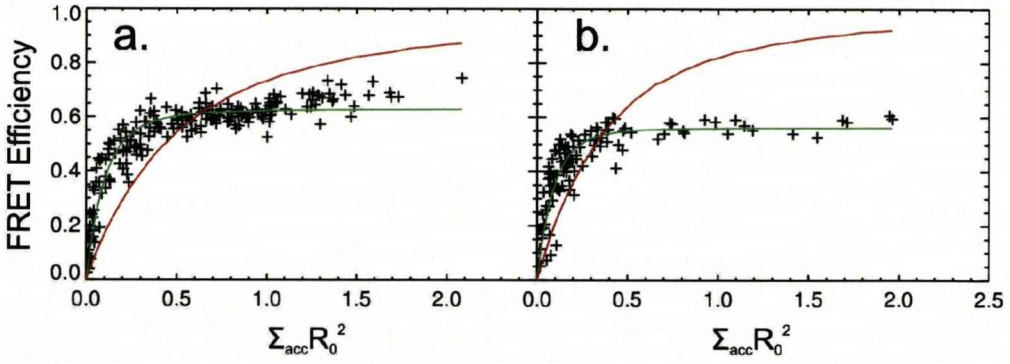

Figure 6.7 FRET efficiency as a function of acceptor density for high-affinity ErbB1 bound EGF-Alexa546 in **a.** wildtype and **b.** Ouabain treated A431 membranes. Red curves show the best fit Monte-Carlo model for $\Sigma_{fac} = 1$ and $E_{frac} = 1$ showing how a model neglecting these parameters cannot fit the steep rise or plateau. Green curves show the best fit Monte-Carlo model allowing Σ_{fac} and E_{frac} to vary. The values of E_{frac} returned are 0.55 and 0.65 for wildtype and depolarized cells respectively. In both cases the value of Σ_{fac} was 3.

The remaining datasets did not contain data over a sufficient Σ_{acc} range to constrain a three parameter model and confirm the presence of a plateau. As the availability of acceptor to ErbB1 receptors should not differ between experimental conditions (note that cholesterol depletion disrupts the formation of lipid rafts, but Dialkylcarbocyanine dyes are excluded from these regions anyway), and since the datasets that did constrain a three parameter model returned a consistent Σ_{fac} value, this value was adopted and fixed for all datasets

It was decided that the consistent E_{frac} values could be used to set a lower limit on this parameter applicable to the other datasets. As there is no correlation between ErbB1 distribution in the membrane and receptor binding affinity[36], the majority of receptors are monomeric and low-affinity receptors are rapidly diffusing[37], it was assumed that for the wildtype and depolarised membrane high- plus low-affinity datasets E_{frac} would be equal or greater than these values. For the other datasets the assumption was also made that $E_{frac} > 0.55$ because none of the other experimental conditions was expected to reduce the fraction of donors able to FRET further than that found in wildtype cells or cells with depolarised membranes for the following reasons. In PMA treated cells the high-affinity state is abolished. As low-affinity receptors have a substantially enhanced diffusion

rate[37] compared to high-affinity, receptors in PKC activated cells are less likely to be confined to particular areas of the membrane that restrict access to acceptor probes or to be part of large acceptor excluding protein complexes. E_{frac} must therefore be equal or larger than that for high-affinity wild type cells. Likewise, in DSA-treated cells ATP dependent processes are inhibited, including actin polymerisation. This would lead to a reduction in 'corralling' effects due to actin membrane-skeleton 'fences' that would compartmentalise the membrane[38]. Both ErbB1 receptors and C_{18}DiD molecules will be able to diffuse in the membrane with greater freedom and we again expect E_{frac} in DSA-treated cells to be larger than in wild-type cells. Cholesterol depletion releases receptors from rafts (an environment with low acceptor levels), which will also have the effect of increasing the fraction of donors able to transfer energy to an acceptor from that in wild type cells.

In order to estimate the variation caused by several Monte-Carlo simulation parameters that were usually fixed (shown in Table 6.2), a range of best fit distances of closest approach of EGF-Alexa 546 to the membrane for each dataset were obtained as follows. For A431 wildtype high-affinity and depolarised high-affinity datasets three parameter fits were obtained to get best fit values of d, Σ_{fac} and E_{frac}. These fits returned a value of $\Sigma_{fac} = 3$ as discussed above. The lowest of the measured values of E_{frac} came from the depolarised high-affinity datasets and this value was used as $E_{fracmin}$, the lower bound of E_{frac}. For the remaining datasets, one dimensional fits were performed to plane separation only, adopting fixed values of $E_{frac} = 1$ and $E_{fracmin}$ and $\Sigma_{fac} = 3$. These sets of three parameter and one parameter fits were carried out for various Monte-Carlo simulations and for both the entire acceptor density range for each dataset and for the range $0< \Sigma_{acc}R_0^2 <0.6$. For each dataset, the minimum and maximum best fit separations obtained from all these fits were used as the most robust constraint on the plane separation. These separation constraints are shown in Figure 6.9. It should be noted that Σ_{fac} values < 3 will result in the same pattern of distance changes with proportionally smaller separations in all cases. Σ_{fac} values >3 will result in distances >15 nm between EGF and the membrane which are inconsistent with the expected crystallographic structure of the ErbB1 ectodomain.

Multimer size	R_{excl}	Distribution algorithm
1	2	Hexagonal plus randomisation
1	1	Simulated annealing for $\Sigma_{acc} R_0^2 < 5$
1	1	Hexagonal plus randomisation
2	1	Hexagonal plus randomisation
4	1	Hexagonal plus randomisation

Table 6.2 The parameters varied in Monte Carlo simulations of donor and acceptor distributions to investigate the variation in the simulated results due to these parameters.

Note that the smallest value of d for which a FRET efficiency curve was simulated was for $d = 0.5$ nm, and that the curves converge rapidly for $d < 3$nm.

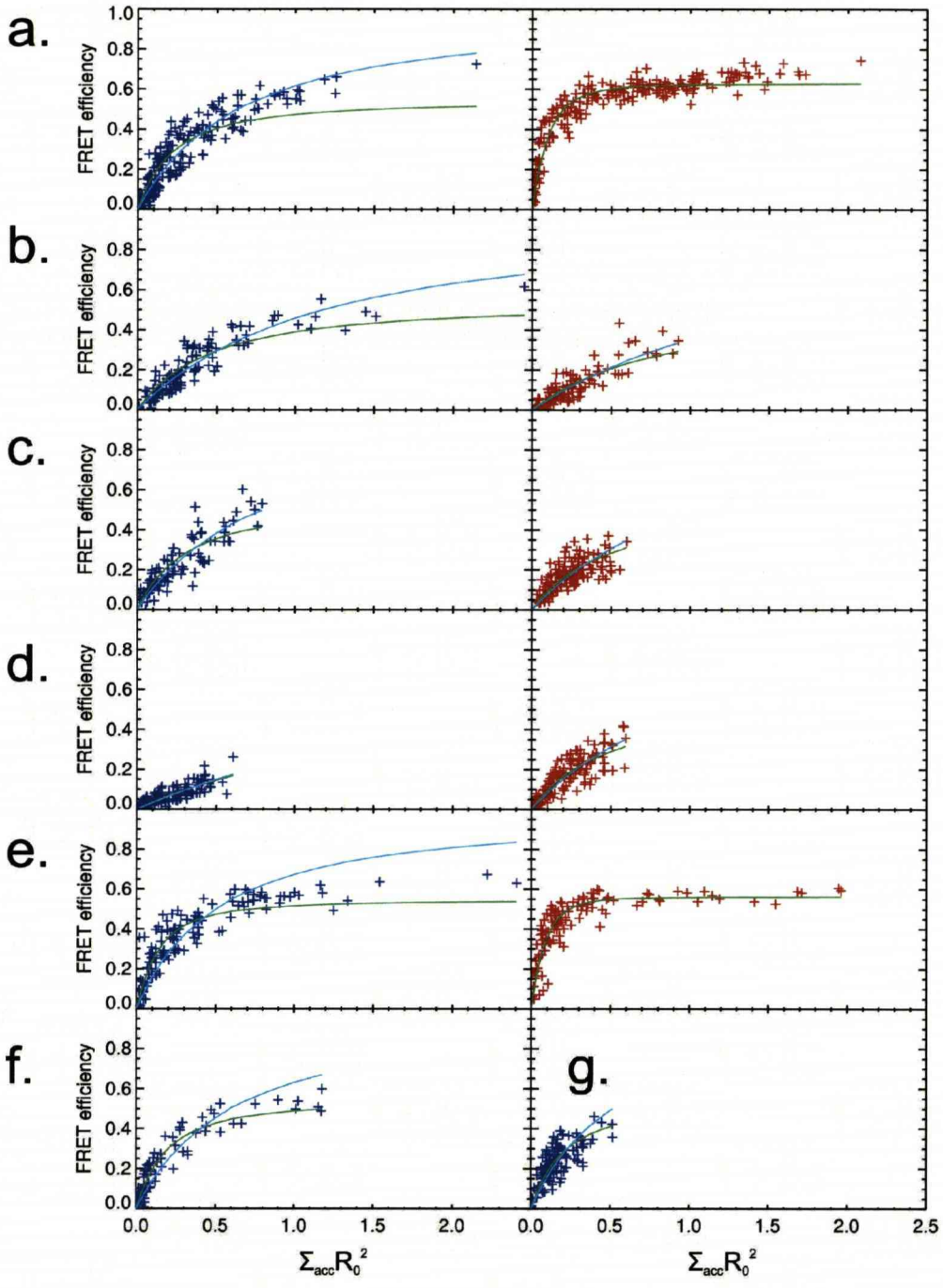

Figure 6.8 a-g. FRET efficiency between EGF-Alexa 546 and Vybrant C_{18}DiD as a function of acceptor density for **a.** wildtype A431 cells (fixed) **b.** DSA treated A431 cells (fixed) **c.** MβCD treated A431 cells (fixed) **d.** PMA treated A431 cells (fixed) **e.** Ouabain treated A431 cells (fixed) **f.** live wildtype A431 cells at 4°C **g.** Wildtype HeLa cells (fixed). Blue curves represent best fits when $\Sigma_{fac} = 3$ and $E_{frac} = 1$, green curves are best fit for $\Sigma_{fac} = 3$, $E_{frac} = E_{fracmin}$. Panels with green curve only (**a.** and **e.**): curve is best fit allowing separation d, Σ_{fac} and E_{frac} to vary. Blue data points represent measurements upon samples where EGF-Alexa 546 can bind to the entire population of ErbB1 receptors and red data points represent measurements upon samples where EGF-Alexa 546 is bound to high-affinity ErbB1 only.

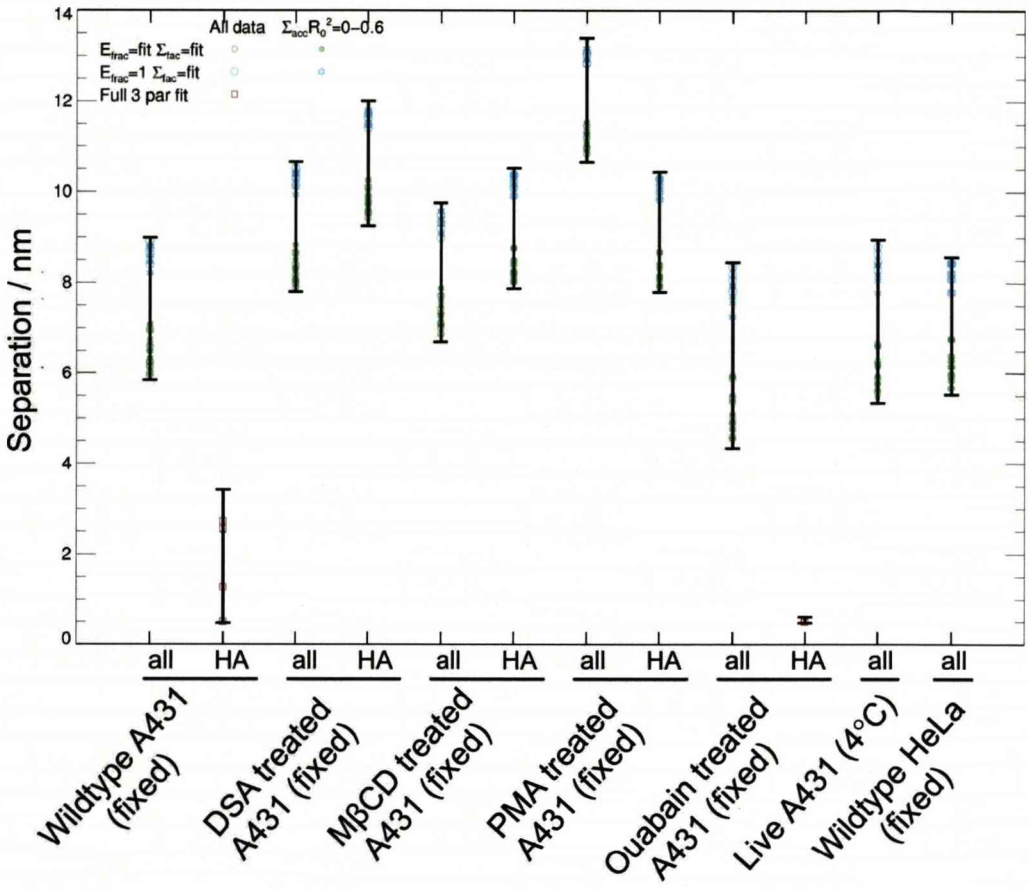

Figure 6.9 Range of best-fit plane separations, *d*, obtained from model variations for each dataset.

In the following five sections the ranges of best fit EGF-Alexa 546 - membrane distances of closest approach obtained by fitting the extended model to the data are discussed in the context of the intended functional disruptions of the ErbB1 receptor under the various experimental conditions.

6.3.3 Distance of closest approach of wildtype ErbB1 ligand binding sites to the cell surface in A431 and HeLa cells

Fitting the extended model to the data obtained in wildtype cells produces short distances of closest approach for ErbB1 receptor binding sites to the cell surface

when LA binding is blocked by mAb 2E9 (best fit <3.5 nm). The corresponding measurement when EGF can bind to all cell surface receptors is longer (6-9 nm). Consistent distances were found for high plus low affinity receptors in A431 and HeLa cells, which express $>10^6$ and $\sim 5x10^4$ receptors respectively. The results suggest that ErbB1 ectodomains adopt at least two different orientations with respect to the membrane[3]. If all ectodomains are locked in the extended crystallographic conformation then it is likely that high-affinity ectodomains lie flat on the membrane while low-affinity receptors stand proud.

6.3.4 Effect of inhibition of ATP dependent processes in A431 cells

EGF binding to ErbB1 receptors bound to mAb 2E9 is preserved after DSA treatment and the range of the distance of closest approach between these sites and the cell surface obtained by model fitting was 9-12 nm. These distances can only be achieved by an ectodomain locked in the extended conformation if the ectodomains were to rotate ~90° around an axis in the plane of the cell surface, from 'flat' to 'proud'. The corresponding data from the high plus low-affinity population returns a range of fitted distances of closest approach between 8 and 11 nm, which may be explained by the orientation change of the high-affinity receptors suggested above. The flat orientation associated with high-affinity receptors therefore appears to be actively maintained by ATP-dependent processes, but the results suggest these are not essential for high-affinity ligand binding.

6.3.5 Effect of A431 cell membrane cholesterol depletion

Cholesterol depletion should also preserve high-affinity binding[25, 36] but MβCD treated A431 cells do not return values of *d* consistent with flat orientations in mAb 2E9 challenged cells (8-11 nm). The range of distances of closest approach obtained from data from the entire population of ErbB1s in cholesterol depleted

cell membranes shows little difference from that seen in wildtype cells. These results imply that disruption of raft-mediated inhibitory interactions results in high-affinity ectodomains rotating towards proud orientations. By depleting cholesterol - a key component of rafts – from the plasma membrane using methyl-β-cyclodextrin (MβCD) raft-localised receptors are relieved of the inhibitory effects of the raft environment, resulting in more effective signalling and decreased ligand-induced internalisation[25]. These effects are partially due to enhanced kinase activity and partially due to an increase in the number of sites that are phosphorylated[25, 26, 36, 39].

6.3.6 Effect of PMA treatment (PKC activation)

The data from cells treated with PMA in which high-affinity binding sites had been pre-selected using mAb 2E9 again returned best fits for the distance of closest approach between the EGF binding site and the cell surface in the range 8 - 10 nm. However, unlike raft disruption, PMA treatment is also associated with even longer distances of closest approach (~11-13 nm) when mAb 2E9 is not bound to receptors. Although these distances are at the extreme range of that which could be expected from ErbB1 crystal structures, the length of the EGF-bound donor probe is ~ 2 nm and the model fits are therefore still consistent with known structures. The archetypical example of an intracellular interaction that attenuates ErbB1 signalling is that with protein kinase C (PKC) which is known to lead to phosphorylation of Thr-654 in the juxtamembrane region, abolition of high-affinity binding[23], tyrosine-kinase inhibition[23] and preferential receptor recycling[22]. The range of distances of closest approach returned by the model fitting suggests that PKC-ErbB1 interactions can result in the loss of flat ectodomain orientations. It is possible that both the orientations of high- and low-affinity ErbB1 ectodomains are regulated via intracellular interactions and that low-affinity reorientation may also be necessary to indirectly abolish high-affinity binding, by a mechanism not yet understood. Alternatively, flat conformations may be a separate consequence of the mechanism responsible for different ligand binding affinities.

6.3.7 Effect of depolarising the plasma membrane in A431 cells

PKC activators such as PMA cause transient membrane depolarisation[27]. As the membrane potential exerts electrostatic forces on membrane proteins, it is possible that the observed PMA-induced ectodomain re-orientation may be due to PKC modulation of ion channels. In order to check this, the Na^+/K^+ ATPase Ouabain was used to depolarise A431 cell membranes and see if a change in membrane potential independent of an intracellular ErbB1 binding event can alter the distance of closest approach of ligand binding sites to the membrane. Ouabain does not alter intracellular [Ca^{2+}] (figure 6.10) so it is assumed that it does not cause indirect activation of PKC.

The distances of closest approach returned by the model fitting are similar to those in wildtype A431 cells. The range of *d* returned for ErbB1 receptors bound to mAb 2E9 is very narrow and centred at a distance of closest approach ~ 0.5 nm. However, this is likely to be a consequence of the fact that the simulated model curves become difficult to distinguish for values of *d* less than 5 nm.

Membrane depolarisation does not appear to affect the orientation of either high or low-affinity ErbB1 ectodomains and changes in the membrane potential therefore do not explain the PMA-induced variation in the distance of closest approach of EGF binding sites to the membrane. It cannot be ruled out that these differences are directly attributable to PKC binding to ErbB1. A possible mechanism for this sort of 'priming' of ectodomain orientation by intracellular interactions with PKC would involve phosphorylation of Thr-654 causing re-orientation of ErbB1's intracellular domain[40]. If the connection between the transmembrane and juxtamembrane regions isn't completely flexible, this re-orientation would be sterically sensed by the transmembrane regions[41] allowing intracellular interactions to alter ectodomain orientations via a change in orientation of the transmembrane domain. In support of steric sensing, the same mechanism operating in the opposite direction would provide a natural mechanism for the activation of preformed inactive ErbB1 homodimers by EGF[42].

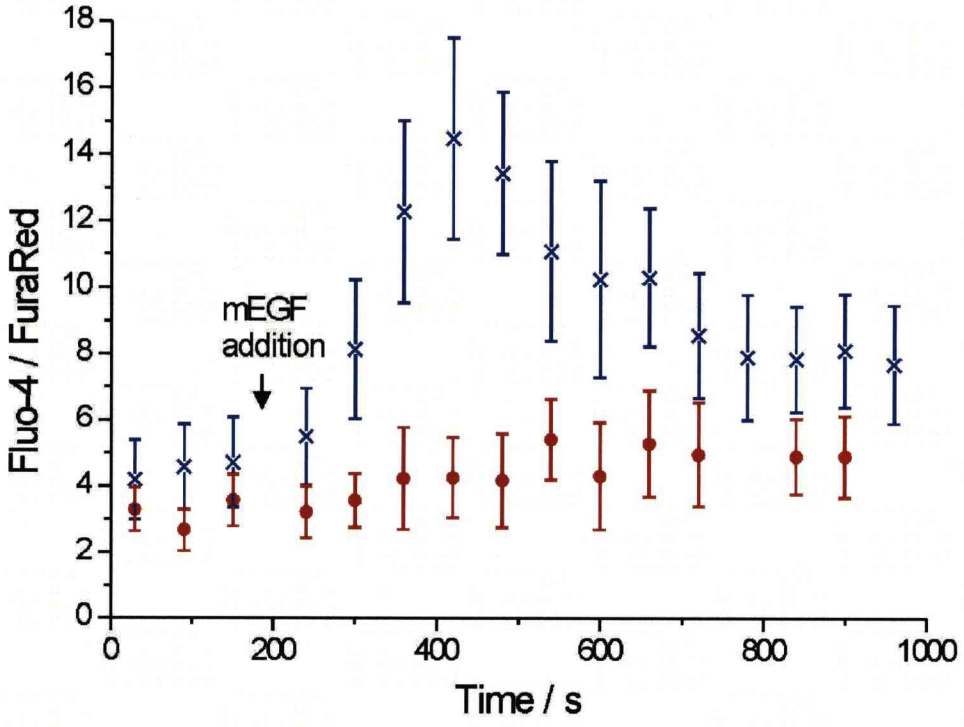

Figure 6.10 The concentration of intracellular calcium as reported by confocal ratio imaging of Fluo-4/FuraRed fluorescence intensity after the addition of 200nM mEGF at 21°C. Data points and error bars represent the mean Fluo-4/FuraRed fluorescence intensity ratio and standard deviation respectively of a sample of 52 wildtype A431 cells (blue crosses) or 41 Ouabain treated A431 cells (red dots). There is little difference in intracellular calcium concentration prior to the addition of EGF as a result of membrane depolarisation but the subsequent transient increase in calcium concentration normally seen in response to EGF is suppressed.

6.3.8 FRET between EGF-Alexa 546 and EGF-Atto 647N in A431 cells

The efficiency of FRET between ErbB1 bound mEGF-Alexa 546 and mEGF-Atto 647 (R_0=5.6 nm) added in a 1:1 ratio to A431 cells is shown in Figure 6.11. Error bars represent the S.D. of 25 cells. High-affinity receptor data is red and data derived from the entire receptor population (including contributions from both high (<10%) and low (>90%) affinity sites) is blue.

There is a clear difference in FRET efficiency between the high affinity and entire receptor population, but all the FRET efficiencies are below ~0.1. In order to begin to understand the cause of these low FRET efficiencies it is first useful to consider the result that would be expected if all ErbB1 receptors were interacting as back to back dimers.

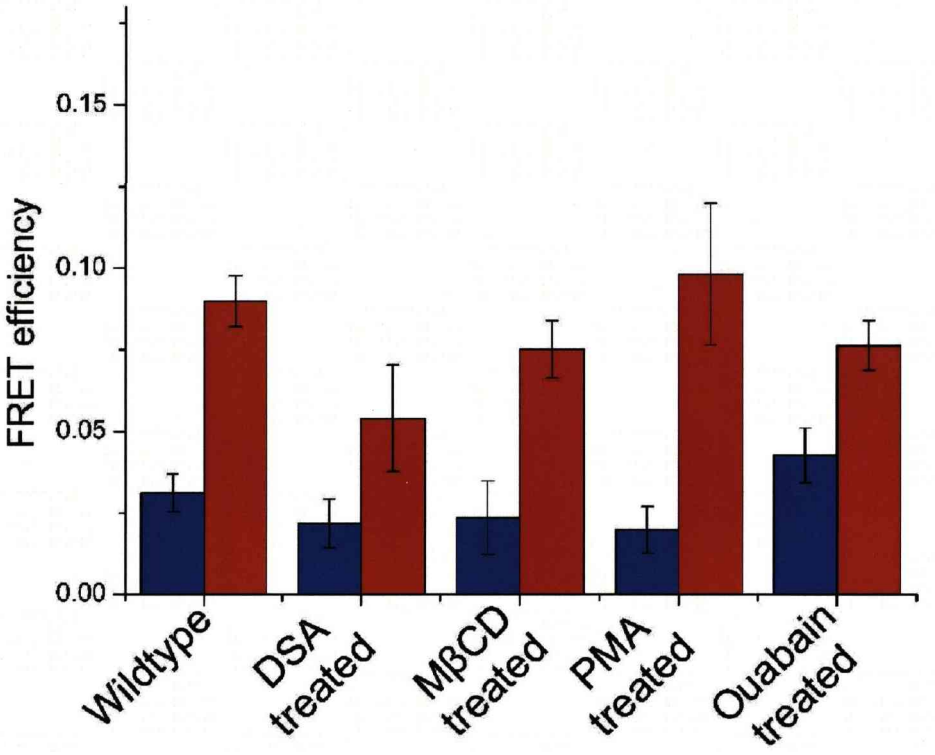

Figure 6.11 FLIM-FRET of mEGF-Alexa 546 and mEGF-Atto 647N bound to the entire cell surface ErbB1 population (blue) or when binding to low-affinity receptors has been blocked with mAb-2E9 (red) in wild-type and treated A431 cells.

The separation of ErbB1 ligand binding sites in the crystallographic back to back dimer is ~ 11nm. The FRET efficiency that would be expected from an ensemble of such dimers can be estimated as follows:

The efficiency of FRET for a single donor – acceptor pair separated by 11nm with $R_0 = 5.6$ nm can be easily calculated

$$E_{FRET}^{SP} = \frac{R_0^6}{R_0^6 + r^6} = \frac{5.6^6}{5.6^6 + 11^6} = 0.017 \qquad \text{Eqn. 6-7}$$

This is in the region where the efficiency of FRET is insensitive to changes in donor-acceptor separation, and as can be seen in figure 6.11 the standard deviation of the ensemble FRET measurements can be of the same order or greater.

However, this FLIM-FRET experiment measures E_{FRET} as a reduction in the fluorescence lifetime of an ensemble of EGF labelled donors and acceptors competing for the same ligand binding sites. Some dimers would also be doubly occupied by donors or acceptors. The probability of having a given number of acceptors (w) in an oligomer of n receptors can be estimated using a binomial distribution

$$P(w) = \left[\frac{n!}{(n-w)!\,w!}\right] p^w q^{n-w} \qquad \text{Eqn. 6-8}$$

For a 1:1 donor:acceptor ratio and receptor dimers n=2 and the probability of a site binding an acceptor, p, and the probability of binding a donor, q, are equal with p=q=0.5. Substitution into Eqn. 6-8 yields $P(1)$=0.5 and $P(0)$=0.25 (the case where w=2 in of no consequence as oligomers containing acceptors only remain unobserved). Therefore the fraction of observed dimers occupied by both a donor and acceptor would be given by

$$\frac{P(1)}{P(0) + P(1)} = 0.67 \qquad \text{Eqn. 6-9}$$

The measured donor lifetime in the presence of acceptor will be the expectation value of the contributions of dimers with both donor and acceptor and donor only

$$< \tau_{DA} >= 0.67\tau_{DA}^{SP} + 0.33\tau_D \qquad \text{Eqn. 6-10}$$

where τ_{DA}^{SP} is the donor lifetime that would be expected from the FRET efficiency of a single FRET pair in a dimer and τ_D is the donor lifetime in the absence of acceptor. As the measured FRET efficiency is given by

$$E_{FRET} = 1 - \frac{< \tau_{DA} >}{\tau_D} \qquad \text{Eqn. 6-11}$$

and

$$E_{FRET}^{SP} = 1 - \frac{\tau_{DA}^{SP}}{\tau_D} = 0.017 \qquad \text{Eqn. 6-12}$$

$E_{FRET} = 0.011$ would be expected for a population consisting entirely of back to back ErbB1 dimers. It is clear from Figure 6.11 that the measured FRET efficiencies are higher than this for measurements of both the entire receptor population and high-affinity receptors. Therefore the low but non-negligible FRET efficiencies observed cannot be due to back-to-back dimers alone. Single molecule fluorescence indicates that they are not due to a single population of oligomers with an inter-ligand binding site separation ~8 nm[13]. It is therefore more reasonable to suspect that there is always a large proportion of ErbB1 monomers or a large population of ErbB1 existing as part of hetero-oligomers with other non-EGF binding members of the ErbB family present in A431 cells. Either of these scenarios will produce a large donor-only population in the measured donor lifetime that would artificially reduce the measured FRET efficiency and could mask a smaller populations of donors placed in closer proximity to acceptors by other interactions.

Consequently it is not appropriate to convert the FRET efficiencies in figure 6.11 to mean donor-acceptor separations. However, the results do semi-quantitatively reflect differences in the proportions of oligomers and the kind of receptor

interactions present in the observed receptor populations that can give insight into the effects of the extracellular conformational changes indicated in sections 6.3.2 to 6.3.5. For example the higher FRET efficiency seen between donor and acceptor-labelled EGF for wildtype high-affinity receptors than the entire population suggests that this class contains a larger proportion of receptor-receptor interfaces different to the crystallographic back-to-back dimer, that place ligand binding sites <10nm apart. In order to determine which datasets had significantly different FRET efficiencies, a 2 sample independent t-test was performed, the results of which are shown in table 6.3. The 2 sample independent t-test is used to determine if the statistical means of a variable property of two populations are equal. The two data sets are assumed to have been drawn from populations that follow a normal distribution with constant variance.

From the results of the t-test the following can be concluded about the mean FRET efficiencies between mEGF-Alexa 546 and mEGF-Atto 647N (added to A431 cells in 1:1 ratio and competing for available ErbB1 binding sites) to a significance level of 0.05.

1) Under all experimental conditions, when high-affinity receptors only were available for EGF binding the mean FRET efficiency obtained is higher than the corresponding FRET efficiency obtained when the entire receptor population was available.
2) The mean FRET efficiency obtained when the entire receptor population is available for ligand binding is higher in cells with depolarised plasma membranes than the other experimental conditions
3) Two pairs of experimental conditions do not produce mean FRET efficiencies between ligands that are significantly different for high-affinity receptors. Cholesterol depleted cells and cells with depolarized membranes, and wildtype cells and PKC activated cells

		All receptors					High-affinity				
		(a)	(b)	(c)	(d)	(e)	(a)	(b)	(c)	(d)	(e)
All Receptors	(a)	-	0.7440	0.0140	0.7190	0.5260	0.0000	0.0000	0.0000	0.0004	0.0000
	(b)	-	-	0.0205	0.9250	0.8370	0.0000	0.0000	0.0000	0.0005	0.0000
	(c)	-	-	-	0.0369	0.0143	0.0000	0.0000	0.00002	0.0062	0.00001
	(d)	-	-	-	-	0.9430	0.0000	0.0000	0.00001	0.00086	0.0000
	(e)	-	-	-	-	-	0.0000	0.0000	0.00001	0.00094	0.000
High-Affinity	(a)	-	-	-	-	-	-	0.0209	0.0385	0.00206	0.0732
	(b)	-	-	-	-	-	-	-	0.6950	0.0178	0.0120
	(c)	-	-	-	-	-	-	-	-	0.0292	0.0072
	(d)	-	-	-	-	-	-	-	-	-	0.00107
	(e)	-	-	-	-	-	-	-	-	-	-

Key:
(a) Wildtype cells
(b) Cells in which cholesterol is depleted using MβCD
(c) Cells treated with Ouabain to depolarised plasma-membranes
(d) Cells in which phosphorylation is inhibited using DSA
(e) Cells in which PKC is activated by PMA

Null hypothesis: $mean(A) - mean(B) = 0$
Alternative hypothesis: $mean(A) - mean(B) \neq 0$

Table 6.3 Results of 2-sample independent t-tests on EGF-Alexa 546 / Atto 647N FLIM-FRET datasets. The table shows the observed significance (P-value) - the probability of obtaining a test value as extreme from that expected by the null hypothesis by chance – for each pair of datasets. At a significance level of 0.05, dataset pairs whose means are significantly different are highlighted.

Point 1) is also valid to a significance level of 0.01. The results of the t-test suggest that most of the different experimental conditions cause changes in the oligomerisation states present in the population of high-affinity receptors from wildtype cells. The higher FRET efficiency measured between donors and acceptors bound to high-affinity ErbB1s indicates that this population of

receptors generally contains a higher proportion of non back-to-back interfaces than the low-affinity population. Depolarisation of the plasma membrane appears to have the effect of increasing non back-to-back interfaces in low-affinity receptors. Blocking of ATP production by DSA and the consequent dephosphorylation of receptors appears to reduce the proportion of non back-to-back receptors in the high-affinity population.

The observation of non back-to-back interfaces in agreement with the results of single molecule FRET experiments that show that in wildtype A431 cells the separation of EGF binding sites in ErbB1 complexes can be less than 5.5 nm[13]. The only solved crystallographic interface capable of explaining the simultaneous occurrence of short inter-ligand separations and a short distance of closest approach of EGF to the cell surface is head-to-head dimer previously rejected as being unphysiological[4]. However, molecular dynamics simulations of extended ErbB1 extracellular domains (based upon the 1IVO crystal structure[5] with missing domain IV residues reconstructed based upon the domain IV co-ordinates of from the tethered 1NQL crystal structure[7] with transmembrane α-helices in a phospholipids bilayer have shown that ErbB1 extracellular domains can lie almost flat with respect to the membrane in at least three different topologies, two of which contain a modified head-to-head interface that is more stable than the one first seen in the 1MOX crystal structure[4] (unpublished observations made by Johannes Kästner and Martyn Winn of Collaborative Computational Project 4). One of the original objections to the head-to-head dimer was the lack of symmetry compared to the back-to-back dimer. However, it has recently been shown that the conformation of active ErbB1 kinase domains is an asymmetric dimer[6]. In light of these results and the results of the bi-directional FRET measurements, it is possible that the head-to-head ErbB1 ectodomain interface is indeed physiologically relevant.

6.3.9 Relating the position of EGF binding sites to receptor oligomerisation and tyrosine phosphorylation

It is not possible to decide from the FRET data alone whether differences in the ensemble FRET efficiency between donor and acceptor-labelled EGF bound to ErbB1 are due to a change in the proportion of monomers, dimers and oligomers, or due to a change in the available interactions. Therefore the data from the bi-directional FRET method was compared to the results of gel electrophoresis of ErbB1 receptors from cells treated to the same experimental conditions outlined in section 6.2.4 before receptor cross-linking and cell lysis. These experiments were performed by Dr Selene Roberts and Dr Sarah Needham at the STFC Daresbury Laboratory and the results are reprinted in this section (figure 6.12) with their kind permission.

Gel electrophoresis separates proteins by mass which can then be probed with anti-ErbB1 and anti-mouse conjugated to horseradish peroxidase and developed to show relative proportions of monomers, dimers and larger oligomers in the lysed cells. Alternatively the blots can be probed with antibodies that bind to phosphorylated ErbB1 tyrosine residues to show the phosphorylation state of the receptors. The developed blots can be quantified to provide estimates of the proportion of receptors in each band or the average amount of tyrosine phosphorylation. Although no firm conclusions can be derived from these semi-quantitative western blots, comparison with the bi-directional FRET results suggests how the variations in ErbB1 structure observed under the different experimental conditions might be related to receptor function. Figure 6.10a, c and e shows images of the probed blots. Receptor monomers appear just above the 171 kDa marker and dimers appear between the 268 kDa and 460 kDa markers. The band above 460 kDa is attributed to oligomers larger than dimers as the exact mass of the receptor complexes in this band could not be determined. The unmarked band in the western blot probed with anti-ErbB1 (figure 6.12a) at 270 kDa (which is not a multiple of the ErbB1 monomer mass) could be due to ErbB1 monomers crosslinked to a ~ 100 kDa protein or protein fragment.

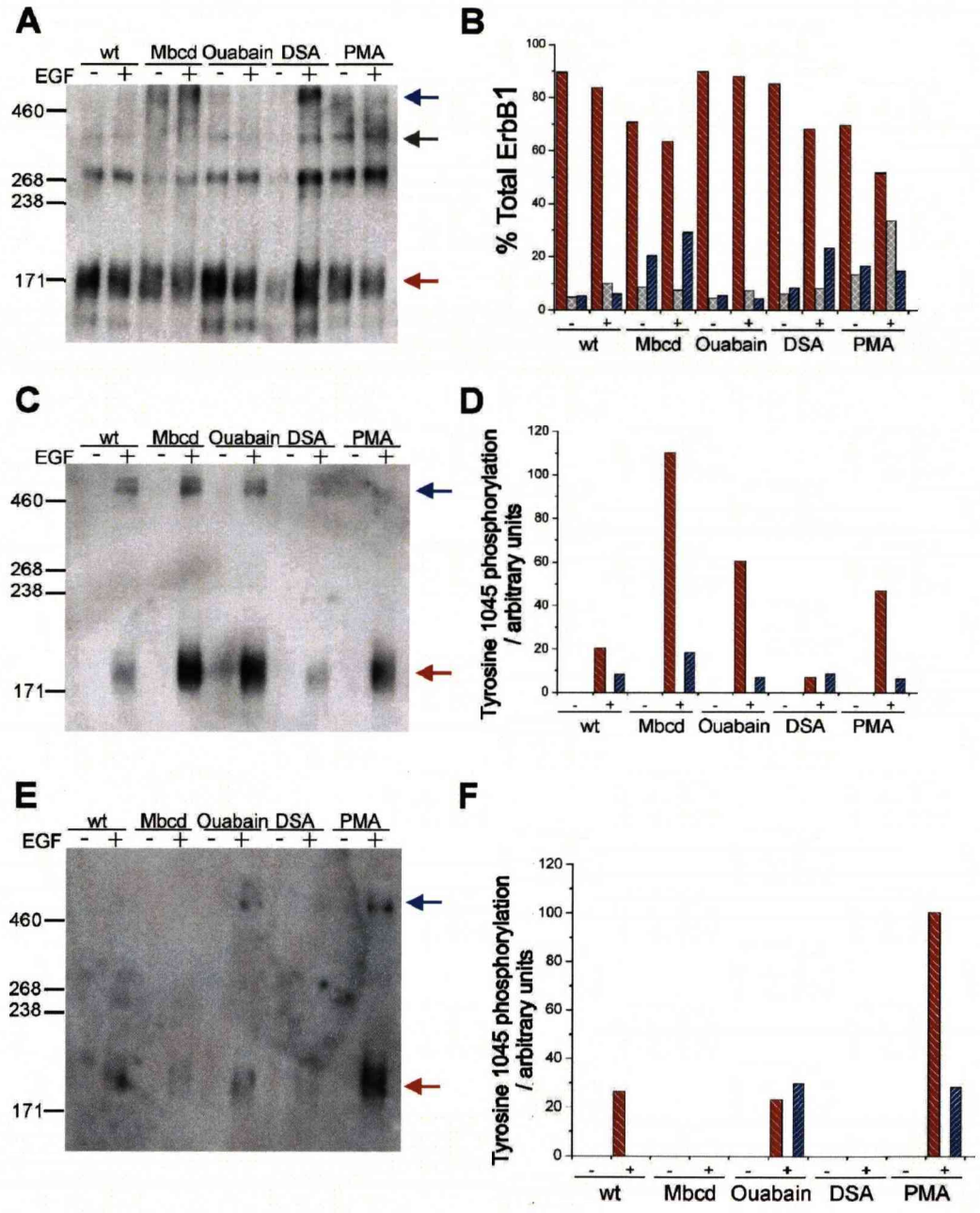

Figure 6.12 Semi-quantified western blots of cross-linked ErbB1 immunoprecipitates under resting (-) and EGF-stimulated conditions (+). **a.** image of the western blot probed with antiErbB1 **c.** and **e.** are images of western blots probed with anti-ErbB1 phosphotyrosine-1045 where EGF is allowed to bind to all receptors or high-affinity receptors only. Colour coded arrows indicate ErbB1 monomer (red), dimer (grey) and oligomer (blue) bands respectively. **b**, **d**. and **f**. are the corresponding semi-quantitative results and follow the same colour code.

From figure 6.12a and b it can be seen that in the absence of ligand the majority of high-affinity ErbB1s in wildtype A431 in the blot are monomers with a small

proportion of dimers and oligomers. When stimulated with EGF the proportion of oligomers increases, but the majority of receptors are still monomers. Combined with the inter-EGF FRET results discussed in the previous section, this suggests that low-affinity ErbB1 receptors are either monomers or back-to-back dimers. Only the small proportion of high-affinity receptor complexes would then be expected to contain head-to-head interfaces. As high-affinity receptors constitute < 5 % of cell surface ErbB1s, this would help to explain why ErbB1 receptors with a point mutation designed to disrupt the head-to-head interface were not found to possess altered functional characteristics whereas a point mutation designed to disrupted the back-to-back interface eliminates high affinity binding and dimerisation[4]. Also consistent with this is the observation that a distance of closest approach that would preclude the head-to-head interface in dephosphorylated high-affinity receptors (see section 6.3.3) does not result in the loss of high-affinity binding.

Comparison of bi-directional FRET data and the biochemical results of the western blots do not provide any direct evidence that the head-to-head interface exists between ErbB1 receptors *in situ*, but it is reasonable to propose that the dimers and oligomers of high-affinity ErbB1s may contain them. Evidence exists that ErbB1 receptors form tetramers[9, 10, 13]. These could either be formed by combinations of back-to-back oligomers placed side by side or asymmetrically by utilising the head-to-head interface. A combination of bi-directional FRET data, fully quantitative biochemical results and molecular modelling could be used in the future to correlate the possible ErbB1 topologies with the different experimental conditions.

Although the different complexes discussed might represent only a fraction of all the possible receptor states[17], the results of the bi-directional FRET method provide a starting point to correlate receptor topology with function. Phosphorylation patterns of intracellular ErbB1 tyrosine residues govern the signalling outcome of the activated receptors[43]. The results of the western blots probing the degree of phosphorylation of different tyrosine residues can therefore provide additional information regarding the signalling outcome from activated ErbB1 receptors under the different experimental conditions that can be related

to the bi-directional FRET results. Tyr-1045 is particularly important as it is the recruiting site for c-Cbl which can ubiquitinate ErbB1, targeting it for trafficking to late endosomes[44] although cbl dissociation and dephosphorylation of Tyr-1045 is necessary for ErbB1 to be degraded in lysosomes[45]. This is a major method for the downregulation of ErbB1 signalling. It can be seen in figure 6.10c-f that the different receptor topologies associated with the different experimental conditions show different degrees of Tyr-1045 phosphorylation. Significantly, it appears that receptor degradation is inhibited under the conditions which also result in the loss of flat ectodomain orientations (cholesterol depletion and PKC activation). This suggests the intriguing possibility that different ectodomain conformations might be associated with different signalling outcomes and may play a part in determining the fate of the receptor.

6.4 Conclusions and summary

In this chapter a combination of FRET measurements probing ErbB1 receptor interactions lateral to the membrane and the orientation of individual receptors with respect to the membrane has provided evidence of previously unknown variations in the ErbB1 ectodomain topology that may be associated with interactions with intracellular effectors. In turn these different ectodomain topologies appear to lead to different signalling outcomes upon ligand binding, demonstrated by differential phosphorylation of ErbB1 intracellular tyrosine residues shown in complementary biochemical data obtained under the same experimental conditions.

The different experimental conditions used disrupt normal ErbB1 interactions with intracellular effectors that have been previously shown to be essential in the modulation of kinase activation, early ErbB1 signalling events and the regulation of EGF binding affinity. It is possible that 'priming' of ErbB1 ectodomains by intracellular interactions regulate ErbB1 signal transduction in a manner analogous to that seen in the integrin receptor[19]. Such priming would provide a

method for the cellular programming of the ErbB1 receptor population to produce different signalling responses to the same EGF signalling molecule and a possible explanation of the complex functionality of ErbB1 at the initial stages of signalling. From the results in this chapter it was proposed that steric regulation of ErbB1 kinase domains (brought about by varying transmembrane domain orientations caused by the primed ErbB1 ectodomain topologies) might result in preferential access of different tyrosine residues in the c-terminal tail of receptors to the kinase domains. The simple on/off nature of the ligand binding event would then lead to different signalling outcomes dependent upon ErbB1 priming.

Finally, as receptor degradation is the ultimate path for downregulation of activated receptors, the ability to modulate c-Cbl-mediated degradation pathways hinted at by the data regarding Tyr-1045 phosphorylation is of particular interest. It is feedback mechanisms such as this that are defective in some cancers[46] or used by cancerous cells to bypass treatments aimed at oncogenic targets[47]. Consequently, primed ErbB1 ectodomain configurations should they exist, could be a robust target for anti-cancer treatments.

References

1. Carpenter, G. Receptors for Epidermal Growth Factor and Other Polypeptide Mitogens. Annual Review of Biochemistry 56, 881-914 (1987).
2. Ullrich, A. & Schlessinger, J. Signal transduction by receptors with tyrosine kinase activity. Cell 61, 203-212 (1990).
3. Ferguson, K. M. et al. EGF Activates Its Receptor by Removing Interactions that Autoinhibit Ectodomain Dimerization. Molecular Cell 11, 507-517 (2003).

4. Garrett, T. P. et al. Crystal structure of a truncated epidermal growth factor receptor extracellular domain bound to transforming growth factor alpha. Cell 110, 763-776 (2002).

5. Ogiso, H. et al. Crystal structure of the complex of human epidermal growth factor and receptor extracellular domains. Cell 110, 775-787 (2002).

6. Zhang, X., Gureasko, J., Shen, K., Cole, P. A. & Kuriyan, J. An Allosteric Mechanism for Activation of the Kinase Domain of Epidermal Growth Factor Receptor. Cell 125, 1137-1149 (2006).

7. Ferguson, K. M. Active and inactive conformations of the epidermal growth factor receptor. Biochemical Society Transactions 32, 742-745 (2004).

8. Ferguson, K. M. Structure-Based View of Epidermal Growth Factor Receptor Regulation. Annual Review of Biophysics 37, 353-373 (2008).

9. Clayton, A. H. A. et al. Ligand-induced Dimer-Tetramer Transition during the Activation of the Cell Surface Epidermal Growth Factor Receptor-A Multidimensional Microscopy Analysis. Journal of Biological Chemistry 280, 30392-30399 (2005).

10. Furuuchi, K., Berezov, A., Kumagai, T. & Greene, M. I. Targeted Antireceptor Therapy with Monoclonal Antibodies Leads to the Formation of Inactivated Tetrameric Forms of ErbB Receptor. Journal of Immunology 178, 1021-1029 (2007).

11. Martin-Fernandez, M., Clarke, D. T., Tobin, M. J., Jones, S. V. & Jones, G. R. Preformed Oligomeric Epidermal Growth Factor Receptors Undergo an Ectodomain Structure Change during Signaling. Biophysical Journal 82, 2415-2427 (2002).

12. Sako, Y., Minoghchi, S. & Yanagida, T. Single-molecule imaging of EGFR signalling on the surface of living cells. Nature Cell Biology 2, 168 - 172 (2000).

13. Webb, S. E. D. et al. Single molecule imaging and FLIM show different structures for high and low-affinity EGFRs in A431 cells. Biophysical Journal 94, 803-819 (2008).

14. Whitson, K. B., Beechem, J. M., Beth, A. H. & Staros, J. V. Preparation and characterization of Alexa Fluor 594-labeled epidermal growth factor for fluorescence resonance energy transfer studies: application to the epidermal growth factor receptor. Analytical Biochemistry 324, 227-236 (2004).

15. Jones, J. T., Akita, R. W. & Sliwkowski, M. X. Binding specificities and affinities of egf domains for ErbB receptors. FEBS Letters 447, 227-231 (1999).

16. Carraway III, K. L., Koland, J. G. & Cerione, R. A. Location of the Epidermal Growth Factor Binding Site on the EGF Receptor. A Resonance Energy Transfer Study. Biochemistry 29, 8741-8747 (1990).

17. Lammerts van Bueren, J. J. et al. The antibody zalutumumab inhibits epidermal growth factor receptor signaling by limiting intra- and intermolecular flexibility. PNAS 105, 6109-6114 (2008).

18. Ullrich, A. & Schlessinger, J. Signal transduction by receptors with tyrosine kinase activity. Cell 61, 203-212 (1990).

19. Kim, M., Carman, C. V. & Springer, T. A. Bidirectional transmembrane signalling by cytoplasmic domain separation in integrins. Science 301, 1720-1725 (2003).

20. Barisas, B. G., Wade, W. F., Jovin, T. M., Arndt-Jovin, D. & Roess, D. A. Dynamics of molecules involved in antigen presentation: effects of fixation. Molecular Immunology 36, 701-708 (1999).

21. Defize, L. H. K. et al. Signal Transduction by Epidermal Growth Factor Occurs Through the Subclass of High Affinity Receptors. The Journal of Cell Biology 109, 2495-2507 (1989).

22. Bao, J. et al. Threonine Phosphorylation Diverts Internalized Epidermal Growth Factor Receptors from a Degradative Pathway to the Recycling Endosome. The Journal of Biological Chemistry 275, 26178-26186 (2000).

23. Davis, R. J. Independent Mechanisms Account for the Regulation by Protein Kinase C of the Epidermal Growth Factor Receptor Affinity and Tyrosine-Protein Kinase Activity. The Journal of Biological Chemistry 263, 9462-9469 (1988).

24. Hunter, T., Ling, N. & Cooper, J. A. Protein kinase C phosphorylation of the EGF receptor at a threonine residue close to the cytoplasmic face of the plasma membrane. Nature 311, 480-483 (1984).

25. Pike, L. J. & Casey, L. Cholesterol Levels Modulate EGF Receptor-Mediated Signaling by Altering Receptor Function and Trafficking. Biochemistry 41, 10315-10322 (2002).

26. Westover, E. J., Covey, D. F., Brockman, H. L., Brown, R. E. & Pike, L. J. Cholesterol Depletion Results in Site-specific Increases in Epidermal Growth

Factor Receptor Phosphorylation due to Membrane Level Effects: Studies With Cholesterol Enantiomers. The Journal of Biological Chemistry 278, 51125-51133 (2003).

27. Pandiella, A., Magni, M., Lovisolo, D. & Meldolesi, J. The effect of epidermal growth factor on membrane potential. Rapid hyperpolarization followed by persistent fluctuations. The Journal of Biological Chemistry 264, 12914-12921 (1989).

28. Wolber, P. K. & Hudson, B. S. An analytic solution to the Forster energy transfer problem in two dimensions. Biophysical Journal 28, 197-210 (1979).

29. Corry, B., Jayatilaka, D. & Rigby, P. A Flexible Approach to the Calculation of Resonance Energy Transfer Efficiency between Multiple Donors and Acceptors in Complex Geometries. Biophysical Journal 89, 3822-3836 (2005).

30. Clayton, A. H. A., Tavarnesi, M. L. & Johns, T. G. Unligated Epidermal Growth Factor Receptor Forms Higher Order Oligomers within Microclusters on A431 Cells That Are Sensitive to Tyrosine Kinase Inhibitor Binding. Biochemistry 46, 4589-4597 (2007).

31. van Belzen, N. et al. Direct Visualization and Quantitative-Analysis of Epidermal Growth Factor-Induced Receptor Clustering. Journal of Cellular Physiology 134, 413-420 (1988).

32. Press, W. H., Teukolsky, S. A., Vetterling, W. T. & Flannery, B. P. Numerical Recipes in C. The Art of Scientific Computing. Second Edition (Cambridge, 1996).

33. Kahya, N., Scherfeld, D., Bacia, K., Poolman, B. & Schwille, P. Probing Lipid Mobility of Raft-exhibiting Model Membranes by Fluorescence Correlation Spectroscopy. The Journal of Biological Chemistry 278, 28109-28115 (2003).

34. Schuler, B., Lipman, E. A., Steinbach, P. J., Kumke, M. & Eaton, W. A. Polyproline and the "spectroscopic ruler" revisited with single-molecule fluorescence. PNAS 102, 2754-2759 (2005).

35. Spink, C. H., Yeager, M. D. & Feigenson, G. W. Partitioning behavior of indocarbocyanine probes between coexisting gel and fluid phases in model membranes. Biochimica et Biophysica Acta (BBA) - Biomembranes 1023, 25-33 (1990).

36. Ringerike, T., Blystad, F. D., Levy, F. O., Madshus, I. H. & Stang, E. Cholesterol is important in control of EGF receptor kinase activity but EGF receptors are not concentrated in caveolae. Journal of Cell Science 115, 1331-1340 (2002).

37. Rees, A. R., Gregoriou, M., Johnson, P. & Garland, P. B. High affinity epidermal growth factor receptors on the surface of A431 cells have restricted lateral diffusion. Embo Journal 3, 1843-7 (1984).

38. Umemura, Y. M. et al. Both MHC Class II and its GPI-Anchored Form Undergo Hop Diffusion as Observed by Single-Molecule Tracking. Biophysical Journal 95, 435-450 (2008).

39. Furuchi, T. & Anderson, R. G. W. Cholesterol Depletion of Caveolae Causes Hyperactivation of Extracellular Signal-related Kinase (ERK). The Journal of Biological Chemistry 273, 21099-21104 (1998).

40. Thiel, K. W. & Carpenter, G. Epidermal growth factor receptor juxtamembrane region regulates allosteric tyrosine kinase activation. PNAS 104, 19238-19243 (2007).

41. Moriki, T., Maruyama, H. & Maruyama, I. N. Activation of preformed EGF receptor dimers by ligand-induced rotation of the transmembrane domain. Journal of Molecular Biology 311, 1011-1026 (2001).

42. Tao, R.-H. & Maruyama, I. N. All EGF(ErbB) receptors have preformed homo- and heterodimeric structures in living cells. Journal of Cell Science 121, 3207-3217 (2008).

43. Sweeney, C. & Carraway, K. L. Ligand discrimination by ErbB receptors: differential signaling through differential phosphorylation site usage. Oncogene 19, 5568-5573 (2000).

44. de Melker, A. A., van der Horst, G. & Borst, J. c-Cbl directs EGF receptors into an endocytic pathway that involves the ubiquitin-interacting motif of Eps15. Journal of Cell Science 117, 5001-5012 (2004).

45. Pennock, S. & Wang, Z. A Tale of Two Cbls: Interplay of c-Cbl and Cbl-b in Epidermal Growth Factor Receptor Downregulation. Molecular Cell Biology 28, 3020-3037 (2008).

46. Shtiegman, K. et al. Defective ubiquitinylation of EGFR mutants of lung cancer confers prolonged signaling. Oncogene 26, 6968–6978 (2007).

47. Sergina, N. V. et al. Escape from HER-family tyrosine kinase inhibitor therapy by the kinase-inactive HER3. Nature 445, 437-441 (2007).

7 Conclusions and Outlook

Experimental research into biological problems is an increasingly interdisciplinary endeavour. It requires combination of the biological and biochemical skills required to prepare samples for investigation with the knowledge to develop and correctly deploy physical techniques to probe the properties of the biological system of interest. Sometimes it also requires computational simulations to build models from, or even interpret the experimental results. The need to relate the structure to the function of interacting proteins is of major importance for the understanding of human diseases, but it is clear that it will only be possible to do this by observing the structure of functioning proteins in their natural environments.

In this thesis a method based on FRET was developed to investigate the 3D structure of membrane proteins in cultured cells. The method involves two different FRET experiments performed under identical experimental conditions that provide information regarding the lateral topology of interacting membrane proteins and the distance of closest approach of a specifically labelled site on the protein to the cell surface. Obtaining spatial information in two directions in the frame of the plasma membrane is a step forward from previous studies which have only attempted to probe one direction or the other. The development of a microscopy based technique suitable for estimating the distance of closest approach of a protein to the plasma membrane in adherent cells was made possible by the implementation of the multidimensional, multicolour confocal microscope described in chapter 4.

The motivation for developing the bi-directional FRET method was to investigate the structure of signalling ErbB1 receptor complexes and this biological system was used to demonstrate the method using fixed cancer cells in chapter 6. The bi-directional FRET method was successfully able to show that the ligand binding sites of ErbB1 receptors display different distances of closest approach to the cell surface and distinct lateral topologies depending upon whether they were bound to the antibody mAb 2E9. mAb 2E9 blocks EGF

binding to low affinity receptors[1] and as it is accepted that the two functionally distinct affinity classes of receptor are the produced as the same translation product[2], this suggests that ErbB1 receptors can adopt different orientations with respect to the cell surface that allow them to interact with other ErbB receptors in novel ways. In the same chapter it was shown that a further way to relate protein structure to function was possible by applying the bi-directional FRET method under experimental conditions designed to disrupt normal ErbB1 receptor function. The variations in ErbB1 receptor structure revealed under these different conditions were compared to semi-quantitative biochemical data which led to the suggestion that intracellular interactions might prime the orientations of ErbB1 ectodomains, which in turn control the topology of ErbB1s within complexes and the eventual signalling outcome produced by ligand binding.

The bi-directional FRET method is complimentary to the single molecule FRET and fluorescence polarisation imaging techniques that have also been developed recently within the STFC Photon Science Department[3, 4]. These single molecule methods have been used to remove the effects of ensemble averaging from the measurement of the distances between FRET donor and acceptor labelled EGF bound to ErbB1, providing evidence for the existence of two extracellular ErbB1 interfaces in the cell membrane environment that are different from the crystallographic back-to-back dimer[4, 5, 6]. Despite this, they lack the capability to reference the positions of the fluorescent labels to the surface of the cell membrane in order to observe large scale conformational differences that might allow different interfaces (such as the head-to-head interface[6]) to form. They also currently depend upon incomplete labelling of receptor populations in order to achieve single molecule sensitivity, which limits their ability to ascertain the stoichiometry and lateral topology of larger receptor oligomers. This is not a problem, however, for super-resolution techniques based upon the high precision localisation (with 2-10 nm accuracy) of single stochastically activated, photo-switchable fluorescent molecules[7, 8] which may soon provide an alternative method to FRET of observing the stoichiometry and lateral topology of receptor complexes in fixed cells.

Both the single molecule fluorescence and bi-directional FRET techniques provide information that can be used to inform atomistic molecular dynamics simulations based upon the solved crystal structures of ErbB1 receptors. The observation of short inter-ligand distances by single molecule FRET, ErbB1 oligomers larger than dimers[4] and the variation in the distances of closest approach of the ligand binding site to the cell membrane reported in chapter 6 of this thesis have prompted members of CCP4 to simulate ErbB1 monomers, dimers and tetramers in a model membrane. This work is currently unpublished, but in all cases stable configurations with the receptors lying 'flat' on the membrane consistent with the unexpected experimental results have been simulated.

Although the bi-directional FRET method has proven to be very promising, there is still vast scope for improving the technique and for future work. The majority of cell samples used to test the technique in chapter 6 were lightly fixed. This was initially employed in a preliminary experiment described in chapter 5 to lock receptors in active and inactive conformations before imaging. It was continued for the experiments in chapter 6 partially to make the results directly comparable to the results of that preliminary experiment, but mostly to remove the vagaries of live samples from the process of developing the technique. In future, the use of live cells would greatly improve the validity of any insights into structure-function relationships claimed from the results of the method. A better way of observing inactive (ligand free) ErbB ectodomains would be to introduce a small peptide tag to the N-terminus to which a functionalised fluorescent dye could be specifically bound to receptors *in situ*[9].

The need to invoke extra unknown variables to fit the simulated FRET efficiencies to experimental data (chapter 6.2.3) is also undesirable. In order to obtain quantitative results in a restricted period of time, it was assumed that these variables arose from variations in acceptor density on a scale below the resolution limit of the microscope and a fraction of donor labelled acceptors that were somehow excluded from acceptor. Efforts should be made to verify these assumptions experimentally by using different lipophilic dyes as the acceptor, which will partition in different areas of the cell membrane. Given more time, the

Monte-Carlo FRET simulation could also be used to investigate the effect of different, non-random distributions of acceptor in the membrane.

Better methods for disrupting receptor function should also be investigated. In the case of ErbB1 receptors, rather than using clumsy chemical methods to affect receptor function more specific perturbations of the functioning receptor such as ErbB1 mutants that lack tyrosine kinase activity or contain point mutations of tyrosine residues could be used. Mutants that alter the binding affinities of the receptor would also allow the relationship between binding affinity and ErbB1 ectodomain orientation to be investigated without the need for binding large antibodies to the receptor[1, 10].

As well as these possible avenues for improving the bi-directional FRET method and the results already obtained, the method offers the immediate opportunity to study the three-dimensional structures of ErbB hetero-oligomers simply by using other fluorescently labelled ErbB ligands. The ensemble FRET efficiencies measured between donor and acceptor labelled EGF in chapter 6 suggest that the majority of cell surface ErbB1s are either monomeric or interacting with receptors that do not bind to EGF. It would be particularly interesting to discover which the case is.

Finally, the bi-directional FRET method is not constrained for use with either the ErbB family of membrane receptors or the microscope described in chapter 4. Adaptation for the investigation of other membrane proteins requires only the characterisation of two FRET pairs appropriate for the expected dimensions of the protein of interest as described in chapter 5, followed by implementation of 1:1, site specific labelling of the extracellular domain of the particular protein of interest with the FRET donor. The method could also be implemented on any other microscope capable of both donor FLIM and acquisition of an intensity image of the acceptor distribution. Indeed, as multidimensional microscopes capable of video rate time-domain FLIM are becoming a reality[11-13] and now have similar accuracy to slower TCSPC systems, a realistic aim for the future development of the bi-directional FRET method could be to follow the

ectodomain structure of an ErbB receptor complex during, before and after ligand binding in real-time.

References

1. Defize, L. H. K. et al. Signal Transduction by Epidermal Growth Factor Occurs Through the Subclass of High Affinity Receptors. The Journal of Cell Biology 109, 2495-2507 (1989).
2. Ullrich, A. & Schlessinger, J. Signal transduction by receptors with tyrosine kinase activity. Cell 61, 203-212 (1990).
3. Webb, S. E. D., Needham, S. R., Roberts, S. K. & Martin-Fernandez, M. L. Multidimensional single-molecule imaging in live cells using total-internal reflection fluorescence microscopy. Optics Letters 31, 2157-2159 (2006).
4. Webb, S. E. D. et al. Single molecule imaging and FLIM show different structures for high and low-affinity EGFRs in A431 cells. Biophysical Journal 94, 803-819 (2008).
5. Ogiso, H. et al. Crystal structure of the complex of human epidermal growth factor and receptor extracellular domains. Cell 110, 775-787 (2002).
6. Garrett, T. P. et al. Crystal structure of truncated epidermal growth factor receptor extracellular domain bound to transforming growth factor alpha. Cell 110, 763-776 (2002).
5. Betzig, E. et al. Imaging Intracellular Fluorescent Proteins at Nanometer Resolution. Science 313, 1642-1645 (2006).
6. Bates, M., Huang, B., Dempsey, G. T. & Zhuang, X. Multicolor Super-Resolution Imaging with Photo-Switchable Fluorescent Probes. Science 317, 1749-1753 (2007).

7. Chen, I. & Ting, A. Y. Site-specific labeling of proteins with small molecules in live cells. Current Opinion in Biotechnology 16, 35-40 (2005).
8. Bellot, F. et al. High-Affinity Epidermal Growth Factor Binding Is Specifically Reduced by a Monoclonal Antibody and Appears Necessary for Early Responses. The Journal of Cell Biology 110 (1990).
9. Elson, D. S. et al. Real-time time-domain fluorescence lifetime imaging including single-shot acquisition with a segmented optical image intensifier. New Journal of Physics 6, 180 (2004).
10. Grant, D. M. et al. High speed optically sectioned fluorescence lifetime imaging permits study of live cell signaling events. Optics Express 15, 15656-15673 (2007).
11. Siegel, J. et al. Whole-field five-dimensional fluorescence microscopy combining lifetime and spectral resolution with optical sectioning. Optics Letters 26, 1338-1340 (2001).